

**Semiconductor Nanowire Josephson Junctions
In the search for the Majorana**

van Woerkom, David

DOI

[10.4233/uuid:8e71db73-d77d-4e53-ae13-33add0a9c5aa](https://doi.org/10.4233/uuid:8e71db73-d77d-4e53-ae13-33add0a9c5aa)

Publication date

2017

Document Version

Final published version

Citation (APA)

van Woerkom, D. (2017). *Semiconductor Nanowire Josephson Junctions: In the search for the Majorana*. [Dissertation (TU Delft), Delft University of Technology]. <https://doi.org/10.4233/uuid:8e71db73-d77d-4e53-ae13-33add0a9c5aa>

Important note

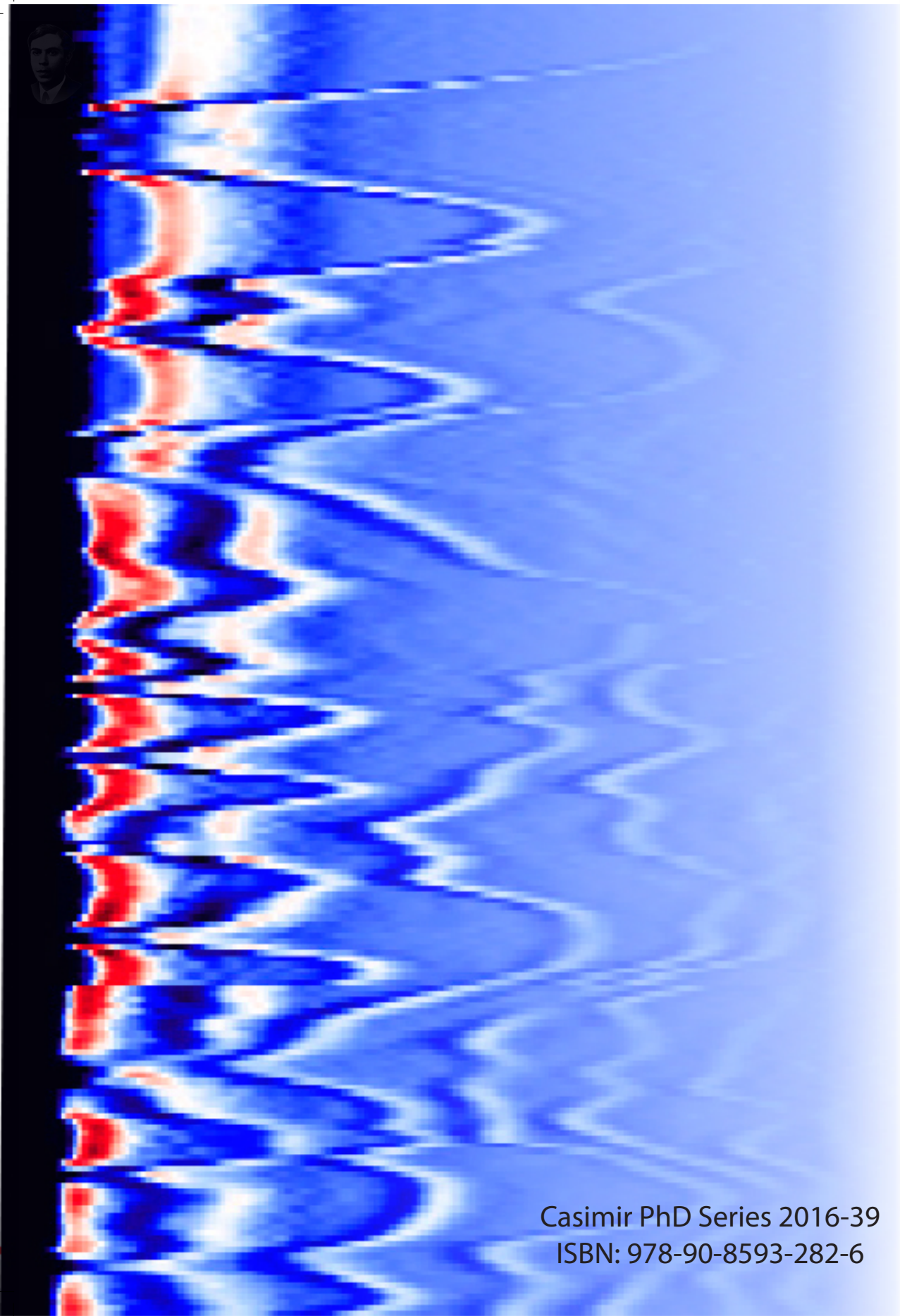
To cite this publication, please use the final published version (if applicable).
Please check the document version above.

Copyright

Other than for strictly personal use, it is not permitted to download, forward or distribute the text or part of it, without the consent of the author(s) and/or copyright holder(s), unless the work is under an open content license such as Creative Commons.

Takedown policy

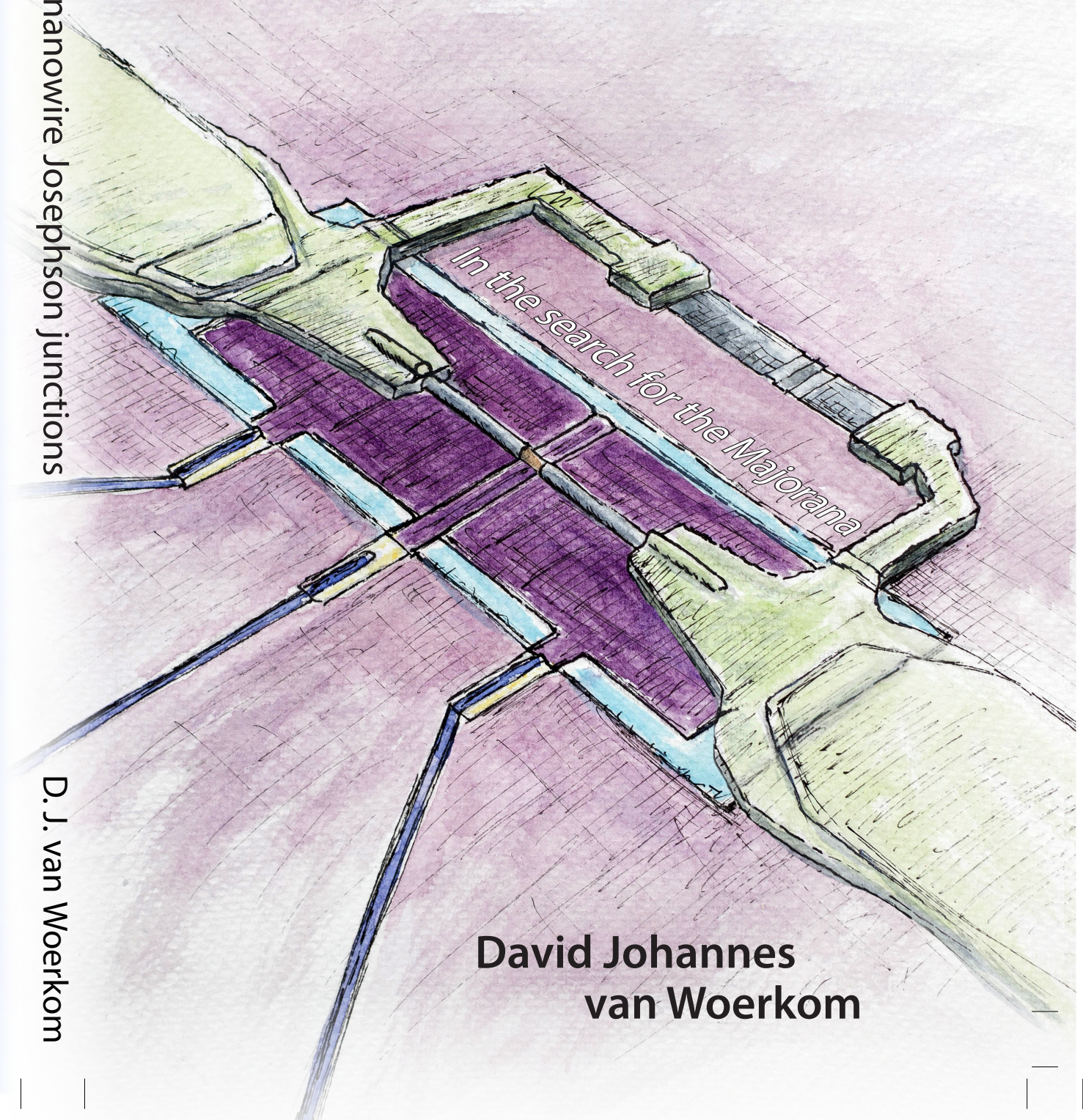
Please contact us and provide details if you believe this document breaches copyrights.
We will remove access to the work immediately and investigate your claim.



Casimir PhD Series 2016-39
ISBN: 978-90-8593-282-6

Semiconductor nanowire Josephson junctions

Semiconductor nanowire Josephson junctions



David Johannes
van Woerkom

D. J. van Woerkom

Propositions

accompanying the dissertation

SEMICONDUCTOR NANOWIRE JOSEPHSON JUNCTIONS IN THE SEARCH FOR THE MAJORANA

by

David Johannes VAN WOERKOM

1. Majorana fermions, as proposed by Ettore Majorana, cannot be measured.
2. Detection of fractional Josephson radiation is a key experiment towards braiding of Majorana zero modes.
3. Theoretical work on topological quantum computation is at least a decade ahead of experimental work.
4. The Nobel prize in physics is a prize of honor and should not come with money.
5. The world would be more peaceful with one religion.
6. Measuring remotely reduces the quality of experimental results.
7. PhD students should also be judged on their social skills.
8. Survival of the fittest in academia is required to guarantee the high standard of a PhD title.
9. Results of elections are determined by fear.
10. Finishing a marathon requires more persistence than finishing a PhD.

These propositions are regarded as opposable and defensible, and have been approved as such by the promotor prof. dr. ir. L. P. Kouwenhoven.

Stellingen

behorende bij het proefschrift

SEMICONDUCTOR NANOWIRE JOSEPHSON JUNCTIONS IN THE SEARCH FOR THE MAJORANA

door

David Johannes VAN WOERKOM

1. Majorana fermionen, zoals voorgesteld door Ettore Majorana, kunnen niet worden gemeten.
2. De detectie van fractionele Josephson straling is een belangrijk experiment richting het vlechten van Majorana toestanden.
3. Theoretisch werk over topologische kwantumcomputatie loopt minimaal een decennium voor op experimenteel werk.
4. De Nobelprijs in de natuurkunde is een prijs van eer en zou niet gepaard moeten gaan met geld.
5. De wereld zou vrediger zijn met slechts één godsdienst.
6. Meten op afstand verlaagt de kwaliteit van experimentele resultaten.
7. Promovendi zouden ook moeten worden beoordeeld op hun sociale kwaliteiten.
8. Het overleven van de sterkste in de academische wereld is nodig om de hoge standaard van de doctors titel te garanderen.
9. Verkiezingsuitslagen worden bepaald door angst.
10. Het uitlopen van een marathon vereist meer doorzettingsvermogen dan het afmaken van een promotietraject.

Deze stellingen worden oponeerbaar en verdedigbaar geacht en zijn als zodanig goedgekeurd door de promotor prof. dr. ir. L. P. Kouwenhoven.

**SEMICONDUCTOR NANOWIRE JOSEPHSON
JUNCTIONS**

IN THE SEARCH FOR THE MAJORANA

SEMICONDUCTOR NANOWIRE JOSEPHSON JUNCTIONS

IN THE SEARCH FOR THE MAJORANA

Proefschrift

ter verkrijging van de graad van doctor
aan de Technische Universiteit Delft,
op gezag van de Rector Magnificus prof. ir. K.C.A.M. Luyben,
voorzitter van het College voor Promoties,
in het openbaar te verdedigen op vrijdag 10 maart 2017 om 10:00 uur

door

David Johannes van Woerkom

Natuurkundig ingenieur
geboren te Schiedam, Nederland

Dit proefschrift is goedgekeurd door de

promotor: prof. dr. ir. L.P. Kouwenhoven

Samenstelling promotiecommissie:

Rector Magnificus,	voorzitter
Prof. dr. ir. L. P. Kouwenhoven	Technische Universiteit Delft, promotor
Dr. A. Geresdi	Technische Universiteit Delft, copromotor

Onafhankelijke leden:

Prof. dr. ir. L. M. K. Vandersypen	Technische Universiteit Delft
Prof. dr. Yu. V. Nazarov	Technische Universiteit Delft
Prof. dr. ir. A. Brinkman	Universiteit Twente
Prof. dr. K. Flensberg	Københavns Universitet
Dr. G. A. Steele	Technische Universiteit Delft



Keywords: Josephson junctions, Majorana, Andreev bound state, semiconductor nanowire, InSb, InAs.

Printed by: Gildeprint.nl

Front cover: by Vincent van Woerkom.

Back cover: experimental data from figure 9.2a of this dissertation.

Copyright © 2017 by D. J. van Woerkom
Casimir PhD series, Delft-Leiden 2016-39

ISBN 978-90-8593-282-6

An electronic version of this dissertation is available at
<http://repository.tudelft.nl/>.

A long time ago in a galaxy far, far away....

Voor mijn liefde en mijn trots.

CONTENTS

Summary	xiii
Samenvatting	xv
1 Introduction	1
1.1 Curiosity leads us onwards	2
1.2 Engineering Majorana zero modes in nanowires	2
1.3 Non-abelian exchange statistics.	2
1.4 The current status of the field	3
1.5 Outline of this thesis	3
2 Background	5
2.1 Introduction	6
2.1.1 Ettore Majorana and his equation	6
2.1.2 The search for Majorana fermions	7
2.2 (Topological) Quantum computation	9
2.2.1 Quantum computation and quantum bits	9
2.3 Topological quantum computation	9
2.3.1 Non-abelian exchange statistics	11
2.3.2 Braiding formalism	11
2.3.3 Braiding Majoranas without moving Majoranas	13
3 Theory	15
3.1 Introduction	16
3.2 Superconductivity	16
3.2.1 BCS Theory	16
3.2.2 The superconductor-normal interface	19
3.3 Josephson junctions	24
3.3.1 The Andreev bound state	24
3.3.2 Supercurrents carried by Andreev bound states	25
3.3.3 Weak links: SIS junctions.	28
3.3.4 Weak links: SNS junctions	32
3.3.5 Split junctions	40
3.4 Majorana physics	42
3.4.1 The Kitaev toy model.	42
3.4.2 The semiconductor/superconductor approach	44
3.4.3 Exponential coupling between Majoranas	48
3.4.4 Topological junctions	48

3.5	Charging and Josephson physics	51
3.5.1	Single electron transistors	51
3.5.2	Single electron transistors with Josephson coupling	52
3.6	Noise theory	56
4	Experimental methods	61
4.1	Introduction	62
4.2	Cryogenics	62
4.2.1	4K dipsticks	62
4.2.2	Dilution refrigerators	63
4.3	Electronic measurement setup	64
4.3.1	Voltage and current bias	64
4.3.2	Two- and four-point measurements	68
4.4	Low-noise electronics and filtering	68
4.5	Low electron temperature.	71
4.6	Cleanroom fabrication	72
5	Towards high mobility InSb nanowire devices	73
5.1	Introduction	74
5.2	Experimental setup	76
5.3	Extracting mobility	76
5.4	Comparison of field effect mobility extraction methods	78
5.5	Simplification of gate voltage-independent interface resistances	80
5.6	Nanowire surface and adsorption	80
5.7	Substrate cleaning	82
5.8	Contact spacing.	83
5.9	Reproducibility	84
5.10	Conclusion	84
5.11	Supplementary information	86
5.11.1	Optimized fabrication recipe.	86
5.11.2	Measurements details	86
5.11.3	Overview of measured devices	87
5.11.4	Average device characteristics obtained from several measurement and fabrication runs	88
6	One minute parity lifetime of a NbTiN Cooper-pair transistor	89
6.1	Introduction	90
6.2	Experimental setup	91
6.3	Measurement technique	93
6.4	Characterization values	93
6.5	Temperature dependence of τ_p	93
6.5.1	Standard shielding	93
6.5.2	Extra shielding	94

6.6	Parity state distillation	95
6.7	Magnetic field dependence of τ_p	96
6.8	Conclusions.	97
6.9	Supplementary information	98
6.9.1	Device fabrication	98
6.9.2	Measurement setup	100
6.9.3	Evaluation of the parity lifetime	101
6.9.4	Measurement of the Dynes parameter of the NbTiN island	103
6.9.5	Superconducting thin film characterization and magnetic field dependence	104
7	Josephson radiation and shot noise of a semiconductor nanowire junction	107
7.1	Introduction	108
7.2	Device fabrication and layout.	108
7.3	Theory	109
7.4	Discussion	111
7.5	Conclusions.	113
8	Fractional Josephson radiation at finite magnetic field	115
8.1	Introduction	116
8.2	Measurement technique	116
8.3	Technical improvements	117
8.4	Radiation at zero magnetic field.	119
8.5	Radiation at finite magnetic field	122
8.6	Detected radiation as a function of gate voltage.	124
8.7	The 1 and 2 slopes	125
8.8	Conclusion and discussion	127
9	Microwave spectroscopy of spinful Andreev bound states in ballistic semiconductor Josephson junctions	129
9.1	Introduction	130
9.2	Device setups	130
9.3	Plasma mode characterization	133
9.4	ABS gate voltage dependence	133
9.5	ABS flux dependence	134
9.6	Hybrid SQUID model	134
9.7	In-plane magnetic field dependence	136
9.8	Conclusion	138
9.9	Supplementary information	139
9.9.1	Device fabrication	139
9.9.2	Measurement setup	139
9.9.3	Device circuit parameters	140
9.9.4	Spectrum analysis	140
9.9.5	$I(V)$ trace of the hybrid SQUID.	142
9.9.6	Fit of ABS with high transmission	145
9.9.7	Symmetry-broken ABS in bipolar magnetic field.	146

9.10 Theory	146
9.10.1 Estimate of the ABS-plasma resonance avoided crossing	146
9.10.2 Hamiltonian description of the hybrid SQUID	147
9.10.3 Equilibrium phase drop	148
9.10.4 Andreev bound states in a proximitized Rashba nanowire in a parallel magnetic field.	149
9.10.5 Orbital field	152
9.10.6 Fits to the data	153
10 Outlook	155
10.1 Introduction	156
10.2 Perspectives on material improvement	156
10.2.1 Gates and dielectric	158
10.3 Perspectives on poisoning dynamics	159
10.4 Perspectives on Majorana and Josephson radiation detection.	160
10.5 Perspectives on Andreev bound state spectroscopy	161
10.5.1 Measure of long-junction Andreev bound states	161
10.5.2 Improve the coupling circuit	161
10.6 Towards braiding of Majorana zero modes	162
A Appendix	165
A.1 Derivation of the braiding operator.	165
A.2 Checking the non-abelianess of MZM.	166
A.3 Using the braiding operator U	166
B Appendix	169
C Appendix	173
D Appendix	175
E Appendix	177
E.1 LCR-network environment	178
E.2 ABS in the environment.	179
F Appendix	181
Bibliography	185
Acknowledgements	203
Curriculum Vitæ	209
List of Publications	211

SUMMARY

Due to the collective behaviour of electrons, exotic states can appear in condensed matter systems. In this PhD thesis, we investigate semiconducting nanowire Josephson junctions that potentially have Majorana zero modes (MZM) as exotic states. MZM are expected to form a robust quantum bit and quantum operations are done by interchange, otherwise known as braiding. The presence of MZM in a Josephson junction creates a topological junction, with properties which are drastically different from a normal Josephson junction. Understanding such topological junctions is of key importance in developing circuits for MZM braiding.

We begin by investigating the InSb nanowire contact recipe and developing a fabrication protocol to obtain the highest possible electron mobilities. We find that it is key to clean the substrate with oxygen plasma before nanowire deposition and thoroughly pump the sample space to obtain high mobilities. We conclude that the presence of water, organic residues or fabrication solvents reduces nanowire quality in terms of the measured field-effect mobility.

To engineer MZM in condensed matter, InSb nanowires are often interfaced with Nb-based superconductor contacts to induce superconductivity. We measure for the first time parity in this superconductor, with parity lifetimes up to 1 minute in NbTiN. Even in an applied magnetic field of 150mT we still observe lifetimes in the millisecond range. Parity conservation is essential in revealing the topological properties of a junction with MZM and it is also a requirement for any MZM braiding experiment.

Topological junctions exhibit the fractional AC Josephson effect. We investigate this effect by analysing the emissions from a nanowire Josephson junction. The dominant frequency should differ by a factor of 1/2 from the standard Josephson frequency. In our initial experiments we characterize the measurement circuit and the photon-assisted-tunneling detection method using an on-chip thin oxide junction. After circuit and device improvements, we are able to make measurements in a magnetic field of up to 300mT. We find a value of e/h^1 for the ratio between detected frequency and applied nanowire voltage at finite magnetic field, instead of the usual $2e/h$. This signature is robust against changes in magnetic field and applied gate voltage. This hints at a topological origin for the detected signal.

The properties of any Josephson junction are determined by the underlying properties of the Andreev bound states. We perform on-chip microwave spectroscopy of these states and introduce them one-by-one with local gate tuning. We use a theoretical model that includes interactions with the plasma mode of the circuit to describe the measured spectrum. We find transmissions of up to 0.9 for the Andreev bound states, indicating ballistic transport. By applying a magnetic field of up to 300mT, we are able to measure spin-split Andreev bound states. These are supported by a model which includes Zee-

¹ Electron charge divided by the Planck constant.

man effect and spin-orbit coupling. In a gate regime with multiple Andreev bound states we observe symmetry-broken Andreev bound states by applying a moderate magnetic field of 40mT.

Important steps are taken in the fabrication, engineering and understanding of nanowire Josephson junction systems. Further identification, control and understanding is needed if we are to develop useful applications of MZM braiding.

SAMENVATTING

Door het collectieve gedrag van elektronen kunnen exotische toestanden voorkomen in vaste stof systemen. In dit proefschrift onderzoeken we het systeem van een halfgeleidende nanodraad Josephson junctie met de mogelijke aanwezigheid van Majorana nul toestanden (MNT). MNT zijn naar verwachting een mogelijkheid om een robuuste kwantumbit te construeren. Kwantum operaties kunnen worden gedaan door middel van het verwisselen (vlechten) van MNT. De aanwezigheid van MNT in Josephson juncties vormt topologische juncties die totaal andere eigenschappen hebben dan de normale Josephson juncties. Het begrijpen van een topologische junctie is van groot belang voor het ontwikkelen van een circuit voor het vlechten van MNT.

De experimenten beginnen met het onderzoeken van het contactrecept voor InSb nanodraden en het ontwikkelen van een fabricageprotocol dat ervoor zorgt dat de elektronenmobiliteit zo hoog mogelijk is. We ontdekten dat het zeer belangrijk is om het substraat voor de nanodraaddepositie schoon te maken met een zuurstofplasma. Ook het vacuüm pompen van het cryogene systeem waarin de nanodraad zich bevindt bleek essentieel voor het verkrijgen van een hoge mobiliteit. We concluderen dat water, organische residuen en de gebruikte fabricage-oplosmiddelen de kwaliteit van de nanodraden negatief beïnvloeden wat betreft de gemeten elektronenmobiliteit.

MNT in vastestof systemen worden vaak gecreëerd door InSb nanodraden in contact te brengen met een op Nb gebaseerde supergeleider. We meten voor het eerst pariteit in deze supergeleiders en tonen pariteitsbehoud aan tot 1 minuut in NbTiN. Zelfs in een magneetveld van 150mT is de tijdschaal van de pariteit nog in de orde van milliseconden. Pariteitsbehoud is essentieel voor het onthullen van de topologische eigenschap van juncties met MNT en is een vereiste voor het vlechten van MNT in een experiment.

Topologische juncties zijn anders dan normale Josephson juncties omdat ze zich gedragen volgens het fractionele AC Josephson effect. Het AC Josephson effect onderzoeken wij door de emissie van een nanodraad Josephson junctie te analyseren. De dominante frequentie zou een factor 1/2 moeten verschillen van de normale Josephson frequentie. In een eerste ronde experimenten karakteriseren we het meetcircuit en het fotongeassisteerd tunnelen in een dunne oxide tunneljunctie als detectie methode. Na verbeteringen aan het circuit en het nanodraadsysteem is het mogelijk om deze metingen bij een magneetveld van 300mT uit te voeren. Hierbij meten we een e/h -ratio² tussen de nanodraadspanning en de gemeten frequentie, in plaats van de gebruikelijke $2e/h$ bij een normale junctie. We concluderen dat het gevonden signaal robuust is als functie van magneetveld en elektrisch potentiaal van de gates onder de nanodraad. Dit wijst in de richting van een topologische oorsprong van het gedetecteerde signaal.

De eigenschappen van elke Josephson junctie worden bepaald door het onderliggende mechanisme van gebonden Andreev toestanden. Met microgolfspectroscopie laten we

²Elektron lading gedeeld door de constante van Planck.

de gebonden Andreev toestanden zien en we kunnen met lokale gates de toestanden één voor één introduceren. We gebruiken een theoretisch model dat ook de interactie met de resonantiefrequentie van het circuit meeneemt om de gemeten spectra in detail te verklaren. We concluderen dat we toestanden hebben met een transmissie tot 0.9, wat ballistisch transport aanduidt. Door een magneetveld van 300mT aan te leggen, meten we spingesplitste gebonden Andreev toestanden. Deze worden ondersteund door een model met het Zeemaneffect en spin-baankoppeling. In een gatespanningsregime met meerdere gebonden Andreev toestanden observeren we Andreevtoestanden waarvan de symmetrie gebroken is in het gemeten spectrum bij een magneetveld van 40mT.

Belangrijke stappen zijn genomen richting het fabriceren, ontwikkelen en begrijpen van het nanodraad Josephson junctiesysteem. Verdere identificatie, controle en inzicht is nodig voor het ontwikkelen van circuits voor het doen van een MNT vlechtexperiment.

1

INTRODUCTION

In the beginning, God created the heaven and the earth.

The Holy Bible

Everything must have a beginning.

For me, it began with my desire to answer questions by doing challenging experiments. Ettore Majorana had a similar motivation when he asked himself the question, 'Is it possible to find a solution to the Dirac equation without a negative energy solution?' He indeed found such a solution, leading him to propose the existence of the particle now known as the Majorana fermion. To realize Majorana state zero modes (MZM), the condensed matter versions of Majorana fermions, Alexei Kitaev suggested combining the properties of a semiconducting nanowire and a superconductor. The interchange properties of these MZM are different from those of regular Majorana fermions, since these modes are expected to be non-abelian. This special property can be used for topological quantum computation, so many research groups are trying to find and control these MZM. We give a brief overview of the current state of research into MZM.

1.1. CURIOSITY LEADS US ONWARDS

It is in the nature of humans to be curious about the world around us. This curiosity has led us to explore the extremes, from the smallest parts of atoms to the origin of stars. Science has made large leaps in understanding in both of these fields, but still there is much that is unknown. It could even be that these diverse problems are related. One particle that *could* exist both in atoms and in outer space is the Majorana fermion[1, 2].

In 1937, the bright young Italian scientist Ettore Majorana proposed the existence of the particle which is now known as the Majorana fermion[3]. This particle is special in the sense that it is its own anti-particle. Where normally an anti-particle has properties opposite to those of its counterpart, in a Majorana fermion all these properties are zero. This is necessary for it to be its own anti-particle, but because all its properties are zero¹ it is very difficult to detect. Indeed, even the Large Hadron Collider at CERN in Geneva, Switzerland has so far failed to detect any signature of this elusive particle[2]. As a result, it is also a candidate to be dark matter.

1.2. ENGINEERING MAJORANA ZERO MODES IN NANOWIRES

Some scientific disciplines, such as high energy physics and astronomy, have to make do with what nature gives them, but thankfully we are able to build our own experiments. It was Alexei Kitaev who came up with the idea of engineering MZM in a condensed matter system[4]. Due to the collective behaviour of electrons in materials, they can have new properties like fractional charge (the fractional quantum Hall effect[5]) or the ability to form charge waves (known as plasmons[6]). Kitaev considered, in a superconducting regime, a one dimensional (1D) grid of lattice sites that could be occupied by electrons in order to form MZM at the end of the grid. Unfortunately, the proposed superconductor needs to be spinless, and such a material is not known to exist in nature. This made Kitaev's proposal an unrealistic toy model at the time.

In 2010, two independent groups, Lutchyn *et al.*[7] and Oreg *et al.*[8], proposed a way to engineer such a spinless superconductor and thus create MZM. Two years later, the group led by Leo Kouwenhoven at the University of Delft in the Netherlands found the first signatures of MZM in the proposed system[9]. Multiple groups subsequently found similar[10, 11], improved [12] and additional signatures [13–15].

1.3. NON-ABELIAN EXCHANGE STATISTICS

Theoreticians have proposed ways of engineering MZM in a realistic experimental setup. These MZM differ from the original Majorana fermions in their exchange statistics.

Currently, all known particles in free space can be divided into two classes, fermions and bosons, differing in their exchange statistics. Suppose you have a system composed of two identical particles and described by $|\psi(x_1, x_2)\rangle$, where the first (second) particle is at x_1 (x_2). Given an operation P that exchanges the particles, exchanging twice gives $P^2|\psi(x_1, x_2)\rangle = |\psi(x_1, x_2)\rangle$, recovering the original state of the system if the particles are indistinguishable. So $P^2 = 1$, implying $P = \pm 1$. These two solutions define fermions ($P = -1$) and bosons ($P = +1$). MZM are not part of either of these two classes. They belong

¹except mass

to their own class, expected to be the class of non-abelian anyons[1, 4]. This is because exchanging twice does not return the state to $|\psi(x_1, x_2)\rangle$, as for MZM the wavefunction ψ itself changes under the action of the operator P [1].

This is interesting from a theoretical point of view, but we also have the opportunity to make a robust 'quantum bit' or qubit out of MZM[16, 17]. Quantum systems with a few qubits (typically ~ 5) already exist, and are promising proofs of the quantum computing concept[18, 19]. However, these qubits are difficult to scale up because of decoherence due to environmental noise. Imagine a qubit as a compass needle, with the value 1 if the needle is pointing north, and 0 if it is pointing south. The slightest movement or gust of wind will make the needle shake, potentially corrupting the pure state of 1 (north) or 0 (south). MZM are expected to be more robust against losing quantum information as it is stored non-locally, making it less sensitive to local noise.

1.4. THE CURRENT STATUS OF THE FIELD

Multiple groups are trying to find more signatures and get better control of MZM. The goal is to exchange MZM and demonstrate their non-abelian properties, leading to the creation of a qubit. This is also the final goal of the work we report in this thesis. We investigate many aspects of systems that can host MZM, ranging from material optimization to parity fluctuations in superconducting islands, switching current measurements and Andreev bound state spectroscopy of nanowire Josephson junctions. All these experiments are performed with materials that are used in, or can host, MZM.

Many other groups have recently conducted experiments related to MZM. The group led by Charles Marcus in Copenhagen has recently made very good progress, and we have also worked together with them on a few projects. The Marcus group developed semiconducting nanowires with a thin aluminium shell[20]. The shell is deposited on the nanowire in vacuum to obtain a clean interface. The aluminium becomes superconducting at low temperatures, nicely inducing superconducting properties in the nanowire [21]. These nanowires are also used for the experiments in Chapters 8 and 9. In one of their first experiments[22] with these nanowires, they created a superconducting island and observed even-odd effects due to the superconductor preferring a $2e$ ground state. In addition they also observed a poisoning effect with a characteristic timescale of 10ms. In a follow-up experiment, Albrecht *et al.*[14] also observed even-odd effects, but after they initially disappeared with increasing magnetic field they then observed oscillations in the effect. They explained these oscillations by the presence of MZM at finite energy due to overlap of the Majorana wavefunctions. Most recently[23], the same effect has been observed in a double superconducting island.

In Delft we have also made progress using the nanowires from the Marcus group. The 2012 experiment with zero-bias-peak detection[9] was recently reproduced in a much cleaner device[12].

1.5. OUTLINE OF THIS THESIS

In the first experiments reported here, we investigate the influence of cleanroom fabrication on nanowire mobility. In Chapter 5 we draw conclusions as to whether the use of solvents, contact recipes and cleaning harms or improves nanowire quality.

1

To begin working towards braiding MZM, we make superconducting islands out of NbTiN. This material was at the time the most used superconductor for Majorana devices. We are able to read out the parity of the superconducting island, something that has already been shown in aluminium islands[24, 25] but never in any other superconductor. In Chapter 6, we show these parity effects in a Nb-based superconductor for the first time and demonstrate very long parity lifetimes even in a moderate magnetic field of $\sim 150\text{mT}$.

In the remaining three chapters, two different techniques are used to investigate nanowire Josephson junctions consisting of two superconducting electrodes in contact with a single nanowire. These systems can host MZM and give strong signatures of their existence.

The experiment described in Chapter 7 investigates the AC Josephson effect in such a nanowire Josephson junction. In this experiment the junction has a bias voltage V_{bias} and emits radiation at the Josephson frequency, $2eV_{\text{bias}}/h$, which changes to eV_{bias}/h in the presence of MZM. The radiation is detected by an on-chip detector via the photon-assisted tunneling current. Due to limitations in the performance of the detector in a magnetic field we were not able to measure at finite magnetic field. After adjusting the design, material system and measurement technique, we are able to observe the e/h radiation in a moderate magnetic field of $\sim 100\text{mT}$. The status of this experiment is described in Chapter 8.

In our final experiment, we perform spectroscopy of Andreev bound states in nanowire Josephson junctions. The device used for this is very similar to the one for the radiation experiments, but with some small adjustments. This time, the junction is embedded in a superconducting quantum interference device (SQUID) loop, giving us the ability to tune the phase of the nanowire. A superconductor-insulator-superconductor (SIS) Josephson junction is used as an on-chip spectrometer, exciting Andreev bound states in the nanowire. This excitation is measured in the spectroscopy junction using an enhanced current. Due to the gate tunability of the nanowire we can investigate both single and multiple Andreev bound states, introducing them one by one. We indirectly observe spin-split and symmetry-broken Andreev bound states in a finite magnetic field.

Suggestions for continuing and improving the reported experiments are presented in the outlook chapter. Here we also discuss possible future steps towards MZM braiding.

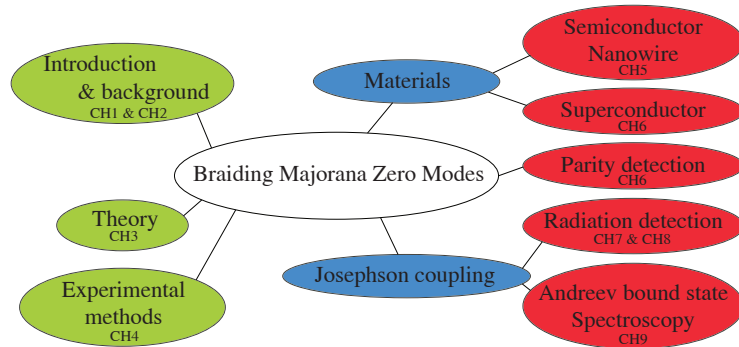


Figure 1.1: Quick overview of the outline of the thesis

2

BACKGROUND

History is important, because you can learn from it. The future is interesting, because you can use the things you have learned there. In this chapter we look back at Ettore Majorana's prediction. From there we start our search for the Majorana fermion and then Majorana zero modes (MZM). Our search is strongly focused on condensed matter systems, the topic of this thesis. For condensed matter systems, theoreticians have found a way to engineer MZM using a combination of one-dimensional InSb or InAs nanowires in close proximity to a superconductor in a parallel magnetic field. Theoreticians have proposed that MZM could be a robust way of storing quantum information and may allow the creation of reliable quantum gates. This is why topological quantum computing is such a promising idea, as we will discuss at the end of this chapter.

2.1. INTRODUCTION

In this chapter, we briefly discuss the background and motivation for the discovery and control of MZM.

Ettore Majorana's proposal of Majorana fermions grew out of his study of the Dirac equation, as shown in Section 2.1.1. The search for these particles in free space is discussed in Section 2.1.2.

MZM are the condensed matter equivalents of Majorana fermions. These states are interesting for quantum computation, as we explain in Section 2.2. In Section 2.3, topological quantum computation is introduced. Starting from the definition of non-abelian exchange statistics, we show that MZM are non-abelian. After that, we go on to explain the formalism of MZM braiding.

2.1.1. ETTORE MAJORANA AND HIS EQUATION

This section is divided into two parts, discussing first Majorana's history before delving into his physics. We believe that he is a person of particular interest, and deserves a fuller introduction.

ETTORE MAJORANA THE PERSON

We begin with two examples, one less and one more famous example of Ettore Majorana's unique talent and personality. Both examples are taken from the book [26], which I received after my master's graduation.

In 1928, at the age of 21, Majorana decided to become a theoretical physicist despite receiving no support from his family. He joined a group of young Italian physicists led by Enrico Fermi, now known as the Via Panisperna boys. Barely adults, they spent their time wagering on who could solve differential equations the fastest and challenging each other to come up with the craziest theories of the universe. When Majorana was first introduced to Enrico Fermi, Fermi presented him with a problem they were working on at the time. Majorana asked a few questions and left enigmatically[26].

The next day, when Majorana met Fermi again, he reproduced the problem, did some quick calculations and congratulated Fermi on not making any mistakes. Majorana continued on the blackboard, rewriting the problem into a well-known textbook example which went on to become the starting point for the problem's solution. Enrico Fermi, later winner of the 1938 Nobel prize, rated himself as merely second class in comparison to Majorana, whom he ranked alongside Newton and Galileo[26].

Unfortunately, Ettore Majorana is more famous for his disappearance in 1938. On Friday, March 25, 1938 he boarded a mail boat in Naples, heading for Palermo. When he arrived in Palermo, he wrote a letter to his boss Antonio Carrelli, Director of the Naples Physics Institute, with the remarkable statement that 'The sea rejected me'. A few days later he returned to Naples, sharing a cabin with two other people, one of whom confirmed that Ettore was still asleep when they arrived at the port. After that, Ettore Majorana was never seen nor heard from again.

ETTORE MAJORANA AND HIS PREDICTION

Majorana also worked on the Dirac equation, trying to solve the remaining mystery, namely the presence of negative energy solutions.

The Dirac equation is given by

$$\frac{E}{c}\Psi(x, t) = \vec{\alpha} \cdot \vec{p}\Psi(x, t) + \beta mc\Psi(x, t), \quad (2.1)$$

where E is the energy of the particle, c is the speed of light, $\Psi(x, t)$ is the wavefunction, \vec{p} is the momentum and m is the mass of the particle. $\vec{\alpha}$ and β are constants, introduced by Dirac to linearize the Klein-Gordon (KG) equation. To maintain consistency with the KG equation, certain constraints must hold and these led Dirac to discover solutions for the electron and the positron[27]. Using the same constraints, Majorana found

$$\begin{aligned} \alpha_x &= \sigma_x \otimes \sigma_x & \alpha_y &= \sigma_z \otimes I \\ \alpha_z &= \sigma_x \otimes \sigma_z & \beta &= -\sigma_x \otimes \sigma_y \end{aligned}$$

where I is the 2 x 2 identity matrix and the σ s are the Pauli matrices. In addition, Majorana divided eq. 2.1 by $-\frac{\hbar}{i}$, substituted $\beta' = -i\beta$ and used $E = i\hbar \frac{d}{dt}$, the energy operator. This gave equation (8)' in ref. [3], namely

$$\vec{\alpha} \cdot \vec{\nabla} \Psi - \beta' \frac{mc}{\hbar} \Psi = \frac{1}{c} \frac{d\Psi}{dt}, \quad (2.2)$$

a completely real equation. This yields a real expression for Ψ , implying that the complex conjugate Ψ^\dagger is equal to Ψ , where Ψ^\dagger is the anti-particle solution to the Dirac equation. This means that the solutions to eq. 2.2 represent particles that are equal to their own anti-particle. Majorana had already concluded that these particles are neutral in charge. The only known neutral particles at that time were the neutron and the neutrino, but he ruled out the neutron due to its large mass[3].

For historical reasons, because eq. 2.2 is effectively the Dirac equation and that equation describes the behaviour of fermions, the particle proposed by Majorana is known as the Majorana fermion.

2.1.2. THE SEARCH FOR MAJORANA FERMIONS

The search for the Majorana fermion started with the first experimental investigation of double β -decay[28]¹. When an atom decays by the emission of two electrons, called double β -decay, two electron anti-neutrinos ($\bar{\nu}_e$) are emitted, as shown in the Feynman diagram in Figure 2.1a and referred to as $2\nu\beta\beta$. The two electrons have a *maximal* energy of $Q_{\beta\beta}$. In the case of Majorana neutrinos all the energy of the W^- boson is transferred to the electrons since no neutrinos escape from the process, so a joint energy measurement on both electrons gives always $Q_{\beta\beta}$. This decay process is called $0\nu\beta\beta$, and is depicted in Figure 2.1b.

There are ~ 10 known isotopes that undergo $2\nu\beta\beta$ -decay. They all have typical half-lifetimes of 10^{18} - 10^{22} years and their natural abundance is low, typically 5-10%. Researchers have tried to use big blocks (up to 1 tonne) of purified isotopes such as ^{76}Ge to study double β -decay. The expected energy distribution is depicted in Figure 2.2a. The two-electron energy is a distribution because the neutrino energies cannot be measured,

¹This reference is used throughout this section.

2

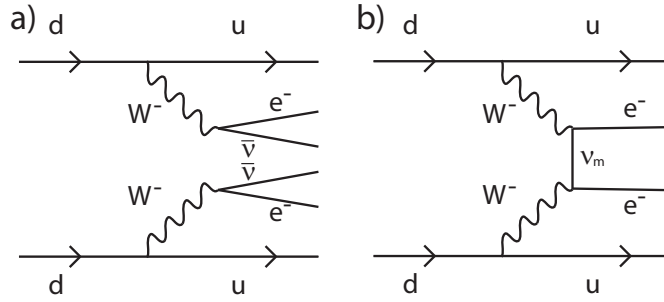


Figure 2.1: Feynman diagrams of double β -decay. u (d) represents the up (down) quark, e^- the electron or β radiation, W^- the W^- boson, $\bar{\nu}_e$ the electron anti-neutrino and ν_m the Majorana neutrino or Majorana fermion. **a)** Double β -decay with the emission of two electron anti-neutrinos, referred to as $2\nu\beta\beta$. **b)** Double β -decay where the Majorana neutrinos ν_m are annihilated and no energy ‘disappears’ from the decay event, referred to as $0\nu\beta\beta$.

and is bounded above by $Q_{\beta\beta}$. The $0\nu\beta\beta$ -decay process only adds counts at $Q_{\beta\beta}$ since no energy leaves the system and all the energy is carried by the emitted electrons.

Figure 2.2b shows a Monte Carlo simulation of the energy spectrum around $Q_{\beta\beta}$. For this simulation a background rate of 1 count per keV and 50 $0\nu\beta\beta$ -decay processes are modelled, with an energy resolution of 3.5%. To make progress, this background rate needs to be reduced and the energy resolution improved, as no $0\nu\beta\beta$ -processes have yet been detected. Based on their sensitivity, experiments only can give lower bounds on the half-lifetimes of $0\nu\beta\beta$, currently known to be $\geq 10^{25}$ years.

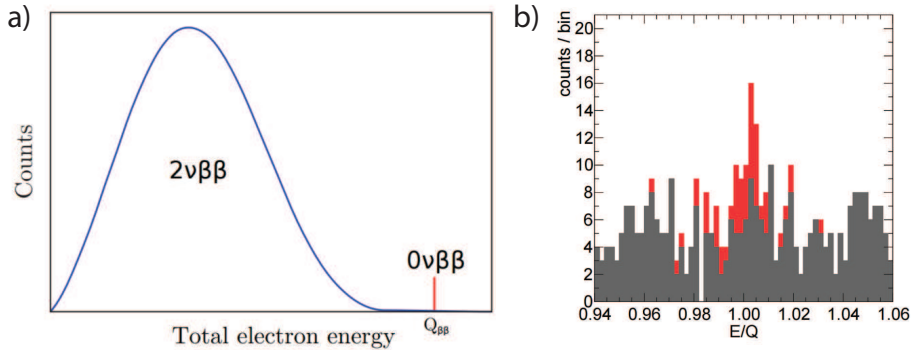


Figure 2.2: **a)** Schematic energy spectrum of the electrons emitted by $2\nu\beta\beta$ -decay (in blue) and $0\nu\beta\beta$ -decay (in red). **b)** Monte Carlo simulation of $2\nu\beta\beta$ (grey) with a rate of 1 count/keV and 50 counts of $0\nu\beta\beta$ (in red) with a full width at half maximum (FWHM) energy distribution of 3.5%. Figure reproduced from [28]. $Q_{\beta\beta} = 2039\text{keV}$, the electron energy of ^{76}Ge -decay. Figure reproduced from [29].

The detection of $0\nu\beta\beta$ -decay would have a great impact on the Standard Model of particle physics. This is because lepton number is not conserved in this process. On the left of the Figures in 2.1 there are only quarks (meaning the lepton number is 0) while on the right, in the $0\nu\beta\beta$ case, there are two electrons for a lepton number of +2. This process violates the conservation of lepton number by generating leptons, something that

has never been observed before. By contrast, in Figure 2.1b the electron anti-neutrinos, $\bar{\nu}_e$, have lepton number -1, meaning that lepton number is conserved in this case. We also observe that processes breaking this conservation law must have occurred at some point in the past, since there is currently more matter in the universe (positive lepton number) than anti-matter (negative lepton number). The observation of $0\nu\beta\beta$ -decay could give more insight into the creation of the universe.

2

2.2. (TOPOLOGICAL) QUANTUM COMPUTATION

In this section we discuss why quantum bits are a promising way to increase the computational power of future computers. Any two-level quantum system can be used as a quantum bit. In particular, the condensed matter version of the Majorana fermion, the MZM, can be used as quantum bit. Quantum computation with MZM is known as topological quantum computation, which we will introduce later in this chapter.

2.2.1. QUANTUM COMPUTATION AND QUANTUM BITS

Currently, the computer that you have in your office or at home is based on bits, which can be either 0 or 1. If you have 3 bits there are $2^3 = 8$ possibilities (namely 000, 001, 010, 011, 100, 101, 110 and 111, which counts from 0 to 7 in the binary number system). In a classical computer these bits can be for example 001, 101 *or* 111. A computation, called (say)² Q , can take one input value and produce one output value, turning 001 into $Q001$ for example.

Quantum computers rely on bits which exist in a regime where quantum mechanics plays a role. The wavefunction of a particle can be interpreted as describing its location (for example) statistically; it need not have a definite position. You can create two local potential minimums (quantum wells) and arrange for the wavefunction to be finite in both of them, known as a superposition state. If the particle is in the left quantum well we can call that a value of 0, and if it is in the right one we can call it a value of 1. If the wavefunction is finite in both wells, we can say that the value is both 0 and 1 at the same time. Such a bit is known as a quantum bit or qubit[30].

With 3 qubits we have the same options, in the binary number system, as with bits but now we can put the system in a quantum superposition state of 001+101+111 for example, including all three options at the same time, as depicted in Figure 2.3. This time, to perform a calculation Q on all three options, we would only have to perform it once.

2.3. TOPOLOGICAL QUANTUM COMPUTATION

In topological quantum computation, the information is stored in multiple (at least four) non-local MZM whose ground states are degenerate and separated from the excited states by an energy gap. There is no energy difference between the 1 and 0 states, because both are ground states of the system. This makes them insensitive to energy exchange decoherence with the environment. Quantum gates rely on braiding the MZM, which is non-trivial due to their non-abelian exchange statistics. The quantum gates must be

²What Q does is not important.

2

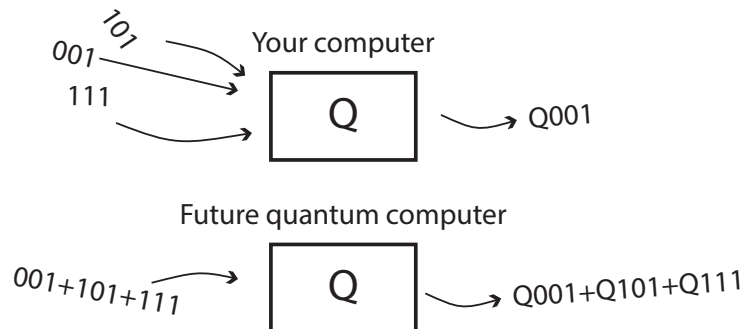


Figure 2.3: Schematic comparison between a computer and a quantum computer performing a calculation Q . A classical computer, such as your computer, can only do calculations one by one, while a future quantum computer will be able to do multiple calculations at the same time depending on how the qubits are prepared.

performed slowly, compared to the energy gap to the excited states, to make sure that the system stays in the computational ground state.

In general, quantum computations using topological systems are expected to be more robust to local perturbations because it is difficult to change the topology of a system[31].



Figure 2.4: A glass of (red) wine is topologically inequivalent to a beer mug or a donut. The beer mug and the donut are topologically equivalent because both objects have a single hole. Parts of this image are adapted from <http://www.freepik.com/>.

To explain topology, we begin with two of the most-used examples. A donut and a beer mug both have one hole and can be slowly transformed into each other. This is not possible with a glass of red wine³. With the glass, at some point you would have to poke a hole in it to make it equivalent to the donut or the beer mug. This makes the donut and the beer mug members of the same topological class, while the glass of wine is part of a different class.

The quasiparticles which we investigate in this thesis are MZM in semiconductor nanowires with induced superconductivity. At zero magnetic field the superconducting gap is ‘positive’ (Δ_{SC}), while with a finite magnetic field this is inverted to a ‘negative’ (Δ_{TOPO}) gap. The moment of gap inversion is like poking a hole in the glass to make it a donut. At the crossing point from Δ_{SC} to Δ_{TOPO} , MZM are created.

³Or white wine.

2.3.1. NON-ABELIAN EXCHANGE STATISTICS

If particles are exchanged twice in 3D space, the resulting wavefunction is the same as it was to start with, i.e. $\Psi(t = t_0) = P^2\Psi(t = 0)$. This assumes that the time $t = 0$ was before the exchanges and at $t = t_0$ the exchange is finished. P is the exchange operator and can return -1 (fermions) or +1 (bosons). That the interchange is performed in 3D is an important consideration. Despite the limitations of this piece of paper or screen, please imagine the sketches in Figure 2.5 in 3D. In Figure 2.5a a particle, drawn as a black circle, moves in a small trajectory that takes it near another particle without enclosing it. If this trajectory is made very small, effectively zero, the wavefunction is unperturbed. Now if this trajectory is enlarged sufficiently the other particle can be enclosed, as depicted in Figure 2.5c. In 3D this can be performed smoothly, because when we reach the situation shown in Figure 2.5b the particle can use the third dimension to avoid the other particle. In 2D the situation in Figure 2.5b is topologically different, as the trajectory is cut by the second particle[31].

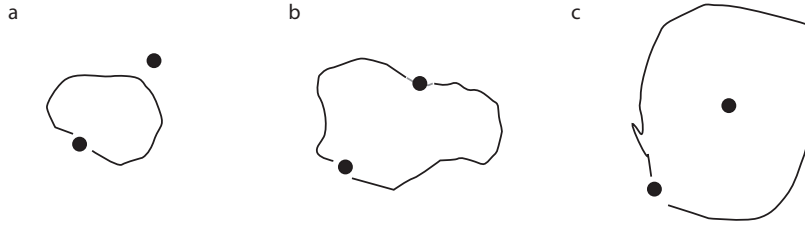


Figure 2.5: **a** A particle (black circle) is moved along a small trajectory without enclosing the other particle. **b** This trajectory is different in 3D because the particle can use the extra dimension to pass by the other particle. In 2D the other particle cuts the trajectory. **c** The particle's trajectory fully encloses the other particle.

2.3.2. BRAIDING FORMALISM

⁴MZM are proposed to be non-abelian states in 1D and 2D condensed matter systems, defined by $U_{12}U_{23} \neq U_{23}U_{12}$. Here U_{ij} is an operator that exchanges MZM i and j . We can see that MZM are clearly different from other states if we try to 'count' them. Normally this count is given by $n_{\text{MZM}} = \gamma^\dagger\gamma$, but because $\gamma^\dagger = \gamma$, n_{MZM} is also equal to $\gamma\gamma$. This does not make sense, as it always gives 1. This comes from the definition introduced by Kitaev[4] in his toy model, which is more extensively explained in Section 3.4.1. With n_{MZM} always returning 1 a different kind of counting is needed.

The normal counting operator for fermions is $n = c^\dagger c$, which can to be translated to MZM operators via $c = \frac{1}{2}(\gamma_1 + i\gamma_2)$ and $c^\dagger = \frac{1}{2}(\gamma_1 - i\gamma_2)$. This gives

$$n_1 = c_1^\dagger c_1 = \frac{1}{2}(1 + i\gamma_1\gamma_2), \quad (2.3)$$

where $n_1 = 0, 1$ corresponds to the fermionic state being occupied or empty and thus also the MZM γ_1 and γ_2 being occupied or empty. From this we can conclude that it does not make sense to talk about individual MZM occupation but only about joint occupation.

⁴For this section reference [32] is extensively used.

Using equation 2.3, the parity operator can be defined as follows:

$$P_1 = 1 - 2n_1 = -i\gamma_1\gamma_2. \quad (2.4)$$

2

The parity operator returns a value of -1 for odd parity ($n_1 = 1$) and +1 for even parity ($n_1 = 0$). The wavefunction describing the MZM can be constructed from the states $|n_1, n_2, \dots, n_j, \dots, n_N\rangle$, where n_j corresponds to MZM γ_{2j-1} and γ_{2j} . The complete wavefunction is then described by including the weights $\alpha_{n_1, n_2, \dots, n_j, \dots, n_N}$, resulting in the expression

$$|\Psi\rangle = \sum \alpha_{n_1, n_2, \dots, n_j, \dots, n_N} |n_1, n_2, \dots, n_j, \dots, n_N\rangle, \quad (2.5)$$

where the summation runs over all 2^{N-1} combinations of 0,1 for the n_j .

Having constructed a wavefunction for the MZM, we need to prove that exchanging MZM is non-abelian. Consider two MZM, γ_1 and γ_2 , and the exchange $\gamma_1 \leftrightarrow \gamma_2$. To find an operator U that achieves this we have to make sure that the operator is unitary, only involves γ_1 and γ_2 , and conserves the total parity of the system. To find such an operator, we sandwich the MZM with the operator U , resulting in $U\gamma_1U^\dagger$. The derivation is given in Appendix A.1, showing that $U = \frac{1}{\sqrt{2}}(1 \pm \gamma_1\gamma_2)$, where + (-) corresponds to clockwise (anti-clockwise) exchange.

Figure 2.6 presents this braiding schematically, with evolved time on the y -axis. Figure 2.6a (c) shows the braiding for + (-), which is defined as clockwise (anti-clockwise) in this thesis. The lines represent the positions of the MZM over time, which can be exchanged by braiding.

Having derived U , it is now possible to check if the MZM exchange is non-abelian, as defined by $U_{12}U_{23} \neq U_{23}U_{12}$. This is shown in Appendix A.2.

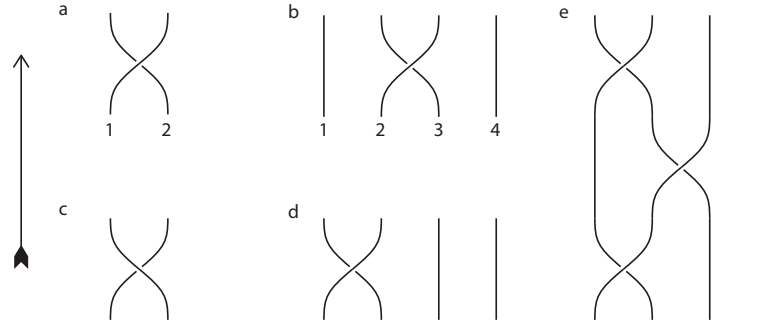


Figure 2.6: Schematic drawing of worldlines representing MZM braiding operations. **a** Clockwise braiding of γ_1 and γ_2 , performed by the operator $U_{12} = \frac{1}{\sqrt{2}}(1 + \gamma_1\gamma_2)$. **b** U_{23} performed with four MZM present, resulting in a superposition of the (individual) parities. **c** Anti-clockwise braiding of γ_1 and γ_2 , performed by the operator $U_{12} = \frac{1}{\sqrt{2}}(1 - \gamma_1\gamma_2)$. **d** $U_{12} = \frac{1}{\sqrt{2}}(1 + \gamma_1\gamma_2)$ performed with four MZM present. **e** The more complex braiding operation $U_{13} = U_{12}U_{23}U_{12}$ with four MZM.

To form a qubit out of MZM, we propose to use the fermion parity states +1 and -1 as a two-level system. We take one pair of MZM, γ_1 and γ_2 , with the corresponding n_1 creating a wavefunction $|n_1\rangle$ according eq. 2.5. From the definition given in eq. 2.4, we

see that the parity operator gives $P|0\rangle = +|0\rangle$ and $P|1\rangle = -|1\rangle$, which we will use as our two levels.

As mentioned before, quantum gates are performed by braiding the MZM, so we use U_{12} to (try to) change the parity of $|n_1\rangle$:

$$\begin{aligned} U_{12}|0\rangle &= \frac{1}{\sqrt{2}}(1+i)|0\rangle \\ U_{12}|1\rangle &= \frac{1}{\sqrt{2}}(1-i)|1\rangle. \end{aligned} \quad (2.6)$$

We see that U_{12} does not bring the wavefunction into a state of parity superposition. ($U_{12}|0\rangle$ is explicitly calculated in Appendix A.3.) This makes sense, since in deriving U_{12} we made the assumption that U is a parity-conserving operation, but this is a good check. Instead, we can extend the wavefunction to four MZM and two fermionic states $|n_1, n_2\rangle$. Now there are more MZM and more exchange options, so let us investigate them:

$$\begin{aligned} U_{12}|00\rangle &= \frac{1}{\sqrt{2}}(1+i)|00\rangle \\ U_{12}|11\rangle &= \frac{1}{\sqrt{2}}(1-i)|11\rangle \\ U_{23}|00\rangle &= \frac{1}{\sqrt{2}}(|00\rangle + i|11\rangle) \\ U_{34}|00\rangle &= \frac{1}{\sqrt{2}}(1+i)|00\rangle. \end{aligned} \quad (2.7)$$

With the operation U_{23} , schematically depicted in Figure 2.6b and explicitly calculated in Appendix A.3, we are able to create a parity superposition for both n_1 and n_2 . However, if we measure the parity of the whole system we obtain 0, so U_{23} is still not changing the overall parity. To check this we define the total parity operator P_{tot} as follows:

$$P_{\text{tot}} = \prod_{j=1}^N P_j = i^N \prod_{j=1}^{2N} \gamma_j. \quad (2.8)$$

Indeed $P_{\text{tot}}|00\rangle$ and $U_{23}|00\rangle$ both return +1, meaning even parity.

To read out the MZM qubit, the parity of a single pair of MZM needs to be determined by measurement. We conclude that pairs of MZM can form qubits by being occupied or empty. To make computations, braiding operations between different pairs of MZM need to be performed. It is also possible to do more complex braiding operations, such as for example $U_{13} = U_{12}U_{23}U_{12}$, schematically depicted in Figure 2.6e.

2.3.3. BRAIDING MAJORANAS WITHOUT MOVING MAJORANAS

To perform braiding, the MZM need to be moved around each other. Early proposals involved moving the MZM with electrostatic gates in T-junction nanowires[16]. This method of MZM control has been tried but found to be difficult[33]. Later, van Heck *et*.

2

al. came up with the idea of using the tunable charging energy E_c via the flux-controlled Josephson coupling E_J to couple different MZM[34]. Effectively, this coupling of different MZM is a basis change. Let us start with the fermionic states $|n_{12}, n_{34}\rangle$, where n_{12} (n_{34}) corresponds to $c_{12} = \frac{1}{2}(\gamma_1 + i\gamma_2)$ ($c_{34} = \frac{1}{2}(\gamma_3 + i\gamma_4)$). The indices of the n s correspond to the numbers of the MZM.

By changing the coupling between the MZM and the ability to read out, for example, γ_1 and γ_4 we have performed a basis change. Say we want to read out $n_{14} = c_{14}^\dagger c_{14}$, where $c_{14} = \frac{1}{2}(\gamma_1 + i\gamma_4)$. To check what n_{14} is, we have to go from $|n_{12}, n_{34}\rangle$ to $|n_{14}, n_{23}\rangle$.

After the basis change we have effectively performed $U_{34}U_{23}$, as shown in Figure 2.7. In the ground state $|0_{12}, 0_{34}\rangle^5$, we obtain the following equality:

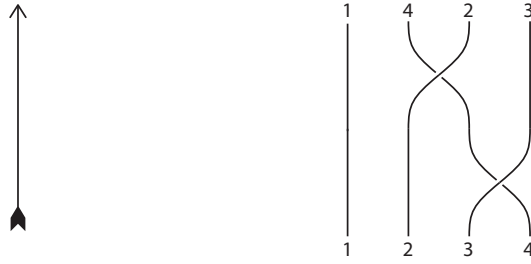


Figure 2.7: The effective braiding performed by changing the basis from $|n_{12}, n_{34}\rangle$ to $|n_{14}, n_{23}\rangle$.

$$|0_{12}, 0_{34}\rangle = \frac{1}{\sqrt{2}} (|0_{14}0_{23}\rangle + i|1_{14}1_{23}\rangle). \quad (2.9)$$

Two proposals[17, 35] to achieve braiding through basis change are being pursued by multiple research groups[36].

⁵We keep the indices to see which MZM belongs to which fermionic state.

3

THEORY

Your theory is crazy, but it's not crazy enough to be true.

Niels Bohr

A proper understanding of the theory is very important if we are to make our experiments work. In this chapter, we discuss most of the effects that are seen in, or are important for, our measurements. Although we try to discuss everything in depth, we would also point the interested reader to the references within this chapter, which often contain a more extensive discussion of the topics.

We start with an introduction to superconductivity but try to move on as quickly as possible to the measurable effects of voltage, current and conductance response. The workhorse systems which we use in our experiments are Josephson junctions with a thin oxide layer or a nanowire as a weak link between the two superconductors. Nanowire systems with superconductivity are especially interesting since it has been proposed that these systems can host Majorana zero modes (MZM) when an external magnetic field is applied.

We also describe an on-chip detection technique for high-frequency radiation that can provide a signature of the fractional Josephson effect and the origin of Majorana bound states (MBS).

Finally, we discuss the subgap response of superconductor-insulator-superconductor (SIS) junctions with an inelastic Cooper-pair tunneling current, which can probe the microwave absorption of an Andreev bound state spectrum.

3.1. INTRODUCTION

Although this is an experimental thesis, theory plays an important role in it. Getting a firm grasp of theory and ‘understanding’ is beneficial for the experimentalist involved in the experiment.

We start this chapter with the (almost magical) phenomenon of superconductivity, in Section 3.2. First, we introduce BCS theory (Section 3.2.1) and from there we go on to the mesoscopic effect of Andreev reflection on a superconductor-normal (SN) interface (Section 3.2.2).

The next section (3.3) is dedicated to Josephson junctions. We start by discussing the underlying cause of the supercurrent in Josephson junctions, namely the Andreev bound states, in Sections 3.3.1 and 3.3.2. Roughly, Josephson junctions can be divided into two types: junctions with a thin insulator as a weak link (Section 3.3.3) and ones with a normal/semiconductor weak link (Section 3.3.4). Lastly, we discuss split junctions in Section 3.3.5.

An important part of the theory of MZM is discussed in Section 3.4, starting with the Kitaev model (the first proposal for MZM in 1D condensed matter systems), in Section 3.4.1. This is followed by a realistic model for the creation of MZM in accessible semiconductor nanowire systems in Section 3.4.2. Coupling between MZM is discussed in Section 3.4.3. We show that the presence of MZM in an superconductor-normal metal-superconductor (SNS) Josephson junction forms a topological junction in Section 3.4.4.

Charging physics with (or without) Josephson coupling is discussed in Section 3.5.

In Section 3.6 we discuss the quasiparticle response of an SIS junction in the presence of a microwave field using noise theory.

3.2. SUPERCONDUCTIVITY

Superconductivity is important in this thesis and needs to be introduced and explained properly. The macroscopic effect of superconductivity is that it is possible to pass a current through a material without any dissipation[37]. Because of this, magnetic fields are prevented from penetrating the material by dissipationless eddy currents, known as the Meissner effect. This effect means that superconducting materials are perfect diamagnets, since no magnetic fields can exist in the core of a superconducting material.

As far as possible, we present an intuitive view of the physics with corresponding formulas. Although the theory of superconductivity was developed by Bardeen, Cooper and Schieffer (BCS)[38], in this section we refer to [39, 40] extensively as well as several recent theses from Saclay[41–43].

3.2.1. BCS THEORY

The origin of superconductivity lies in the formation of electron-electron bound states, called Cooper pairs. The formation of Cooper pairs seems on the face of it unlikely since electrons have a negative charge, leading to mutual repulsion. Actually, this repulsion is screened by the presence of a large background of free electrons and negatively charged ions in the lattice. This screening effect does not lead to superconductivity since it does not cause an attractive interaction between the electrons, but it does reduce the strength of the repulsion.

The attractive term comes in through the introduction of an electron-lattice interaction. The idea of electron-lattice interaction is as follows: when an electron passes through the positively-charged ion lattice of a metal, the negative electron will disturb the positive lattice locally, as shown in Figure 3.1a. Due to this interaction, the lattice is deformed, increasing the local charge density slightly and making it more attractive for another electron. The distortion of the lattice by the first electron is actually absorbed by the second electron[44, 45]. This is schematically depicted in Figure 3.1. The lattice distortion is called a phonon. If this phonon interaction is stronger than the screened Coulomb repulsion, this leads to superconductivity. Lattice distortion is a key feature of the theory of superconductivity and was experimentally confirmed in 1950. These experiments measured multiple isotopes of superconducting mercury and found that the superconducting transition temperature T_c is related to the mass of the nucleus (m) via $T_c \propto m^{-\frac{1}{2}}$, indicating that the vibration of nuclei of different masses gives a small deviation in T_c . This is known as the *isotope effect*[46, 47].

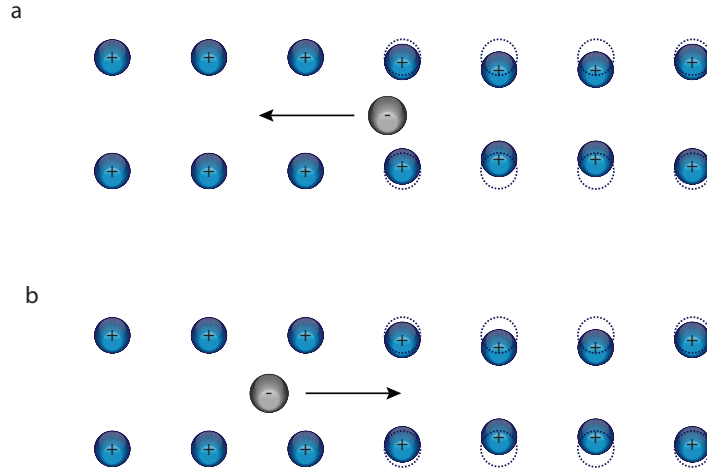


Figure 3.1: **a** An electron disturbs the positively charged lattice by exciting a vibrational mode, or phonon. This makes it locally attractive to another electron, which absorbs the phonon in **b**.

Electrons preferentially form singlet pairings, since this is the lowest energy state. A theoretical description that favours the lowest energy state, through singlet pairings and zero-momentum states, seems reasonable since metals only exhibit superconductivity at low temperatures, where the system is most likely to be in its lowest energy (or ground) state. An important contribution by Cooper to the BCS theory was that only k and $-k$ correlations were necessary and not all possible options between k and k' . This pairing between k and $-k$ gives Cooper pairs zero net momentum, the lowest energy state.

The BCS Hamiltonian shown in eq. 3.1 adds Cooper-pair creation and annihilation operators to the Schrödinger equation. Second quantization language is used where c^\dagger (c) creates (annihilates) an electron. The mean-field approximated Hamiltonian is

$$H_{\text{BCS}} = \sum_{\mathbf{k}} \left[\xi_{\mathbf{k}\uparrow} c_{\mathbf{k}\uparrow}^\dagger c_{\mathbf{k}\uparrow} + \xi_{\mathbf{k}\downarrow} c_{\mathbf{k}\downarrow}^\dagger c_{\mathbf{k}\downarrow} + \Delta c_{\mathbf{k}\uparrow}^\dagger c_{-\mathbf{k}\downarrow}^\dagger + \Delta c_{\mathbf{k}\downarrow} c_{-\mathbf{k}\uparrow} \right], \quad (3.1)$$

where $\xi_{k,\uparrow} = \frac{\hbar^2 k^2}{2m} - \mu$ comes from the Schrödinger equation. The first part is the kinetic energy, where \hbar is the reduced Planck constant, k the momentum, and m the mass. μ is the (chemical) potential. Δ is the bound-state energy of the Cooper pairs, which we assume to be real and positive. The Hamiltonian conserves spin (\uparrow, \downarrow) and parity and these are still good quantum numbers. However, the number of particles is not a good quantum number due to the creation and annihilation of Cooper pairs in the last two terms, which is a direct consequence of the mean field approximation.

3

BOGOLIUBOV-DE GENNES EQUATIONS

To investigate the BCS Hamiltonian further, we consider the Bogoliubov-de Gennes (BdG)

Hamiltonian. Introducing $\Psi_{\mathbf{k}} = \begin{pmatrix} c_{\mathbf{k}\uparrow} \\ c_{-\mathbf{k}\downarrow}^\dagger \end{pmatrix}$ it is as follows:

$$H_{\text{BCS}} = \sum_{\mathbf{k}} \Psi_{\mathbf{k}}^\dagger \begin{pmatrix} \xi_{\mathbf{k}\uparrow} & \Delta \\ \Delta & -\xi_{\mathbf{k}\downarrow} \end{pmatrix} \Psi_{\mathbf{k}} + \sum_{\mathbf{k}} \xi_{-\mathbf{k}\downarrow} = \sum_{\mathbf{k}} \Psi_{\mathbf{k}}^\dagger H_{\text{BdG}} \Psi_{\mathbf{k}} + \sum_{\mathbf{k}} \xi_{-\mathbf{k}\downarrow}. \quad (3.2)$$

This approach divides H_{BCS} into two parts, where the second part is the vacuum state, which fills the complete k parameter space up to the Fermi energy. This depends on the definition of $\Psi_{\mathbf{k}}$, as is extensively discussed in ref. [42].

The first part describes excitations from the vacuum state. The energies (eigenvalues) of H_{BdG} are $E_{\pm} = \pm \sqrt{\xi_{\mathbf{k}}^2 + \Delta^2}$, indicating that there are two (eigen)states. We propose $|k+\rangle = \begin{pmatrix} u_{\mathbf{k}} \\ v_{\mathbf{k}} \end{pmatrix}$, corresponding to E_+ , and $|k-\rangle = \begin{pmatrix} v_{\mathbf{k}} \\ -u_{\mathbf{k}} \end{pmatrix}$ ¹, corresponding to E_- . Solving $H_{\text{BdG}}|k\pm\rangle = E_{\pm}|k\pm\rangle$ and normalizing the eigenstates gives

$$u_{\mathbf{k}} = \sqrt{\frac{1}{2} + \frac{1}{2} \frac{\xi_{\mathbf{k}}}{\sqrt{\xi_{\mathbf{k}}^2 + \Delta^2}}} \quad (3.3)$$

$$v_{\mathbf{k}} = \sqrt{\frac{1}{2} - \frac{1}{2} \frac{\xi_{\mathbf{k}}}{\sqrt{\xi_{\mathbf{k}}^2 + \Delta^2}}}. \quad (3.4)$$

To understand this result, we turn superconductivity off by setting $\Delta \rightarrow 0$ and compare the result to eq. 3.1, which is now the normal Schrödinger equation. This gives $|k+\rangle = \begin{pmatrix} 1 \\ 0 \end{pmatrix}$, corresponding to $E_+ = \xi_{\mathbf{k}}$, which are the energies from the Schrödinger equation. We can conclude that $u_{\mathbf{k}} = 1, v_{\mathbf{k}} = 0$, together with the positive energy solutions, describe electron excitations due to this correspondence with the Schrödinger equation solutions. Similarly, $|k-\rangle$ and the negative energy solution ($E_- = -\xi_{\mathbf{k}}$) describes a hole² excitation or annihilation of an electron for $E < 0$. $|k-\rangle = \begin{pmatrix} 0 \\ -1 \end{pmatrix}$.

When we turn superconductivity back on by setting $\Delta \neq 0$, we always obtain finite values for both $u_{\mathbf{k}}$ and $v_{\mathbf{k}}$, indicating that we have both electron and hole excitations at

¹The states are defined so as to guarantee orthogonality and u and v are assumed to be real.

²The positive and negative energy solutions are like particle (electron) and anti-particle (hole or absence of electron) solutions in the Dirac equation.

the same time. For the E_+ solution, we obtain an electron-like excitation since $u_k > v_k$, as we can see from eqs. 3.3 and 3.4. In the same way, the E_- solution gives a more hole-like excitation since $u_k < v_k$. It is convenient to introduce new particle operators that describe these excitations as electron and hole superpositions, called quasiparticles:

$$b_+ = u_e c_{k\uparrow}^\dagger + v_e c_{-k\downarrow} \quad E > 0 \quad (3.5)$$

$$b_- = u_h c_{k\uparrow}^\dagger + v_h c_{-k\downarrow} \quad E < 0. \quad (3.6)$$

To make it clearer whether u and v are electron- or hole-like, we redefine $|k+\rangle = \begin{pmatrix} u_k \\ v_k \end{pmatrix} \equiv \begin{pmatrix} u_e \\ v_e \end{pmatrix}$ and $|k-\rangle = \begin{pmatrix} v_k \\ -u_k \end{pmatrix} \equiv \begin{pmatrix} u_h \\ v_h \end{pmatrix}$. For larger positive (negative) energies ($\xi_k \rightarrow \pm\infty$) we obtain more pure electron (hole) states due to the divergence of eqs. 3.3 and 3.4, leading to $u_e \gg v_e$ ($u_h \ll v_h$). At very high positive or negative energies the quasiparticles do not feel the presence of the Cooper pairs any more.

We have introduced Cooper pairs and shown that we cannot talk about electrons or holes individually any more, introducing instead the quasiparticle states b_\pm . The corresponding energies are $E_\pm = \pm\sqrt{\xi_k^2 + \Delta^2}$, giving a minimum energy of $\pm\Delta$ when $\xi_k = 0$. The Cooper-pair creation not only introduced quasiparticle states but also a minimum excitation energy of Δ to the available states. This gap, without any quasiparticle states, is called the superconducting gap, as was already briefly mentioned in Section 2.3.

In the absence of superconductivity ($\Delta \rightarrow 0$), electron momenta are described by $k = \sqrt{\frac{2m}{\hbar^2}(E + \mu)}$. With superconductivity ($\Delta \neq 0$) we have $\xi = \pm\sqrt{E^2 - \Delta^2} = \frac{\hbar^2 k^2}{2m} - \mu$, giving the momenta as

$$k_\pm = \sqrt{\frac{2m\mu}{\hbar^2} \pm \frac{2m}{\hbar^2} \sqrt{E^2 - \Delta^2}}, \quad (3.7)$$

where k_+ is actually k_e and k_- is k_h . This is an important variable in describing Andreev reflection at an SN interface.

QUASIPARTICLE DENSITY OF STATES

In early (condensed matter) Majorana experiments the density of states (DOS) was investigated using tunnel spectroscopy. The DOS is proportional to $\frac{d\xi}{dE}$ and is given by[39]

$$\text{DOS} \propto \begin{cases} \frac{|E|}{\sqrt{E^2 - \Delta^2}} & |E| > \Delta \\ 0 & |E| < \Delta \end{cases}. \quad (3.8)$$

This is shown in Figure 3.2. There is a clear gap of 2Δ and the DOS has peaks at around $\pm\Delta$.

3.2.2. THE SUPERCONDUCTOR-NORMAL INTERFACE

In the previous section, via eqs. 3.3, 3.4 and 3.7, we found complete expressions for quasiparticle states in superconductors. When investigating the interface between the superconductor (S) at $x > 0$ and the normal metal (N) at $x < 0$, we have to satisfy boundary conditions at $x = 0$. Assuming no (δ -function) barrier between the superconductor

3

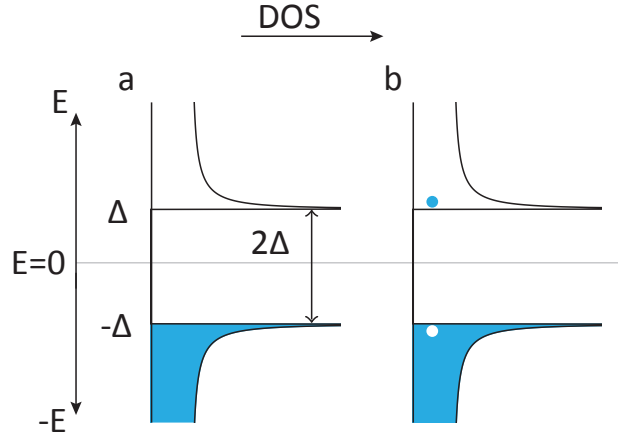


Figure 3.2: **a** Superconductor DOS with all the available states below $E = 0$ filled. There is a 2Δ gap around $E = 0$, known as the superconducting gap. **b** Same as **a** but a single quasiparticle is excited, forming an electron-hole pair.

and the normal metal, these conditions are[48]:

$$\Psi_{\text{SC}}(0) = \Psi_{\text{N}}(0) \quad (3.9)$$

$$\frac{d\Psi_{\text{SC}}(0)}{dx} = \frac{d\Psi_{\text{N}}(0)}{dx}. \quad (3.10)$$

The wavefunctions for the N and S sides are given by

$$\Psi_{\text{N}}(x) = \begin{pmatrix} 1 \\ 0 \end{pmatrix} e^{ik_{\text{N,e}}x} + B \begin{pmatrix} 1 \\ 0 \end{pmatrix} e^{-ik_{\text{N,e}}x} + A \begin{pmatrix} 0 \\ 1 \end{pmatrix} e^{ik_{\text{N,h}}x} \quad (3.11)$$

$$\Psi_{\text{SC}}(x) = C \begin{pmatrix} u_e \\ v_e \end{pmatrix} e^{ik_e x} + D \begin{pmatrix} u_h \\ v_h \end{pmatrix} e^{-ik_h x}. \quad (3.12)$$

The momenta $k_{\text{N,e}}$ and $k_{\text{N,h}}$ can be obtained from eq. 3.7 with $\Delta = 0$. We continue by assuming $\mu \gg \Delta \sim E$, which is typically the case for metals where $\mu \sim 1 - 10\text{eV}$ and superconductors where $E \sim \Delta \sim 0.1 - 3\text{meV}$. Thus $k_{\text{N,e}} \simeq k_{\text{N,h}} \simeq k_e \simeq k_h \simeq k_{\text{F}} = \frac{\sqrt{2m\mu}}{\hbar}$. This simplification makes the boundary condition given by eq. 3.10 easier to fulfill.

ANDREEV REFLECTION

We now consider an electron coming in from the N side by setting the electron amplitude of the term with $+k_{\text{N,e}}$ in the exponent to one in eq. 3.11. The trajectory of this electron is coloured blue in Figure 3.3. At the SN interface the electron can either reflect specularly, via an Andreev process, or both. We start by analyzing full specular reflection, shown as event 2 in Figure 3.3³.

³In eq. 3.11 the incoming electron is perpendicular to the SN interface, which is why there is a minus sign in front of the momentum for the reflected electron. In Figure 3.3a the electron is depicted as coming in at an angle to make drawing it easier.

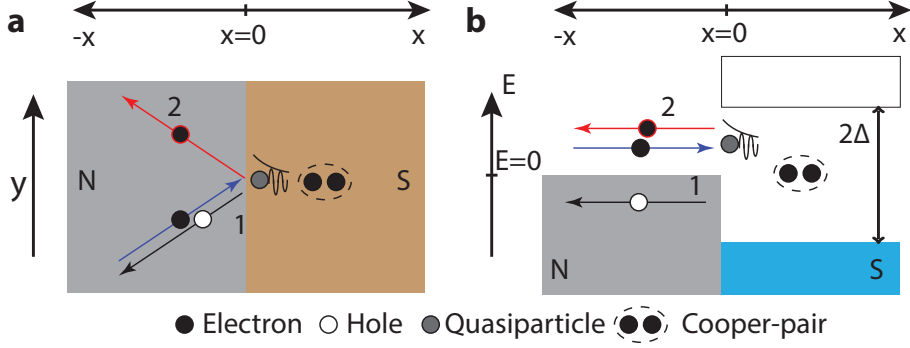


Figure 3.3: **a** Schematic drawing of specular reflection where an electron (blue arrow) bounces off the SN interface due to the presence of a high barrier. Alternatively, it could undergo Andreev reflection, where the incoming electron is reflected by a hole (black arrow), leaving a Cooper pair on the S side. **b** The same event as in **a** but now showing energy versus position (x).

With full specular reflection there is a barrier at the SN interface that effectively makes the superconductor irrelevant, and since the wavefunction does not penetrate the superconductor we can set $C = D = 0$. If we also set $A = 0$ and $B = 1$, indicating full electron reflection, the current I_{NS} is as follows[49]:

$$I_{NS} = \frac{G_N}{e} \int_{-\infty}^{\infty} [f(E - eV) - f(E)] [1 - |B(E)|^2 + |A(E)|^2] dE, \quad (3.13)$$

where e is the electron charge, G_N the normal state conductance of the barrier and $f(x) = \left(1 + e^{-\frac{x}{k_b T}}\right)^{-1}$ the Fermi-Dirac distribution. T is the temperature and k_b is Boltzmann's constant. For the case of specular reflection $1 - |B(E)|^2 + |A(E)|^2 = 0$ and hence the total current is zero for all voltages, V , as expected for full reflection.

If there is no barrier, the transmission $T = 1$ and the specular reflection amplitude $B = 0$. Transmission now happens via Andreev reflection, namely via retroreflection of a hole from the interface (event 1 in figure 3.3a) and the creation of a Cooper pair on the S side. The probability of retroreflection is $|A|^2$, derived by using the boundary condition (eq. 3.9) at $x = 0$. We obtain

$$1 = Cu_e + Du_h \quad (3.14)$$

$$A = Cv_e + Dv_h. \quad (3.15)$$

Since the inbound electron has an excitation $E > 0$, it makes sense that the quasiparticle on the S side should also have positive energy. We can therefore set the hole-like excitation amplitude $D = 0$, giving the Andreev probability $|A|^2 = \left|\frac{v_e}{u_e}\right|^2$. The amplitude $|A|$ and the argument $\arg(A)$ are plotted in Figure 3.4a and b. In the region $|E| < \Delta$, $|A|^2$ is 1. For this region $1 - |B(E)|^2 + |A(E)|^2 = 2$, indicating a doubling of the current as a function of applied voltage, V . This current enhancement can also be seen from the

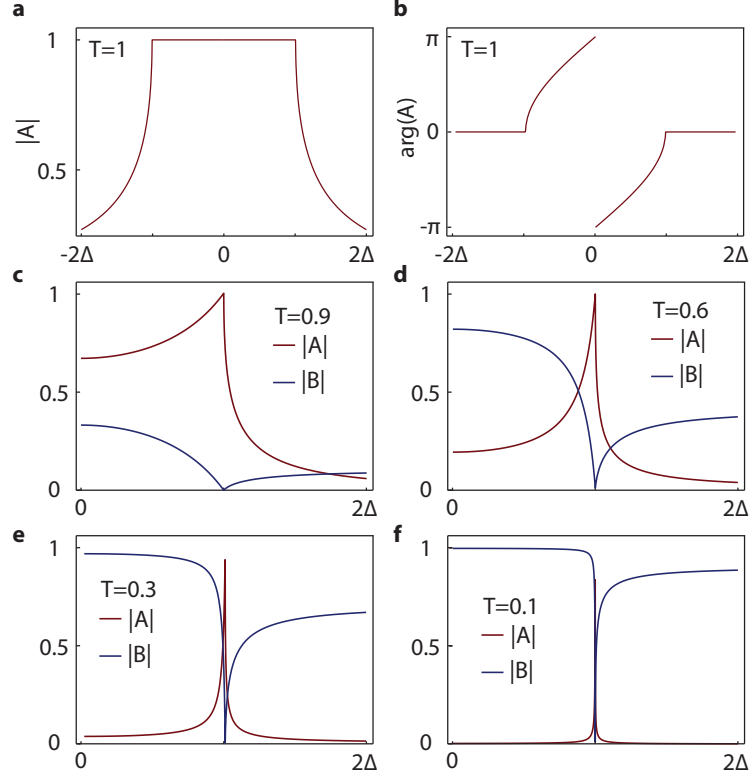


Figure 3.4: **a** The amplitude of A with no barrier at the SN interface, and hence $T = 1$. **b** The same as **a** but now plotting the phase of A . **c-f** The amplitudes of A and B for transmissions of 0.9, 0.6, 0.3 and 0.1.

wavefunction since for every incoming electron a hole is reflected back. The momentum of the hole on the N side is the same⁴ as the incoming electron but in the opposite direction. Before we analyse what happens on the S side after the Andreev reflection, we analyse the case where the probability of transmission is finite, $0 < T < 1$.

By introducing a barrier (I) we obtain an SIN system, and by adjusting the barrier height we can obtain any finite transmission, $0 < T < 1$. The barrier is a δ -function at $x = 0$, which breaks the boundary condition eq. 3.10[48]. By solving the boundary conditions we can find B and A , which are given in ref. [49] as

$$B = \frac{u_e v_e T}{u_e^2 + (T-1)v_e^2} \quad (3.16)$$

$$A = \frac{\sqrt{1-T}(u_e^2 - v_e^2)}{u_e^2 + (T-1)v_e^2}. \quad (3.17)$$

⁴We do not analyse the momentum in this thesis, but it has been done in ref. [40]. There is actually a small momentum difference, on the order of $\frac{\Delta}{\mu}$. μ (the Fermi energy) is typically measured in electronvolts but Δ is at most a few millielectronvolts, so this is negligible.

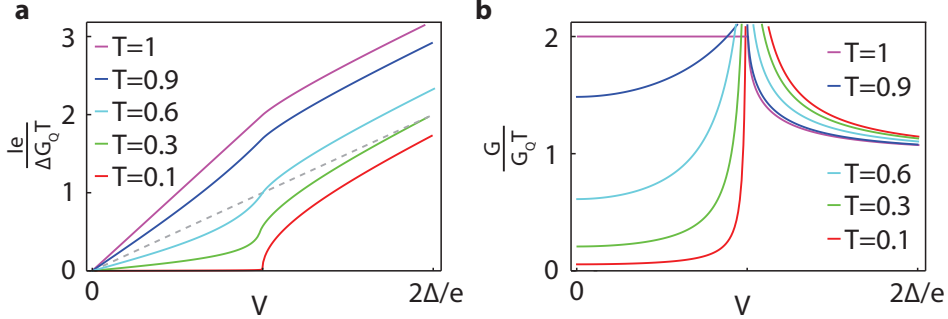


Figure 3.5: In **a** the current is calculated as function of applied voltage V using eq. 3.13. The dashed line is the current-voltage relation of a linear element. **b** The differential conductance G of the SN interface as a function of V , obtained by $\frac{dI}{dV}$, normalized to the the normal state conductance $G_Q T$. $G_Q = \frac{2e^2}{h}$ is the conductance quantum.

$|B|$ and $|A|$ are plotted for a few different transmission values in Figure 3.4c-f. From the amplitudes of B and A it is possible to calculate the current through the SIN junction and the differential conductance as a function of applied V using eq. 3.13. These are plotted in Figure 3.5 for the same transmission values.

From Figure 3.5b it can also be seen that the conductance within the gap depends only on the transmission. Beenakker derived a formula for the ratio between the conductance outside the gap ($V \rightarrow \infty$) and at zero voltage[50]:

$$\frac{G(0)}{G(\infty)} = \frac{2T}{(2-T)^2}. \quad (3.18)$$

This conductance ratio is often used to claim that Andreev reflection is the dominant effect at an SN interface.

From the conductance trace shown in Figure 3.5b for $T = 1$ we can see that the conductance doubles. For each incoming electron, a hole is reflected and a Cooper pair is created on the S side. This doubling is not obvious from eq. 3.11. That wavefunction only includes eigenstates of H_{BdG} , which are quasiparticle excitations from the ground state. The ground state, however, consists of Cooper pairs, which are not described by H_{BdG} . If we take a closer look at the quasiparticles on the S side, we observe that the wavefunction is an exponentially decreasing function due to the complex momenta defined by eq. 3.7 within the gap ($|E| < \Delta$). This effectively means the quasiparticle wavefunction is composed of evanescent waves. The current carried by these quasiparticles is transferred to the Cooper-pair condensate, and is calculated in the supplement of ref. [49]. The decaying wavefunction increases the charge of the Cooper-pair condensate. Also, the Andreev reflection itself increases the charge of the condensate, since the electron charge $-e$ is not fully absorbed by the quasiparticle, which has charge $(v_e^2 - u_e^2)e$. This charge mismatch at the S(I)N-interface directly increases the Cooper-pair condensate charge.

This intermediate state of quasiparticle decay is shown in Figure 3.3. For $T = 1$, there

is no quasiparticle decay since C and D are zero, the Cooper pairs being directly created in the condensate by the Andreev reflection.

In the model used in this section and in ref. [43, 49] the proximity effect is not taken into account. To do this (even more) properly, we need to take $\Delta = \Delta(x)$ in H_{BdG} , which makes it self-consistent since Andreev reflection leads to the proximity effect. In addition the electron, hole and quasiparticle momenta are expected to be unperturbed because only ballistic trajectories are described. This is not expected to be the case for quasiparticles in strong disorder superconductors such as NbTiN. Another important assumption we made is that $k_{\text{N},e} \simeq k_{\text{N},h} \simeq k_e \simeq k_h \simeq k_F$, which is correct when the N side is a metal but not when it is replaced by a semiconductor.

It is almost magical that the model can still be used and works even with a semiconductor, a finite-size barrier, the proximity effect and scattering[12, 21, 51].

3

3.3. JOSEPHSON JUNCTIONS

Josephson junctions consist of two superconducting electrodes, where the superconducting phases are linked via a bound state. The bound state is hosted in a weak link which could be almost anything. To derive the bound states in the weak link we use an N section so that we can make use of the formulas derived in Section 3.2.2. Our model therefore describes a SNS junction, as drawn in Figure 3.6. This gives us two SN interfaces where Andreev reflections can occur. Also, since there is now a bound region due to the interfaces, bound states can be established. Due to the Andreev reflection at the interfaces such a bound state is called an Andreev bound state (ABS).

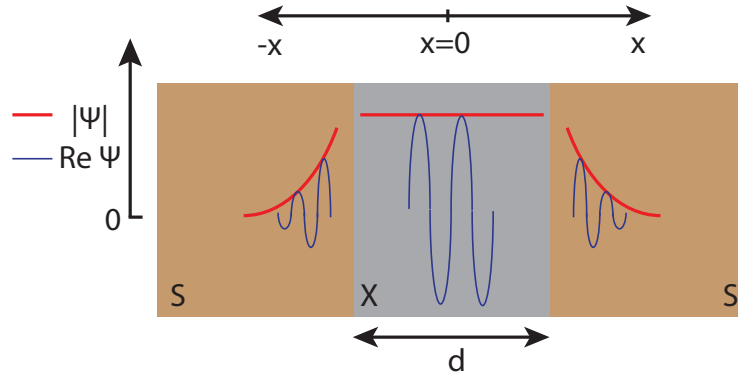


Figure 3.6: Schematic drawing of an SNS Josephson junction showing the real part of the wavefunction versus position. An Andreev bound state is present between the two SN interfaces, allowing Cooper pairs to transfer from one side to the other.

3.3.1. THE ANDREEV BOUND STATE

To understand the physics of Josephson junctions we have to introduce the superconducting phase that we neglected before. In general, the superconducting phase (ϕ) can be neglected if only a single superconductor is considered. We have seen this, for ex-

ample, with Andreev reflection. If there are multiple superconductors, however, a phase difference can be defined which can host interesting physics. A Josephson junction is such an example and in Appendix B we derive the allowed energies of the ABS. Due to their confinement between the two SN interfaces, not all energies are allowed. Only discrete energy states that depend on the superconducting phase difference δ are found.

There is a clear difference between the energy states in long N regions, $d \gg \xi_{\text{COH}}$, and short ones, $d \ll \xi_{\text{COH}}$, where d is the length of the weak link, see Figure 3.6, and ξ_{COH} is the superconducting coherence length. When $d \ll \xi_{\text{COH}}$, the junction is considered short. Effectively, the SN interfaces are so close to each other that only one ABS per channel can be established in the N part of the junction. The energy dispersion of this state with perfect transmission is

$$E_A = \pm |\Delta| \cos \frac{\delta}{2}. \quad (3.19)$$

This dispersion is depicted in Figure 3.7b by the black line.

In the derivation of the ABS energy, a single subband is assumed. We find that each conductance channel can handle a single ABS in the short junction limit. And since the Andreev reflection mechanism does not mix up conductance bands, additional conductance channels do not affect each other.

It is possible to add an impurity to the channel that can cause backscattering. The Andreev bound state energy is then

$$E_A = \pm |\Delta| \sqrt{1 - T \sin^2 \frac{\delta}{2}}. \quad (3.20)$$

Short-junction ABS with $T = 1$ and $T = 0.5$ are depicted in Figure 3.7b.

The opposite limit, $d \gg \xi_{\text{COH}}$, is known as the long junction limit and the ABS energies are given by

$$\pm E_{A,\pm,l} \simeq \hbar \frac{v_F}{d} \left[\frac{\delta}{2} - \pi \left(\frac{1}{2} \pm l \right) \right], \quad (3.21)$$

where $l = 0, 1, 2, \dots, N$. N is reached when E_A is close to $|\Delta|$ and the approximation $\arcsin \frac{E_A}{|\Delta|} \approx 0$ ceases to hold. This assumption is used in Appendix B. The energy levels of the ABS in a long junction are depicted in Figure 3.7a, both for perfect and finite transmission.

For long junctions the arcsin-term causes non-linear dispersion in the ABS, increasing as $E_A \rightarrow |\Delta|$. This dispersion will be important when we discuss the supercurrents carried by ABS in long Josephson junctions.

3.3.2. SUPERCURRENTS CARRIED BY ANDREEV BOUND STATES

We need to find an expression for the supercurrent in a Josephson junction. For this we use the general expression for the power P , which is

$$P = \frac{dE}{dt} = \frac{dE}{d\phi} \frac{d\phi}{dt} = IV. \quad (3.22)$$

The voltage across a Josephson junction is given by the AC Josephson effect, namely [52, 53]

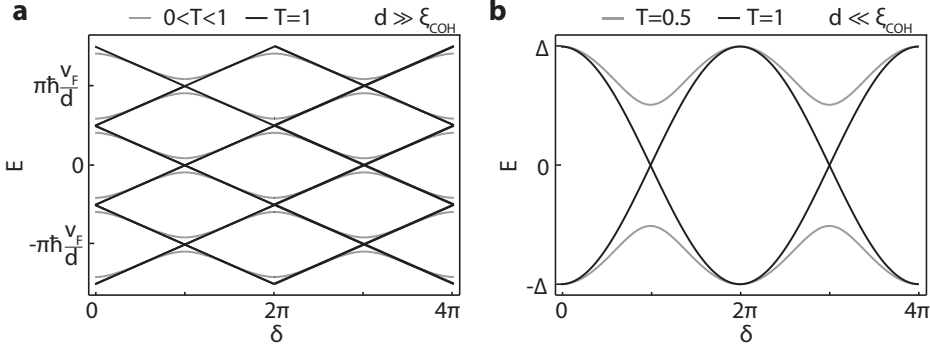


Figure 3.7: **a** The energy levels of ABS in long junctions with perfect transmission (black line) and finite transmission (grey line). **b** The energy levels of ABS in short junctions with perfect transmission (black line) and a transmission of $T = 0.5$ (grey line).

$$V = \frac{\hbar}{2e} \frac{d\phi}{dt}. \quad (3.23)$$

By combining eqs. 3.22 and 3.23 we find the following general expression for the current carried by phase-dependent energy states:

$$I = \frac{2e}{\hbar} \frac{dE}{d\phi}, \quad (3.24)$$

where E represents the energy states that are occupied. In the low temperature limit $|\Delta| \ll k_B T$, all the ABS below $E = 0$ are occupied.

When only the state below $E = 0$ is occupied we are in the ground state, which we call the zero state, $|0\rangle$. When the state is occupied by a quasiparticle, this changes the parity of the ABS to the one state, $|1\rangle$. This uncontrolled process of ABS occupation by quasiparticles is called *quasiparticle poisoning*. In the $|1\rangle$ state either both Andreev bound states are occupied or both are empty. If a second quasiparticle joins a $|1\rangle$ state, or a Cooper pair breaks from a $|0\rangle$ state, the ABS changes to $|2\rangle$. In this state, the state $-E_A$ is empty and E_A is filled. These four states can be viewed in two different ways, the semiconductor picture and the excitation picture. Both pictures describe the same physical situation but visualize it differently, as shown in Figure 3.8.

Now we shall consider the corresponding supercurrent for all four possible states. We are going to use both pictures to explain the supercurrent and the excitations shown in Figure 3.8. In the $|0\rangle$ state, the state corresponding with $-E_A$ is filled since we are in the ground state. The supercurrent in this case, assuming perfect transmission, is⁵

$$I_{|0\rangle} = -\frac{2e}{\hbar} \frac{dE_A}{d\phi} = \frac{e|\Delta|}{2\hbar} \sin \frac{\delta}{2} \quad -\pi < \delta < \pi. \quad (3.25)$$

The range of δ is set to ensure that E_A is the ground state. The excitation picture shows no excitation since in the ground state only Cooper pairs are considered. The

⁵We do not take into account the 2-fold spin degeneracy of the ABS.

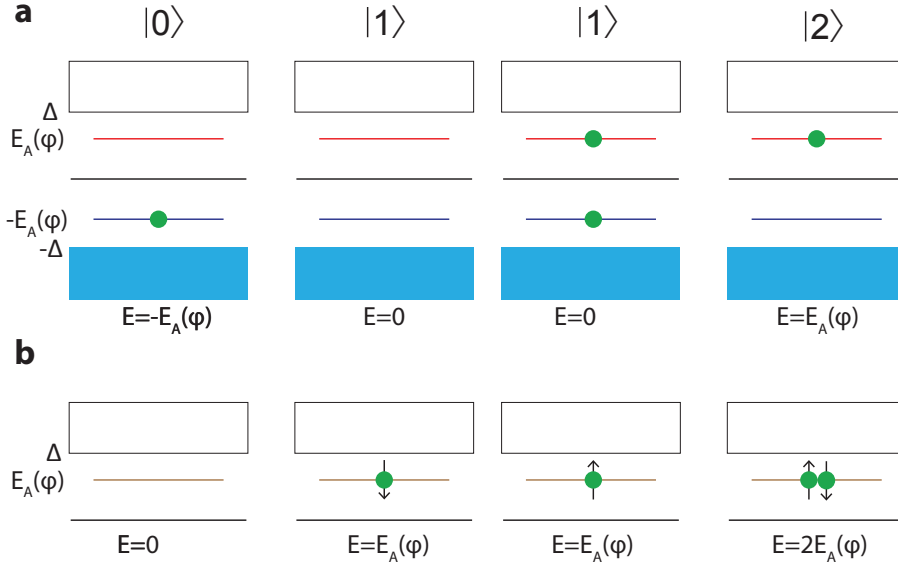


Figure 3.8: **a** The four occupation possibilities for Andreev bound states in the semiconductor picture. **b** As **a** but shown using the excitation picture.

excitation is better described by this picture since adding a single quasiparticle occupies E_A , changing the state to $|1\rangle$. The same state can be reached by either adding or removing a quasiparticle in the semiconductor picture. Changing to the excitation picture changes the quasiparticle representation defined in eqs. 3.5 and 3.6, as these were defined for the semiconductor picture. Now instead we have

$$b_+^\dagger = b_\uparrow^\dagger \quad (3.26)$$

$$b_- = b_\downarrow^\dagger. \quad (3.27)$$

In the second quantization formalism, the possible transitions to the $|1\rangle$ state can be described as follows: $|1\rangle = b_+^\dagger|0\rangle = b_-|0\rangle = b_\uparrow^\dagger|0\rangle = b_\downarrow^\dagger|0\rangle$. The two different pictures also give different energies for the states, as shown in Figure 3.8. Both views are still physical since the Hamiltonian H can be raised by any constant potential, in this case E_A . The relative energies between all states are equal in both views.

The semiconducting picture better describes the supercurrent. For example, as can be seen from the picture the state $|1\rangle$ does not carry any supercurrent, since the states are either symmetrically filled or empty around zero energy. This indicates that either there is no supercurrent or there is a supercurrent in both directions at the same time, which is effectively the same as having no supercurrent.

The last case we need to consider is the $|2\rangle$ state, where only the excited level is occupied (in the semiconductor picture), or the ABS is double-occupied (in the excitation picture). This state can be reached either by adding another quasiparticle ($|2\rangle = b_+^\dagger|1\rangle = b_-|1\rangle = b_\uparrow^\dagger|1\rangle = b_\downarrow^\dagger|1\rangle$) or by breaking a Cooper pair to go directly from $|0\rangle$ to $|2\rangle$. In the

semiconductor picture this second possibility is described as $|2\rangle = b_+^\dagger b_- |0\rangle = b_- b_+^\dagger |0\rangle$, while in the excitation picture it is $|2\rangle = b_1^\dagger b_1^\dagger |0\rangle = b_1^\dagger b_1^\dagger |0\rangle$.

In the semiconductor picture, it is clear that the state occupation is the mirror (about zero energy) of that for the ground state. The energy is E_A , meaning the supercurrent is as follows:

$$I_{|2\rangle} = \frac{2e}{\hbar} \frac{dE_A}{d\phi} = -\frac{e|\Delta|}{2\hbar} \sin \frac{\delta}{2} \quad -\pi < \delta < \pi. \quad (3.28)$$

The supercurrent has changed without changing the shape of the ABS itself, comparing the $|2\rangle$ state to the $|0\rangle$ state. The $|1\rangle$ state does not carry any supercurrent.

As we have seen, it takes two quasiparticles to go from the $|0\rangle$ state to the $|2\rangle$ state. This means they have the same parity, namely even parity. This is clearly visible in the excitation picture but not in the semiconductor picture. In general, superconducting systems prefer even-parity ground states, defining the ground state parity. In experiments this even ground state is often found, but sometimes quasiparticle poisoning is also observed[54, 55].

3.3.3. WEAK LINKS: SIS JUNCTIONS

In an SIS junction the weak link is an insulator (I). Often aluminium (Al) is used for the superconducting leads and aluminium oxide (AlO_x) for the insulating barrier, as in Chapters 7, 8 and 9. A schematic drawing of an Al/ AlO_x /Al SIS junction is shown in Figure 3.9a. However, one superconducting lead can also be a different metal, such as the NbTiN that is used in Chapter 6.

Since the barrier is insulating the transmission is low, because the electrons can hardly penetrate the high barrier of the insulator. To obtain the desired supercurrent the barrier thickness, d , can be tuned – typically from a few Ångströms up to 10 nanometers. This is often done by adjusting the oxidation time of the aluminium, as was done for the SIS junction in this thesis.

The number of channels (N_{CH}) is large for a SIS junction, typically $5 \cdot 10^3 / \mu\text{m}^2$ [56, 57]. Combining the transmission with the number of channels gives the normal state resistance, G_N , as follows:

$$G_N = G_Q \sum_{i=1}^{N_{\text{CH}}} T_i. \quad (3.29)$$

This is known as the Landauer formula[53], where $G_Q = \frac{2e^2}{h} = R_Q^{-1}$ is the conductance quantum G_Q and $R_N = G_N^{-1}$ is the normal state resistance or conductance.

JOSEPHSON EQUATIONS FOR SIS JUNCTIONS

To calculate the supercurrent in an SIS junction we use eq. 3.24, where in the ground state (low temperature) all ABS with transmission T_i are occupied. Since Andreev reflection does not mix up conductance channels, we can write the ground state energy for an SIS junction as

$$E_{\text{SNS}} = -|\Delta| \sum_{i=1}^{N_{\text{CH}}} \sqrt{1 - T_i \sin^2 \frac{\delta}{2}}. \quad (3.30)$$

Eq. 3.24 can be used to derive the supercurrent:

$$I_{\text{SNS}} = \frac{e|\Delta|}{2\hbar} \sum_{i=1}^{N_{\text{CH}}} \frac{T_i \sin \delta}{\sqrt{1 - T_i \sin^2 \frac{\delta}{2}}}. \quad (3.31)$$

In the limit of low transmission in all channels ($T_i \ll 1$) and making use of the Landauer formula we obtain

$$I_{\text{SIS}} = \frac{\pi|\Delta|}{2eR_N} \sin \delta = I_C \sin \delta. \quad (3.32)$$

This last equation shows the DC Josephson effect. First derived by Brian D. Josephson[52], it won him the Nobel prize in 1973. It describes the current that flows in an SIS junction as a function of the phase difference δ between the superconductors. The upper limit on the current that the ABS of an SIS junction can carry is $I_C = \frac{\pi|\Delta|}{2eR_N}$. The maximum current is obtained when $\delta = \pm \frac{\pi}{2}$. If a current larger than I_C is applied, the junction becomes resistive and a voltage drop appears across the SIS junction. This voltage drop winds the phase evaluation according to the AC Josephson effect, given in eq. 3.23.

From the AC and DC Josephson equations the Josephson inductance for an SIS junction can also be derived:

$$V = L \frac{dI}{dt} \quad \rightarrow \quad L = V \left(\frac{dI}{dt} \right)^{-1} = \frac{\hbar}{2eI_C \cos \delta}. \quad (3.33)$$

The Josephson inductance can be tuned by changing the phase between the superconductors, which makes it a non-linear element. The phase can be tuned by current-biasing the Josephson junction using the DC Josephson effect.

Finally, we also would like to know how to include an SIS junction in a Hamiltonian. For this, start from eq. 3.30 and do a Taylor expansion for a single energy solution to first order in T_i (since we have assumed $T_i \ll 1$), which yields:

$$E_A \simeq -|\Delta| \sum_{i=1}^{N_{\text{CH}}} \left(1 - T_i \sin^2 \frac{\delta}{2} \right) = -\frac{|\Delta|}{4} \sum_{i=1}^{N_{\text{CH}}} (T_i \cos \delta - T_i + 4). \quad (3.34)$$

Since Hamiltonians do not care about constants, we drop those and redefine $\frac{|\Delta|}{4} \sum_{i=1}^{N_{\text{CH}}} T_i = E_J$. E_J is called the Josephson coupling strength and is proportional to I_C as follows: $E_J = \frac{\hbar I_C}{2e}$. The SIS junction Hamiltonian therefore becomes

$$H = -E_J \cos \delta. \quad (3.35)$$

This is the Hamiltonian we will use for the analysis in Section 3.5.

THE RCSJ MODEL

The RCSJ model describes the current-voltage (IV) characteristic of a Josephson junction in a realistic environment. The environment is modelled by a capacitor and a resistor in parallel, depicted in Figure 3.9b. SIS junctions often have a thin barrier between the two superconductors, and this overlap naturally forms a shunting parallel-plate capacitor, as can be imagined from the drawing in Figure 3.9a. Often this intrinsic capacitance makes the largest contribution to the total capacitance.

The intrinsic resistance for an SIS junction is made up of the quasiparticle resistance R_{QP} , for $|V| < \frac{2e}{\Delta}$, and the normal state resistance R_N , for $|V| \gg \frac{2e}{\Delta}$. The quasiparticle resistance is high for $k_B T \ll \Delta$, due to the superconducting gap present in the DOS which suppresses the current flow. The normal state resistance is determined by the thickness and area of the barrier, typically (in this thesis) in the range $5k\Omega$ – $100k\Omega$.

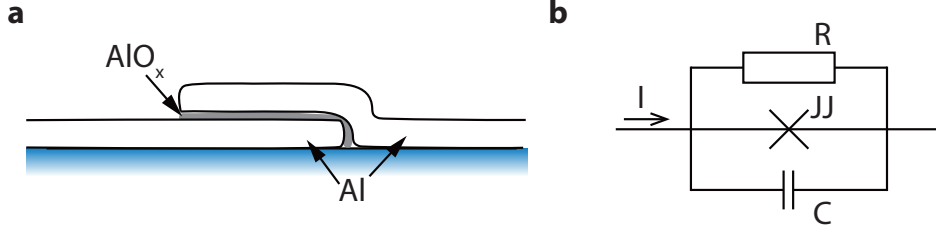


Figure 3.9: **a** Schematic drawing of an SIS junction made out of aluminum/aluminium oxide/aluminum (Al/AIO_x/Al). Due to the large overlap and the thin barrier, the parallel-plate capacitance of the two superconductors is the dominant capacitance. **b** Schematic drawing of the electronic circuit that represents an SIS junction in the RCSJ model.

The current through an SIS junction is described by Kirchhoff's circuit laws, giving a total current of

$$I = I_C \sin \delta + \frac{V}{R} + C \frac{dV}{dt}. \quad (3.36)$$

This gives the total current in terms of two variables. To eliminate one variable we use the AC Josephson relation (eq. 3.23):

$$0 = I_C \sin \delta - I + \frac{\hbar}{2eR} \frac{d\delta}{dt} + \frac{\hbar C}{2e} \frac{d^2\delta}{dt^2}. \quad (3.37)$$

This is similar to the equation of motion but with the phase difference δ instead of the position x :

$$0 = \frac{dU(x)}{dx} + c \frac{dx}{dt} + m \frac{d^2x}{dt^2}, \quad (3.38)$$

where $U(x)$ is the potential of an object with mass m and friction c . This makes the friction proportional to $\frac{1}{R}$ and the mass proportional to the capacitance C . In this analogy, the potential is then given by⁶

$$U(\delta) = -\frac{\hbar I}{2e} \delta - E_J \cos \delta. \quad (3.39)$$

The potential for different bias currents is shown in Figure 3.10a. This potential is often referred to as the washboard potential⁷.

Since SIS junctions also have an inductance, given by equation 3.33, we can also consider the circuit as a parallel LCR circuit, meaning we can define a plasma resonance $\omega_P = \frac{1}{\sqrt{LC}} = \sqrt{\frac{2eI_C \cos \delta}{\hbar C}}$ and a quality factor $Q = \omega_P RC = R \sqrt{\frac{2eCI_C \cos \delta}{\hbar}}$.

⁶We have multiplied $U(\delta)$ by $\frac{\hbar}{2e}$ to give it the proper units of potential energy.

⁷Named after the bumpy metal plate that our (great-)grandparents used for washing clothes. Do not worry if you have not heard of it, it is not relevant.

THERMAL FLUCTUATIONS

To maintain the analogy with the equation of motion, we are tilting the potential $U(\delta)$ by current-biasing the SIS junction. For $I < I_C$ there is a potential minimum, which gives a static solution of δ . The bias current fluctuates due to noise, which means the potential tilt also fluctuates. We can incorporate this by rewriting the current as $I = \bar{I} + \delta I$, i.e. as an average current of \bar{I} with fluctuations on the order of δI .

The fluctuations in current change the tilt of the potential (on top of the \bar{I} tilt), while phase fluctuations change the minima of the washboard potential. These two equivalent views of the noise in the system are drawn in Figure 3.10b. If the noise gets too large, it can overcome the remaining barrier height $\Delta U \approx 2E_J \left(1 - \frac{\bar{I}}{I_C}\right)^{\frac{3}{2}}$, as depicted in Figure 3.10c. In this case, the system settles into the next minimum, winding the phase. This phase winding will produce a voltage according to the AC Josephson effect. If the ‘mass’, C , is large ($Q > 1$) the system will not stop at this next minimum and instead will continue to gain phase and voltage[58]. The phase velocity will increase until the V of the resistor R is high enough to take all the DC current. Ideally, the resistor R will now be the normal state resistance R_N because the quasiparticle resistance is too large to allow enough current to flow.

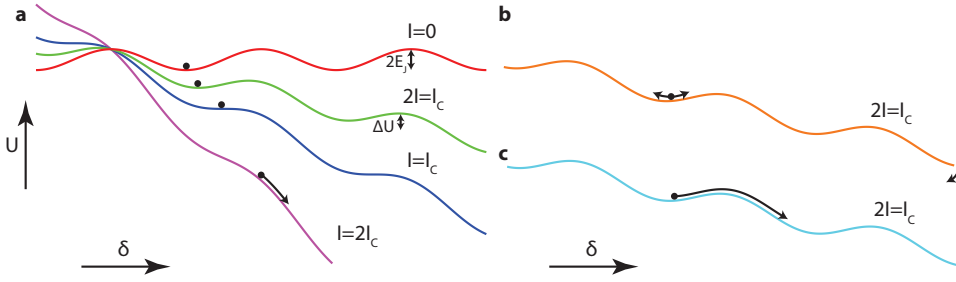


Figure 3.10: **a** The potential of an SIS junction for different bias current values. This potential is often called the washboard potential due to its bumpy shape and tilt. **b** Fluctuations in the bias current effectively tilt the potential, and can also be seen as fluctuations in the phase of the system. **c** For a bias current of $I < I_C$, it is possible for the additional noise to overcome the potential barrier ΔU , in which case the system settles into the next minimum and the phase winds by 2π . When C is large, the system can continue winding the phase and enter the running state.

The current needed to prematurely cause a voltage across the junction in this way is called the switching current I_{SW} . I_C is only the maximal value of the experimentally accessible I_{SW} . After many successive measurements, the average value of I_{SW} can be approximated by[59]⁸

$$\langle I_{SW} \rangle \approx I_C \left[1 - \left[\frac{k_B T}{2E_J} \ln \left(\frac{\omega_P \Delta t}{2\pi} \right) \right] \right], \quad (3.40)$$

where Δt is the time that is needed to sweep the current through the distribution of switching currents. It is important to note that for constant temperature $\langle I_{SW} \rangle$ seems to be proportional to I_C , but this is not actually the case since both E_J and ω_P depend on I_C .

⁸The exact limits on the validity of this formula are given in ref. [59].

To give an example of the reduction of the measured $\langle I_{\text{SW}} \rangle$ versus I_C , let us assume an SIS junction with $C = 2\text{fF}$, $I_C = 20\text{nA}$, $T = 20\text{mK}$ and a Δt of 0.1s. This gives $\langle I_{\text{SW}} \rangle = 8.1\text{nA}$, compared to only 0.7nA for $I_C = 10\text{nA}$.

$$R_0(I) = \frac{h}{4e^2} \frac{\hbar\omega_P}{k_B T} e^{-\frac{\Delta U}{k_B T}}. \quad (3.41)$$

$Z(\omega)$ -ENVIRONMENTS

We investigated switching currents in SIS junctions by considering their intrinsic capacitance and resistance. In real measurements, there could also be stray capacitances from the grounding leads or additional inductances. Large inductances can result from the kinetic inductance of the superconducting leads. We model the environment as a parallel element $Z_{\text{env}}(\omega)$ in Figure 3.9b. The Josephson junction is an AC current source at finite voltage with an output of $I = I_C \sin \frac{2eVt}{\hbar} = I_C \sin \omega_J t$, where ω_J is the Josephson frequency. The total DC and AC dissipation is then

$$P = IV = \frac{I_C^2}{2} \Re[Z(\omega)] + \frac{V^2}{R_{\text{QP}}}, \quad (3.42)$$

which gives an extra current term of $I = \frac{I_C^2}{2V} \Re[Z(\omega)]$, where we combined $Z_{\text{env}}(\omega)$ and C to form $Z(\omega)$. The possibility of dissipation into the environment changes eq. 3.37, and influences I_{SW} .

In general, $Z_{\text{env}}(\omega)$ is constant due to fixed resistors, capacitors and geometric/kinetic inductance. However, if there are multiple junctions in a circuit, the Josephson inductance can change a lot due to gate- or flux-dependent I_C .

In Chapter 7 and 8, the environment is dominated by a resistor R . This case is studied extensively in [41, 60], and the influence of temperature on the subgap current is plotted in Figure 3.11a. The zero temperature result is exact. The other IV traces are for $E_J \approx k_B T$, but the approximation in the equation used is also valid for $E_J \ll k_B T$. The results are close to what is expected based on the exact results in refs. [41, 60].

We see two clear regions. One is the zero-voltage region where the supercurrent branch is, although due to phase diffusion a voltage develops at finite temperature. The second region is where the current drops as the voltage rises, since the power that the environment can absorb stays constant. This effect explains the experimental IV trace shown in Figure 3.11b.

In Appendix E, we discuss and show the subgap current ($0 < 2eV_{\text{bias}} < \Delta$) of an SIS junction in different $Z(\omega)$ -environments. This is essential to understanding the experiments in Chapters 7 and 8, and especially in Chapter 9.

3.3.4. WEAK LINKS: SNS JUNCTIONS

The important difference between an SIS junction and an SNS junction is that we cannot take the limit of many channels and low transmission which brought us from eq. 3.31 to eq. 3.32. If we stick to eq. 3.31, however, we can do all the same derivations as in Section 3.3.3.

We give an overview of the SNS junctions used in our lab in Figure 3.12a and indicate typical transmission ranges, numbers of ABS and the short- and long-junction limits.

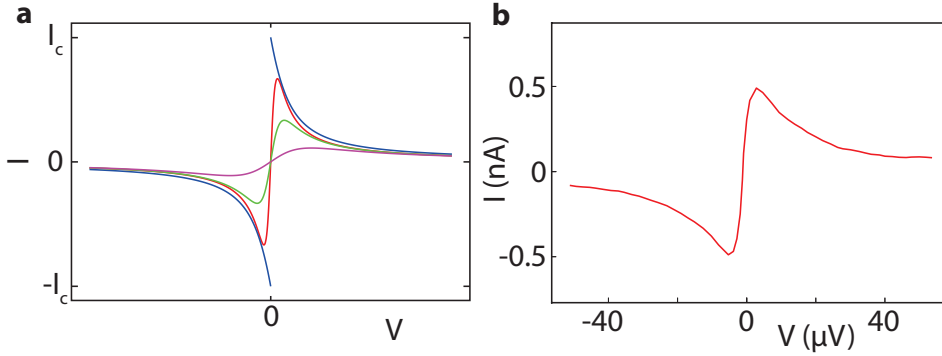


Figure 3.11: **a** Simulated IV of a Josephson junction for $V < \Delta$, for zero temperature (blue) and increasing temperature (blue<red<green<purple). The zero temperature result is an exact solution, while the other IV traces are analytic approximations for $E_J \ll k_B T$ and $10 - 100R \approx R_N$. The equations given in ref. [60] are used. **b** Measured IV trace of a device used in Chapter 8, with a parallel resistance of $\sim 500\Omega$ when $R_{QP} \approx 0.5M\Omega$.

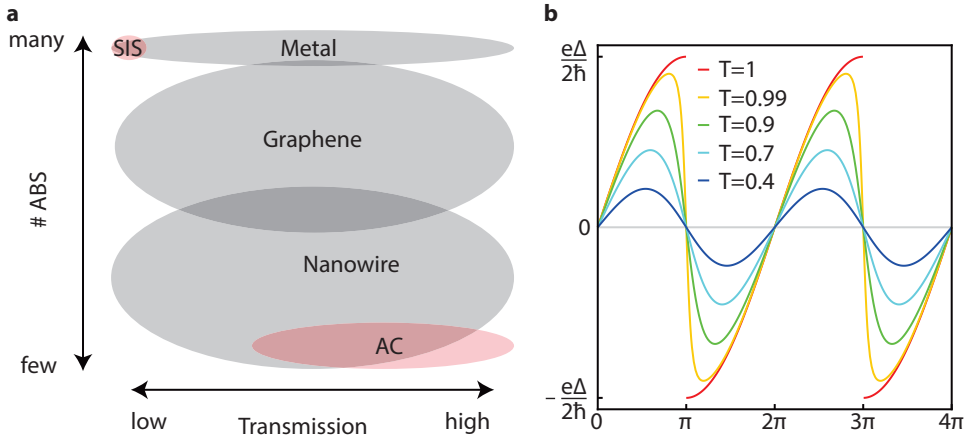


Figure 3.12: **a** Junctions with $\xi \sim d$ ($\xi \gg d$) are shown in light grey (red). Information about typical transmission ranges and numbers of ABS is extracted from refs. [43, 56, 61–63] with large error bars. **b** The CPRs for a single-channel SNS junction in the short-junction limit, for several different transmissions.

Many junctions are not *clearly* short or long, which makes analysis of the ABS more difficult. For this thesis we use nanowire junctions with typical lengths of 50–200nm and a coherence length in the nanowire of 260nm[14]. This makes them more like short junctions than long junctions, so we will use the short junction ABS equations.

SUPERCURRENTS IN SNS JUNCTIONS

We use eq. 3.31 to calculate the supercurrent and for simplicity we assume one channel. A single-channel regime is easily achieved in the nanowires used in this thesis[12, 64, 65]. Additional channels can also be added to the mode since Andreev reflection does not mix

channels. The supercurrent can be calculated as a function of the phase:

$$I_{\text{SNS}} = \frac{e|\Delta|}{2\hbar} \frac{T \sin \delta}{\sqrt{1 - T \sin^2 \frac{\delta}{2}}}. \quad (3.43)$$

In Figure 3.12b the current phase relations (CPRs) for different transmissions are shown. The CPRs for high transmission are skewed forward compared to a normal sinusoidal CPR. The CPR can be expressed in terms of Fourier series as follows:

3

$$I_{\text{SNS}} = \frac{e|\Delta|}{2\hbar} \sum_{n=1}^{\infty} A_n(T) \sin n\delta, \quad (3.44)$$

where the Fourier coefficient $A_n(T)$ is transmission-dependent. It is important to notice that the only higher frequencies that can occur are multiples of the CPR frequency. The amplitudes of the higher harmonics increase with increased transmission. The presence of the higher harmonics can be observed directly by Shapiro measurements[33, 66].

LANDAU-ZENER TUNNELING

If a system is driven by a non-adiabatic source, it can change its eigenstate. This is also possible in a system with ABS and we call this effect Landau-Zener (LZ) tunneling. This is shown in Figure 3.13a (b) for long (short) junctions. We consider the short junction model. The gap at $\delta = \pi, 3\pi, \dots$ is given by $E_{\text{A,gap}} = 2\Delta\sqrt{1-T}$. When the system is driven with a voltage V , on the order of $E_{\text{A,gap}}/e$, it is possible to change ABS occupation at $\delta = \pi, 3\pi, \dots$. Such a transition is allowed since it conserves parity, as can be seen in both the excitation and semiconductor pictures in Figure 3.13d. Intuitively, LZ tunneling can be understood as follows. The voltage is proportional to the phase velocity, which is essentially the same as the velocity, as we move along the x -axis of the energy spectrum. At higher velocities $\delta = \pi, 3\pi, \dots$, there is a larger probability to shoot through to the other branch. This probability p is given by[67]:

$$p = e^{-\frac{(1-T)\Delta}{eV}}. \quad (3.45)$$

We are going to investigate the ABS case with $T = 0.99$, depicted in Figure 3.13b. The gap at $\delta = \pi$ is 0.1Δ , and if we apply a voltage of $V = 0.1\Delta/e$ the probability of LZ tunneling is $\sim 73\%$. This means that there is a large double-period (half-frequency) component in the current-phase relation at this voltage. The probability is plotted for different transmissions and applied voltages in Figure 3.13g.

At small magnetic fields, such that the ABS split linearly, LZ transitions can also occur. It was not possible to find a proper reference for LZ transitions at finite magnetic field, but since this effect is important for the experiments in Chapter 8 we still discuss it here. In Figure 3.13c, two possible LZ transitions are drawn. Possibility 1, shown at $\delta = \pi$, is for both spin ABS to change branch. In this case (for small fields) the energy difference stays the same, indicating that the LZ probability does also. The transition is parity-conserving, as can be seen in the excitation picture in Figure 3.13e. Possibility 2 is shown at $\delta = 3\pi$. In principle this is not an allowed transition but due to quasiparticle poisoning

it may be possible⁹. An important difference between this and possibility 1 is that the energy gap of possibility 2 is smaller, indicating a larger probability of LZ tunnelling. However, not only is this transition not allowed by parity, it is also not spin conserving. This will (probably) reduce the probability, but by precisely how much is unclear.

It is also possible to LZ tunnel at $\delta = 0, 2\pi, \dots$. The system loses or gains two particles depending on the availability of quasiparticles above or below the gap. After a successful LZ tunneling event at $\delta = \pi, 3\pi, \dots$, it is also possible to LZ tunnel to the continuum at $\delta = 0, 2\pi, \dots$, giving again a CPR with a normal period [68].

THE ANDREEV HAMILTONIAN

In Figure 3.8 the the four possible ABS are shown, with their corresponding energies. The Hamiltonian can be constructed both in the semiconductor and the excitation picture, and both give the same result up to an energy difference, which is irrelevant as previously discussed. Using the semiconductor picture, we obtain

$$H_A = E_A (b_+^\dagger b_+ - b_-^\dagger b_-). \quad (3.46)$$

We can introduce $\Psi_A = \begin{pmatrix} b_- \\ b_+ \end{pmatrix}$ to obtain

$$H_A = -E_A \Psi_A^\dagger \begin{pmatrix} 1 & 0 \\ 0 & -1 \end{pmatrix} \Psi_A = -E_A \sigma_z, \quad (3.47)$$

where σ_z is the Pauli z matrix. It is important to note that we have obtained a Hamiltonian with only two eigenvalues, $\pm E_A$. These energies correspond to the parity-conserving states $|0\rangle$ ($-E_A$) and $|2\rangle$ (E_A).

The Hamiltonian of eq. 3.47 is valid for a constant or adiabatically slowly-changing phase difference between the superconductors. In the case of phase dynamics, LZ can, for example, result in different state occupations with certain probabilities p . To show this we assume a time-dependent state $|\psi(t)\rangle = a(t)|0\rangle + b(t)|2\rangle$, governed by the time-dependent Schrödinger equation:

$$i\hbar \frac{\partial |\psi(t)\rangle}{\partial t} = H_A |\psi(t)\rangle \quad (3.48)$$

$$i\hbar \left[\frac{\partial a}{\partial t} |0\rangle + \frac{\partial b}{\partial t} |2\rangle + \frac{\partial \delta}{\partial t} \left(a \frac{\partial |0\rangle}{\partial \delta} + b \frac{\partial |2\rangle}{\partial \delta} \right) \right] = -E_A [b(t)|2\rangle - a(t)|0\rangle]. \quad (3.49)$$

We take the following relation from ref. [43]:

$$\frac{\partial |0\rangle}{\partial \delta} = c(\delta, T) |2\rangle \quad (3.50)$$

$$\frac{\partial |2\rangle}{\partial \delta} = -c(\delta, T) |0\rangle, \quad (3.51)$$

⁹The phase winding in experiments is typically 5–40GHz, and quasiparticle poisoning on that timescale seems unlikely given the results of experiments with similar setups [43].

3

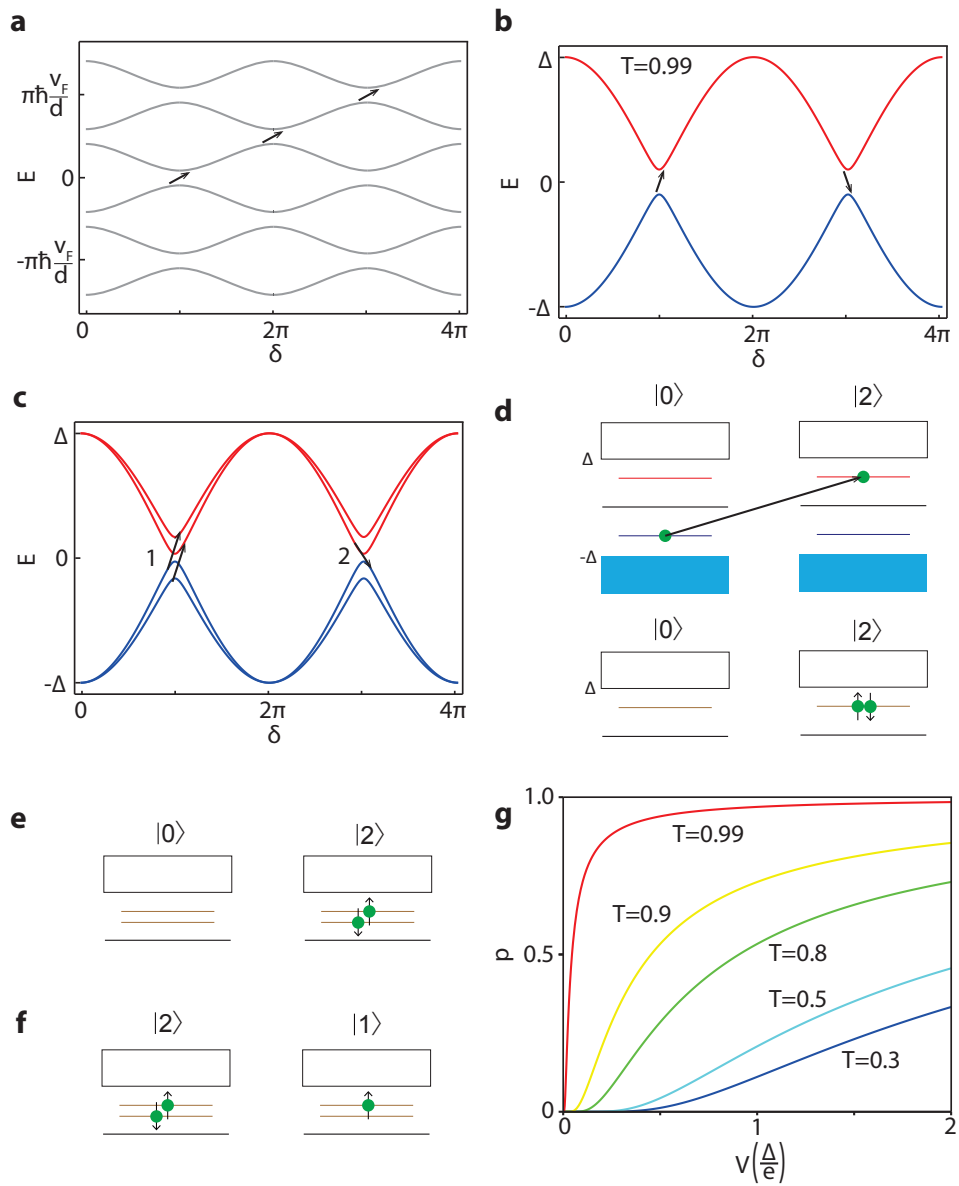


Figure 3.13: **a** Long-junction Andreev bound states, with multiple gaps in the spectrum where LZ can occur. **b** Short-junction ABS with $T = 0.99$. At $\delta = \pi, 3\pi, \dots$, LZ can occur with probability p . This doubles the period of the current-phase relation in SNS junctions. **c** Possible LZ events in ABS with small applied magnetic fields which give spin-split ABS. **d** Semiconductor and excitation pictures of the (parity-conserving) LZ depicted in **b**. **e** Excitation picture of the LZ tunneling event which is drawn as event 1 in **c**. **f** Same as **e** but for LZ event 2. It can clearly be seen that this event is not parity conserving.

where $c(\delta, T)$ is a constant that depends on the phase difference δ and the transmission T . Combining this with eq. 3.49, we can calculate $\langle 0|H_A|\psi(t)\rangle$ and $\langle 2|H_A|\psi(t)\rangle$.

$$i\hbar \left[\frac{\partial a}{\partial t} + \frac{\partial \delta}{\partial t} b \right] = a(t)E_A \quad (3.52)$$

$$i\hbar \left[\frac{\partial b}{\partial t} + \frac{\partial \delta}{\partial t} a \right] = -b(t)E_A \quad (3.53)$$

The ABS states are coupled. We can rewrite the static Hamiltonian H_A as the dynamic Hamiltonian \widetilde{H}_A [43, 69]

$$\widetilde{H}_A = \begin{pmatrix} -E_A & i\hbar c \frac{\partial \delta}{\partial t} \\ -i\hbar c \frac{\partial \delta}{\partial t} & E_A \end{pmatrix} = -E_A \sigma_z - \hbar c \frac{\partial \delta}{\partial t} \sigma_y. \quad (3.54)$$

For any phase dynamics (finite $\frac{\partial \delta}{\partial t}$) the Pauli y matrix, σ_y , is part of the Hamiltonian, meaning that $|0\rangle, |2\rangle$ are no longer eigenstates of the Hamiltonian.

The last thing that we need to take into account is the quantum behaviour of the phase and charge. It is not possible to talk about well-defined phase and charge states as we did in Figure 3.8 to derive the eigenstates if the ABS system is hooked up to an external circuit. The reason for this is that the charge and phase operators, \hat{N} and $\hat{\delta}$, do not commute: $[\hat{\delta}, \hat{N}] = i$. This also needs to be taken into account for the Andreev Hamiltonian, which was done by Zazunov *et al.*[70, 71]. The result is

$$\widehat{H}_A = -\Re(U)\sigma_z - \Im(U)\sigma_y, \quad (3.55)$$

where $U = \Delta \left[\cos \frac{\delta}{2} + i\sqrt{1-T} \sin \frac{\delta}{2} \right] e^{-\sqrt{1-T} \frac{\delta}{2}}$. This is the proper expression for the Andreev Hamiltonian, as will also be used in Chapter 9.

JOSEPHSON EQUATIONS – SNS

We have seen in the derivation of the CPR for SNS junctions that it is not perfectly sinusoidal. In eq. 3.44 we wrote the CPR as a Fourier series, indicating the clear presence of higher harmonics. Due to LZ tunneling, subharmonics are also possible: Figure 3.13b shows a halving of the frequency due to LZ tunneling. The DC Josephson relation can be written as[41, 72]

$$I_{\text{ABS}} = \frac{e|\Delta|}{2\hbar} \sum_n \sum_m A_{n,m}(T) \sin \frac{n}{m} \delta. \quad (3.56)$$

We did not say that n, m range from 1 to ∞ . In principle this should be the case, but typically in experiments (performed using short junctions with high transmission) the range for n is between 1 and 4 while m is 1 or 2[41, 73].

The phase winding is still given by the AC Josephson effect, namely $\delta = \frac{2\pi V}{\hbar} t$. By substituting this into eq. 3.56, it can be seen that there are now current oscillations with frequencies of $\frac{2\pi n}{m} V$. This could result in fractional voltage steps, called Shapiro steps[41, 66].

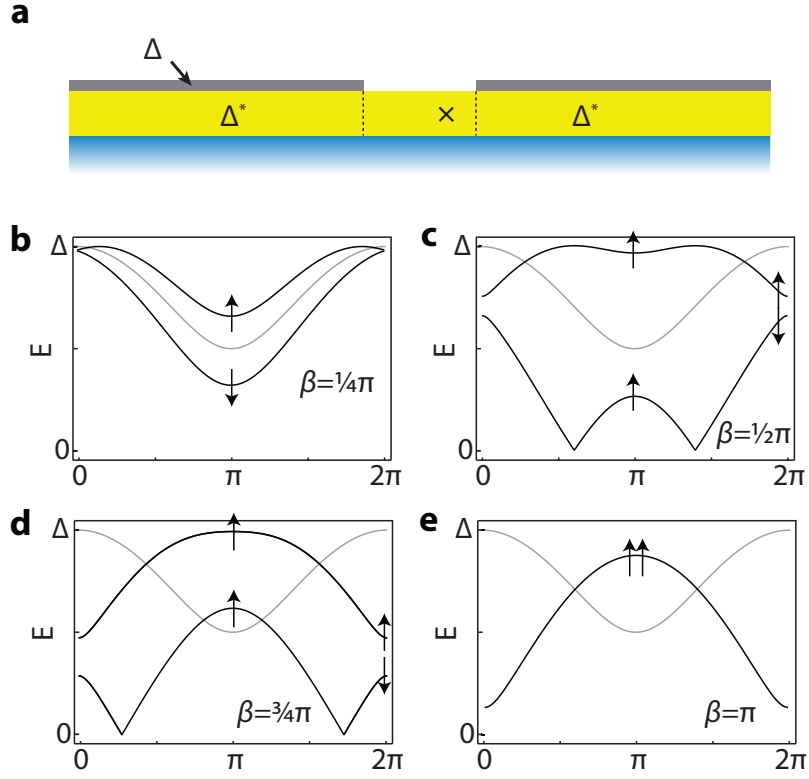


Figure 3.14: **a** The nanowire model used in this section, where Δ^* is the induced gap in the nanowire. The grey region is a superconductor with a gap of Δ , which is kept constant in all models. **b-e** ABS with transmission $T = 0.74$ and gap Δ are shown in grey. For all subfigures the magnetic field is varied according the inset value of β .

π AND ϕ_0 JUNCTIONS

The ABS in the previous section are textbook in the sense that they only interact with the NS interface twice and have a scatter point giving a transmission of $0 < T < 1$. In MZM research, we also need to consider magnetic field and spin-orbit coupling in ABS. In refs. [64, 74, 75], ABS are calculated accounting for magnetic field and spin-orbit coupling.

The model we consider is an SNS junction where only the N part is exposed to the magnetic field. This leaves the S parts unmodified by the magnetic field¹⁰. The nanowire in Figure 3.14a has two regions with induced superconductivity Δ^* and an N part with a scatter point which reduces the transmission from unity. The ABS energy solutions are given in ref. [75] and plotted in Figure 3.14b-e. The strength of the magnetic field is expressed by $\beta = \frac{\mu_B B d}{\hbar v_F}$, where d is the junction length. When $\beta = \pi$, the ABS is fully

¹⁰In Chapter 9 a theory will be discussed (arising out of the theory collaboration with Yale University on that project), which includes the reduction of the induced gap in the nanowire due to Zeeman splitting. See also ref. [64].

inverted, as shown in Figure 3.14e. The lowest energy is now at $\delta = \pi$ ¹¹ and this junction is called a π junction. The magnetic field is applied along the nanowire in the model of ref. [75]. The dispersion relation (without superconductivity, $\Delta = 0$) is plotted in Figure 3.21c-d and is strictly symmetric. This also results in symmetric ABS. Due to the angle-dependence of the magnetic field and the effective spin-orbit field, however, the dispersion is asymmetric [76]. This can lead to φ_0 junctions, which were recently demonstrated experimentally [77].

JOSEPHSON RADIATION

When a Josephson junction is voltage-biased, the phase winds according to the AC Josephson relation. By putting the AC relation into the DC relation, we obtain (for SIS junctions) $I = I_C \sin \frac{2eV}{\hbar} t$, where $\frac{2eV}{\hbar} = \omega$. For ABS we obtain

$$I_{\text{ABS}} = \frac{e|\Delta|}{2\hbar} \sum_{i=1}^{N_{\text{CH}}} \frac{T_i \sin \omega t}{\sqrt{1 - T_i \sin^2 \frac{\omega t}{2}}}. \quad (3.57)$$

Both the SIS and SNS junction expressions give an oscillating supercurrent at finite voltage. These supercurrents are composed of Cooper pairs oscillating from one superconductor to the other. Figure 3.15a shows a visualisation of the way these Cooper pairs jump forwards and backwards.

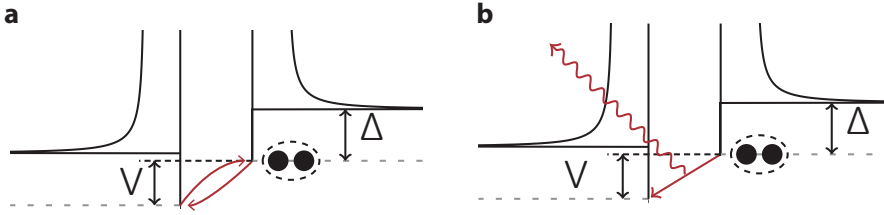


Figure 3.15: **a** Oscillating supercurrent, shown as Cooper pairs tunneling forwards and backwards. **b** A Cooper pair jumps to the other side by emitting a photon ($E_{\text{photon}} = \hbar\omega = 2eV$). The Cooper pair cannot tunnel back to its original side, due to the inelastic process of emitting a photon.

When a Cooper pair jumps in Figure 3.15a, we can visualize this as the emission of a (virtual) photon. This photon is then reabsorbed by the Cooper pair so that it can tunnel back to the original side. In Figure 3.15b, this photon is instead absorbed by the environment, meaning that the Cooper pair tunnels inelastically.

We can look at the spectrum that is emitted due to these current oscillations. For an SIS junction, the spectrum is

$$S_{\text{SIS}}(\omega) = \frac{I_C^2}{4} \left[\delta\left(\omega + \frac{2eV}{\hbar}\right) + \delta\left(\omega - \frac{2eV}{\hbar}\right) \right], \quad (3.58)$$

where $\delta(x)$ is a Dirac-delta pulse (0 everywhere, except at $x = x_0$ where the function is ∞) and the integral over all x is one. The peak in the spectrum at negative frequency indicates *emission* and the one at positive frequency is due to *absorption*. We will continue this noise spectrum analysis in Section 3.6.

¹¹We only show $+E_A$, but the ground state energy is $-E_A$.

3.3.5. SPLIT JUNCTIONS

A split junction is also known as a superconducting quantum interference device (SQUID). It consists of two superconducting arms, with a Josephson junction in each. Figure 3.17a and b shows a DC-SQUID. The DC-SQUIDS used in this thesis have SIS junctions in both arms (Chapter 7 and 8) or an SIS junction in one arm and a nanowire junction in the other (Chapter 9). Scanning electron microscope (SEM) images of these two cases are shown in Figure 3.16.

3

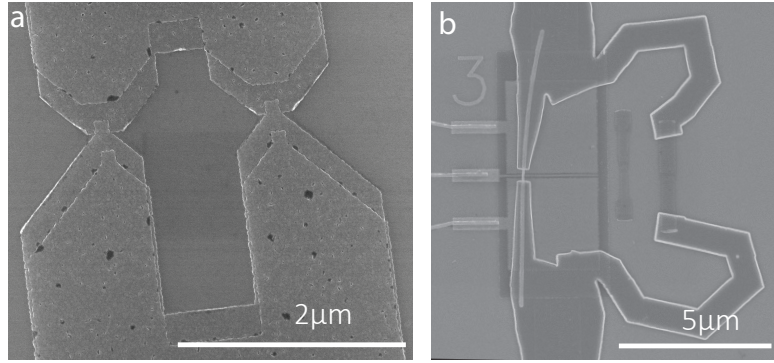


Figure 3.16: **a** SEM image of a SQUID with an SIS Josephson junction in both arms. The tunnel junctions are Al/AlO_x/Al overlap junctions, as shown in Figure 3.9a. **b** SEM image of a hybrid SQUID with an SIS junction in the right arm and an SNS nanowire Josephson junction in the other.

The total current in the SQUID is conserved and in case of two SIS junctions it is

$$I_{\text{tot}} = I_{C,1} \sin \delta_1 + I_{C,2} \sin \delta_2. \quad (3.59)$$

We now have to calculate the maximum allowed supercurrent I_{tot} . For this we have to find the allowed values of δ_1, δ_2 . If we neglect any possible phase gradients in the arms, except at the SIS junctions, we obtain the following relation for the magnetic flux applied to the loop:

$$\delta_1 - \delta_2 = \frac{2\pi}{\Phi_0} \int B \cdot dA = 2\pi \frac{\Phi}{\Phi_0} = \varphi, \quad (3.60)$$

where the surface A is defined by the dashed square in Figure 3.17b. If we fill in this relation we get

$$I_{\text{tot}} = I_{C,1} \sin(\varphi + \delta_2) + I_{C,2} \sin \delta_2. \quad (3.61)$$

We have now obtained a CPR for a SQUID where we can set φ using the external flux. If the SQUID is current-biased, the phase δ_2 will adjust to conform to eq. 3.61 up to a maximum current of I_{tot} , which is the critical current of the SQUID. The critical current for different ratios between $I_{C,1}$ and $I_{C,2}$ is shown in Figure 3.17c. For large current asymmetries ($I_{C,1} \ll I_{C,2}$), $\delta_2 \approx \frac{\pi}{2}$ and the applied flux drops over the weaker junction, determining the critical current oscillations. In this limit the CPR of a junction with $I_{C,1}$ can be probed by a $\frac{\pi}{2}$ phase shift.

If we keep $I_{\text{tot}} = 0$ and instead phase-bias the junction, we get $\delta_2 \approx 0$ in the asymmetric limit and the phase applied via the flux will drop over the weaker junction.

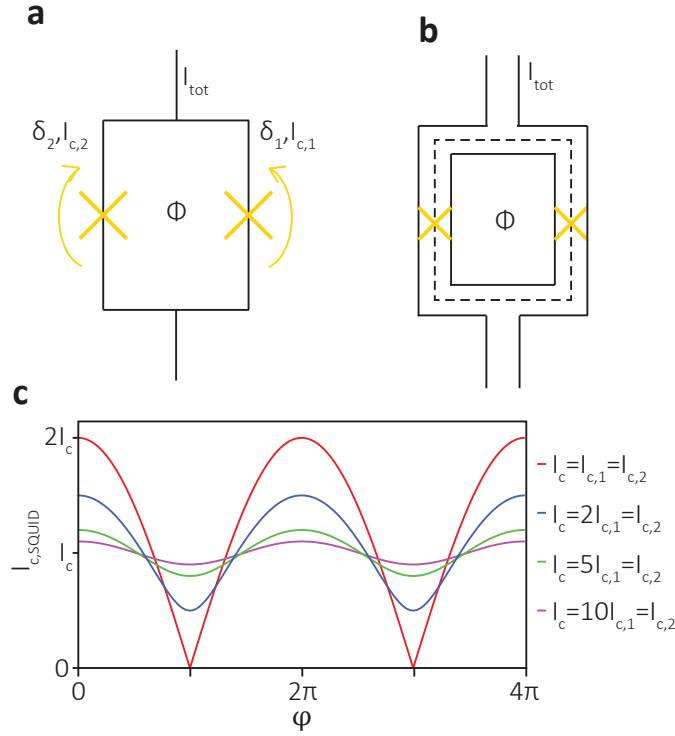


Figure 3.17: **a** Schematic of a SQUID with one Josephson junction in each arm. **b** Schematic of a SQUID with finite-size arms, where the dashed box shows the region that encloses the flux, Φ . **c** Critical current oscillations as a function of applied flux, obtained by maximizing eq. 3.61 for δ_2 .

The other case we consider is a SQUID with an SIS junction in one arm and a nanowire junction in the other, described using the SNS model. This SQUID is drawn as an inset to Figure 3.18d and is called a hybrid SQUID. For simplicity, we assume a single channel ($N_{CH} = 1$), giving a total current of

$$I_{tot} = \frac{e|\Delta|}{2\hbar} \frac{T \sin(\varphi + \delta_2)}{\sqrt{1 - T \sin^2 \frac{\varphi + \delta_2}{2}}} + I_{C,1} \sin \delta_1. \quad (3.62)$$

In this case, the SQUID is asymmetric for $\frac{e|\Delta|}{2\hbar} T \ll I_{C,1}$ and all of the phase due to the applied flux drops over the nanowire junction. In the supplement to Chapter 9, we discuss the case where $\frac{e|\Delta|}{2\hbar} T < I_{C,1}$. There we give an analytic approximation and an exact numerical result for the phase drop δ_1 over the SIS junction in a nanowire SQUID. In Figure 3.18 we show, for $\frac{e|\Delta|}{2\hbar} T \approx I_{C,1}$ and $\frac{e|\Delta|}{2\hbar} T < I_{C,1}$, the ABS winding, δ_2 and critical current of a nanowire SQUID as a function of applied flux, φ . More examples are shown in Appendix D.

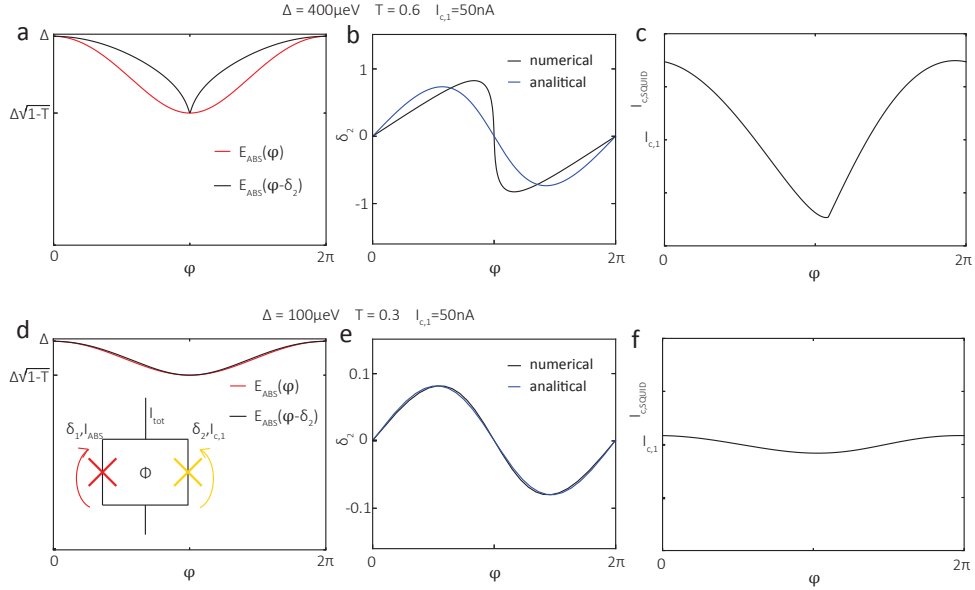


Figure 3.18: **a-c** For $\frac{e|\Delta|}{2\hbar}T \approx I_{C,1}$, we show in **a** the ABS with $\delta_2=0$ and the analytically exact results obtained from eq. 3.62. **b** Numerically exact values and analytical approximations of the phase drop δ_2 . **c** The maximum allowed supercurrent for a nanowire SQUID. **d-f** The same as **a-c** but in the limit $\frac{e|\Delta|}{2\hbar}T < I_{C,1}$.

3.4. MAJORANA PHYSICS

The goal of the research group within which this PhD was conducted is to further understand and control MZM. The theory of MZM is therefore important and will be discussed in this section. There have been many developments in the theory after the initial experiment confirming the existence of MZM[9]. We cannot discuss them all, and will only discuss the landmark papers which led to the initial idea of creating MZM in semiconductor nanowires. We start with the Kitaev (toy) model that shows the existence of MZM in one-dimensional systems. This is followed by a discussion of the proposed experimentally-accessible system, which models 1D nanowires including spin-orbit coupling, superconductivity and magnetic fields. Possible signatures of MZM in Josephson junctions are discussed in Section 3.4.4.

3.4.1. THE KITAEV TOY MODEL

The system proposed by Kitaev is a 1D system with N lattice sites, where each site j can be occupied by a single (spinless!) electron[4]. The Hamiltonian is

$$H_{\text{chain}} = \sum_{j=1}^N -t(c_j^\dagger c_{j+1} + c_{j+1}^\dagger c_j) - \mu c_j^\dagger c_j + \Delta^* c_j c_{j+1} + \Delta c_{j+1}^\dagger c_j^\dagger, \quad (3.63)$$

where the creation and annihilation of electrons is represented by the operators c^\dagger and c . t is the hopping term, μ the on-site charging energy and Δ the superconducting gap.

The last two terms of H_{chain} represent the creation and annihilation of a paired electron, i.e. a Cooper pair.

The idea of ‘spinless’ electrons does not seem right. Actually, however, if eq. 3.63 included spin it still would work, but all the spins would have to be \uparrow or \downarrow : the system would have to be spin-polarized.

Due to the creation and annihilation terms for Cooper pairs in the Hamiltonian, particle number is not a conserved quantity. This gives rise to a superposition state of an electron c^\dagger and the absence of an electron c . These excitations are called Bogoliubov quasiparticles, which were introduced in Section 3.1. They can be defined as follows:

$$\gamma_{2j-1} = \gamma_{2j-1}^\dagger = (c_j^\dagger + c_j) \quad (3.64)$$

$$\gamma_{2j} = \gamma_{2j}^\dagger = i(c_j^\dagger - c_j). \quad (3.65)$$

This is a special case, since the superposition is an equal superposition of c^\dagger and c , meaning $\gamma = \gamma^\dagger$. This is (so far) not a realistic system since the electrons c^\dagger are spinless, but it is still useful.

The definitions given in eqs. 3.64 and 3.65 make the Majoranas in this system non-fermionic. The normal fermionic commutation relations are

$$\{c_n, c_m^\dagger\} = \delta_{nm} \quad (3.66)$$

$$\{c_n, c_m\} = \{c_n^\dagger, c_m^\dagger\} = 0, \quad (3.67)$$

where δ_{nm} is 1 (0) if $n = m$ ($n \neq m$). These commutation relations allow us to calculate commutation relations for the MZM, which are

$$\{\gamma_i, \gamma_j\} = \{\gamma_i^\dagger, \gamma_j^\dagger\} = \{\gamma_i^\dagger, \gamma_j\} = 2\delta_{ij} \quad (3.68)$$

$$\gamma\gamma^\dagger = \gamma^\dagger\gamma = 1. \quad (3.69)$$

These are not the same as the fermionic commutation relations.

To rewrite H_{chain} using Majorana operators γ , we rewrite eqs. 3.64 and 3.65:

$$c_j = \frac{1}{2}(\gamma_{2j-1} + i\gamma_{2j}) \quad (3.70)$$

$$c_j^\dagger = \frac{1}{2}(\gamma_{2j-1} - i\gamma_{2j}). \quad (3.71)$$

Kitaev’s Hamiltonian using Majorana operators is therefore

$$H = \sum_{j=1}^N i(t + |\Delta|)\gamma_{2j-1}\gamma_{2j+2} + i(t - |\Delta|)\gamma_{2j+1}\gamma_{2j} - \mu(i\gamma_{2j-1}\gamma_{2j+1}). \quad (3.72)$$

A special case arises when $t = -|\Delta|$ and $\mu = 0$, as now

$$H = it \sum_{j=1}^{N-1} \gamma_{2j}\gamma_{2j+1}. \quad (3.73)$$

This is interesting, since γ_1 and γ_N are no longer part of the Hamiltonian; they are unpaired MZM at the end of the 1D lattice[4]. The uncoupled MZM form a non-local fermion, $c = \frac{1}{2}(\gamma_1 + i\gamma_N)$ and $c^\dagger = \frac{1}{2}(\gamma_1 - i\gamma_N)$. This means that in this limit the Hamiltonian does not have a preference for an odd or even number of electrons, due to this non-local fermionic state with zero energy.

This creation of unpaired MZM happens at the sweet spot $t = -|\Delta|$ and $\mu = 0$. Ref. [4] shows that in fact the condition for unpaired MZM is $|\mu| < |2t|$ and $\Delta \neq 0$, making it robust against small fluctuations in μ , t or Δ . The difference between this and the sweet spot is that the wavefunctions of the unpaired MZM do not extend into the rest of the system and the MZM do not overlap.

3

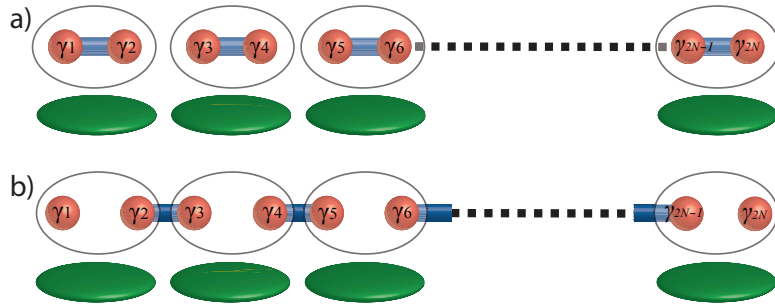


Figure 3.19: **a** A representation of lattice sites (green plates) occupied by electrons which contain two coupled MZM. **b** In the limit of $|\mu| < |2t|$ and $\Delta \neq 0$, MZM of neighboring sites are coupled, leaving two unpaired MZM at the end of the 1D chain.

If the wavefunctions of the outer MZM do overlap with strength t' , the contribution to the Hamiltonian is

$$H_{\text{overlap}} = i t' \gamma_1 \gamma_N = t' (2n_{\text{MZM}} - 1), \quad (3.74)$$

which is actually the parity operator introduced in Section 2.3. We can conclude that filling the outer MZM with an electron without MZM wavefunction overlap costs no energy. If there is an overlap, it costs an additional energy of $2t'$ [78].

3.4.2. THE SEMICONDUCTOR/SUPERCONDUCTOR APPROACH

As was mentioned in the previous section, a p-wave superconductor is effectively needed to create MZM in condensed matter systems. Unfortunately, no materials with that kind of superconducting property exist in nature. To create a p-wave superconductor, we need to combine several material properties[7, 8]. At the heart of this proposal is a 1D semiconducting nanowire. The necessary ingredients of the nanowire are strong spin-orbit interaction (SOI), a large g-factor and low disorder¹². This, in combination with applied magnetic field and induced superconductivity, can lead to the emergence of MZM.

As we will see, the orientation of the 1D nanowire compared to the spin-orbit direction and magnetic field is important. We define the nanowire direction to be along the x -axis, which is also the direction of the magnetic field. The nanowire is on a surface with

¹²This is not derived or explained in this thesis, but good references are [79, 80]

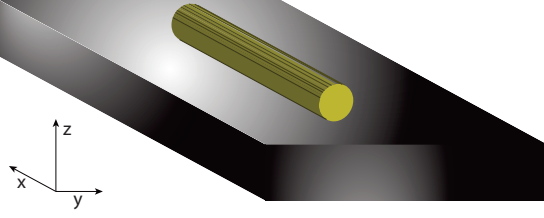


Figure 3.20: Schematic depiction of a cylindrical nanowire on a surface. This picture is important in defining the co-ordinate system of the nanowire.

a gate dielectric in the negative z direction. This nanowire orientation is shown in Figure 3.20. We can construct a full Hamiltonian for this system, including all the necessary effects to create MZM, similarly to eq. 3.1. If we take eq. 3.1 without the superconductivity ($\Delta = 0$), we obtain the Schrödinger equation. The kinetic and potential energy solutions for the Hamiltonian[48] are

$$E_{\uparrow,\downarrow} = \frac{\hbar^2 k_x^2}{2m} - \mu. \quad (3.75)$$

We obtain two solutions since we treat particles with different spins separately. The direction of spin \uparrow, \downarrow is chosen arbitrarily since the Hamiltonian has no direction preference. The energy solutions are shown in Figure 3.21a.

The first ingredient of MZM that we discuss is the SOI. The Hamiltonian for the spin-orbit interaction, derived in Appendix C, is

$$H_{\text{SO}} = -\frac{\alpha}{\hbar} p_x \sigma_y. \quad (3.76)$$

Due to the potential gradient in the nanowire, the moving electron sees an effective magnetic field. The electron spin aligns with this effective magnetic field, giving the spin a preferred direction, namely the eigenstates of σ_y , which we define as \leftarrow, \rightarrow . The energy solutions are

$$E_{\leftarrow, \rightarrow} = \frac{\hbar^2 k_x^2}{2m} - \mu \pm \alpha k_x, \quad (3.77)$$

as shown in Figure 3.21b. The two parabolas are shifted in momentum by the spin-orbit effect, with an offset of $k_{\text{SO}} = \frac{m\alpha}{\hbar^2}$. They are also shifted down in energy by the spin-orbit energy $E_{\text{SO}} = \frac{m\alpha^2}{2\hbar^2}$.

The magnetic field is aligned with the nanowire direction, i.e. the x -axis. The Hamiltonian for the magnetic field¹³ is

$$H_Z = \frac{1}{2} g \mu_B (B \cdot \sigma) = \frac{1}{2} g \mu_B B_x \sigma_x. \quad (3.78)$$

g is the g -factor, which is material-dependent and is like an amplification factor between the magnetic field and the Zeeman energy, E_Z . μ_B is the Bohr magneton. The energy solutions with only a magnetic field are given by $E_Z = \pm \frac{1}{2} g \mu_B B_x$ for the two spin directions of σ_x . The solutions are plotted in Figure 3.21c.

¹³We use the index Z for the magnetic field Hamiltonian because the effect of magnetic field on spin is called the Zeeman effect.

3

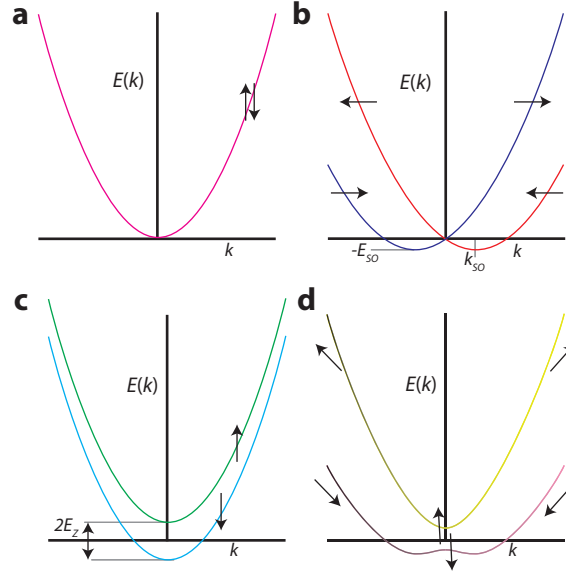


Figure 3.21: Energy dispersion of a nanowire Hamiltonian with different combinations of effects. In all cases, $\mu = 0$. **a** Solutions to the Schrödinger equation alone **b** Solutions including the spin-orbit effect or **c** only the Zeeman effect. **d** The spin-orbit and Zeeman effects combined. The limit $E_{SO} = 2E_Z = m = \hbar = 1$ is used for plotting.

More interesting is the combination of the Schrödinger equation with both a magnetic field and the spin-orbit effect. The energy solutions are

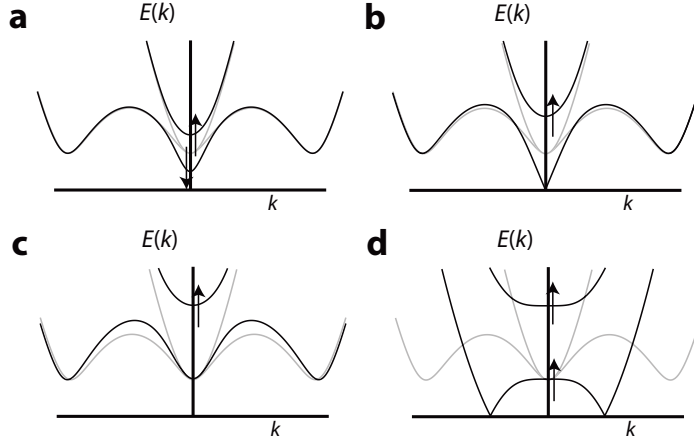
$$E_{\pm} = \frac{\hbar^2 k_x^2}{2m} - \mu \pm \sqrt{\alpha^2 p_x^2 + E_Z^2}. \quad (3.79)$$

These energy solutions are plotted in Figure 3.21d for $1 = E_{SO} = 2E_Z = m = \hbar$. At zero momentum the spin-orbit effect does not play a role, and the spin states are simply eigenstates of H_Z . For large momentum, when $\alpha^2 k_x^2 \gg E_Z$, the eigenstates are defined by the spin-orbit effect. This is also shown by the spin orientation in Figure 3.21d.

Without superconductivity we have seen that there is pairing, which results in the zero momentum and singlet-spin configuration shown earlier in this section. If we turn on superconductivity ($\Delta \neq 0$) the only available states at $-k$ and $+k$ are electrons with spins of \searrow, \swarrow . This results (partly) in triplet pairing of Cooper pairs if superconductivity is induced in the system. One can ask why SOI is necessary in the first place, as from Figure 3.21c it looks like it would be possible to obtain full p-wave pairing with only a magnetic field. We will try to explain this in the next section.

Adding superconductivity to the Hamiltonian, we get a gapped system, as shown at the beginning of this chapter and also in Figure 3.22 (grey line). In this gapped system, two different gaps can be defined. The gap at zero momentum ($k = 0$) is given by

$$E_{\text{gap},k=0} = \sqrt{\Delta^2 + \mu^2} - |E_Z|. \quad (3.80)$$



3

Figure 3.22: Energy dispersion of a nanowire Hamiltonian including superconductivity ($\Delta = 1$) and with $\mu = 0$. For all subfigures, the grey lines are for the energy solutions with $\frac{1}{2}E_{\text{SO}} = m = \hbar = 1$ and $E_Z = 0$. The spin direction is drawn for the $k = 0$ case but offset to finite k for visibility. **a** $\frac{1}{2}E_{\text{SO}} = m = \hbar = 2E_Z = 1$ **b** $\frac{1}{2}E_{\text{SO}} = m = \hbar = E_Z = 1$ **c** $\frac{1}{2}E_{\text{SO}} = m = \hbar = \frac{1}{2}E_Z = 1$ **d** $m = \hbar = \frac{1}{2}E_Z = 1$ and $E_{\text{SO}} = 0$.

When we increase the magnetic field in Figure 3.22a-c, we indeed see the gap at zero momentum closes when $\Delta = |E_Z|$. But after this point the gap opens up again for $\Delta < |E_Z|$. This inverted gap is topologically different from the gap shown by the grey line (Figure 3.22c). If we have an inverted gap in the nanowire system (at $x = x_0$), there must also be two points where it crosses to the trivial gap (one at $x < x_0$ and the other at $x > x_0$), as shown in Figure 3.22b. These crossings between the trivial and topological gaps are the locations of the MZM. Although not shown here, the eigenstates obey the Majorana condition of eqs. 3.64 and 3.65. The parameters Δ and μ can change as a function of x , getting us in and out of the topological gap. There are MZM at all these transitions.

The gap at finite momentum is given approximately by[33]

$$E_{\text{gap},k} \simeq \frac{2\Delta E_{\text{SO}}}{\sqrt{E_{\text{SO}} \left(2E_{\text{SO}} + \sqrt{E_Z^2 + 4E_{\text{SO}}^2} \right)}}. \quad (3.81)$$

For $\frac{E_{\text{SO}}}{E_Z} \ll 1$, this simplifies to $E_{\text{gap},k} \approx \frac{\Delta \sqrt{E_{\text{SO}}}}{\sqrt{E_Z}}$. In this limit, it is clear that E_{SO} needs to be finite to obtain a gapped system. The opposite limit is $\frac{E_{\text{SO}}}{E_Z} \gg 1$, where the gap is given by Δ .

The gap can also be closed by changing the angle of the magnetic field to line up with the effective magnetic field of the SOI. This tilts the spectrum of Figure 3.22, where we find the gap also closes at finite magnetic field as shown in ref. [76].

3.4.3. EXPONENTIAL COUPLING BETWEEN MAJORANAS

We have seen that MZM are zero-energy states and that they always come in pairs. The MZM wavefunctions are described by [81]

$$\Psi(x) \propto e^{-\frac{x}{\xi}} e^{ik_F x}, \quad (3.82)$$

where ξ is the effective coherence length of the MZM (measured at 260nm in ref. [14]) and k_F is its effective Fermi momentum. Both parameters depend on E_{SO} , E_Z and μ as we will discuss later, the exact expressions being given in ref. [81]. The MZM wavefunction overlap makes the MZM couple, giving them a finite energy splitting. They push each other away from zero energy. The splitting is given by

$$\Delta E \approx \hbar^2 k_F \frac{e^{-\frac{2L}{\xi}}}{m\xi} \cos(k_F L), \quad (3.83)$$

where L is the distance between the MZM. Assuming this distance is fixed, changing k_F gives energy oscillations and weak amplitude changes. The effective coherence length, ξ , strongly influences the amplitude due to being in the exponent. When E_Z is increased, ξ and the oscillation amplitude also increase[81].

If it is possible to extend the topological region (by gate tuning[16]) the MZM become more separate and the coupling and oscillation amplitude decrease. If the induced superconductivity gap is larger, then the coherence length decreases ($\frac{1}{\xi} \sim \Delta$). The discussion of E_{SO} is more complicated, though it is discussed in certain limits in ref. [81].

3.4.4. TOPOLOGICAL JUNCTIONS

Topology was introduced in Section 2.3 as the study of different classes of objects. Now we would like to discuss the difference between trivial junctions (such as the ones we have already discussed) and the non-trivial junctions we will consider in this section. Non-trivial junctions are often referred to as topological junctions. These junctions are topologically different because the bound state has an odd number of crossings with $E = 0$ (for $0 < \delta < 2\pi$), where trivial junctions have an even number of crossings as can be seen in the examples in Figure 3.7b and 3.13b. A trivial ABS with $T = 1$ seems to have an odd number of crossings, but the whole lower branch is the same parity state ($|0\rangle$), so in fact there are no crossings there.

As a consequence, the ABS states for a topological junction are 4π -periodic, instead of the 2π periodicity of the trivial junctions discussed before.

MAJORANA BOUND STATES

No phase dependence was introduced in the Kitaev model in Section 3.4.1 when we defined the MZM. This is important when there are multiple superconductors involved, as we have seen in Appendix B. Taking phase into account, eqs. 3.64 and 3.65 become

$$\gamma_1 = (c_1^\dagger e^{i\frac{\phi_1}{2}} + c_1 e^{-i\frac{\phi_1}{2}}) \quad (3.84)$$

$$\gamma_2 = i(e^{-i\frac{\phi_2}{2}} c_1^\dagger - c_1 e^{i\frac{\phi_2}{2}}), \quad (3.85)$$

where ϕ_1, ϕ_2 are the superconducting phases on the left and right superconductors and γ_1, γ_2 are overlapping as shown in Figure 3.23a. These are the only MZM used in deriving

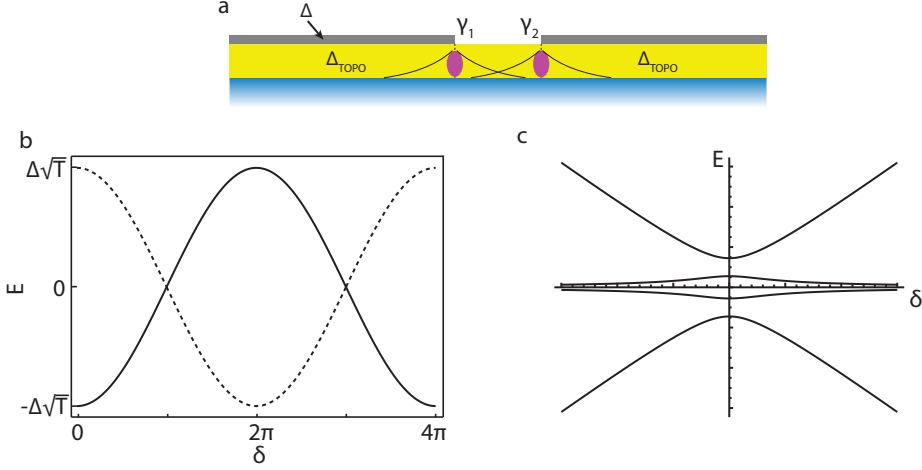


Figure 3.23: **a** Schematic view of MZM (in purple) overlapping in a topological junction. **b** The energy-phase relations for MBS states with even parity (solid line) and odd parity (dashed line). **c** Zoomed-in view of the MBS at $\delta = \pi, 3\pi, \dots$, where the outer Majorana's overlap with the middle ones is taken into account, leading to opening of a gap. Figure adapted from ref. [82].

MBS. (Perhaps this junction is a ring, or extends very far in both directions compared to the coherence length.) When γ_1 and γ_2 overlap, they form a fermionic state whose occupation n can be defined via eq. 2.3. Defining $\phi_2 = \frac{\delta}{2}$ and $\phi_1 = -\frac{\delta}{2}$, we get a phase difference of $\phi_2 - \phi_1 = \delta$ and the joint occupation n_1 becomes

$$n_1 = \frac{1}{2}(1 + i\gamma_1\gamma_2) = \frac{1}{2}(1 - e^{i\frac{\delta}{2}}) + c_1^\dagger c_1 \cos \frac{\delta}{2}, \quad (3.86)$$

which is indeed eq. 2.3 if we take $\delta = 0$. When we wind the phase ($\delta = 2\pi$), the occupation is opposite because we obtain $n_1 = 1 - c_1^\dagger c_1$; a fermion has effectively been transferred to the MBS[4]. Another wind ($\delta = 4\pi$) is necessary to change back to the original situation. The occupation of MBS is now again given by $n_1 = c_1^\dagger c_1$ and another fermion is transferred to the MBS, making the Josephson current 4π -periodic and topologically different from a trivial ABS.

The energy of the bound state between the two MZM is[83, 84]

$$E_{\text{MBS}} = \pm \Delta_{\text{TOPO}} \sqrt{T} \cos \frac{\delta}{2}, \quad (3.87)$$

which is 4π -periodic as expected and, as with the trivial junction, has positive and negative solutions. These two energy solutions are plotted in Figure 3.23b. One MBS state is bound to $E = 0$, the other instead bound to the gap edge. The two energy solutions differ by occupation difference, as with ABS. The solid line shows even parity ($n = 0$) and the dashed line odd parity ($n = 1$). This means that the ground state parity changes if we wind the phase. Now there is no parity preference (for even parity) as there was with trivial ABS, since there are now zero-energy Majoranas. If there are quasiparticles and the

phase winds slower than the quasiparticle poisoning time, MBS can change occupation and the energy becomes 2π -periodic.

We have neglected the presence of MZM at the other end of the topological region. If there were, for example, also MZM at the leftmost and rightmost sides of the junction in Figure 3.23a, these MZM could also overlap with the MZM at the junction. The overlap of these MZM opens the gap at $\delta = \pi, 3\pi, \dots$, as shown in Figure 3.23c. But when the phase is driven quickly compared to the energy gap, the system can LZ tunnel to the other branch and still show 4π -periodicity.

3

JOSEPHSON EQUATIONS - TOPO

Using eq. 3.24, we can calculate the DC Josephson effect for an MBS, giving

$$I = \frac{e\Delta_{\text{TOPO}}\sqrt{T}}{2\hbar} \sin \frac{\delta}{2} = I_{\text{MBS}} \sin \frac{\delta}{2}, \quad (3.88)$$

assuming that the system cannot change occupation due to a long quasiparticle poisoning time. If it is possible to relax to the ground state, the CPR is $I \propto |\sin \frac{\delta}{2}|$, which is 2π -periodic. Apart from the difference in periodicity, there is also a clear difference in the strength of the supercurrent. In the MBS case $I \propto \sqrt{T}$, while for ABS it is $I \propto T$. The last important difference is the gap. In case of MBS, it is a topological gap, which is (far) above the topological transition given by eq. 3.81 and depends on the spin-orbit strength, the initial zero-magnetic-field gap Δ and the adjustable Zeeman energy.

If we substitute the conventional AC Josephson relation, $\hbar\omega = 2eV$, into eq. 3.88, we obtain current oscillations at half the characteristic Josephson frequency. Often this effect is described in the literature as the fractional Josephson effect[85].

MAJORANA RADIATION

Due to the 4π -periodicity of the MBS, the CPR is also 4π -periodic. The noise spectrum of the current changes to

$$S_{I,\text{MBS}}(\omega) = \frac{I_{\text{MBS}}^2}{4} \left[\delta \left(\omega + \frac{eV}{\hbar} \right) + \delta \left(\omega - \frac{eV}{\hbar} \right) \right]. \quad (3.89)$$

Where before we could describe the Josephson radiation in terms of Cooper pairs jumping and emitting photons, we now have photons with half the energy. We can see this as electrons jumping and emitting photons with energy $\hbar\omega = eV$.

When the junction is voltage-biased with a finite voltage which is smaller than the energy gap due to the overlap of the outer MZM (see Figure 3.23c), the CPR is 2π -periodic but the amplitude of the current oscillation is still I_{MBS} . A detailed analysis is performed by Pikulin and Nazarov in ref. [82]. Another way of recovering 2π -periodicity is by quasiparticle poisoning, discussed in detail by San-Jose *et al.* in ref. [86]. The last possible effect that can restore the 2π -periodicity is LZ tunneling to the continuum, which was discussed in ref. [68] by Houzet *et al.* When there is LZ tunneling to the continuum, the state also changes occupation and 2π -periodicity can be restored naively. In the supplement to ref. [68], the noise spectrum for this case is calculated but no strong 2π signal is found. This effect leads to broadening of the 4π signal.

These three effects set limits on the voltage bias. Without discussing the three papers in detail, we set a voltage window where 4π -periodicity should be observed. For a $2\mu\text{m}$ -long topological section, the MZM coupling strength is less than a microvolt [14]. If we then set a (low) voltage bias, $V = 2\mu\text{V}$, $\Delta_{\text{TOPO}} = 30\mu\text{V}$ and a transmission of $T = 0.5$ we obtain an LZ probability of 0.75. This is enough to reveal a clear strong 4π effect, as is shown in ref. [82].

We can analyse LZ tunneling to the continuum with the same gap and transmission. If we take a high voltage bias of $V = 15\mu\text{V}$, the probability to LZ is 0.3^{14} . This probability still shows a strong 4π contribution in the noise spectrum, as is seen in the supplement to ref. [68].

The quasiparticle poisoning time in nanowire devices has been shown to be around 10ms[22], and the voltage range needed is 2–15 μV . This corresponds to 1–10GHz, which is much faster than the expected quasiparticle poisoning time. It is therefore not expected that quasiparticle dynamics can destroy the 4π periodicity.

3.5. CHARGING AND JOSEPHSON PHYSICS

The proposed realization of MZM braiding relies on charging and Josephson physics[17, 35]. As discussed earlier, braiding changes the parity of the MZM and for this reason we investigate the parity of NbTiN in Chapter 6. To do this we put two Josephson junctions in series with NbTiN in-between forming an island, with charging energy $E_C = \frac{e^2}{2C}$. This setup is shown in Figure 3.24a. The maximum allowed supercurrent depends on the parity of the island, giving us access to the parity lifetime.

3.5.1. SINGLE ELECTRON TRANSISTORS

Single electron transistors (SET) are often mixed up with quantum dots (QD). The difference is that on the island of a SET there are many electrons. The only additional energy required to add an electron is the charging energy E_C , since the orbital energy is negligible. A QD exists in a few-electron regime where the orbital energy is sizeable. A SET is schematically depicted in Figure 3.24b. In direct current measurements, the current flows from the source (S) to the drain (D). This is possible since the capacitors drawn in Figure 3.24b are (normal) tunnel junctions. The island is capacitively coupled to a gate which can change the ground state energy of the system. The gate is not a tunnel junction. The Hamiltonian of an island is given by

$$H_{\text{island}} = E_C \left(n - \frac{V_g C_g}{e} \right)^2 = E_C (n - n_g)^2, \quad (3.90)$$

where n is the discrete number of electrons on the island, V_g the voltage potential of the gate and C_g the capacitance of the gate to the island. The total charging energy is defined by $E_C = \frac{e^2}{2C_\Sigma}$, where $C_\Sigma = C_g + C_1 + C_2$, which are all the capacitances between the island and the outside world. The energy levels are shown in Figure 3.24c, where although we are in the many-electron regime we start counting from $n = 0$ for convenience. If the gate voltage is changed slowly, the system will stay in the ground state, indicated by the

¹⁴We read this off from Figure 1 in ref. [68], which gives numerical results for LZ tunneling to the continuum.

thick black line. For $n_g = \frac{1}{2}, \frac{3}{2}, \dots$ the island adds or removes an electron to the source or drain to stay in the ground state.

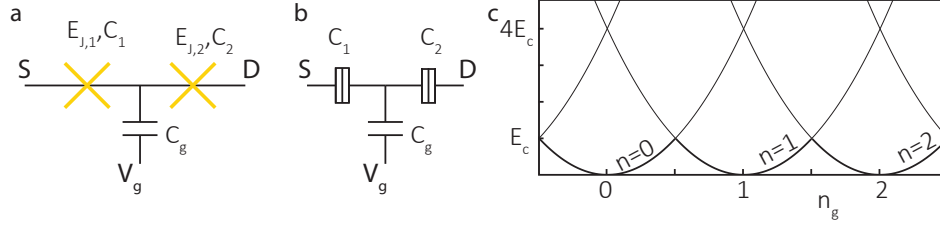


Figure 3.24: **a** An island is formed with two SIS junctions in series and a gate coupled to the island. **b** A SET with two tunnel junction with capacitance C_1 , C_2 and a gate with capacitance C_g . Electrons can tunnel from the tunnel junction to change n and keep the system in the ground state. **c** The energy solutions of the Hamiltonian eq. 3.90, with the thick line indicating the ground state of the system.

3.5.2. SINGLE ELECTRON TRANSISTORS WITH JOSEPHSON COUPLING

A superconducting single-electron transistor is often referred to as a Cooper-pair transistor (CPT) since Cooper pairs are the main charge carriers for zero or low voltages. In addition, the ground state of the island has a preference for an even number of charges due to the double-charge nature of Cooper pairs. A new charging energy can be defined for a Cooper pair, namely $E_{C,\text{super}} = \frac{2e^2}{C_\Sigma} = 4E_C$. We can also redefine the charging energy in eq. 3.90, taking n as the number of Cooper pairs¹⁵.

A single quasiparticle can only occupy a state above the gap Δ . In Chapter 6 we will also see that there is a finite subgap DOS due to oxidization of the NbTiN, recently analyzed in detail in ref. [87]. We can describe the quasiparticles in the Hamiltonian using $H_{\text{QP}} = \sum_j \epsilon_j b_j^\dagger b_j$, for j quasiparticles with energy ϵ_j [88]. This Hamiltonian describes quasiparticle poisoning, which is uninteresting in the ideal case.

For a CPT, the tunnel junctions are replaced by SIS junctions, as shown in Figure 3.9a and b. Both junctions have a Josephson energy and for a CPT the Hamiltonian derived in eq. 3.35 becomes[88]

$$H_{\text{JJ}} = -E_{J,1} \cos \delta_1 - E_{J,2} \cos \delta_2. \quad (3.91)$$

We can define the total phase difference of a CPT as $\delta = \frac{1}{2}(\delta_1 + \delta_2)$. Similarly, we can define the difference in the phases of the two junctions as $\theta = \delta_1 - \delta_2$, which is zero for symmetric junctions. For symmetric junctions $E_{J,1} = E_{J,2} = \frac{1}{2}E_J$, giving a Hamiltonian of $H = -E_J \cos \delta$ ¹⁶. Thus the total Hamiltonian is

$$H = -E_J \cos \delta + E_C (n - n_g)^2 + \sum_j \epsilon_j b_j^\dagger b_j. \quad (3.92)$$

In a CPT both phase and charge are operators but they do not commute. A measurement of charge makes the phase undetermined and vice versa.

¹⁵Except in Chapter 9, where we use $E_{C,\text{super}}$

¹⁶We left out the $\cos \theta$ term, which is zero if the junctions are symmetric.

The Josephson effect changes the ground state by adding or removing a Cooper pair. A complete charge-based Hamiltonian is given by[53]

$$H|n\rangle = E|n\rangle = E_C(n - n_g)^2 |n\rangle - \frac{E_J}{2} (|n-2\rangle + |n+2\rangle). \quad (3.93)$$

In our case, $j = 0$, so there are no quasiparticles. This is the Hamiltonian we will use to obtain any further results unless stated otherwise.

THE LIMIT $E_J \ll E_C$

In the limit where the Josephson coupling is small compared to the charging energy, the charge number n is well-defined. This can be seen from the energy solutions, plotted for $E_C = 10E_J$ in Figure 3.25. The bands are very similar to the case where $E_J = 0$, except that around $n_g = 1, 3, \dots$ there is an anti-crossing since the Josephson energy couples bands of different charge. Due to the coupling to the source and drain leads, Cooper pairs can flow, making the charge number uncertain. At exactly $n_g = 1$, the system is in a superposition of charge states $|0\rangle \pm |2\rangle$.

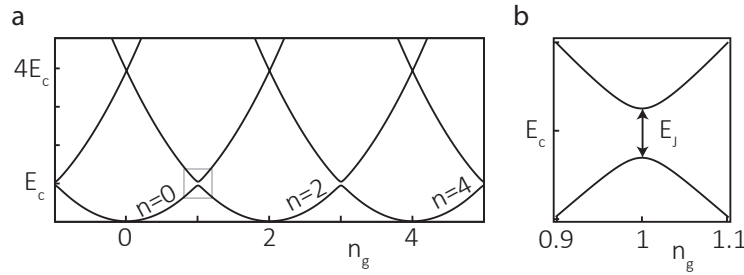


Figure 3.25: **a** The energy solutions of eq. 3.92 with $10E_J = E_C$ and no quasiparticle poisoning. **b** Zoomed-in view of **a**, showing the anti-crossing due to the Josephson coupling.

THE LIMIT $E_J \gg E_C$

In the limit where the Josephson energy dominates, we expect to find that phase is well-defined. There is a potential minimum at $\delta = 0$, giving a ground state energy close to $-E_J$ with phase fluctuations of $\sim \left(\frac{E_C}{E_J}\right)^{\frac{1}{4}} \ll \pi$ [53]. The cosine-shaped potential is approximated by $\frac{E_J}{2}\delta^2$ around $\delta = 0$, as can be seen in Figure 3.26a for $E_J = 50E_C$. This quadratic potential is known as a harmonic potential with equidistant energy solutions. This can also be seen in the energy spectrum depicted in Figure 3.26b. The energy difference between the ground state and the first excited state is $\sqrt{8E_J E_C}$, which is indeed similar to the energy difference between the first excited state and the second excited state up to a correction of E_C (which is expected to be small). The excitation $\sqrt{8E_J E_C}$ is called ω_p , the plasma mode of the circuit.

The harmonic potential has wavefunction solutions around a phase of zero, making it well-defined¹⁷. The charge is undefined as every energy solution is independent of

¹⁷For a nanowire SQUID with $\frac{E_J}{E_C} \sim 7$, these wavefunctions are calculated in Chapter 9.

gate charge and there is no preferred charge state, as can be seen in Figure 3.26b and d. In Figure 3.26c we see that there is actually a very small charge dispersion, with an amplitude of

$$U \simeq (-1)^m E_C \frac{2^{4m+5}}{m!} \frac{1}{\sqrt{2\pi}} \left(\frac{E_J}{2E_C} \right)^{\frac{m}{2} + \frac{3}{4}} e^{-\sqrt{8\frac{E_J}{E_C}}}, \quad (3.94)$$

where $m = 1$ for the ground state and increases by one for every higher mode.

In Figure 3.26b-d we have also added a grey line, which is the same as the black line but shifted by one charge. This represents the situation where a quasiparticle tunnels to the island and shifts the solution's charge by one. After the tunneling of a quasiparticle, the plasma mode changes by an amount on the order of $2U_1$, which is exponentially small with respect to $\frac{E_J}{E_C}$ and makes it charge-insensitive. Ref. [89] has been used for this section, and is recommended for further reading.

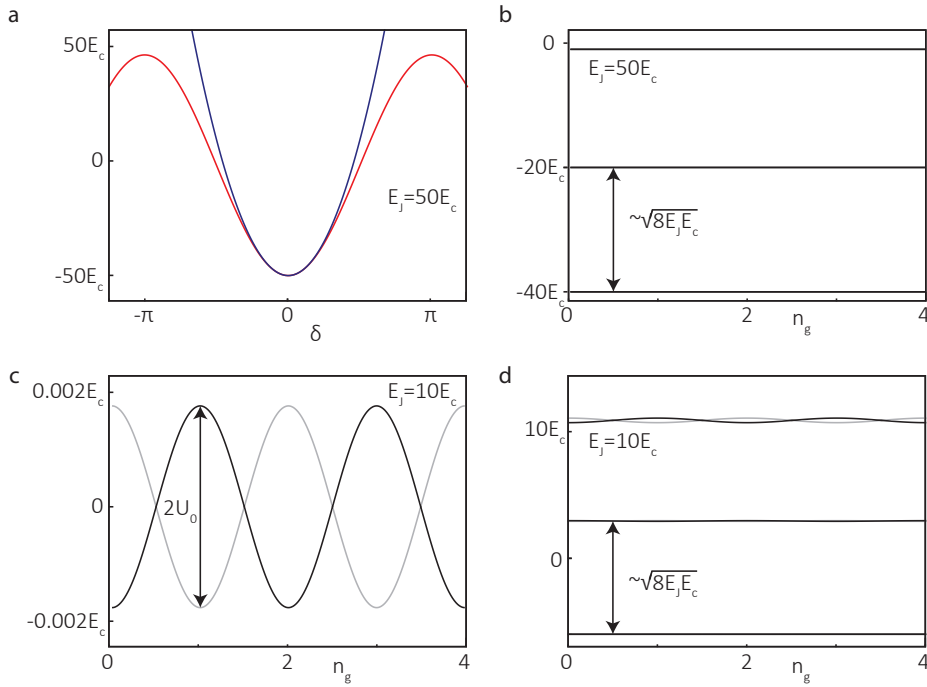


Figure 3.26: **a** The Hamiltonian as function of phase for $E_J = 50E_C$ (in red). For small δ the potential can be approximated as a harmonic oscillator, as explained in the text. **b** Energy level as function of gate charge n_g . In this limit there is almost no state dispersion as a function of gate charge. **c** Zoomed-in view of the ground state of **d**, where a small dispersion as a function of gate charge can be seen. The amplitude of the dispersion is exponentially small, as can be seen from eq. 3.94. The y -axis is offset to zero so that the oscillation amplitudes can be more clearly read off. **d** The same as **b** but with no visible energy dispersion at higher plasma modes. The oscillations become more apparent as the energy of the state approaches $+E_J$.

THE CASE $E_J \sim E_C$

We have looked at the two extremes of the $\frac{E_J}{E_C}$ ratio and now we are going to discuss the intermediate regime where $E_J \sim E_C$. The actual crossover regime is $4E_C = \frac{E_J}{2}$ [53], but here we focus on $E_J \sim E_C$ as this is relevant for Chapter 6.

We can set the phase, δ , externally over the two junctions using a bias current and the gate charge, n_g , at the island. We can solve for these two parameters using eq. 3.92, and the results are plotted in Figure 3.27a. We can see that it is $2e$ -periodic in gate charge, but this changes when quasiparticles poison the island, shifting the gate charge by one. Due to this poisoning we can calculate the two ground state (GS) energies, as shown in Figure 3.27b. The ground states have clear differences in modulation: the $n_g = 0$ has the maximal slope at $\frac{\pi}{2}$, whereas for $n_g = 1$ it is at $\delta \rightarrow \pi$. This maximal slope gives the maximal allowed supercurrent, shown in Figure 3.27c in blue. The red line in Figure 3.27c shows the maximal allowed supercurrent when the island is poisoned.

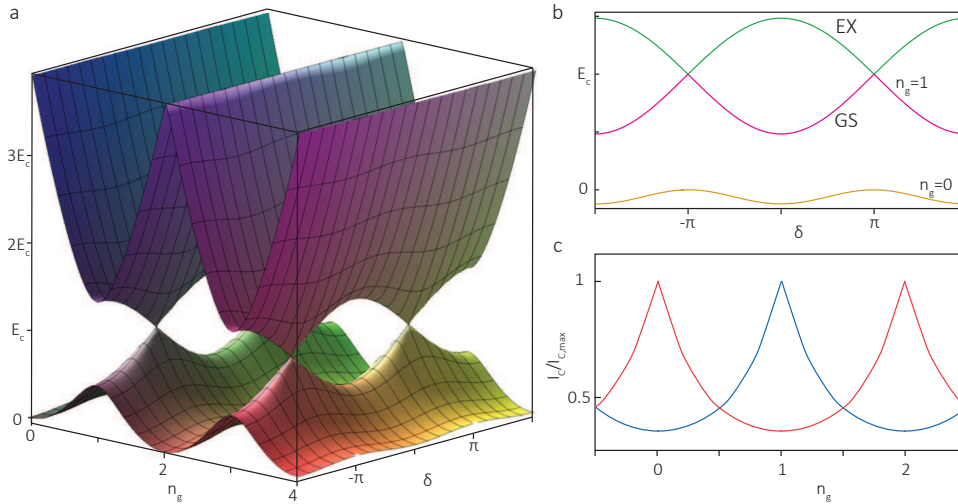


Figure 3.27: **a** The energy bands of an island with external gate charge n_g , with $E_J = E_C$. The energy levels depend strongly on n_g and δ . **b** The GS of a CPT at $n_g = 0$ and the GS and excited state (EX) at $n_g = 1$. **c** The maximal allowed supercurrent, calculated as a function of gate charge, is in blue. In red, we also depict the blue line, except shifted by e due to possible quasiparticle poisoning. Figure obtained from ref. [90].

As with highly-transmitting ABS, there could also be LZ tunneling in CPT. At a gate charge of $n_g = 1$, there is no gap at $\delta = \pm\pi$. When LZ tunneling occurs, the energy-phase relation and the CPR are both 4π -periodic, leading to a fractional Josephson effect without topological origin, as shown by Billangeon *et al.*[91].

For the switching-current experiments performed in Chapter 6, the RSCJ model can be described by a junction with a washboard potential similar to the GS energy in Figure 3.27b. Depending on the parity, we may get large modulation and high switching current ($n_g = 1$) or a low switching current ($n_g = 0$). Thus, in the absence of an exact circuit model the reduction in switching current can be used to define the parity states.

3.6. NOISE THEORY

For this section we use references [36, 92, 93], to which we would direct the reader seeking more details. We start by introducing noise. We have already described the current oscillations of the (fractional) AC Josephson effect using the power spectral density S_I . In these examples, oscillations were described by a spectrum. Experimentally, the current I through a wire fluctuates with amplitude $\delta I(t) = I(t) - \bar{I}$, where \bar{I} is the average current. The fluctuations $\delta I(t)$ can have arbitrary shape. To analyse the noise we would like to see if there are, for example, beats or repeating patterns in the fluctuations. For this reason, we define the correlation function

$$C(\tau) = \langle \delta I(\tau + t) \delta I(t) \rangle. \quad (3.95)$$

From the correlation function we can obtain the power density function via the Fourier transform

$$S_I(\omega) = \int_{-\infty}^{\infty} e^{i\omega\tau} C(\tau) d\tau, \quad (3.96)$$

which we also used to obtain eqs. 3.58 and 3.89. The positive frequencies in the power density function $S(\omega)$ represent the absorption part of the spectrum and $S(-\omega)$ the emission. For a system at low temperature, $\hbar\omega \sim k_B T$, the emission spectrum is expected to be lower than the absorption spectrum. At zero temperature, a system cannot emit photons because it has reached the ground state and can only be excited by absorption.

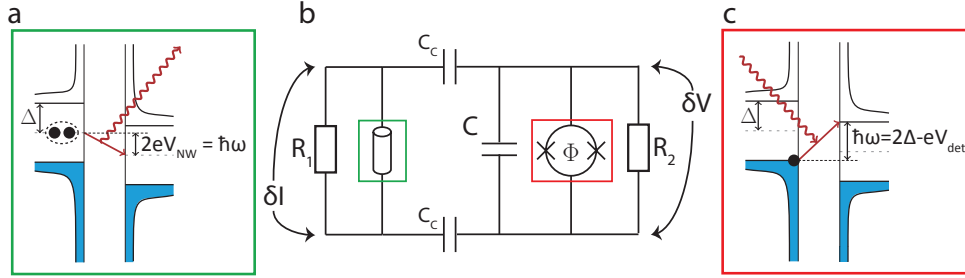


Figure 3.28: **a** Schematic view of the noise source of a voltage-biased nanowire, $0 < V_{\text{bias}} < 2\Delta$, with a power-density spectrum given by eqs. 3.58 and 3.89. **b** View of the electrical circuit used in Chapter 7 and 8, with all significant elements. The junctions in the red and green boxes are Josephson junctions that can be modelled by the RSCJ model. **c** Schematic view of detection in an SIS junction via photon-assisted-tunneling.

The current fluctuations of the AC Josephson effect cause voltage fluctuations in the rest of the circuit. The strength of the voltage oscillations is described by the coupling, which we call transimpedance:

$$S_V(\omega) = S_I(\omega) |Z(\omega)|^2. \quad (3.97)$$

We are interested in the voltage oscillations over the detector (red box), as shown in Figure 3.28b. The voltage oscillations due to an AC Josephson junction are $V(t) = Z \cdot I_C \cos \omega t$.

We use the Tien-Gordon approach [92], combined with the review of Tucker and Fieldman[93], to understand this voltage oscillation, try to measure it and extract the

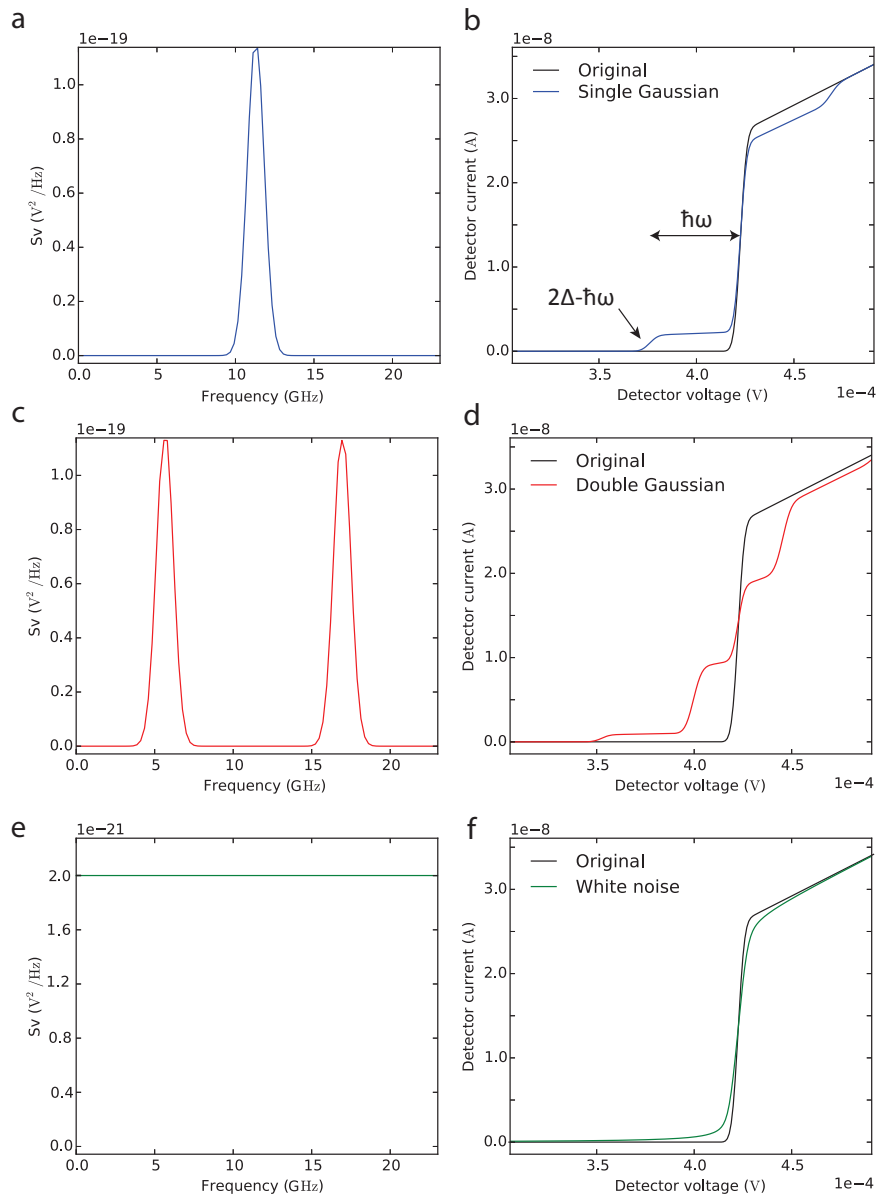


Figure 3.29: **a-f** Analysis of noise detection in an SIS junction. All S_V are a factor of ~ 100 larger than typical spectrums in the measurements for clarity. Figure obtained from ref. [94]. **a** Noise spectrum of a single-frequency $23\mu\text{V}$ (11.3GHz) source with a full width at half maximum (FWHM) of $3\mu\text{V}$. **b** The IV trace of an irradiated SIS junction with a single gaussian noise source. **c** Noise spectrum of a double-frequency, $11.5\mu\text{V}$ (5.6GHz) and $35\mu\text{V}$ (17GHz) source. **d** IV trace of an irradiated SIS junction with a double-gaussian noise source. **e** White noise spectrum. **f** SIS junction irradiated with a white noise spectrum, smoothing $I_{QP,0}$.

radiation frequency. The voltage oscillations are in the microwave regime. We can see these oscillations as microwave photons, offsetting the Hamiltonian. An arbitrary Hamiltonian will change as follows: $H = H_0 + eZ \cdot I_C \cos \omega t$. Without knowing the exact form of the initial Hamiltonian, we can write the new solution as follows:

$$\Psi(\vec{\mathbf{r}}, t) = f(\vec{\mathbf{r}}) e^{-\frac{iEt}{\hbar}} \left(\sum_{\mathbf{n}} J_{\mathbf{n}}(\alpha) e^{-in\omega t} \right), \quad (3.98)$$

where $f(\vec{\mathbf{r}})$ is the spatial solution of H and the $J_{\mathbf{n}}(\alpha)$ are the Bessel functions with argument $\alpha = \frac{eZ \cdot I_C}{\hbar\omega}$. In principle, n ranges up to $\pm\infty$ but in our case only $n = 0, \pm 1$ are visible, so those are the only values we consider. The energy solutions for this case are $E, E \pm \hbar\omega$, i.e. the original solution with the addition of lower and higher energy solutions offset by the oscillation frequency ω .

An unperturbed Hamiltonian with solutions $f(\vec{\mathbf{r}})$ would result in a DOS of $\rho(E)$, while the irradiated DOS would become:

$$\rho'(E) = \sum_{\mathbf{n}} \rho(E + n\hbar\omega) J_{\mathbf{n}}^2(\alpha). \quad (3.99)$$

The original DOS changed, due to the microwave field, into an effective DOS, changing the current flow in the process. To measure the change in the DOS, a (highly) non-linear DOS is needed. For this, we use the DOS of an SIS junction. Figure 3.28c shows the DOS of an SIS junction with an extra quasiparticle current induced by the microwave field. This subgap current is only possible due to the presence of the microwave field, and as a result the current is called a photon-assisted-tunneling (PAT) current.

Due to the PAT current, flow is already possible within the gap. Since the modified DOS is actually a shift of the normal DOS with an energy difference of $\hbar\omega$, the current within the gap is actually a step. Where normally the current onset is at 2Δ , with irradiation by a signal with frequency ω it is at $2\Delta - \hbar\omega$. For single-frequency photon absorption and for $\alpha \ll 1$, we obtain the following approximate formula for the PAT current[93]¹⁸:

$$I_{\text{PAT}}(V, \omega) = \left(\frac{e|Z| \cdot I_C}{2\hbar\omega} \right)^2 I_{\text{QP},0} \left(V + \frac{\hbar\omega}{e} \right), \quad (3.100)$$

where $I_{\text{QP},0}(V)$ is the normal IV trace of a tunnel junction without radiation, such as the black curve in Figure 3.29. We make the approximation $J_1 = \frac{\alpha}{2}$ in the limit $\alpha \ll 1$. We can extend the case of single-frequency photon absorption to an arbitrary noise spectrum of $S_V = |Z|^2 S_I$, giving[36]

$$I_{\text{PAT}}(V) = \int_0^\infty d\omega \left(\frac{e}{\hbar\omega} \right)^2 S_V(\omega) I_{\text{QP},0} \left(V + \frac{\hbar\omega}{e} \right). \quad (3.101)$$

Figure 3.29 shows three examples of power spectral densities: single- and double-frequency and white noise radiation are plotted, together with the corresponding IV traces of an SIS junction irradiated using each spectrum. The examples use an S_V that

¹⁸We used refs. [92, 93] to obtain this expression for the PAT current, which is a factor of $\frac{1}{2\pi}$ different than that given in ref. [36], eq. (3.9). The error in ref. [36] originates from eq. (3.6), which was taken from ref. [95] but where (we believe) h and \hbar were misinterpreted.

is a factor of 100 higher than is typical in experiments, to make the distortion of the microwave field more visible in the current. For detector voltages $V < 2\Delta \sim 425\mu\text{V}$ the IV trace is dominated by photon absorption (enhancing the current), while for $V > 2\Delta \sim 425\mu\text{V}$ it is photon emission (lowering the current). The behaviour of the current for $V < 2\Delta \sim 425\mu\text{V}$, is described by eq. 3.101. The full IV trace for all detector voltages is covered by eq. 3.9 in ref. [36].

The black IV trace which we have called $I_{\text{QP},0}$ is the current through an SIS junction without irradiation. It has a sharp onset of current at $V_{\text{det}} = 425\mu\text{eV}$, which is 2Δ . At zero temperature and without any (background) radiation, this current onset should be a step. In the experiment we do not have access to the real IV trace of the SIS junction due to quasiparticle heating for large currents (see Chapter 7 and 8). For this reason we constructed a smoothed IV trace for $I_{\text{QP},0}$ and investigated I_{PAT} .

Before, we only focused on photon absorption in the SIS junction, but for completeness we also plot the emission spectrum in Figure 3.29. The full equation was obtained from ref. [36].

In Figure 3.29a and b, we investigate a noise source of $23\mu\text{V}$ with a FWHM of $3\mu\text{V}$ in a voltage-biased SIS junction. We clearly see current within the superconducting gap $eV < 2\Delta$ for the IV curve with irradiation. The current is a step of size $\hbar\omega$. This makes (the steepest point of) the onset of the current $2\Delta - \hbar\omega$, which is then a measure of the frequency. Above $eV > 2\Delta$ we see a reduction of the current due to emission of quasiparticles. This emission will be neglected from now on. The detector SIS junction is a SQUID which is set up such that there is no Josephson coupling. This SIS junction is not a source of Josephson radiation, or is at least a negligible one.

In Figure 3.29c and d we show the radiation and PAT detection of a spectrum with two single frequencies with finite FWHM. This radiation source could be a nanowire junction, which can have multiple frequencies in the CPR according to eq. 3.56. The detected current through the SIS junction also has two steps, corresponding to the two frequencies. The higher-frequency PAT reaches a lower subgap voltage in the SIS junction. The higher frequency also has a lower current, as expected due to the ω^{-2} -dependence of the PAT current in eqs. 3.100 and 3.101.

We also consider the example of the noise emitted due to a current flowing through a conductor. In the limit of $eV_{\text{bias}} \gg \hbar\omega, k_{\text{B}}T$, this noise is given by [36, 53]

$$S_{\text{sn.}}(\omega) = 2e\bar{I} \frac{\sum_i T_i (1 - T_i)}{\sum_i T_i} = 2e\bar{I}F, \quad (3.102)$$

where F is the Fano factor.

The shot noise has no frequency dependence, making it a white-noise radiation source, as shown in Figure 3.29e and f. The white noise radiation rounds off $I_{\text{QP},0}$. When SIS and SNS junctions are used as a noise source, white noise is emitted when the voltage bias is larger than 2Δ . This is an unwanted background signal in the experiments of Chapters 7 and 8. This white noise radiation is measured in a similar setup in ref. [36].

4

EXPERIMENTAL METHODS

It shouldn't do that.

Giorgio Frossati

This chapter describes the basic methods needed to conduct the experiments in this thesis. As true experimentalists, we learn by practice and not by the book, but it is still important to have a basic understanding of cryogenics since refrigerators are increasingly used as a general tool. The same goes for electronics, as we work with current and voltage bias modules. These modules are almost ideal, but proper understanding is needed to know their limitations. We show that particular measurement techniques can sometimes hide interesting features. Low-noise modules for electronic control and measurement are developed. With the addition of three stages of electronic filters, we achieve electron temperatures down to 25mK. Finally, we briefly discuss (and highlight important references for) cleanroom fabrication, including deterministic nanowire deposition.

4.1. INTRODUCTION

This chapter provides a brief overview of the methods used in the experiments in this thesis. In Section 4.2, we discuss two different cryogenic techniques that were used to cool down the samples. This is followed, in Section 4.3, by a discussion of the electronic measurement setup, with particular emphasis on the bias setup in Sections 4.3.1 and 4.3.2. We explain how filtering was used to obtain a high signal-to-noise ratio in the current and voltage measurements in Section 4.4, and show that we were able to achieve low electron temperatures in Section 4.5.

Finally, we briefly discuss cleanroom fabrication and highlight relevant references in Section 4.6.

4

4.2. CRYOGENICS

Cryogenics is an essential ingredient of the experiments reported in this thesis. Most experiments involving quantum effects are cooled down to a temperature close to absolute zero. Although each experiment has its own requirements, in general the temperature must be lowered to a point where the thermal energy¹ is not the dominant energy scale, as otherwise it can wash out or hide the physics of interest.

The temperature also needs to be low enough to reduce thermal population, which can smear features via the Fermi-Dirac distribution, as we saw in eq. 3.13. Another important example is quasiparticle number, which depends exponentially on the temperature, see eq. 6.6.

4.2.1. 4K DIPSTICKS

The 4K dipstick is an insertable probe for helium storage dewars. Its advantages are the simplicity of the setup, low cost and throughput time of sample exchange. Dewars have a double wall between the outside and the helium reservoir with a vacuum in-between, called the outer vacuum chamber (OVC), providing almost ideal isolation. A drawing of the inside of a dewar and a picture of the outside is shown in Figure 4.1a-b.

The helium dewar can be opened from the top to load the dipstick, depicted in Figure 4.1c. The dipstick has a flange (indicated by the yellow arrow) to mount it on top of the helium dewar. The flange can slide along the dipstick to slowly lower the probe until it reaches the liquid helium. The sample is mounted at the lowest point of the probe on a copper block known as a cold finger, see Figure 4.1d. The sample is mounted in the inner vacuum chamber (IVC) of the probe, which is created by enclosing the sample space with the brass vacuum can, also shown in Figure 4.1d. The red arrow in Figure 4.1d points to the 1-K pot of the dipstick. This can be slowly filled with liquid helium from the dewar. At room temperature, a pump can be connected to the 1-K pot to pump the liquid helium and the vapour. The vapour particles carry more heat and are removed from the 1-K pot by the pump, making the pot cooler. Due to the pump capacity and the sizes of the 1-K pot and 1-K pot inlet, high cooling powers and temperatures down to 1.5K can be obtained.

¹ $k_B T$, where k_B is Boltzmann's constant and T is the temperature in Kelvin.

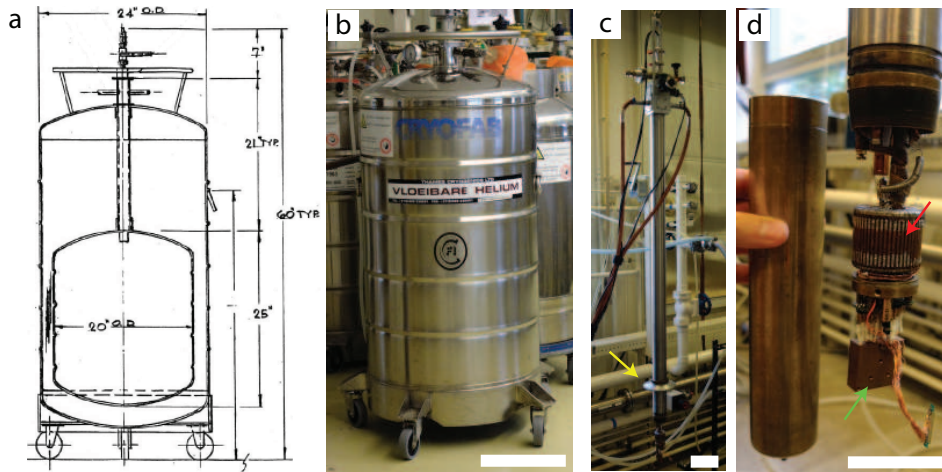


Figure 4.1: **a** Drawing of the helium dewar (Cryofab CMSH 100) used for the 4K insertable probe. Sizes are denoted in inches. Drawing obtained from www.cryofab.com. **b** Picture of the same helium dewar, used for storage of liquid helium. The white scale bar denotes 30cm. **c** 4 Kelvin insertable probe from Desert Cryogenics. On the top there are connections to access the measurement lines, the 1-K pot and the IVC. The sample can be mounted at the bottom of the probe. The white scale bar denotes 10cm. **d** The lowest copper block of the probe (indicated by the green arrow) is used for mounting the sample. On the left, the vacuum can used to enclose the sample space to form the IVC is shown. The white scale bar denotes 5cm.

4.2.2. DILUTION REFRIGERATORS

A dilution refrigerator (dilfridge) is used in all the experiments, except the one reported in Chapter 5. The great advantage of a dilfridge is that it gives continuous access to low temperatures (~ 10 mK). The operating costs are higher and running the dilfridge is more involved, but the ability to reach much lower temperatures enables more interesting experimental physics.

Currently, there are two different types of dilfridge on the market, wet and dry. Wet ones are very similar to 4K dipsticks, except that the probe is much wider and contains more elements. The probe of a wet dilfridge also hangs in liquid helium and has a 1-K pot, which is used for condensing ^3He in the condenser. A calibrated impedance regulates the flow to the mixing chamber, where at sufficiently low temperatures (< 0.8 K) two phases are present, ^3He - and ^4He -rich. Since ^3He is lighter, it lies on top of the ^4He -rich phase. The ^3He -rich phase is practically pure, but the ^4He -rich phase includes 6.5% ^3He . Due to the design, the ^4He -rich phase is sucked into the still (which is at ~ 700 mK), and there some of the ^3He evaporates. This leaves the ^4He -rich phase with a lower dilution of ^3He . The ^3He in the ^3He -rich phase then expands into the ^4He -rich phase, trying to restore the 6.5% ^3He equilibrium. This expansion of the ^3He extracts heat from the environment, including the sample to be measured. The ^3He vapour is sucked out by a pump from the still (typical still pressure $5 \cdot 10^{-2}$ mbar), compressed to 100mbar and returned to the condenser. The ^3He thus circulates in a closed loop.

Dry dilfridges do not need a helium bath, because a closed loop of compressed helium cools the condenser to 3.5 K. The ^3He cannot directly condense in the condenser,

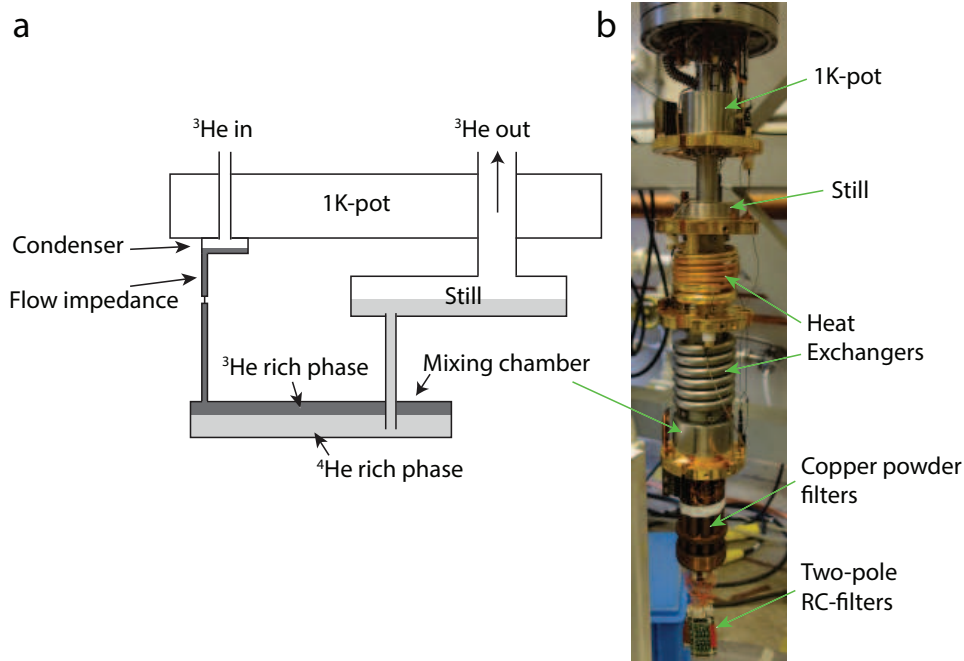


Figure 4.2: **a** Schematic view showing the means by which a (wet) dilfridge achieves cooling. **b** Picture of a (wet) dilfridge, indicating the most important elements. The fridge is from Leiden Cryogenics.

but a compressor is used to make the mixture condense at this higher temperature. The biggest advantage of dry dilfridges, compared to wet ones, is that operation is less involved because there is no need to fill it with liquid helium (bi-)daily.

4.3. ELECTRONIC MEASUREMENT SETUP

All the experiments in this thesis are relatively easy current-voltage (IV) measurements. We apply a bias current or voltage and measure the response of the sample/device. However, performing good IV measurements is rather difficult in the presence of a strong non-linear element such as a superconductor-insulator-superconductor (SIS) or superconductor-normal metal-superconductor (SNS) junction. In this section, we will discuss the important differences between ideal voltage and current biases and the actual biases involved in our measurements. This is followed by a discussion of the low-noise electronics and filtering used in our measurement setup. We show that this setup can achieve low noise and low electron temperature.

4.3.1. VOLTAGE AND CURRENT BIAS

A perfect voltage source can deliver a constant voltage, regardless of the resistance of the sample/device to which it is connected. It has an internal resistance $r=0\Omega$, so there is no voltage drop within the source itself. The electrical symbol for a voltage source is shown in Figure 4.3a.

A perfect current source can deliver a constant current, regardless of the resistance of the sample/device to which it is connected. The electrical symbol for a current source is shown in Figure 4.3b. A battery is a simple example of a voltage source that can deliver (say) 1.5V, but there is no such example of a current source. A current source, in the simplest case, consists of a voltage source and a large internal resistance in series, as illustrated by Figure 4.3c (r is large compared to the resistance of the sample). If we take, for example, a bias current of $1\mu\text{A}$ and an internal resistance of $100\text{G}\Omega$, the voltage source would need to deliver 100kV , which is unrealistic for a battery. For this reason, current sources often consist of operational amplifiers with feedback, as this is more realistic than a battery-based setup[96]. A non-ideal current source, shown in figure 4.3d, can be modelled with a parallel internal resistance.

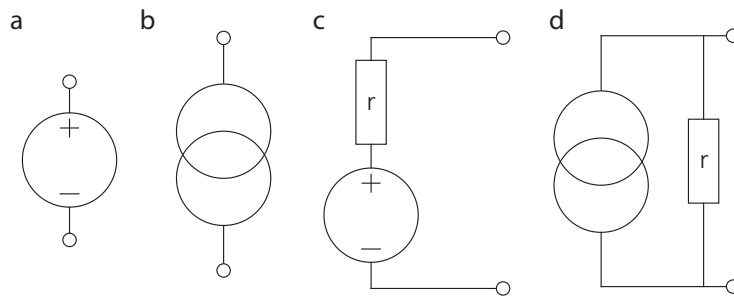


Figure 4.3: Electrical circuit diagram of **a** an ideal voltage source and **b** an ideal current source. **c** Realistic representation of a voltage source with internal resistance r , which is ideally low compared to the sample resistance R . **d** Realistic representation of a current source with internal resistance r , which is ideally high compared to the sample resistance R .

We assume for the purposes of further discussion that the internal resistances are ideal for our current and voltage sources. This changes when the voltage source is actually connected to the sample. Due to line resistances and RC filters, not all the applied voltage drops over the device. Typically this series resistance is $2\text{-}15\text{k}\Omega$. If this resistance is negligible compared to the device resistance, an almost ideal voltage bias can be achieved.

The devices we consider are often comparable to a series resistance, and we will examine this case by drawing the ideal curve of an SIS junction. First, Figure 4.4b shows the case of perfect voltage bias ($r = 0\Omega$), where we can completely map out the solid line of the ideal IV curve. This is because all points on the IV curve can be reached by going perpendicular to the voltage bias axis. In the current-bias case (Figure 4.4c), there are two clear switches to and from the supercurrent. The current source cannot apply a finite voltage and zero current, so we ‘miss’ the subgap regime of the SIS junction completely. In most of our experiments we use a voltage source with series resistance comparable to that of the sample. In this case we do not have access to the IV curve of the device perpendicular to the I or V axis. Instead, we have access to the datapoints on a slope across the ideal IV curve. This slope is determined by the resistance ratio between r and R , as shown by the arrow in Figure 4.4d. We can compare this with the measured IV curve (Figure 4.4e) of a device used in Chapter 8. Here, we see that it is impossible to

apply a small current in the voltage region $-170 \dots 370 \mu\text{V}$. At the switching point ($+40\text{nA}$) the voltage applied to the circuit drops completely over the series resistance r . At that point, the sample is superconducting and thus has resistance $R = 0\Omega$, which is the worst possible scenario for the voltage bias.

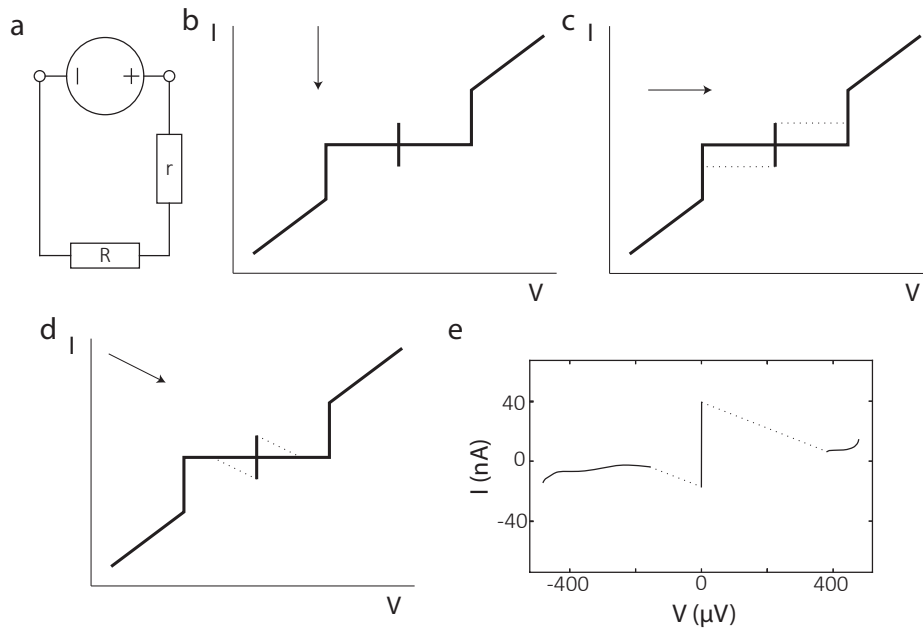


Figure 4.4: **a** Setup for voltage-biasing a sample with resistance R , including a line or internal resistance r . **b** IV trace of an SIS junction from a voltage bias perspective. Datapoints from the IV trace can only be taken perpendicular to the x -axis, the voltage axis. **c** IV trace of an SIS junction from a current bias perspective. Datapoints from the IV trace can only be taken perpendicular to the y -axis. Due to the supercurrent (finite current, zero voltage) the subgap is not accessible via this technique. **d** When a sample is voltage-biased but the line resistance r is of the same order as the sample resistance R , only datapoints along an angle in the IV plane can be reached. In this case the supercurrent is partially 'shadowing' the subgap of the SIS junction. **e** The subgap of a voltage-biased SIS junction with finite line resistance, showing partial shadowing of the subgap.

We have seen that supercurrent switches can hide features in the IV trace. Another effect of imperfect voltage bias is that the voltage points are not equidistant. Supercurrent switches are an extreme example, but this is also noticeable when measuring peaks in the current of the SIS detector in Chapter 8. In Figure 4.5, we show, for two settings of r , the measured voltage and current through the sample as a function of applied bias voltage. All the data was taken using the same device settings, only the line resistance being changed (at room temperature) from $r=13\text{k}\Omega$ (the left side of Figure 4.5) to $r=2.5\text{k}\Omega$ (right side). When we take a look at Figure 4.5b, we see that there is a supercurrent and a few bumps/peaks in the subgap current. With a high r , not all the current bumps are fully visible. With a lower r , we see three bumps in current but we miss any that are still hidden by the supercurrent switch.

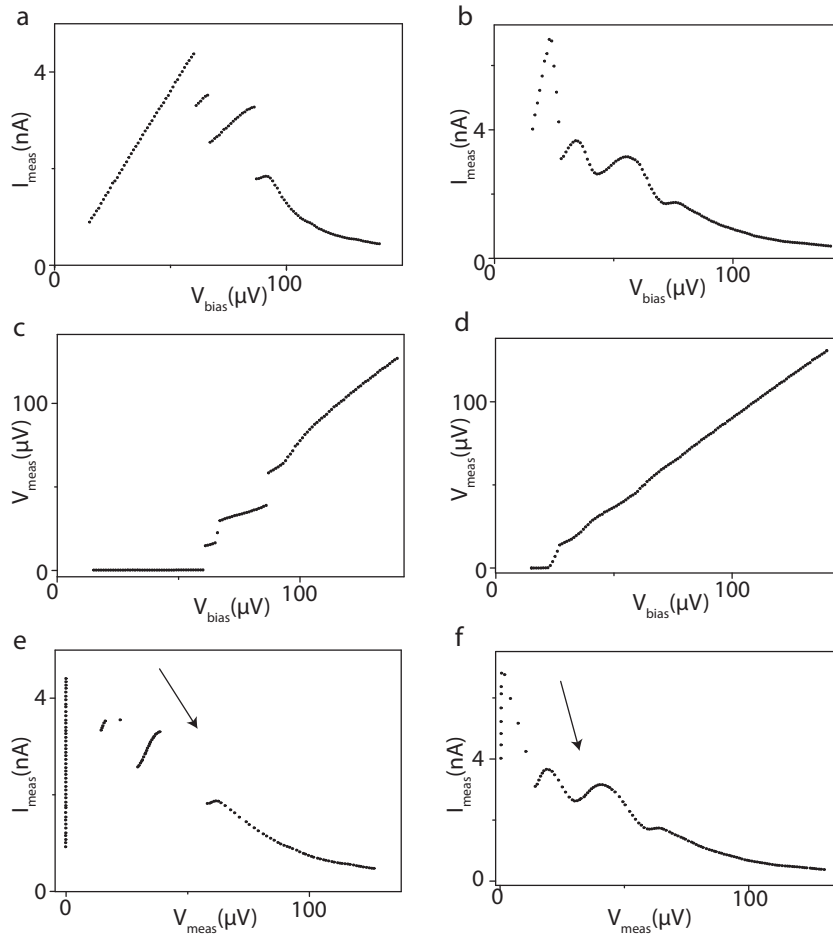


Figure 4.5: Comparison of highly non-linear IV traces with different line resistances r . For all the plots on the left side of this figure, $r=13\text{k}\Omega$, and for the right side, $r=2.5\text{k}\Omega$. **a-b** Bias voltage vs measured current. **c-d** Bias voltage vs measured voltage. **e-f** Measured voltage vs measured current. The datapoints are clearly not equidistant.

Figure 4.5c-d shows measured voltage as a function of the applied bias. Because the IV trace is highly non-linear, the voltage jumps at several points. These extra jumps are often interpreted differently or not understood at all. Another side-effect of non-ideal voltage biasing is that the datapoints are not equidistant, as we can clearly see in Figure 4.5e-f from the bump at $\sim 50\mu\text{V}^2$. For high line resistance r the bumps are only half-displayed, and for low r there are more datapoints on one side compared to the other.

²Within the group, Ruben van Gulik developed direct data plotting software which allowed measured voltage and measured current to be plotted against each other. The software is available at github.com/Rubenknex/qtplot

4.3.2. TWO- AND FOUR-POINT MEASUREMENTS

In Chapters 7 and 8, an SIS junction is used for high frequency detection. The frequency emitted by the nanowire junction can be directly measured from the voltage at which the PAT current arises. In Chapter 9, an SIS junction is used as a spectrometer, where the measured voltage indicates the frequency. In all these experiments, it is important to know the exact voltage over the sample. In a two-point voltage bias geometry, depicted in Figure 4.6a, the voltage across R can be calculated when the resistance r and the current is known. A large part of r is determined by the on-chip resistors, fabricated from thin Pt strips. This resistance is typically $0.8\text{--}1.2\text{k}\Omega/\mu\text{m}$. Due to large inaccuracies and our desire to measure the voltage and thus the frequency directly, we instead use a four-point voltage bias geometry. The sample has four leads on-chip, and four measurement lines also leave the fridge. A voltage is applied across two of them, and we measure the current that flows. In these lines, resistances develop due to the current. A voltage measurement is performed on the other two lines (depicted on the right side of the sample in Figure 4.6c). The voltmeter has a very high internal resistance, at least much larger than r , so no current flows through it, meaning no voltage develops across the line resistors used in this part of the circuit and only the voltage over R is measured.

The SIS junction can also carry a supercurrent, a finite current that develops no voltage. Because we have access to the actual voltage over the sample we can also measure this zero-voltage state, see Figure 4.5c-f.

In Chapter 6, we measure the maximum allowed current through the sample. We do this using a four-point current bias geometry. Here again, four leads are created as close as possible to the sample, leaving the dilfridge via four measurement lines. At room temperature, two of the four lines are used for current bias and two for voltage measurement. Again, no current flows through the line resistances of the voltmeter and only the voltage over the sample is measured.

4.4. LOW-NOISE ELECTRONICS AND FILTERING

In the institute where this research was performed, a group led by Raymond Schouten[96] develops low-noise equipment. The low-noise equipment can be placed in a rack, controlled by a computer via an optical fibre. The measurement equipment is in the same rack and is connected, after amplification, to commercial electronics which are read out using a GPIB connection. The low-noise equipment is visible in Figure 4.7a and the commercial electronics are shown in Figure 4.7b.

The measurement lines typically have three stages of filtering (unlike the 4K dipstick). At the back of the central rack, in Figure 4.7a, there are π filters³. The π filters cover the 'middle' part of the spectrum, see Figure 4.7c. This part of the spectrum needs to be 'covered' because the RC filters which are used as low-pass filters are limited to a certain working frequency. Ideally, a low-pass RC filter should attenuate completely at high frequencies, but due to stray inductances of (electronic) elements, LC resonances with high transfer can also arise. These resonances typically arise at $100\text{MHz--}1\text{GHz}$ [96], the range where the π filters are effective. The RC filters are two-

³5dB att. at 10MHz, 45dB att. at 100MHz and 70dB att. at 1–10GHz

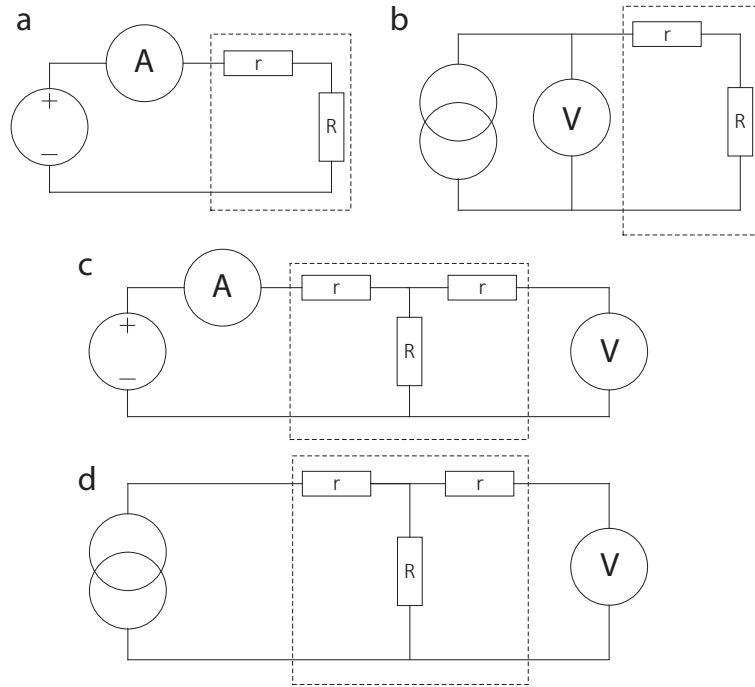


Figure 4.6: Possible ways of connecting a two-terminal sample. The region indicated by the dashed box is within the cryogenics setup. **a** Two-point voltage bias geometry. The line resistance, r , is in series with the sample resistance, R . **b** Two-point current bias geometry. The voltage is measured at room temperature, and is not the same as the voltage over the sample since there is also a voltage drop over r . **c** Four-point voltage bias geometry. The two-terminal sample is split at the device to have four leads, two for the voltage bias and current measurements and two for measuring the voltage across the device. **d** Four-point current bias geometry. The two-terminal sample is split at the device to have four leads.

pole ($R_1 = 470\Omega$, $C_1 = 10\text{nF}$, $R_2 = 2\text{k}\Omega$, $C_2 = 470\text{pF}$) and were used in all the experiments except for the 4K experiments in Chapter 5. The RC filters are visible at the bottom of Figure 4.2b. Similarly to the RC filters, copper powder filters are mounted at the mixing chamber stage. The copper powder filters start to attenuate above 100MHz–1GHz[96], where the π filters start to leak due to stray capacitances and inductances. The copper powder filters are important in achieving low electron temperatures[97] because high-frequency electrons have a large thermal energy ($1\text{GHz} \approx 4\mu\text{eV}$).

Figure 4.7d shows the current noise (δI) within the subgap of an SIS junction (used in Chapter 8). Figure 4.7e shows the noise (δV) in the voltages measured over a nanowire SNS junction (used in chapter 8). In both cases, a digital multimeter integration time of 20ms is used to avoid 50Hz interference.

⁴Except for device 2 in Chapter 9, where it is 100Ω

4

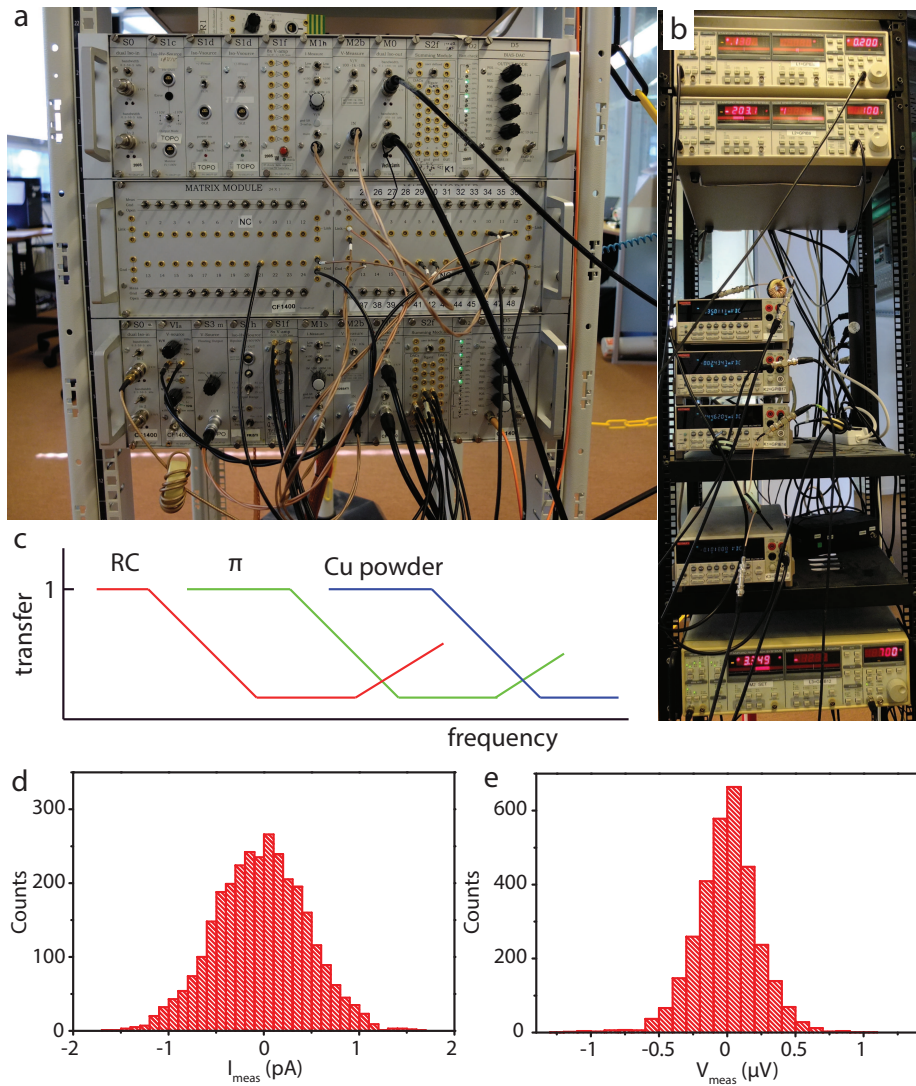


Figure 4.7: **a** Three racks, with the upper and lower ones containing low-noise bias and low-noise measurement modules. The middle rack is connected at the back to the measurement wires. From the front the low-noise modules can be connected to the measurement wires. At the back of the middle rack, π filters are present. **b** Commercial electronics to read out the modules of the low-noise rack. At the top of the picture two lock-ins (SR830) can be seen, while in the middle there are four digital multimeters (Keithely 2000) and at the bottom there is another lock-in. **c** Schematic view of the transfer of the filter stages used in the experiment. **d** Measurements of the subgap current in the SIS detector used in Chapter 8 (corrected for offset, only showing δI). **e** Measurements of the voltage over the nanowire junction used in Chapter 8 (corrected for offset, only showing δV).

4.5. LOW ELECTRON TEMPERATURE

At the start of this PhD, the cryogenic setup (Leiden Cryogenics CF-1200) was new and equipped with all the filters described in the previous section. For characterization, electron temperatures were measured with a many-electron nanowire quantum dot. In the weak coupling regime, tunneling to the lead Γ is smaller than $k_B T$, and the Coulomb peak's width is determined by temperature[98]. We used this to see what the electron temperature was in the device. The results are plotted against the temperature of the RuO_x thermometer in Figure 4.8a. We see that the electron temperature follows that of the thermometer, but starts to deviate around $\sim 50\text{mK}$. We concluded from these measurements that the electron temperature was roughly $35 - 50\text{mK}$. We also changed the location of the thermometer to be closer to the sample, which perhaps explains the discrepancy around 100mK . With this adjustment, we made the measurements described in Chapter 6, resulting in particular in the data plotted in Figure 6.2e. With the extra improvements made in Chapter 6, we performed new electron temperature measurements with an NIS thermometer[99]. These results are shown Figure 4.8b and indicate that the improvements worked, since now the electron temperature follows that of the thermometer down to 25mK^5 .

4

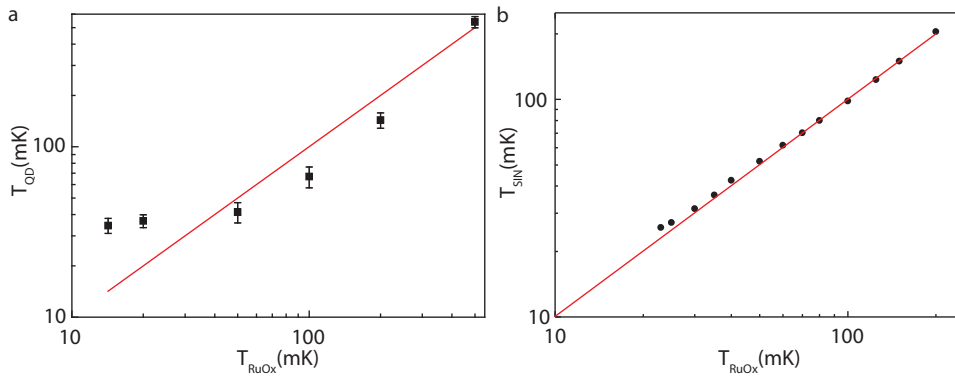


Figure 4.8: **a** Measurements of the electron temperature in a nanowire quantum dot in the many-electron regime. **b** Measurements of the electron temperature in an NIS junction, fabricated by the group led by Jukka Pekola and measured by Attila Geresdi. After the improvements discussed in the text the electron thermalization is much improved.

Electron temperatures in a nanowire Josephson junction were also measured. The switching current (eq. 3.40) and the phase diffusion (eq. 3.41) are both temperature-dependent. A more careful analysis is currently being performed[100].

⁵We were not able to go below 23mK on the RuO_x thermometer with this particular cooldown. Normally, $10-14\text{mK}$ can be achieved.

4.6. CLEANROOM FABRICATION

All the cleanroom fabrication was performed in the cleanroom of the Kalvi Institute of Nanoscience, except for the nanowire growth. The rest of the fabrication is standard: electron beam patterning, (angle) evaporation, (reactive) sputter, (reactive) rf-etching and milling. A detailed description of sample fabrication for MZM research is given in refs. [33, 76].

For the nanowires, we collaborated with the Bakkers group at the Technical University of Eindhoven (InSb) and Jasper Nygård and Peter Krogstrup at the University of Copenhagen (InAs with an epitaxial aluminium shell). For the experiments in Chapters 5 and 7, InSb nanowires were used. InSb is interesting due to its high g -factor and earlier reports of MZM[9] using these nanowires. The growth of these wires is extensively described in the thesis of Diana Car[101].

The nanowires from Copenhagen are unique in the sense that an aluminium shell is grown *in situ*[20]. The *in situ* growth of the aluminium shell leaves the interface clean and good induced superconductivity has been observed[21]. These nanowires were available at a later stage and were used in Chapters 8 and 9.

For proper nanowire gating, the nanowire has to be deposited straight onto a local fine gate structure. The nanowire is then also aligned with the magnet axis of the cryogenic setup. For this purpose we installed a nanowire deposition setup similar to the one used in ref. [102], see Figure 4.9.

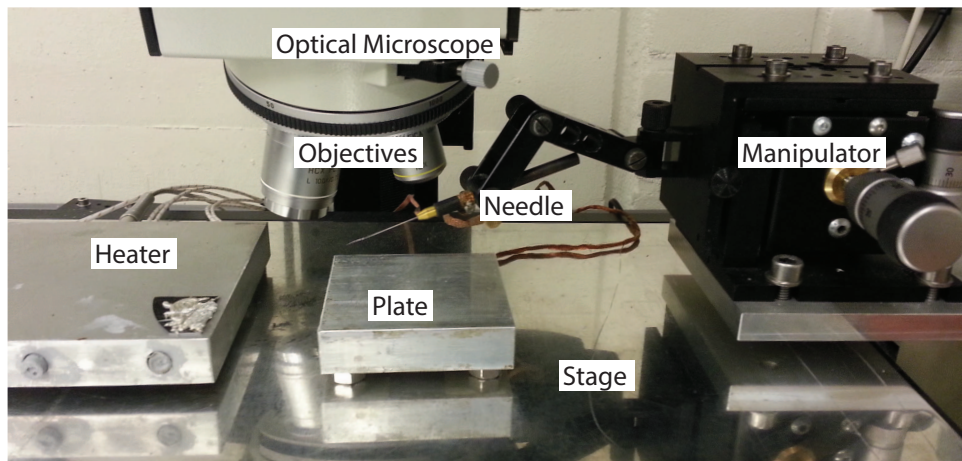


Figure 4.9: Nanowire deposition tool with an optical microscope. A sharp tip (radius $\sim 50 - 200\text{nm}$) is made using liquid indium and nanowires are deposited via a sub-micrometre XYZ manipulator. The setup was designed according to ref. [102] and operated as described in ref. [76].

The operation of a (reactive) sputter machine is relatively easy, but the precise process and using it to deliver good (reproducible) superconducting films is more complex. For this reason two bachelor's students under my supervision performed multiple characterizations[103, 104]. These film characterizations are extensively used within the group.

5

TOWARDS HIGH MOBILITY INSB NANOWIRE DEVICES

**Ö. Gül, D. J. van Woerkom, I. van Weperen,
D. Car, S. R. Plissard, E. P. A. M. Bakkers,
L. P. Kouwenhoven**

We study the low-temperature electron mobility of InSb nanowires. We extract the mobility at 4.2 Kelvin by means of field effect transport measurements using a model consisting of a nanowire-transistor with contact resistances. This model enables an accurate extraction of device parameters, thereby allowing for a systematic study of the nanowire mobility. We identify factors affecting the mobility, and after optimization obtain a field effect mobility of $\sim 2.5 \times 10^4 \text{ cm}^2/\text{Vs}$. We further demonstrate the reproducibility of these mobility values which are among the highest reported for nanowires. Our investigations indicate that the mobility is currently limited by adsorption of molecules to the nanowire surface and/or the substrate.

This chapter has been published in Nanotechnology **26** 215202 (2015).

In the first section 5.2 the nanowire setup for FET measurement is introduced. Followed by the new model for extracting the mobility which is introduced in section 5.3 and is also compared with the old extraction model in section 5.4. For this model we assume gate independent interface resistance which we show is valid for our measurements in section 5.5. The core of this chapter is in section 5.6 and 5.7 where we investigate the cleaning of the nanowire surface before nanowire deposition and after full device fabrication respectively. A relation between nanowire channel length and the mobility is found, and being reported in section 5.8, which could indicate that the FET method is not a proper extraction method of the nanowire mobility because the nanowires are not diffusive over μm scale. Finally, in section 5.9 reproducibility of the used fabrication method is shown and a conclusion is discussed in section 5.10. Supplementary Information can be found in section 5.11.

5.1. INTRODUCTION

Advances in nanowire growth have led to development of novel quantum devices, such as Cooper-pair splitters [105], hybrid semiconductor-superconductor devices [106] and spin-orbit qubits [107]. Nanowire devices thus allow exploration of mesoscopic transport in a highly confined system and show potential as a quantum computation platform. Outstanding nanowire transport properties, such as a high level of tunability of device conductance and low disorder, have been essential to the realization of these experiments.

Recently, hybrid superconductor-semiconducting nanowire devices have been identified [7, 8] as a suitable platform to study Majorana end modes [3], zero-energy bound states that exhibit topological properties. Among various systems, InSb nanowires emerged as a very promising candidate due to their large spin-orbit interaction and large g factor. Reports on signatures of Majorana bound states in InSb nanowire-based systems followed quickly after their theoretical prediction [9, 10, 108]. To further develop this topological system, a reduction of the disorder in the nanowire is essential [109, 110]. Disorder reduces or even closes the topological gap that gives Majoranas their robustness, thereby impairing their use as topological qubits. Disorder is quantified by measurements of carrier mobility, which relates directly to the time between scattering events. Evaluation of carrier mobility in nanowires therefore indicates their potential for transport experiments and is thus crucial to further development of nanowire-based quantum devices.

According to the Matthiessen rule, various scattering mechanisms altogether determine the net mobility through [111]

$$\frac{1}{\mu} = \frac{1}{\mu_1} + \frac{1}{\mu_2} + \dots \quad (5.1)$$

Here μ represents the net mobility which results from distinct scattering mechanisms each giving rise to a separate mobility μ_n . In other words, the most dominant scattering contribution limits and hence determines the net mobility. Therefore the mobility can be improved by identifying the limiting mechanism and subsequently reducing or eliminating it.

Apart from the recently introduced Hall effect measurements on nanowires [112, 113], field effect transport measurements are the most common and experimentally most feasible method to extract charge carrier mobility in these systems. Here, one measures the current flowing through the nanowire channel contacted by two electrodes as a function of the gate voltage with fixed voltage bias. The conductance of the channel is described by the linear region of the accumulation regime of a field effect transistor (FET) [114]. In this case the conductance of the channel is

$$G(V_g) = \frac{\mu C}{L^2} (V_g - V_{th}), \quad (5.2)$$

with gate voltage, V_g , mobility, μ , capacitance, C , channel length, L , and threshold voltage, V_{th} . If the capacitance and the channel length are known, the field effect mobility can be determined from the transconductance, $g_m = dG/dV_g$. In most cases, to extract the mobility, the maximum (peak) transconductance is used. One should note that both the mobility and the field effect transport is described using the Drude model where charge carrier transport is classical and diffusive.

Previous studies showed that low-temperature field effect mobility for nominally undoped III-V nanowires is mainly limited by crystal defects such as stacking faults [115–119], and surface effects such as surface roughness [120, 121]. Point defects are also thought to have an effect on the mobility [122]. However, as they are difficult to detect so far no direct connection between impurities and mobility has been reported. Highest reported low-temperature field effect mobilities are $1.6 - 2.5 \times 10^4 \text{ cm}^2/\text{Vs}$. Such mobilities are observed in InAs nanowires [115, 123], InAs/InP core-shell nanowires [124, 125] and GaN/AlN/AlGaIn core-shell nanowires after correction for contact resistances [126]. However, in most of these studies either data on a single device is reported, or the average mobility of several devices is significantly lower than the reported maximum [125]. Systematic studies of such high-mobility nanowire FETs are thus largely lacking.

Concerning field effect mobility, the InSb nanowires we investigate differ in several respects from their oft-studied InAs counterparts: the InSb nanowires we use have a larger diameter of approximately 100 nm, reducing their surface-to-volume ratio compared to the thinner InAs nanowires, and are likely to have no surface accumulation layer. Instead, upward band bending leading to surface carrier depletion has been reported for both clean [127] and oxygen-covered InSb surfaces with (110) orientation, the orientation of our InSb nanowire facets. As the InSb facets are atomically flat no surface roughness is expected. Finally, the nanowires are purely zinc-blende and are free of stacking faults and dislocations. The growth of InSb nanowires we study is described in [128] and [129]. Given the differences between InSb nanowires and other nanowire materials it is an open question what determines the low-temperature mobility in InSb nanowires. We note that while in [128] field effect mobilities of these InSb wires are reported, no systematic investigation of the nanowire mobility was performed. The mobility extraction method presented here allows such a thorough investigation, thereby revealing new insights on nanowire mobility.

To identify the factors affecting the mobility of InSb nanowires, we characterized the low-temperature mobility of nanowire FETs fabricated using different experimental parameters. We tailored the extraction of field effect mobility for the nanowires we study

to accurately determine the essential transistor parameters of nanowire FETs. By systematic studies we developed a recipe that results in reproducible average mobilities of $\sim 2.5 \times 10^4 \text{ cm}^2/\text{Vs}$. While this value represents an average over many devices, the extracted mobility from a single measurement may exceed $3.5 \times 10^4 \text{ cm}^2/\text{Vs}$. After optimizing the fabrication, we also find that adhesion of molecules to the nanowire and/or the substrate currently limits the extracted mobility. Although such adsorption effects are known to modify the nanowire conductance [116, 130] and also the room-temperature mobility [131–133] (note that ref. [132] reports an increase of mobility upon adsorption, whereas ref. [133] a reduction), our identification of surface adsorption being the limiting factor to low-temperature field effect mobility is new. The amount of adsorbates is reduced by evacuating the sample space for longer time prior to cool down and suggestions for further reduction of the adsorbates as well as to minimize their contribution to the field effect transport are made.

5

5.2. EXPERIMENTAL SETUP

InSb nanowire FETs are fabricated on a heavily doped (p++) Si substrate (used as a global back-gate) terminated with a 285-nm-thick dry thermal SiO_2 (Fig. 5.1b). The substrate is patterned with alignment markers prior to nanowire deposition. Nanowires are positioned on the substrate using a micro-manipulator [102]. Two terminal contacts are realized by electron beam lithography, metal evaporation (Ti/Au 5/145 nm) and lift-off. Argon plasma etching is employed prior to contact deposition. The samples are measured in a two-point geometry (see section 4.3.2) in a 4K-dipstick which was discussed in section 4.2.1. Further details about the fabrication process can be found in section 5.11.1 and further details about measurements can be found in sections 5.11.4 and 5.11.3.

5.3. EXTRACTING MOBILITY

Due to the absence of a surface accumulation layer in InSb nanowires, an interface resistance of a few kilo ohms cannot be eliminated upon contacting the nanowire [134]. Such interface resistances are known to reduce the transconductance, resulting in an underestimation of the intrinsic mobility [135, 136]. Moreover, at a temperature of 4 K universal conductance fluctuations complicate the extraction of mobility from transconductance. We therefore tailor the extraction of field effect mobility to our InSb nanowire FETs [137]. We model the interface resistances by a resistor R_s with a fixed value (no gate voltage dependence, see section 5.5), connected in series to the nanowire channel, schematically depicted in Fig. 5.1a. A substantial part of the device resistance at high gate voltage stems from the interface resistances, strongly affecting the gate voltage dependent conductance. This complicates accounting for a possible change of mobility with gate voltage. We therefore assume a mobility independent of gate voltage. The device conductance is then given by

$$G(V_g) = \left(R_s + \frac{L^2}{\mu C (V_g - V_{th})} \right)^{-1} \quad (5.3)$$

This equation allows for extraction of field effect mobility using a fit to the measured $G(V_g)$. Here, the mobility μ , the interface resistances R_s , and the threshold voltage V_{th}

are the free fit parameters. We restrict the fitting range to $G^{-1}(V_g) \leq 100 \text{ k}\Omega$. We independently calculate the capacitance from a finite element model of the device (see Fig. 5.1c inset), where we take into account that quantum confinement in our nanowires reduces the classical capacitance by $\sim 20\%$ [138, 139]. Neglecting quantum effects in our capacitance calculation would lower the extracted mobility values by $\sim 20\%$. We compared the mobility values extracted by a fit using eq. 5.3 with the mobility values obtained from peak transconductance in the next paragraph. For a representative fabrication run, mean forward mobility of 11 devices is found to be $2.9 \times 10^4 \text{ cm}^2/\text{Vs}$ using our fit method, whereas peak-transconductance method yields $2.7 (1.9) \times 10^4 \text{ cm}^2/\text{Vs}$ with (without) taking into account the interface resistances. Our fit method, however, differs from peak transconductance method where the mobility is extracted from the maximum value of the transconductance using a small gate voltage range. Because we consider the transconductance in a wide gate voltage range by fitting a large section of $G(V_g)$, the extracted mobility is insensitive to small conductance fluctuations. This is contrary to the peak transconductance where conductance fluctuations greatly affect the extracted mobility. We show in section 5.5 that our simple model with gate voltage-independent interface resistances is a valid approximation for our measurements. However, despite our thorough analysis a general drawback of field effect mobility remains: the uncertainty in the calculated capacitance value affects the extracted mobility directly. Nanowires suffer from this drawback as their small dimensions do not allow a straightforward experimental extraction of capacitance.

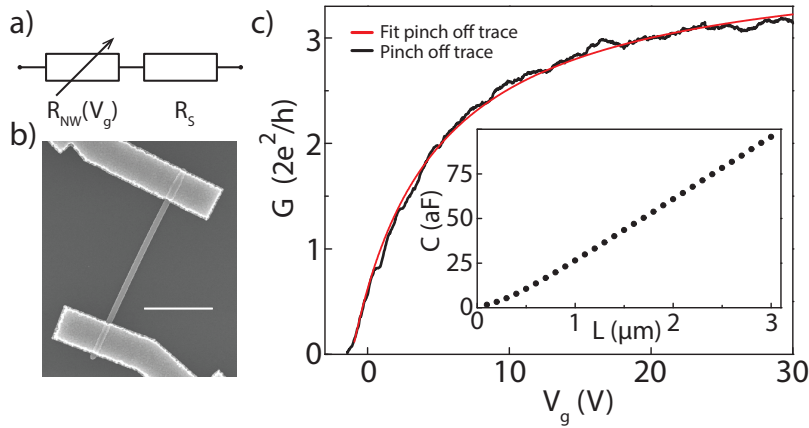


Figure 5.1: **a)** Electrical diagram of the InSb nanowire FET. The FET is modelled as a nanowire channel with a resistance controlled by a nearby backgate with voltage V_g , $R_{NW}(V_g) = G_{NW}^{-1}(V_g)$, in series with fixed interface resistances, R_s . **b)** Electron microscope image of an InSb nanowire FET. Nanowire diameter is $\sim 100 \text{ nm}$. The nanowire is deposited onto a Si substrate covered with 285 nm dry thermal SiO_2 . Ti/Au ($5/145 \text{ nm}$) contacts have spacing of $1, 1.5, 2$ or $2.5 \mu\text{m}$. Scale bar is $1 \mu\text{m}$. **c)** Conductance G , as a function of back gate voltage V_g (black curve). Source-drain bias is set to 10 mV throughout the study. Field effect mobility is extracted from a fit to the conductance (red curve) using eq. 5.3. All measurements are performed at a temperature of 4.2 K . Inset: Gate-nanowire capacitance C , as a function of source-drain contact spacing L . Capacitance is extracted from a finite element model of the device geometry. Contacts are included in the simulated device geometry and lead to a non-linear $C(L)$ at small contact spacing.

To determine what limits the mobility in our devices, we systematically studied the effect of various experimental parameters by measuring ~ 10 devices simultaneously fabricated on the same substrate. We then change one parameter at a time for each fabrication run to deduce its effect on the field effect mobility.

5.4. COMPARISON OF FIELD EFFECT MOBILITY EXTRACTION METHODS

We extract mobility values by fitting the conductance curves $G(V_g)$ in a large gate voltage range. However, in the literature mobility is commonly extracted from a small gate voltage range where the transconductance has its maximum value (peak transconductance). This gate voltage range is typically close to the threshold voltage where the mobility is expected to be the highest. Here, we compare the field effect mobility obtained using our method – fitting the conductance curves $G(V_g)$ – to the field effect mobility obtained from peak transconductance, the standard method for extracting mobility in nanowires. We denote the mobility obtained using the latter as peak-mobility. We describe the extraction of peak-mobility in the following: By numerically differentiating the measured $G(V_g)$ shown in Fig. 5.2a, one obtains the transconductance $g_m = dG/dV_g$. This transconductance is shown in Fig. 5.2b (black curve). After taking the numerical derivative, an averaging is performed to remove the fluctuations in transconductance (red curve in Fig. 5.2b). The peak-mobility is then obtained from the maximum value of transconductance using $\mu = g_m L^2 / C$ (see eq. 25.2). Peak-mobility depends strongly on the chosen averaging range. This dependence is shown in Fig. 5.2c. Here, mean forward peak-mobility of 11 devices from a single fabrication run is plotted against the averaging range. We choose the averaging range to be 1.8 V, the value at which the rapid decrease of peak-mobility with respect to averaging range diminishes.

Next interface resistances are taken into account since they affect the extracted peak-mobility. This is done by subtracting the contribution of a gate-independent series resistance R from the measured conductance curve $G(V_g)$. Fig. 5.2f shows an example of such a conductance curve corrected for interface resistances. From such a curve we determine the transconductance, and from the maximum value of transconductance peak-mobility is extracted. The peak-mobility depends on the subtracted R , shown in Fig. 5.2d. Here, as mentioned above, mean forward peak-mobility of 11 devices from a single fabrication run is plotted. (The peak-mobility for $R = 0$ is the one indicated with a green arrow in Fig. 5.2c.) For zero subtracted resistance ($R = 0$), the transconductance has a global maximum near pinch-off (Fig. 5.2b, red curve). Upon increasing the value of R subtracted from $G(V_g)$, the transconductance values increase for all gate voltages, with the amount of increase being larger for higher gate voltages. When R exceeds the value of interface resistances R_s , the transconductance no longer has a global maximum near pinch-off. When R is increased even further, transconductance starts to increase with gate voltage, a case we regard to be unrealistic. R_s for individual devices varies between 1.5 k Ω and 4 k Ω , with an average R_s of ~ 3 k Ω . After the subtraction of R_s , the mean peak-mobility of 11 devices obtained using forward sweep direction is $(27.1 \pm 4.2) \times 10^3$ cm²/Vs (see Fig. 5.2d) compared to $(28.7 \pm 4.8) \times 10^3$ cm²/Vs obtained from fits to the conductance curves. Both values are within error margin the same. Comparing mo-

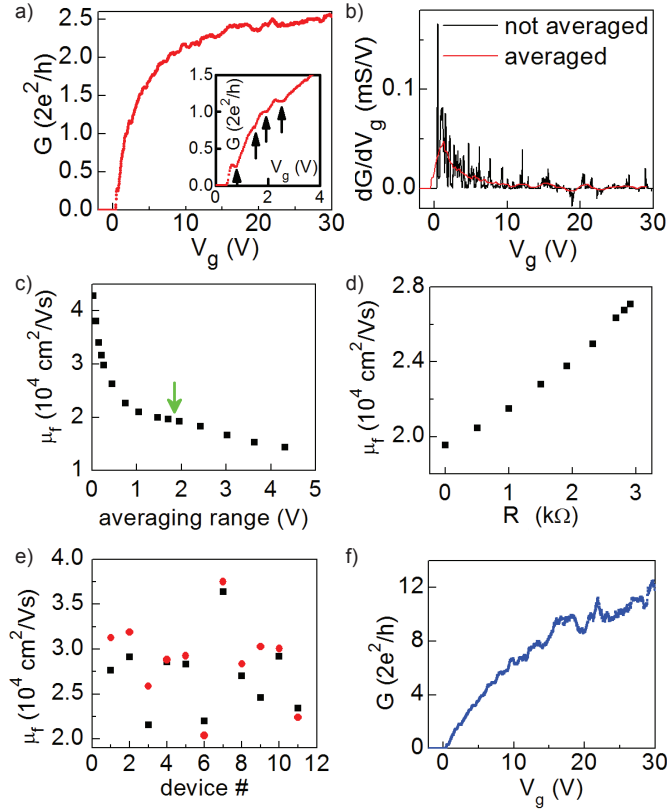


Figure 5.2: **a)** Conductance G , as a function of gate voltage V_g . Inset: Zoom-in of the conductance near pinch-off. The arrows point at universal conductance fluctuations resulting in fluctuations in transconductance. **b)** Transconductance dG/dV_g without (black) and with (red) averaging over 1.8 V gate voltage range. Averaging is applied to remove the fluctuations that lead to peaks and dips in the transconductance. **c)** Field effect mobility μ_f obtained from peak transconductance as a function of gate voltage averaging range. Plotted values of peak-mobility is the average of 11 devices on the same chip (long evacuation time experiment, Fig. 5.4). The green arrow denotes the averaging range of 1.8 V used for the averaged curve in panel b. This averaging window is used in further analysis to obtain peak-mobility. **d)** Peak-mobility as a function of series resistance subtracted from $G(V_g)$. Peak-mobility is the average of 11 devices on the same chip. **e)** Comparison between field effect mobility μ_f obtained for individual devices using the fit according to eq. 5.3 (red points) and the mobility obtained from peak transconductance (black points). **f)** Conductance as a function of gate voltage after the correction for interface resistances. For this device an interface resistance $R_s = 4 \text{ k}\Omega$ is assumed. Conductance curve without the correction for R_s is shown in panel a.

bilities of individual devices obtained using both methods (Fig. 5.2e), we conclude that both methods give similar values. The small difference is due to slightly larger interface resistances obtained from the fitting method, giving an average R_s of 3.7 k Ω .

5.5. SIMPLIFICATION OF GATE VOLTAGE-INDEPENDENT INTERFACE RESISTANCES

Here we check our simplification of modelling the interface resistances R_s to be gate voltage independent. We fit the measured device conductance $G(V_g)$ using eq. 5.3 to determine R_s , the mobility μ , and the threshold voltage V_{th} . The measured device conductance after the subtraction of R_s is denoted by $G_{ch}(V_g)$. In our model $G_L(V_g)$ has the form $G_L(V_g) = (V_g - V_{th})\mu C/L^2$, which corresponds to a conductance linear in gate voltage with the transport properties extracted from the fit mentioned above. In Fig. 5.3 we plot representative curves of $G_{ch}(V_g)$ (black) and compare them with $G_L(V_g)$ (red). We find that $G_L(V_g)$ matches well with $G_{ch}(V_g)$, demonstrating that our simple model with gate voltage-independent interface resistances is a valid approximation for our measurements.

5

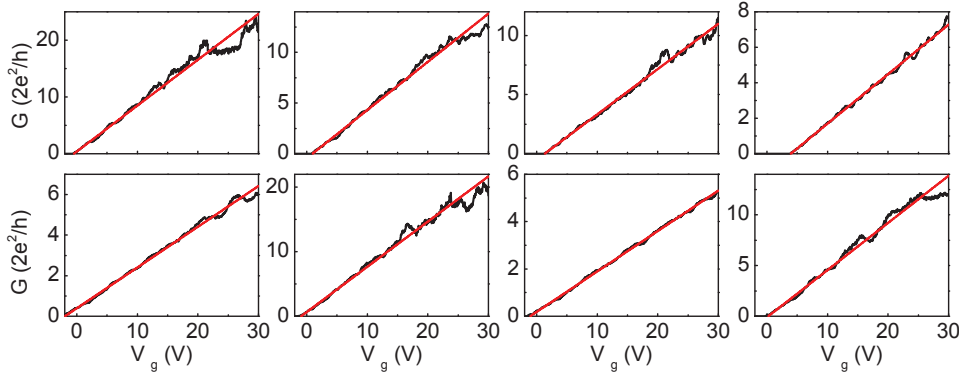


Figure 5.3: Panels show the measured device conductance after subtracting the interface resistance, $G_{ch}(V_g)$ (black), together with $G_L(V_g)$ (red), which is the conductance linear in gate voltage with the transport properties extracted from the fit. $G_{ch}(V_g)$ shown in upper row (lower row) are from the data set presented in Fig. 5.2 and Fig. 5.4.

5.6. NANOWIRE SURFACE AND ADSORPTION

Nanowire conductivity at room temperature is known to increase after evacuation of the sample space following mounting of devices [116, 140]. We find that evacuation also strongly affects $G(V_g)$ at low temperature (4 K). Comparing the $G(V_g)$ measured for short and long sample space evacuation time prior to cool down, we observe a steeper increase of conductance with gate voltage after long-time evacuation (Fig. 5.4a). Considering a number of devices on the same measurement chip, we find almost a doubling of the mobility values after long-time sample evacuation (Fig. 5.4b). The re-exposure of samples to air after long-time evacuation results in a reduction of mobility (Fig. 5.4c) with values

very similar to those obtained from the initial measurements with a short-time sample space evacuation. The transconductance is larger when the gate is swept from low towards high voltages (forward sweep direction) leading to higher mobility compared to the case of sweeping from high gate voltages to low (reverse sweep direction) (Fig. 5.4c). Moreover, after long-time evacuation a shift of the threshold voltage towards more negative values is observed (Fig. 5.4d) together with a reduced hysteresis (Fig. 5.4e). Both the threshold voltage and the hysteresis regain their initial values obtained from short-time evacuation once the sample is re-exposed to air, similar to the extracted mobility: exposing the devices to air has a reversible effect on the field effect transport parameters we extract from the fits. All extracted fit parameters can be found in Table 5.1.

A hysteresis in transconductance dependent on ambient conditions has been studied before by Kim *et al* [141] and Wang *et al* [142], and was attributed to the adsorption of water onto the nanostructure and onto the SiO₂ substrate. Evacuation of the sample environment leads to desorption of water, thereby reducing the hysteresis. However sample evacuation alone is insufficient to fully remove the adsorbed water. The similarities between our observations and those reported by Wang *et al* and Kim *et al*, considering both the influence of gate voltage sweep direction on the shift of the threshold voltage, as well as the reduction of hysteresis with evacuation time and the reversibility of the effect when reexposing samples to air, strongly suggest that the field effect transport is affected by molecules adsorbed to the nanowire and/or the SiO₂ substrate. Water is highly likely to be the main adsorbate because reexposing the device to ambient atmosphere following long evacuation time of sample space yields values of mobility, threshold voltage and hysteresis similar to those obtained from the measurements with short evacuation time. InSb nanowires have however also shown decreased conductance in response to isopropanol and acetone [130].

It is an open question how adsorbates affect device conductance at low temperature. The alignment of polar molecules by gate electric field may result in an additional gating [142]. However, the mechanism through which such alignment causes hysteresis is not clear. Another scenario is charge trapping by adsorbed molecules [141]. Such trapping could possibly lead to an asymmetry between forward and reverse sweep direction, yielding the observed hysteresis and sweep direction dependent mobility. The observed trapping mechanism is likely to have a long response time, as our measurements are taken at relatively low gate voltage sweep rates (120 mV/s). Unlike refs. [131, 141, 142], we find no dependence on sweep rate for rates between 3 – 600 mV/s. Nonetheless, repeated measurements yield the same $G(V_g)$, implying that between scans the traps are emptied.

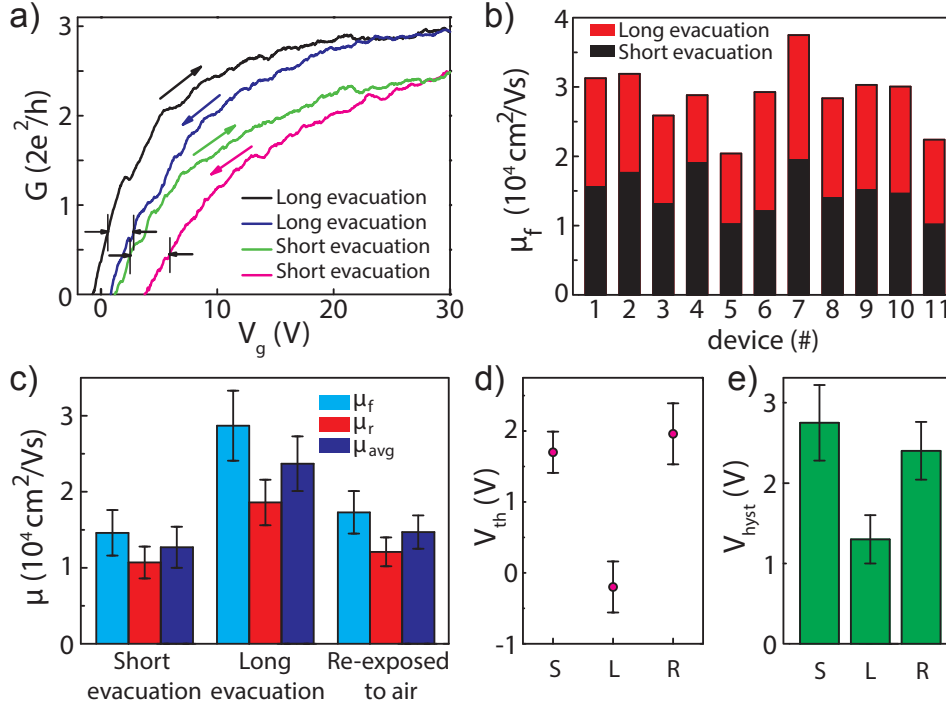


Figure 5.4: **a)** Conductance $G(V_g)$ of samples measured after evacuation of the sample space for a short or long period of time prior to cool down. Samples are evacuated for ~ 15 minutes (~ 65 hours), giving the green and pink (black and blue) conductance curves for forward and reverse sweep direction respectively. Arrows indicate sweep direction. The same chip with nanowire devices is first evacuated only shortly (yielding the data denoted with 'short evacuation'), then evacuated for longer-time ('long evacuation' data), reexposed to air for ~ 90 hours and evacuated shortly (~ 15 minutes) again ('re-exposure' data), see panel c. The substrate was cleaned prior to nanowire deposition. Hysteresis of both pairs of conductance curves is indicated with arrows and vertical lines. Although the hysteresis is indicated at non-zero G , the hysteresis reported in panel c is extracted from the difference in threshold voltage between conductance curves with forward and reverse sweep direction. **b)** Mobility obtained with forward sweep direction, μ_f , of individual devices after short (black) or long (red) device evacuation time. **c)** Mobility after short-time evacuation, long-time evacuation, and reexposure to air. μ_{avg} is the average of the mobility obtained with forward sweep direction, μ_f , and with reverse sweep direction, μ_r . **d)** Threshold voltage extracted from forward sweep direction, V_{th} after short-time evacuation (S), long-time evacuation (L) and reexposure to air (R). **e)** Hysteresis V_{hyst} , after short-time evacuation (S), long-time evacuation (L) and reexposure to air (R). The hysteresis is given by the difference in threshold voltage between forward and reverse sweep direction. All values in panels c, d and e are an average, obtained from fits to the conductance curve of each device on the measurement chip. Error bars in panels c, d and e indicate the standard deviation.

5.7. SUBSTRATE CLEANING

We further find that cleaning of Si/SiO₂ substrates by remote oxygen plasma prior to nanowire deposition results in an enhanced gate dependence of low-temperature conductivity. Fig. 5.5a shows $G(V_g)$ curves of individual devices, while Fig. 5.5b shows an average over extracted mobilities obtained from measurements of ~ 10 FETs with and without substrate cleaning. All other fabrication and measurement steps are the same

for both sets of devices. The remote oxygen plasma most probably removes hydrocarbons that remain on the substrates after fabrication of alignment markers or during storage of samples in a polymer-containing environment. We verified that the oxygen plasma cleaning does not decrease the thickness of the SiO_2 gate dielectric within the measurable range < 1 nm.

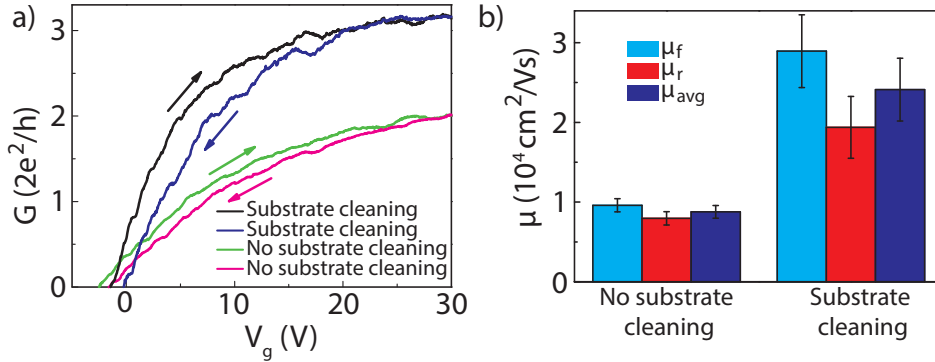


Figure 5.5: **a)** Conductance curves $G(V_g)$ obtained from samples without and with substrate cleaning. Forward and reverse sweep direction are indicated with arrows. Samples have been evacuated for ~ 60 hours before cool down. **b)** Forward, reverse and average mobility with and without substrate cleaning. Values are averages obtained from fits to conductance curves of individual devices. Error bars indicate standard deviation.

5.8. CONTACT SPACING

A correlation between FET source-drain contact spacing and extracted field effect mobility is found (Fig. 5.6). Although the spread in mobility at a given contact spacing is substantial, an overall increase of extracted mobility is observed with increasing contact spacing. To determine whether the dependence of the field effect mobility on contact spacing originates from the length of the used nanowire, FETs with short ($1 \mu\text{m}$) contact spacing were realized both on short wires, and on long wires using three contact electrodes resulting in two FETs in series. Devices made from both long and short wires with $1 \mu\text{m}$ contact spacing give similar mobility (see Fig. 5.6). The contact spacing dependence is thus a device property rather than a nanowire property.

A reduced mobility for short contact spacing is expected when transport is (quasi-)ballistic rather than diffusive [143, 144]. We have observed ballistic transport in our wires [134] with a device geometry and measurement conditions different from those here. Here we expect quasi-ballistic transport in our devices with a mean free path comparable to nanowire diameter $l_e \sim 0.1 \mu\text{m}$. While devices with $L/l_e \gg 1$ are preferable, our InSb nanowires can currently not be grown longer than $\sim 3.5 \mu\text{m}$. However, while for channel length of $1 \mu\text{m}$ (quasi-)ballistic effects may play a role, mobility values obtained from our devices with longer contact spacing yield a better estimate of field effect mobility. Moreover, effects related to the metal contacts are expected to play a larger role in devices with short contact spacing and can possibly contribute to the observed decrease of $\mu(L)$ in short channel devices. Possible explanations are that (1) the contacts reduce

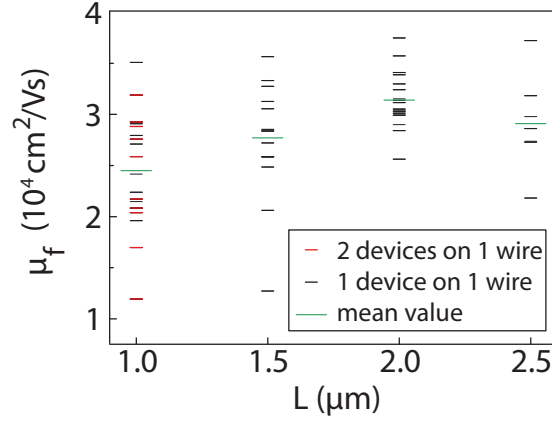


Figure 5.6: Mobility obtained by sweeping the gate voltage in forward direction, μ_f , as a function of source-drain contact spacing L . Data from 5 different measurement chips (see section 5.11.3). Red lines indicate mobility values obtained from long nanowires on which three contact electrodes were placed, resulting in two FETs in series, while black lines correspond to the mobility of single FET devices. Mean forward mobility for each contact spacing is $\mu_{f,m}(L = 1 \mu\text{m}) = 2.4 \times 10^4 \text{ cm}^2/\text{Vs}$, $\mu_{f,m}(L = 1.5 \mu\text{m}) = 2.8 \times 10^4 \text{ cm}^2/\text{Vs}$, $\mu_{f,m}(L = 2 \mu\text{m}) = 3.1 \times 10^4 \text{ cm}^2/\text{Vs}$ and $\mu_{f,m}(L = 2.5 \mu\text{m}) = 2.9 \times 10^4 \text{ cm}^2/\text{Vs}$.

5

the capacitance of short devices more than expected from the Laplace simulations (in which the nanowire is assumed to be metallic) or (2) electrons are injected from and absorbed over a finite length underneath the contacts, leading to an effective L larger than the contact spacing.

5.9. REPRODUCIBILITY

Altogether, cleaning the SiO_2 substrate before wire deposition and applying a long sample evacuation time yields $\mu_{avg} \approx 2.5 \times 10^4 \text{ cm}^2/\text{Vs}$ for devices with a contact spacing $L = 2 \mu\text{m}$. This mobility is the average value of $\mu_f = 3.1 \times 10^4 \text{ cm}^2/\text{Vs}$ (see Fig. 5.6) and $\mu_r = 1.9 \times 10^4 \text{ cm}^2/\text{Vs}$. These high mobilities result from measurements of ~ 15 devices fabricated in different fabrication runs (see section 5.11.3 for details) using the same fabrication recipe. Fig. 5.7 demonstrates the reproducibility of our results: mobility obtained from three different fabrication runs are very similar. The optimized nanofabrication recipe as well as an overview of all the parameters extracted from the fits to the conductance vs. gate voltage curves that yield Fig. 5.7 are given in section 5.11.1 and table 5.1, respectively.

5.10. CONCLUSION

Low-temperature field effect mobility of InSb nanowires is extracted by measuring the conductance as a function of gate voltage. Taking surface adsorption and substrate cleaning into consideration, an optimized nanofabrication recipe has been obtained yielding average field effect mobilities of $\sim 2.5 \times 10^4 \text{ cm}^2/\text{Vs}$. It is demonstrated that the obtained mobility values are highly reproducible.

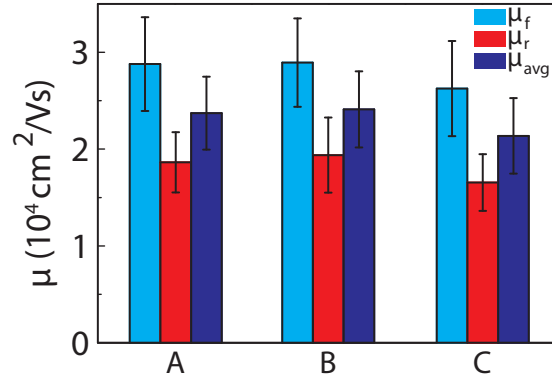


Figure 5.7: Average mobilities obtained with forward (μ_f) and reverse (μ_r) sweep direction. First group of data (batch A) corresponds to the fabrication run presented in Fig. 5.4 (long-time evacuation), batch B is presented in Fig. 5.5b (with substrate cleaning), whereas batch C is a separate batch to demonstrate the reproducibility of our results. Average mobility μ_{avg} is the average of forward and reverse mobility. All results are obtained by improved cleaning of the substrate and long evacuation time of the sample space. Error bars indicate standard deviation.

As we show that surface adsorption has a large impact on field effect mobility, further studies should be directed towards minimizing the adsorbates and analysis of surface properties. An improved design of the measurement setup allowing for heating and better evacuation of the sample space is likely to facilitate a further desorption of adsorbates. Exposing the devices to UV-light during evacuation, which may assist desorption, can also be investigated [130]. Further, passivating the nanowire surface by removing the native oxide followed by application of a high quality dielectric likely reduces surface adsorption. Possible methods are atomic hydrogen cleaning [145] or chemical etching followed by dielectric deposition [146]. Alternatively, by suspending the nanowires above a metallic gate using vacuum as a dielectric, one can minimize the effects of the substrate adsorption, leaving the wire adsorption as the predominant constituent affecting the field effect mobility. In the case of adsorbates creating a fluctuating potential profile along the wire resulting in charge scattering, a core-shell structure is expected to yield a higher field effect mobility because the potential fluctuations due to adsorbates are spatially separated from the channel owing to the shell. Finally, to study the surface composition of the nanowire and the substrate, x-ray photoelectron spectroscopy or Auger electron spectroscopy could be used [147].

5.11. SUPPLEMENTARY INFORMATION

5.11.1. OPTIMIZED FABRICATION RECIPE

- Substrate cleaning: 10 minutes remote oxygen plasma cleaning (Tepla 300 Plasma Asher) of the p^{++} -Si substrate covered with 285 nm dry thermal SiO_2 with pre-defined Au alignment markers (oxygen pressure 1 mbar, plasma power 600 W). All substrates were from the same wafer.
- Wire deposition: deterministic positioning of wires using a setup similar to that described in ref. [35]. Wires were always taken from the same section on the same growth chip.
- SEM imaging of the nanowires with surrounding alignment markers. Images are used for the subsequent design of the contacts.
- Spin resist: PMMA 950A4 at 4krpm, baking > 15 minutes at a temperature of 175°C .
- Electron beam writing of the contact design.
- Development: MIBK:IPA 1:3 60 s, IPA 60 s.
- Ar etching (AJA International sputtering system) using rf-plasma: pressure 3 mTorr, Ar flow 50 sccm, power 100 W, duration 300 s, no rotation of the sample holder. A voltage of 300 V is applied to the sample holder.
- Contact deposition: e-beam evaporation of Ti/Au 5/145 nm with deposition rate 0.5 \AA/s and 2 \AA/s respectively.
- Lift-off in acetone: the sample with acetone is heated for several hours and left in acetone for ≥ 12 h.
- Samples were stored in an Ar glove box between fabrication and mounting.

5.11.2. MEASUREMENTS DETAILS

- Sample space (IVC) evacuated for ~ 60 hours after mounting (insert type: Desert Cryogenics).
- For thermalisation, He of ~ 10 mbar is added to sample space at room temperature before cooling down the devices. During low-temperature measurements samples are kept in a vacuum environment.
- $G(V_g)$ measured using 10 mV bias, gate voltage range from -6 V to $+30$ V with sweep rate 6 mV/50 ms . Measured in forward and reverse sweep direction.
- To check a possible sweep rate dependence of $G(V_g)$, gate voltage steps of 0.15, 0.3, 0.6, 1.5, 3, 6, 15, 30 [mV/(50 ms)] is used both in forward and reverse sweep direction. No dependence on sweep rate was found.

5.11.3. OVERVIEW OF MEASURED DEVICES

- Evacuation time experiment (fabricated according to our optimized recipe described above). Mobility was extracted from measurements of 11 devices with contact spacing between 1 and 2 μm . Average contact spacing 1.41 μm . Data reported in Fig. 5.4. Long evacuation time data is also included in Fig. 5.2, 5.3, 5.6 and 5.7 (Batch A).
- FETs without substrate cleaning and with long-time evacuation. Fabricated according to our optimized recipe, with the exception that we used different settings for Ar etching. Here we used 400 V on the sample holder and etched for 150 s while keeping all the other settings the same. This yields the same amount of etching of InSb nanowire (~ 70 nm) as etching at 300 V for 300 s. 11 devices, contact spacing of all devices is 2 μm . Data reported in Fig. 5.5.
- FETs with substrate cleaning and with long-time evacuation. Fabricated according to our optimized recipe, with the exception that we used different settings for Ar etching. Here we used 400 V on the sample holder and etched for 150 s while keeping all the other settings the same. This yields the same amount of etching of InSb nanowire (~ 70 nm) as etching at 300 V for 300 s. 11 devices, contact spacing between 1 and 2 μm . Average length 1.42 μm . Data reported in Fig. 5.5, Fig. 5.6, and Fig. 5.7 (Batch B).
- FETs fabricated according to our optimized recipe. 13 devices, contact spacing between 1 and 2.5 μm . Average contact spacing 1.73 μm . Data reported in Fig. 5.6 and Fig. 5.7 (Batch C).
- FETs fabricated according to the recipe, with the addition of a thin layer of perfluorodecyltrichlorosilane (FDTS) deposited onto the devices after fabrication. No improvement of mobility was observed with respect to devices without FDTS. 11 devices, contact spacing between 1 and 2.5 μm . Average contact spacing 1.64 μm . Data reported in Fig. 5.6.
- FETs fabricated according to our optimized recipe, but with substrate oxygen plasma cleaning of 60 s instead of 10 minutes. After oxygen plasma cleaning a thin layer of FDTS was deposited onto the substrate, after which fabrication proceeded according to the recipe. No improvement of mobility was observed with respect to devices without FDTS and with the usual 10 minutes cleaning. 10 devices, contact spacing between 1 and 2.5 μm . Average contact spacing 1.85 μm . Data reported in Fig. 5.6.

5.11.4. AVERAGE DEVICE CHARACTERISTICS OBTAINED FROM SEVERAL MEASUREMENT AND FABRICATION RUNS

	Short evacuation	Long evacuation	Reexposed to air
μ_f ($10^3 \text{ cm}^2/\text{Vs}$)	14.6 ± 3.0	28.7 ± 4.6	17.3 ± 2.8
μ_r ($10^3 \text{ cm}^2/\text{Vs}$)	10.7 ± 2.1	18.6 ± 3.0	12.1 ± 1.9
μ_{avg} ($10^3 \text{ cm}^2/\text{Vs}$)	12.7 ± 2.7	23.7 ± 3.6	14.7 ± 2.2
V_{th} (V)	1.70 ± 0.29	-0.20 ± 0.36	1.96 ± 0.43
V_{hyst} (V)	2.75 ± 0.47	1.31 ± 0.30	2.40 ± 0.36
R_s ($k\Omega$)	3.7 ± 0.7	3.7 ± 1.0	4.1 ± 1.2

Table 5.1: Mobility, threshold voltages V_{th} , hysteresis, V_{hyst} and series resistances, R_s , extracted from fits to conductance curves $G(V_g)$ of the evacuation time experiment. Mobility is obtained with forward sweep direction, μ_f and reverse sweep direction, μ_r . The average mobility of these two sweep directions, μ_{avg} , is also reported. V_{th} is the threshold voltage obtained from fits to $G(V_g)$ taken with forward sweep direction. Mobility, threshold voltage and hysteresis are also shown in Fig. 2c, d and e, respectively.

5

Batch	A	B	C
μ_f ($10^3 \text{ cm}^2/\text{Vs}$)	28.7 ± 4.6	28.9 ± 4.4	26.0 ± 4.7
μ_r ($10^3 \text{ cm}^2/\text{Vs}$)	18.6 ± 3.0	19.4 ± 3.9	16.4 ± 3.0
μ_{avg} ($10^3 \text{ cm}^2/\text{Vs}$)	23.7 ± 3.6	24.2 ± 3.9	21.2 ± 3.8
V_{th} (V)	-0.20 ± 0.36	-0.51 ± 0.45	-0.37 ± 0.39
V_{hyst} (V)	1.31 ± 0.30	1.14 ± 0.22	1.41 ± 0.28
R_s ($k\Omega$)	3.7 ± 1.0	3.0 ± 0.8	4.8 ± 1.8

Table 5.2: Mobility, threshold voltage, V_{th} , hysteresis, V_{hyst} , and series resistance, R_s , obtained from fits to the conductance curves $G(V_g)$ of three batches of high-mobility devices. Mobility is obtained with forward sweep direction, μ_f and reverse sweep direction, μ_r . The average mobility of these two sweep directions, μ_{avg} , is also reported. V_{th} is the threshold voltage obtained from fits to $G(V_g)$ taken using forward sweep direction. Mobilities and series resistances are also shown in Fig. 5.

6

ONE MINUTE PARITY LIFETIME OF A NBTiN COOPER-PAIR TRANSISTOR

D. J. van Woerkom, A. Geresdi, L. P. Kouwenhoven

Vaak moet er iets gebeuren voordat er iets gebeurt.

Johan Cruijff

In a small superconducting island, hosting an even number of electrons, all charge carriers form Cooper pairs, defining the ground state of the Cooper-pair transistor (CPT). An additional, unpaired electron can only occupy a higher energy level, determined by the superconducting order parameter. This even-odd (parity) energy difference makes the CPT a very sensitive charge detector as well as a prototype superconducting qubit, whose coherence relies on the conservation of the parity of the island. Here we report parity conservation in a niobium-based superconductor, NbTiN, for the first time. NbTiN is a popular superconductor since it can sustain high parallel and perpendicular magnetic fields which is often a requirement for hybrid devices. The parity conservation resulted in the first $2e$ -periodicity measurements in a non-Aluminium CPT. The highest reported parity lifetime ever, which was longer than one minute, was measured. The parity lifetime did not saturate down to a base temperature of 12mK, showing state-of-the-art device shielding of thermal photons. We show that our CPT is magnetic field compatible, opening new possibilities for coupling spin degrees of freedom to superconducting circuits and qubits and for topological superconductivity, enabling qubits based on MZM.

This chapter has been published in Nature Physics **11**, 547-550 (2015).

The experimental setup is discussed in section 6.2 followed by the measurement technique, in section 6.3, which was found decisive in the success of the experiment. Characterization is performed to find the range of Josephson coupling and charging energy ratio in section 6.4. The main results of the measurements are in section 6.5 where also the comparison between standard and extra electromagnetic shielding is shown. The long parity lifetime is also extracted with an additional method which confirms the lifetime to be in the order of 1 minute. This additional method is also used to show a direct $2e$ -effect, both of these measurements are described in section 6.6. In the last section 6.7 the magnetic field compatibility of the parity lifetime is investigated. The final conclusion is reported in section 6.8. Supplementary information is given in section 6.9

6.1. INTRODUCTION

The parity modulation of the ground state of a superconducting island is a direct consequence of the presence of the Cooper pair condensate preferring an even number of charge carriers [24, 148]. The addition energy of an odd, unpaired quasiparticle equals to the superconducting gap, Δ , suppressing single electron hopping in the low temperature limit, $k_B T \ll \Delta$. Controlling the quasiparticle occupation is of fundamental importance for superconducting qubits as single electron tunneling results in decoherence [149, 150]. In particular, topological quantum computation relies on the parity control and readout of Majorana bound states [151, 152]. Here we present parity modulation for the first time of a niobium titanite nitride (NbTiN) Cooper-pair transistor coupled to aluminium (Al) leads. We show that this circuit is compatible with the magnetic field requirement $B \sim 100$ mT of inducing topological superconductivity in spin-orbit coupled nanowires [7–9]. Our observed parity lifetime exceeding 1 minute is several orders of magnitude higher than the required gate time of flux-controlled braiding of MZM [17].

Experimentally, the parity modulation of a superconducting island can be observed via the ground state charge [24], the even-odd modulation of the charge stability diagram [153, 154], or the parity dependence of the switching current, I_{sw} [25, 155]. The interplay of the charging energy $E_c = e^2/2C$ and the Josephson coupling $E_J = I_c \hbar/2e$ makes the Cooper-pair transistor (CPT) a single, gate-modulated Josephson junction [25, 156] with a $2e$ charge periodicity in the absence of parity switches.

Recent, direct measurements of τ_p [150, 157] yielded values up to the millisecond regime for aluminium devices. Despite considerable efforts, however, no $2e$ periodicity has been reported for non-aluminium superconductors [158, 159], such as niobium or vanadium. Comparative studies of aluminium and niobium CPTs suggested that the elusiveness of parity effects is related to the material properties [159], in particular the formation of a surface oxide layer under ambient conditions. While aluminium tends to form a few nanometer thick *insulating* oxide layer [160], niobium is prone to oxidize through the bulk material [161] mostly forming *metallic* NbO_x compounds. This process then leads to localized metallic states in the island, which prevents parity control.

In contrast, nitridized niobium compounds, such as niobium titanite nitride (NbTiN), have been shown to be less prone to form oxides [161] and hence are good candidates for parity-conserving superconducting circuits. Furthermore, NbTiN forms transparent contacts with spin-orbit coupled semiconductor nanowires [9], and has become a preferred superconductor to investigate Majorana bound states.

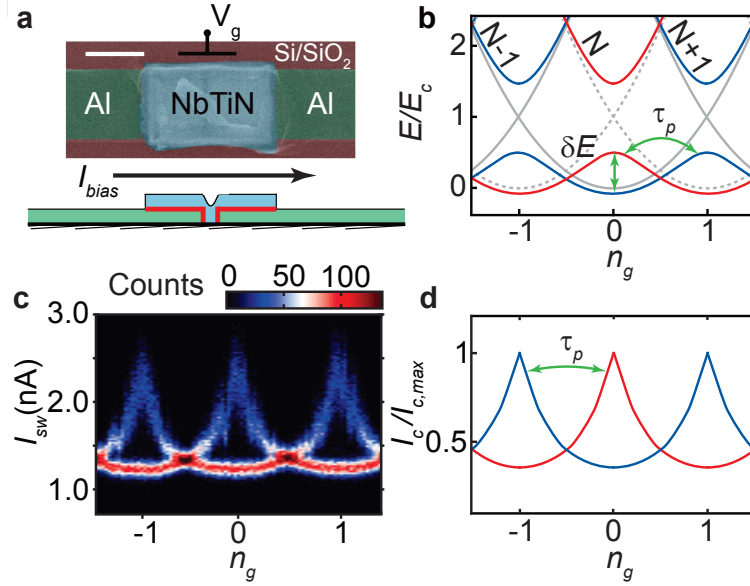


Figure 6.1: **Device layout and parity-dependent switching current.** (a) Scanning electron microscope image and schematic cross-section of a typical Al/NbTiN/Al hybrid Cooper-pair transistor (CPT). The NbTiN island dimensions are 250 nm × 450 nm. Scale bar denotes 200 nm. The AlO_x oxide barriers are indicated by thick red lines. (b) Energy level diagram as a function of the gate charge, n_g , in the presence of low energy subgap states restoring $1e$ periodicity. The maximum even-odd energy difference is denoted by δE . Gray lines represent energy levels in the absence of Josephson coupling, i.e. $E_J = 0$. Red and blue lines show energy levels for even and odd charge parity respectively, both for $E_J = E_c$. Parity switches occur on the timescale of τ_p due to quasiparticle tunneling. Measured switching current histogram (c) and calculated $I_c(n_g)$ (d) in the low temperature limit. Note that in (d) the two possible $I_c(n_g)$ values corresponding to the even and odd charge states are denoted by blue and red lines respectively. In the measured data (c) the two branches are superimposed, see text.

6.2. EXPERIMENTAL SETUP

The measurements were performed in a Leiden Cryogenics CF-1200 dry dilution refrigerator with a base temperature of 12 mK equipped with Cu/Ni shielded twisted pair cables thermally anchored at all stages of the refrigerator.

The current bias and gate voltage were applied through battery operated and optically isolated sources in order to reduce line interference. Similarly, the first stage of the V_{sd} amplifier was isolated from the commercial readout electronics. Filtering of the measurement lines was achieved by room temperature LC π filters with a cutoff frequency of ~ 100 MHz followed by a sequence of a high frequency copper powder filter [97] and a two-pole RC filter with a nominal $f_{-3dB} = 50$ kHz, both thermally anchored to the 12 mK stage.

Special care was taken to avoid stray microwave radiation by using an outer and an inner copper shield enclosing the device. The inner surface of both shields was treated with commercially available Aeroglaze Z306 paint absorbing far infrared stray radiation [162]. We note that the inner shield was not present for device N.

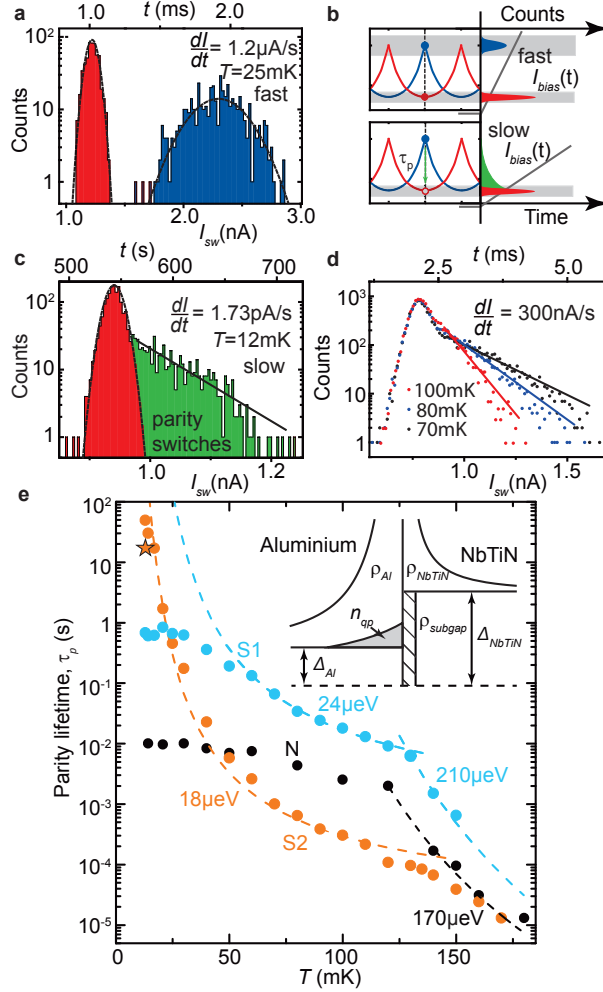


Figure 6.2: **Characterization and temperature dependence of the parity lifetime.** (a) Linecut histogram at integer n_g of Fig. 6.1c showing a bimodal distribution. We attribute the two peaks to the two parity states of the CPT (colored red and blue, respectively). (b) For a *fast* current ramp (upper panel), the histograms of the two parity states are independently probed showing the characteristics of data in panel (a). In the *slow* limit (lower panel in (b)), parity switches occur during the current ramp, leading to an exponential tail of the distribution (shown in green), quantifying τ_p . The $I_{bias}(t)$ current ramp is represented by a dark gray line. (c) Experimental dataset in the *slow* limit. Note the change in the current- and timescale compared to panel (a). We show the exponential cutoff in green, and extract $\tau_p = 49$ s (solid black line). The dash black lines are guide to the eye envelopes for the peaks in panels (a) and (c). (d) Experimental data at different temperatures show the temperature dependence of τ_p . (e) τ_p as a function of temperature for non-shielded device N, and shielded devices S1, S2. All CPTs exhibit an activated behavior with $\Delta \approx 170 \dots 210 \mu\text{eV}$ in the high temperature limit corresponding to the gap of the aluminium leads. Saturation of device N without shielding and no quasiparticle traps is observed below $T \approx 100$ mK. Shielded devices S1 and S2 exhibit a minigap-activated behavior $\Delta^* \approx 20 \mu\text{eV}$ in the low temperature limit. Star symbol shows $\tau_p = 15$ s at $T = 12$ mK extracted from parity distilled data for device S2 (see Fig. 6.3d).

6.3. MEASUREMENT TECHNIQUE

The switching current histograms were acquired using a Rigol DG4062 arbitrary waveform generator controlling the isolated current bias source with a triangle wave signal resulting in a dI/dt current ramp. A finite voltage response above the preset $V_{\text{ref}} \sim 10 \mu\text{V}$ triggers the recording of I_{sw} (Fig. 6.7c). We note that the delay of the low pass filters were accounted for on the basis of circuit simulations. Subsequent I_{sw} measurements were taken with setting zero I_{bias} for approximately 100 ms in between to avoid overheating effects. We did not observe a difference in the switching current histograms taken with waiting times in the range of 20 ms and 10 s.

The schematics of the measurement and typical waveforms are shown in Fig. 6.7.

6.4. CHARACTERIZATION VALUES

Our device features a NbTiN island sputtered onto Al leads (Fig. 6.1a). The tunnel barriers between the island and the leads are created by means of controlled *in-situ* surface oxidation of Al, resulting in amorphous AlO_x barriers [160].

We extract a charging energy $E_c \approx 50 \mu\text{eV}$ and $E_J \approx 30 \dots 50 \mu\text{eV}$ for different devices. A detailed list of parameters and characterization methods are presented in section 6.9.1. Our devices are in the intermediate coupling regime with $E_J \sim E_c$, where the energy diagram (Fig. 6.1b) and the critical current (Fig. 6.1d) are sensitive to the charge parity. It is important to note that our CPTs are in the optimal regime to establish flux-controlled braiding of MZM with $E_J \sim E_c \gg k_B T$ [17] and hence a useful platform to establish the parity lifetime for Majorana circuits [163].

6

6.5. TEMPERATURE DEPENDENCE OF τ_p

We model the CPT as a two level system which can exist in either parity state (red and blue bands in Fig. 6.1, respectively), and switches state on the timescale of τ_p [164] due to quasiparticle tunneling. We collect the switching current histograms by repetitively sweeping the bias current from zero (non-dissipative state) to beyond the switching current. Here, in the resistive state, quasiparticle tunneling causes a random reinitialization of the parity state of the CPT for the next measurement. This results in the apparent Ie periodicity in Fig. 6.1c. Nevertheless, as long as the parity remains constant during each sweep, we expect to find the two branches as a bimodal histogram, as we indeed observe in Fig. 6.2a. In these measurements, the current ramp time is much shorter than the parity lifetime, τ_p (*fast* measurement limit).

6.5.1. STANDARD SHIELDING

We quantify τ_p in the *slow* measurement limit. In this regime parity switches occur during the current ramp (Fig. 6.2b lower panels) such that reaching the upper branch (depicted as blue in Fig. 6.2a and 6.2b) becomes exponentially suppressed (Fig. 6.2c). The exponential tail represents parity switches during the current bias ramp, resulting in an observable decay of the upper branch (depicted as green in Fig. 6.2b and 6.2c), $p_u(t) = p_u(0) \exp(-t/\tau_p)$. Thus, from the decay of the histogram (black solid line in Fig. 6.2c), we can directly obtain τ_p .

The observed τ_p is a result of single electron tunneling events through the junctions of the CPT. In the zero voltage state, we can link τ_p to the subgap density of states on the island and the quasiparticle density in the leads (for details see the supplementary material):

$$\tau_p^{-1} = \frac{2n_{\text{qp}}}{e^2 R_N \rho_{\text{Al}}} \frac{\rho_{\text{subgap}}}{\rho_{\text{NbTiN}}}, \quad (6.1)$$

where R_N is the normal state resistance of the CPT. It is instructive to note that equation 6.1 is similar to the tunneling rate derived in [165] for a device with a normal metallic island, which stems from our assumption of a finite subgap density of states in the island. In our case, the parity lifetime is determined by the quasiparticle density in the leads [163] and the *phenomenological* Dynes parameter [166] of the island material. Assuming a thermal quasiparticle density

$$n_{\text{qp}}(T) = \rho_{\text{Al}} \sqrt{2\pi k_B T \Delta_{\text{Al}}} e^{-\frac{\Delta_{\text{Al}}}{k_B T}} \quad (6.2)$$

in the leads, we find $\Delta_{\text{Al}} = 170 \dots 210 \mu\text{eV}$ (Fig. 6.2e) for temperatures exceeding 120 mK, in good agreement with the superconducting gap of the aluminium leads extracted from the charge stability diagram. Furthermore, by inserting eq. 6.2 into eq. 6.1, we get an estimate of the Dynes parameter to be $\sim 10^{-2}$. This is in good agreement with $\sim 10^{-3}$ that we get based on our measurements of a single NbTiN/AlO_x/Al junction shown in the supplementary material. We can therefore attribute the observed parity lifetime for $T > 120 \text{ mK}$ to the *thermal* quasiparticle population in the leads.

For device N, however, we find a saturated $\tau_p = 9.5 \text{ ms}$ in the low temperature limit, a common observation in superconducting qubits [150] and hybrid single electron transistors [165] signifying the presence of *non-thermal* quasiparticle excitations

6.5.2. EXTRA SHIELDING

A common strategy to drain non-thermal quasiparticles is to introduce traps, i.e. normal metal junctions attached to the leads. We note that the trapping efficiency of a quasiparticle trap is influenced by its distance from the CPT with respect to the quasiparticle diffusion length on the timescale of the recombination time [167]. Our choice of a nominal $5 \mu\text{m}$ separation is much shorter than the typical diffusion length of $\gtrsim 100 \mu\text{m}$ even at the highest temperature of $T = 150 \text{ mK}$. However, since this distance is much longer than the estimated coherence length of $\xi_{\text{Al}} \approx 100 \text{ nm}$, the inverse proximity effect does not influence the transport at the junction of the CPT [168].

By introducing quasiparticle traps and microwave-tight shielding coated with infrared absorber painting for devices S1 and S2, we find a non-saturated behaviour of τ_p (Fig. 6.2e). We observe a minigap activated temperature dependence with $\Delta^* \approx 20 \mu\text{eV}$ for both devices which we attribute to a minimum excitation energy on the island. This activation energy is consistent with the maximum even-odd energy difference of $\delta E \approx 20 \dots 30 \mu\text{eV}$ (Fig. 6.1b) which promotes $\tau_p \sim \exp(\delta E / k_B T)$ [169].

It is to be stressed that the lack of saturation signals that the effective quasiparticle temperature of the CPT follows the bath temperature down to the 10 mK regime which is in clear contrast to the saturated behaviour of device N. We find $\tau_p = 49 \text{ s}$ at $T = 12 \text{ mK}$ for device S2. To put this number into context, we note that the Josephson frequency $f_J =$

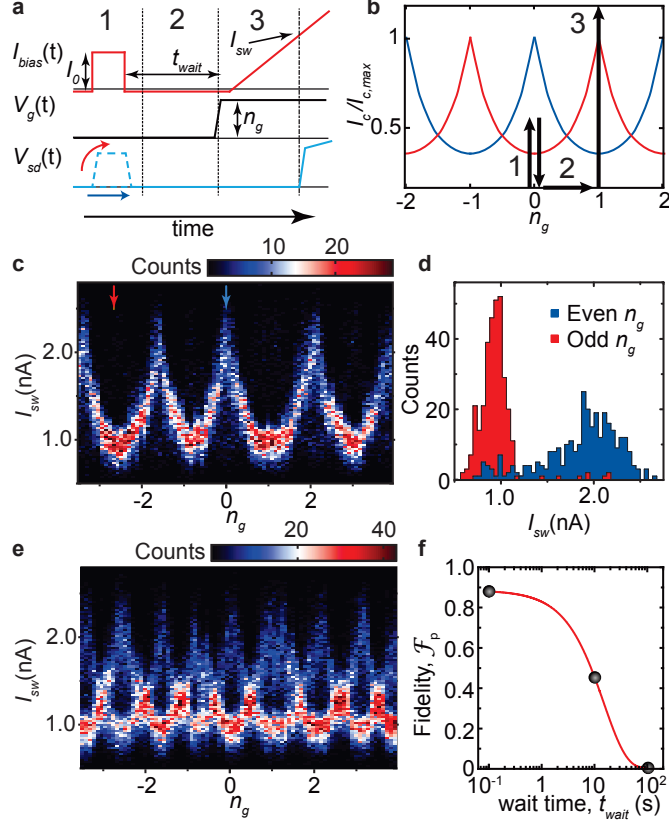


Figure 6.3: **Parity state distillation.** (a) Schematic current bias and gate voltage waveforms applied to the device. First, current bias pulse with an amplitude between the two branches is applied (1). At the same time the measured voltage $V_{sd}(t)$ is recorded to initialize the parity state. Then the gate voltage is ramped (2) and finally, the switching current is recorded (3). (b) The schematic representation of the applied waveforms overlaid on the parity-dependent critical current. (c) Parity distilled switching current histogram exhibiting $2e$ periodicity with $t_{wait} = 100$ ms. Linecut histograms are shown in panel (d) for an even (blue) and odd (red) n_g denoted by arrows in panel (c). (e) Raw histogram without parity distillation exhibiting $1e$ periodicity. Slight shifts in panels (c) and (e) are caused by gate charge switches which occur on the timescale of several 10 minutes. (f) Parity distillation fidelity as a function of t_{wait} , see text. Solid red line denotes the fit $\sim \exp(-t_{wait}/\tau_p)$ with $\tau_p = 15$ s. All data was recorded on device S2.

$E_J/h \approx 10$ GHz and thus a single quasiparticle event occurs only once for every $\tau_p f_J \sim 10^{11}$ Cooper pairs tunneling through the junctions. This signifies the low probability of parity switches for an open device with $E_J \approx E_C$ required for flux-tunable Majorana braiding schemes.

6.6. PARITY STATE DISTILLATION

Thus far, we started each switching current measurement from an unknown parity state because of the random reinitialization in the dissipative state of the CPT for $I_{bias} > I_{sw}$.

In order to reproducibly select the same parity state, we employ a parity distillation protocol (Fig. 6.3) where, by selecting a single parity state without switching to the resistive state, we ensure that the parity remains well defined for the subsequent measurement. This protocol indeed results in a $2e$ periodic switching current pattern (Fig. 6.3c) which is observed for the first time for a non-aluminium CPT.

We quantify the effectiveness of the parity distillation by defining the fidelity as:

$$\mathcal{F}_p = \frac{p_{u,f} - p_{u,i}}{1 - p_{u,i}}, \quad (6.3)$$

where $p_{u,f}$ is the conditional probability of the upper branch in the final step (3), and $p_{u,i}$ is the initial probability. We note that the above expression is valid for an arbitrary $0 < p_{u,i} < 1$ value set by the average quasiparticle occupation of the CPT. For device S2 we find $\mathcal{F}_p = 0.88 \pm 0.05$ for $t_{\text{wait}} = 100$ ms demonstrating the high degree of parity distillation (Fig. 6.3d). By changing t_{wait} between the parity initialization (1) and measurement (3), we acquire an independent measurement $\tau_p = 15$ s for device S2 at $T = 12$ mK (Fig. 6.3f).

Finally, we investigate the evolution of $\tau_p(B)$ in different magnetic field directions. In parallel magnetic field, we observe a gradual decrease of τ_p . The onset of the steep decay at $B_{\parallel} = 110$ mT (yellow arrow in Fig. 6.4a) is in agreement with the condition for vortex penetration through a mesoscopic superconducting island [170] with $\Phi \approx 1.1\Phi_0 \gtrsim \Phi_0$, where $\Phi_0 = h/2e$ is the magnetic flux quantum. We note that the measurement geometry shown in the inset of Fig. 6.4a may give rise to a Fraunhofer-like interference on the same magnetic field scale, however the upper critical magnetic field of 320 mT of the Al leads did not allow for evaluating τ_p over a larger magnetic field range, i.e. several flux quanta.

These results underline the significance of the sample geometry of the CPTs for maintaining parity control in a finite magnetic field. However, our device exhibits $\tau_p > 10$ ms in $B_{\parallel} > 100$ mT, required to induce MZM [7–9].

6.7. MAGNETIC FIELD DEPENDENCE OF τ_p

By applying a perpendicular field first results in an increase of τ_p reaching a maximum value $\tau_p = 94$ s at $B_{\perp} \approx 10$ mT, before dropping at higher magnetic fields (Fig. 6.4b). Notably, the typical switching current values, shown in the supplementary material, do not follow the same trend. Making use of the relation between the lower critical field and the stripe width, $B_{c1,\perp}(w) \sim \Phi_0/w^2$ [171] we attribute the initial increase to vortex formation and hence more effective quasiparticle trapping in the wide lead sections ($w \approx 2 \mu\text{m}$) of the device (see the yellow sections in Fig. 6.4b). Upon reaching $B_{\perp} \approx 10$ mT, the vortex phase becomes stable in the close vicinity of the CPT ($w \approx 250$ nm) causing a gradual decrease of τ_p . We note that due to $\xi_{\text{Al}} \approx 100$ nm $\sim w$ for our devices, we cannot make a quantitative comparison between our measurement data and theoretical expressions of critical magnetic field of thin stripes. We however conclude that vortices induced by a perpendicular magnetic field can increase the efficiency of quasiparticle traps, but the formation of a vortex phase in the near vicinity of the CPT enhances quasiparticle transport in agreement with earlier observations [171, 172].

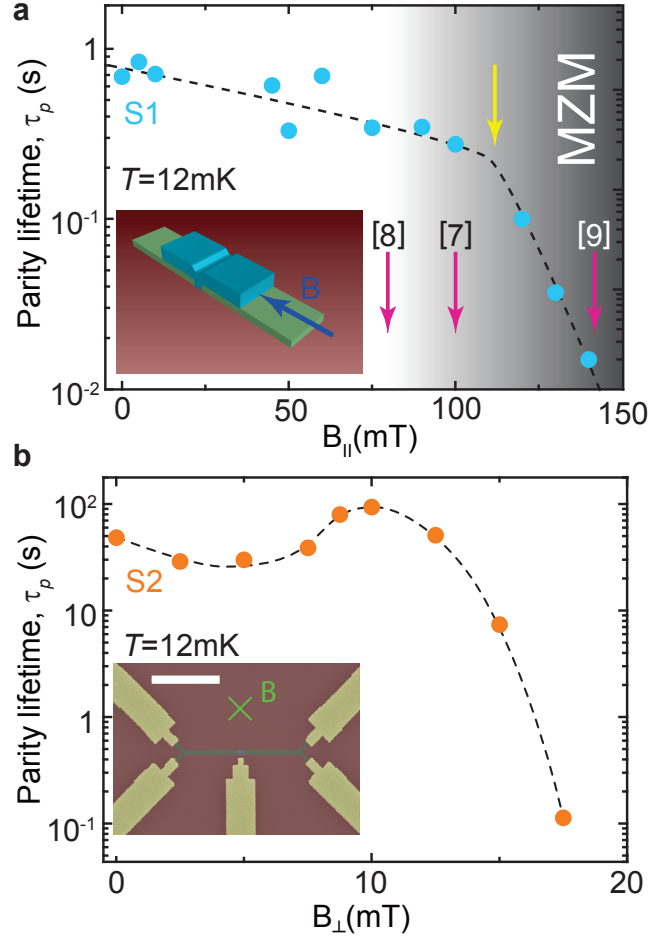


Figure 6.4: **Influence of the magnetic field on the CPT.** The parity lifetime as a function of in-plane field, $B_{||}$ (a) and perpendicular field, B_{\perp} (b), respectively. In panel (a), the shaded region depicts the condition for inducing MZM in spin-orbit coupled semiconductor wires [7–9] and the yellow arrow shows the onset of the steeper decay at $B_{||} \approx 110\text{mT}$. The inset depicts the relative orientation of the CPT with respect to the magnetic field. In panel (b), the inset shows the false colour electron microscope image of the device with the white scale bar denoting $5\mu\text{m}$. In both panels, the dash lines serve as a guide to the eye.

6.8. CONCLUSIONS

Cooper-pair transistors were fabricated with Aluminium leads and NbTiN islands with E_J/E_C ratio of ~ 1 . Switching current measurements were performed as function gate voltage to investigate the gate periodicity. A clear $1e$ -periodicity is found and is explained by trapping of strong localized quasi-particles after a switching current event. In the dissipationless state the parity lifetime is investigated and was measured up to 1 minute with extensive shielding and in the presence of quasiparticle traps. With parity distilla-

tion a clear $2e$ -periodicity in gate is observed for the first time in a Niobium-based superconductor. Finally, minor reduction of parity lifetime was observed moderate magnetic field in the limited were experiments are claiming the existence of MZM.

6.9. SUPPLEMENTARY INFORMATION

6.9.1. DEVICE FABRICATION

The Cooper-pair transistors (CPTs) were fabricated using electron beam lithography and thin film deposition starting with a p^{++} doped silicon wafer with a 285 nm thick thermally grown SiO_2 surface layer. First, aluminium leads were defined and evaporated in a high-vacuum chamber ($p_{\text{base}} \sim 10^{-7}$ Torr) at a rate of 0.2 nm/s with a thickness of 30...35 nm. Subsequently, the mask for the NbTiN island was defined in a second lithography step. The sample was loaded into an ultra high vacuum AJA International ATC 1800 sputtering system ($p_{\text{base}} \sim 10^{-9}$ Torr), where first a ~ 5 nm Al layer was removed by means of argon plasma etching at $p = 3$ mTorr. This step was followed by *in-situ* oxidation to create AlO_x tunnel barriers. Without breaking vacuum, the NbTiN island was then sputtered with a layer thickness of 70...100 nm.

We used a $\text{Nb}_{0.7}\text{Ti}_{0.3}$ target with a diameter of 3". Reactive sputtering resulting in nitridized NbTiN films was performed in an Ar/N process gas with a typical 10 at% nitrogen content at a pressure of 3 mTorr using a DC magnetron source. During deposition, a -45 V bias was applied to the sample with respect to the target. The critical temperature of the superconducting transition temperature of thin films with a layer thickness of 100 nm was measured to be 14.1 K in zero magnetic field.

For the shielded samples S1 and S2, quasiparticle traps were fabricated by first cleaning the Al surface by means of argon plasma milling at $p = 0.2$ mTorr and *in-situ* evaporation of 25 nm Ti and 100 nm Au films at a base pressure of $\sim 10^{-7}$ Torr.

Care was taken to remove resist mask residues after each electron beam writing step using a remote oxygen plasma etch with a pressure of 1 mbar.

We show the scanning electron microscope images of the devices investigated in Fig. 6.5 and define the fabrication parameters in Table 6.1.

device	island size (nm \times nm)	junction size (nm \times nm)	NbTiN thickness (nm)	traps	oxygen exposure (Torr \times s)	R_N (k Ω)
N	500 \times 500	200 \times 200	70	no	7400	58
S1	450 \times 200	200 \times 200	100	yes	150	125
S2	450 \times 250	200 \times 250	100	yes	150	66

Table 6.1: Device fabrication parameters of the CPTs discussed in this chapter.

BASIC CHARACTERIZATION OF THE CPT

We estimate the charging energy, $E_c = e^2/2C$, based on the periodicity of characteristic resonances visible for $eV_{\text{sd}} = \Delta_{\text{Al}} \dots 2\Delta_{\text{Al}}$. We attribute these lines to resonant Andreev tunneling through single levels of the CPT [173]. The resonances occur with a vertical periodicity of $eV_{\text{sd}} = 2E_c$ and the onset defines $eV_{\text{sd}} = \Delta_{\text{Al}}$ as well.

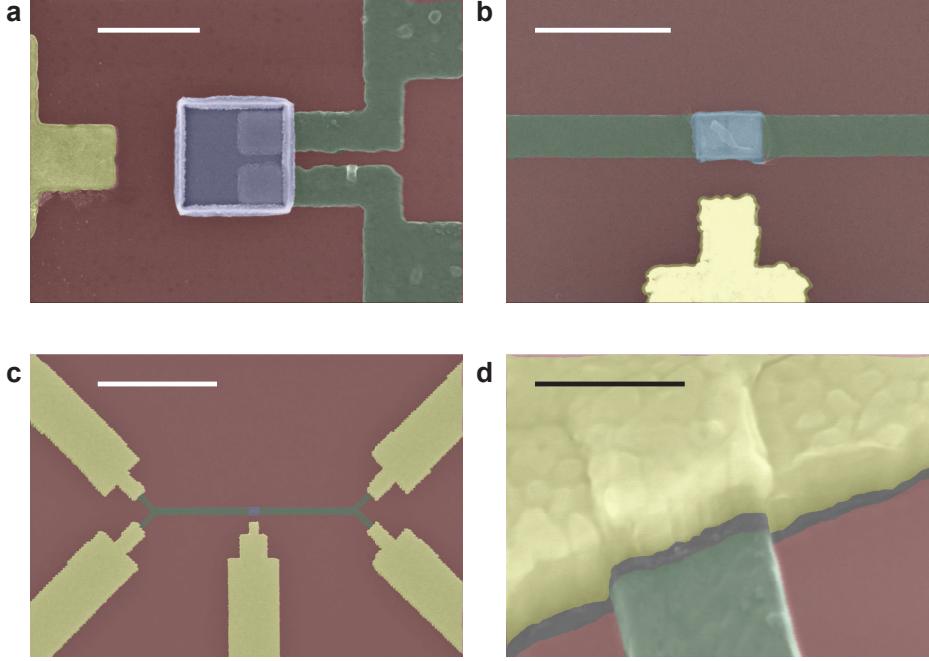


Figure 6.5: **Scanning electron microscope images of the CPTs.** (a) Non-shielded device N without quasiparticle traps. (b), (c), (d) Shielded device S2 featuring quasiparticle traps. Colour legend: dark red: Si/SiO₂ substrate; light blue: NbTiN island, green: aluminium leads and yellow: normal metal (Ti/Au) gate and quasiparticle traps. Scale bars denote 500 nm (a), 1000 nm (b), 5 μm (c) and 200 nm (d), respectively.

The onset of quasiparticle transport is defined by $eV_{sd} = 2(\Delta_{\text{NbTiN}} + \Delta_{\text{Al}})$, which then defines Δ_{NbTiN} . Typical $I(V)$ and $dI/dV(V)$ traces are shown in Fig. 6.6 and the recovered parameters are tabulated in Table 6.2.

We evaluate the Josephson coupling for a *single* tunnel junction [174]:

$$E_J = \frac{\hbar}{2e^2} \frac{\Delta_{\text{Al}}}{R_N/2} K\left(\sqrt{1 - \left(\frac{\Delta_{\text{Al}}}{\Delta_{\text{NbTiN}}}\right)^2}\right) \quad (6.4)$$

with $K(x)$ being the complete elliptic integral of the first kind. This expression is valid in the zero temperature limit, assuming symmetric tunnel junctions of the resistance of $R_N/2$.

Alternatively, we can estimate the E_J/E_c ratio based on the modulation of I_{sw} as a function of the gate charge, n_g (last column of Table 6.2) [175]. We find a good agreement between the E_J/E_c values acquired by the two independent methods. Finally, we provide $\delta E(E_c, E_J)$ based on [176].

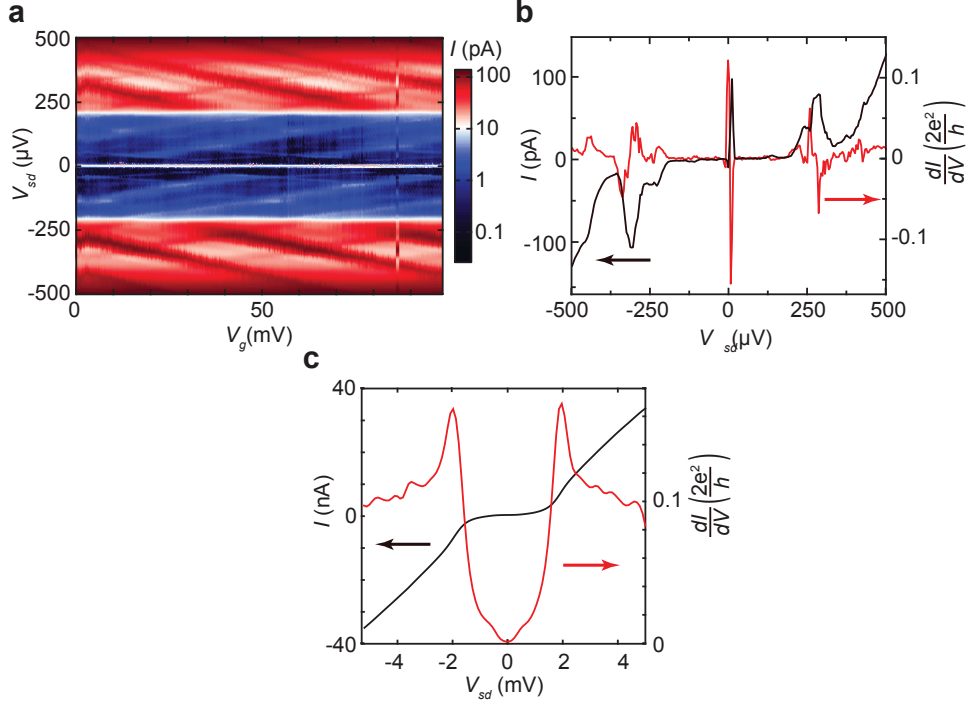


Figure 6.6: **Basic characterization of the CPT.** (a) Stability diagram: $\log|I|$ as a function of V_{sd} and V_g of device S1. We estimate E_c based on the resonant Andreev processes (see text). (b) Linecut $I - V$ traces at V_g values depicted by arrows in (a). Characteristic resonant tunneling processes occur in the bias voltage range of $eV_{sd} = \Delta_{Al} \dots 2\Delta_{Al}$. (c) $I - V$ (black) and dI/dV (red) line traces of device S2. Quasiparticle transport is enhanced above a bias voltage of $eV_{sd} = 2(\Delta_{NbTiN} + \Delta_{Al})$.

device	Δ_{Al} (μ eV)	Δ_{NbTiN} (μ eV)	R_N (k Ω)	E_J (μ eV)	E_c (μ eV)	E_J/E_c calc.	E_J/E_c I_{sw}
N	210	1390	58	54	50	1.08	1.25
S1	218	810	125	17	62	0.28	0.32
S2	220	1300	66	48	49	0.98	1.16

Table 6.2: **Device transport parameters.**

6.9.2. MEASUREMENT SETUP

A typical DC $V - I$ trace of device S2 at 12mK temperature is presented in Fig. 6.7b exhibiting a sharp transition between the dissipationless and the resistive state at the switching current, I_{sw} .

It is important to note that we find a finite subgap conductance at $eV_{sd} < 2\Delta_{NbTiN}$ which is consistent with the presence of the subgap quasiparticle states justifying the analysis leading to equation 6.1. Furthermore, we observe reduced $\Delta_{NbTiN} < 1.4$ meV values compared to that of bulk films ($\Delta > 2$ meV) [179], which we attribute to the chemical

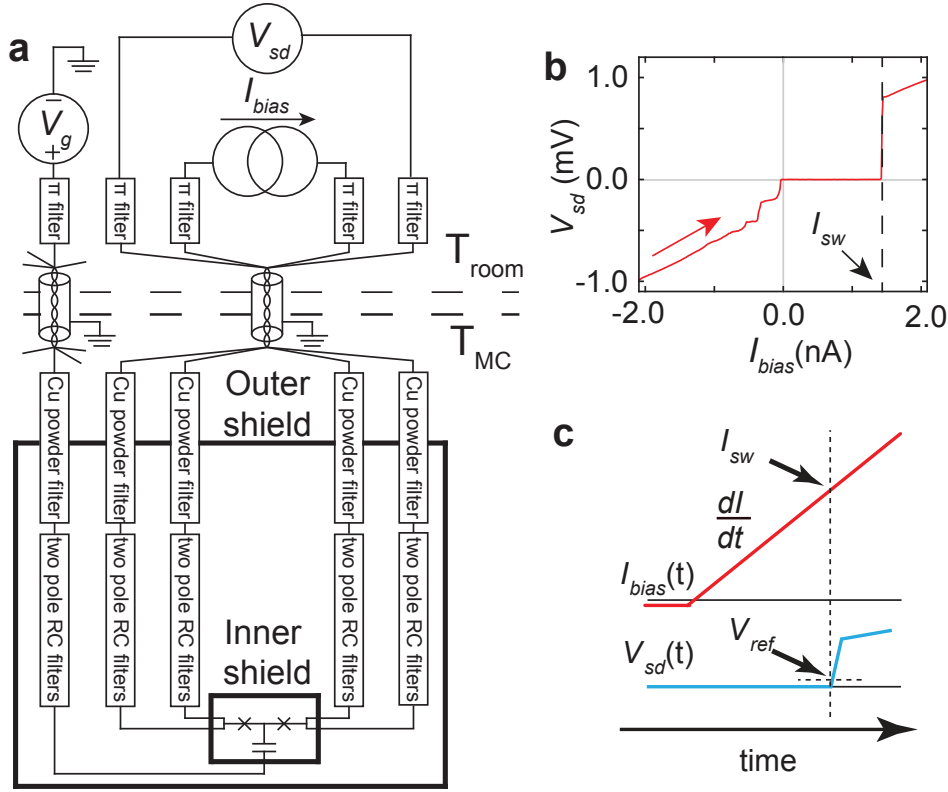


Figure 6.7: **Measurement electronic setup and typical waveforms.** (a) Schematics of the measurement. (b) Typical experimental $V - I$ trace exhibiting a well-defined switching current, I_{sw} . We observe a retrapping current $I_r \ll I_{sw}$ characteristic to unshunted Josephson junctions in the low temperature limit [177]. The additional features in the resistive state are consistent with Fiske steps [178]. (c) Current ramp (red) with a slope of dI/dt probing I_{sw} which is recorded when the measured V_{sd} (blue) reaches $V_{ref} \sim 10 \mu\text{V}$.

interaction between the AlO_x tunnel barrier and the NbTiN film. Indeed, it was shown earlier that the critical temperature of Nb films is particularly very sensitive to contamination with oxygen [180, 181]. However, the nitrized NbTiN compound is presumably less prone to oxidization [161].

6.9.3. EVALUATION OF THE PARITY LIFETIME

We checked the robustness of the extracted parity lifetime against changing the current ramp rate. Typical datasets are shown in Fig. 6.8, giving $\tau_p = 1.2 \text{ ms}$ and $\tau_p = 0.98 \text{ ms}$ for $dI/dt = 100 \text{ nA/s}$ (red) and $dI/dt = 400 \text{ nA/s}$ (black), respectively. We estimate the typical uncertainty to be 25%, concluding that τ_p does not depend on dI/dt which validates the analysis. However, we do not discuss here the intrinsic peak shapes of the bimodal switching current histogram. Since fast gate charge noise influences the measured distribution [88], we cannot distinguish between thermally activated [182] and macroscopic

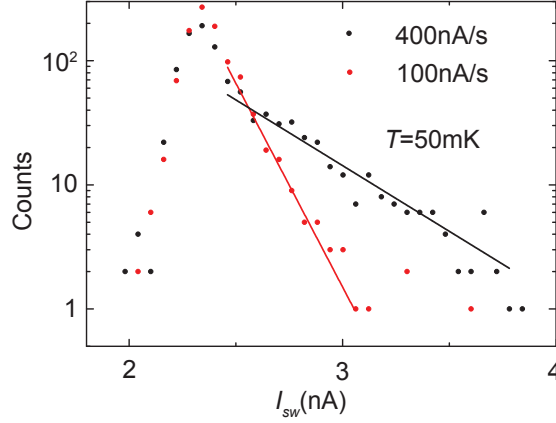


Figure 6.8: **Measured switching current histograms at different dI/dt ramp rates.** Colour legend: red: $dI/dt = 100$ nA/s, black: $dI/dt = 400$ nA/s. The data was acquired on a CPT similar to device N.

quantum tunneling behaviour [149, 177].

We now turn to the temperature dependence of τ_p . In order to get equation 6.1, we assume the following:

1. The superconducting gap of the island ($\Delta_{\text{NbTiN}} \gtrsim 1.3$ meV) is much higher than the effective thermal energy describing the quasiparticle population and the gap of the leads ($\Delta_{\text{Al}} \approx 200$ μ eV).
2. The density of states in the leads is BCS-type: $\rho_{\text{lead}}(E) = \rho_{\text{Al}} \times |E| / \sqrt{E^2 - \Delta_{\text{Al}}^2}$ for $|E| > \Delta_{\text{Al}}$ and zero otherwise.
3. There is a constant, finite subgap density of states ρ_{subgap} for energies below Δ_{NbTiN} in the island.
4. the energy dependence of the single electron tunnel probability is negligible over the energy range of $\sim \Delta_{\text{NbTiN}}$, meaning that the tunnel barrier is much higher than Δ_{NbTiN} .
5. The tunnel barriers are identical, each characterized by half the normal state resistance of the full device, R_N .

Considering only single electron tunneling and zero voltage bias across the tunnel barriers, following [165], we get the quasiparticle tunnel rate:

$$\tau_p^{-1} = \frac{2}{e^2 (R_N/2) \rho_{\text{Al}}} \frac{\rho_{\text{subgap}}}{\rho_{\text{NbTiN}}} \int_0^\infty \rho_{\text{lead}}(E) f(T, E) dE = \frac{2n_{\text{qp}}}{e^2 R_N \rho_{\text{Al}}} \frac{\rho_{\text{subgap}}}{\rho_{\text{NbTiN}}}. \quad (6.5)$$

Assigning an effective temperature to the quasiparticle population in the leads, we find:

$$n_{\text{qp}}(T) = 2 \int_0^\infty \rho_{\text{lead}}(E) f(T, E) dE = \rho_{\text{Al}} \sqrt{2\pi k_B T \Delta_{\text{Al}}} e^{-\frac{\Delta_{\text{Al}}}{k_B T}} \quad (6.6)$$

in the limit of $k_B T \ll \Delta_{\text{Al}}$. For temperatures exceeding 100 mK, we assume that the quasiparticle population is in thermal equilibrium, and therefore the lattice temperature is equivalent to the effective quasiparticle temperature: $\tau_p^{-1}(T) \propto \sqrt{T} \exp(-\Delta_{\text{Al}}/k_B T)$.

We verify this picture by fitting the observed parity lifetimes with Δ_{Al} as a free parameter, and find values ranging 170...210 μeV for different devices in good correspondence with the gap determined by voltage bias spectroscopy (Δ_{Al} in Table 6.2).

Notably, the ratio $\rho_{\text{subgap}}/\rho_{\text{NbTiN}}$ is the Dynes parameter [166] of the island material, characterized to be $\lesssim 10^{-3}$ based on measurements of highly resistive single junctions (Fig. 6.9). With this value and using $\rho_{\text{Al}} = 1.45 \times 10^{47} \text{ J}^{-1} \text{ m}^{-3}$ [165], we get $n_{\text{qp}} \sim 3 \mu\text{m}^{-3}$ for device N based on the observed parity lifetime of 9.5 ms in the low temperature limit. We now comment on the observed $\Delta^* \approx 20 \mu\text{eV}$ activation energy observed for devices S1 and S2. We estimate the maximal even-odd energy difference to be $\delta E \approx 20 \dots 30 \mu\text{eV}$ based on $E_J \approx E_c \approx 50 \mu\text{eV}$ [176] which is in range of the experimentally observed Δ^* . Similar, activated behaviour of the parity lifetime scaling as $\sim \exp(\delta E/k_B T)$ was reported earlier [169].

Providing another possible explanation, we note that a grain size of $\approx 50 \text{ nm}$ can lead to a level spacing of the order of 10 μeV which can influence single electron transport and hence τ_p if the grains are weakly coupled, i. e. for disordered superconducting films [183]. Disorder-induced fluctuations may also explain the broadening of the coherence peaks (Fig. 6.6c and Fig. 6.9) [184, 185].

In recent theoretical studies also disorder in the form of common nonmagnetic scatterers and pairing-potential impurities was used for the explanation of sub gap DOS and the existence of the mini gap behaviour [87, 186].

6.9.4. MEASUREMENT OF THE DYNES PARAMETER OF THE NbTiN ISLAND

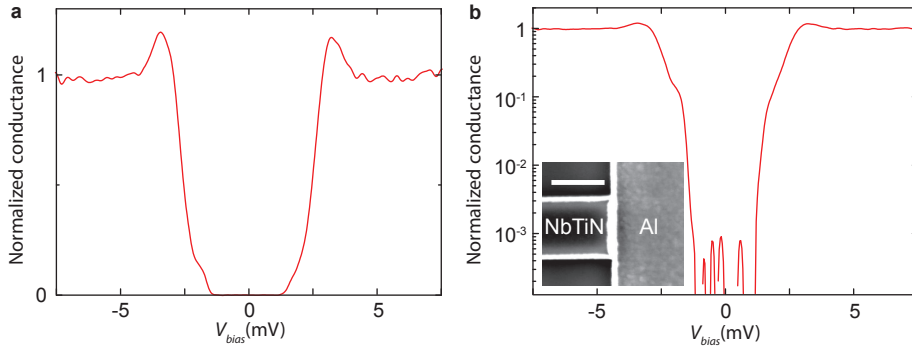


Figure 6.9: dI/dV characteristics of a single NbTiN/ AlO_x /Al tunnel junction with a normal state resistance of $R_N = 2.4 \text{ M}\Omega$ on the linear (a) and on the logarithmic scale (b), respectively. The measurement was performed at $T = 300 \text{ mK}$. The inset in (b) shows the scanning electron microscope image of the device. The scale bar denotes 500 nm.

We estimate the Dynes parameter in equation 6.1 by evaluating the subgap conductance of a single NbTiN/ AlO_x /Al tunnel junction, where higher order tunneling, i.e. Andreev reflection is strongly suppressed. Based on the measurement data in Fig. 6.9, we estimate the Dynes parameter to be $\lesssim 10^{-3}$.

We can get an independent estimate of the Dynes parameter by combining eq. 6.5 and eq. 6.6:

$$\tau_p^{-1} = \frac{2\sqrt{2\pi k_B T \Delta_{\text{Al}}}}{e^2 R_N} \frac{\rho_{\text{subgap}}}{\rho_{\text{NbTiN}}} e^{-\frac{\Delta_{\text{Al}}}{k_B T}}. \quad (6.7)$$

We fit the high temperature part of $\tau_p(T)$ shown in Fig. 6.2e with the functional form of $\tau_p(T) = \frac{A}{\sqrt{T}} e^{\frac{\Delta_{\text{Al}}}{k_B T}}$ where the prefactor A contains the Dynes parameter in addition to known parameters of the device. However, the uncertainty of the fitting makes an order of magnitude estimate possible, and we conclude $\frac{\rho_{\text{subgap}}}{\rho_{\text{NbTiN}}} \sim 10^{-2}$ for all devices which is consistent with the previous estimate.

6.9.5. SUPERCONDUCTING THIN FILM CHARACTERIZATION AND MAGNETIC FIELD DEPENDENCE

Next, we consider the properties of superconducting stripes with layer thickness d , and a width w to find the London penetration depth λ_L and the coherence length ξ . We characterize the upper critical field in the parallel ($B_{c\parallel}$) and perpendicular geometry ($B_{c\perp}$) based on the dI/dV traces of the tunnel junctions of the CPT. In addition, we measure the normal state resistivity of the films that gives an estimate for the mean free path, l_m [187].

First, we establish the length scales of the island material, NbTiN. We find films superconducting at $B_{\perp} = 9\text{ T}$ which leads to an upper limit of $\xi_{\text{NbTiN}} < 6\text{ nm}$ following [39]:

$$B_{c\perp} = \frac{\Phi_0}{2\pi\xi^2}. \quad (6.8)$$

The penetration depth can be estimated using the normal state resistivity of $\rho = 98\ \mu\Omega\text{cm}$ and the critical temperature of $T = 14.1\text{ K}$ using the following semi-empirical formula [179]:

$$\lambda_{\text{NbTiN}} = \sqrt{\frac{\rho[\mu\Omega\text{cm}]}{T_c[\text{K}]}} \times 105\text{ nm} \approx 280\text{ nm}. \quad (6.9)$$

Next we estimate length scales of the Al leads based on the electronic transport through the CPT. Typical thin Al films are type-II superconductors in the dirty limit ($l_m < \xi_0$) with a reduced coherence length of $\xi \approx 0.85\sqrt{\xi_0 l_m}$ and with a London penetration depth of $\lambda \approx \lambda_0\sqrt{\xi_0/l_m}$, where $\xi_0 \approx 1500\text{ nm}$ and $\lambda_0 \approx 16\text{ nm}$ are the bulk values [39]. For our films, we estimate $l_m \approx 8.5\text{ nm}$ based on the resistivity of $\rho = 4.3\ \mu\Omega\text{cm}$ [187]. From the stability diagram of the devices, we extract upper critical fields of $B_{c2,\perp} = 36.4 \pm 4\text{ mT}$ (Fig. 6.10e) and $B_{c2,\parallel} = 320 \pm 10\text{ mT}$ (Fig. 6.10) leading to a coherence length of $\xi_{\text{Al}} = 96\text{ nm}$ and $\lambda_{\text{Al}} = 230\text{ nm}$ which enables vortex formation in the aluminium leads in perpendicular magnetic field.

It is important to observe that $\xi_{\text{NbTiN}} \ll d \approx 100\text{ nm}$ enables vortex formation for an *in-plane* geometry in the NbTiN island. We find a characteristic suppression of τ_p at $B_{\parallel} = 70\text{ mT}$ for device S2 (orange dots in Fig. 6.10a) and at $B_{\parallel} = 110\text{ mT}$ for device S1 (cyan dots in Fig. 6.9a). Considering the effective cross-sectional areas (see Table 6.1 for dimensions), we find $\Phi \approx 1.5\Phi_0$ and $\Phi \approx 1.1\Phi_0$ for S2 and S1, respectively, which is in qualitative agreement with the threshold of a single vortex formation in a mesoscopic

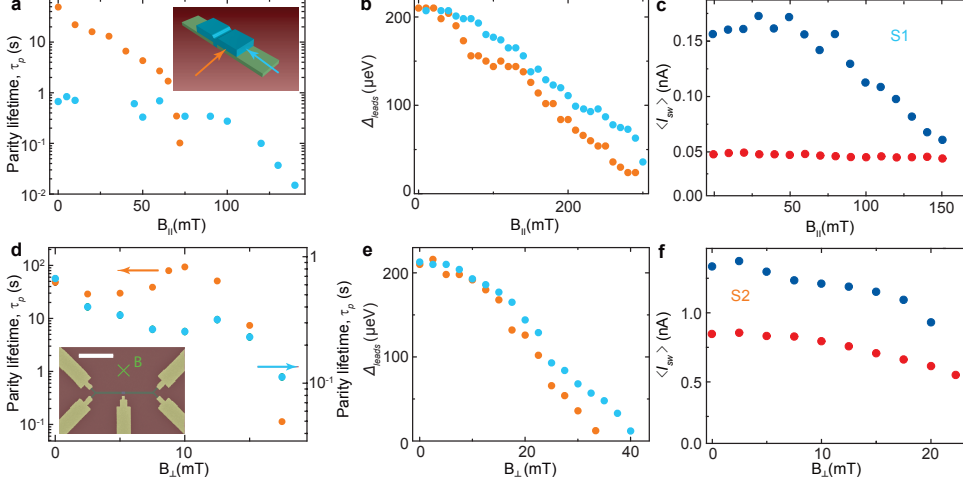


Figure 6.10: **Supplementary data on magnetic field dependence of the CPT.** (a), (b) Measured parity lifetime and superconducting gap of the leads as a function of in-plane magnetic field. The inset of panel (a) shows the relative orientation of the field for the two devices. (c) The expectation value of the switching current of the lower and upper branch, respectively in the *fast* limit as a function of the magnetic field for device S1. (d), (e) The parity lifetime and the superconducting gap as a function of the perpendicular magnetic field. The inset of panel (d) shows the electron microscopy image of the device. The scale bar denotes $5\mu\text{m}$. (f) The expectation value of the switching current of the lower and upper branch, respectively in the *fast* limit as a function of the magnetic field for device S2. All measurements were performed at $T = 12\text{ mK}$. Colour legend for panels (a), (b), (d) and (e): cyan: device S1; orange: device S2. Colour legend for panels (c) and (f): blue: upper branch, red: lower branch.

island [170, 188, 189]. We also note that $B_{c2,\parallel}$ of the leads (Fig. 6.10b) does not depend on the direction of B_{\parallel} , therefore the different evolution of τ_p can only be explained by the different alignment of B_{\parallel} with respect to the NbTiN islands.

We also note the decrease of switching currents of the upper branch on the same magnetic field scale (Fig. 6.10c). This is consistent with a Fraunhofer-like interference arising from the current path through the junctions being perpendicular to the applied magnetic field. A clear evaluation of the parity lifetime is possible as long as $\langle I_{sw,u} \rangle > \langle I_{sw,l} \rangle$, which in our geometry leads to the same magnetic field range as that of the vortex formation discussed above. However, we did not recover subsequent lobes in higher B_{\parallel} which is characteristic for Fraunhofer interference.

In a perpendicular geometry, the vortex phase is stable in a thin stripe above the magnetic field

$$B_{c1,\perp}(w) = \alpha \frac{\Phi_0}{w^2}, \quad (6.10)$$

where α is a model-dependent prefactor [171, 190, 191] of the order of unity. We reproducibly find the same non-monotonic behaviour of τ_p for devices S1 and S2 with the maximum at $B_{\perp} \approx 10 \dots 13\text{ mT}$ (Fig. 6.10d), which is in range of $B_{c1,\perp}(w)$ for $w = 200 \dots 250\text{ nm}$, the width of the Al leads near the island. However, both the superconducting gap of the leads (Fig. 6.10e) and the switching current values (Fig. 6.10f) decrease monotonously.

7

JOSEPHSON RADIATION AND SHOT NOISE OF A SEMICONDUCTOR NANOWIRE JUNCTION

**D. J. van Woerkom, A. Proutski, R. J. J. van Gulik,
T. Kriváchy, D. Car, S. R. Plissard, E. P. A. M. Bakkers,
L. P. Kouwenhoven, A. Geresdi**

We measured the Josephson radiation emitted by an InSb semiconductor nanowire junction utilizing photon assisted quasiparticle tunneling in an AC-coupled superconducting tunnel junction. We quantify the action of the local microwave environment by evaluating the frequency dependence of the inelastic Cooper-pair tunneling of the nanowire junction and find the zero frequency impedance $Z(0) = 492\Omega$ with a cutoff frequency of $f_0 = 33.1\text{ GHz}$. We extract a circuit coupling efficiency of $\eta \approx 0.1$ and a detector quantum efficiency approaching unity in the high frequency limit. In addition to the Josephson radiation, we identify a shot noise contribution with a Fano factor of $F = 0.88$ which is consistent with the presence of single electron states in the nanowire channel.

7.1. INTRODUCTION

The tunneling of Cooper pairs through a junction between two superconducting condensates gives rise to a dissipationless current [52] with a maximum amplitude of the critical current, I_c [174]. Upon applying a finite voltage bias V , the junction becomes an oscillating current source

$$I_s(t) = I_c \sin(2\pi f t), \quad (7.1)$$

with a frequency set by $hf = 2eV$ where h is the Planck constant and e is the electron charge.

The Josephson radiation, defined by Eq. 7.1 has mostly been investigated for superconducting tunnel junctions [192–194], metallic Cooper-pair transistors [91] and in circuit QED geometries [195]. Recently, it has also been proposed as a probe for topological superconductivity [68, 82, 86], which requires gateable semiconductor Josephson junctions [106].

In contrast to superconductor-insulator-superconductor (SIS) junctions, Josephson junctions with a semiconductor channel feature conductive modes of finite transmission probabilities [64, 196], leading to deviations from a sinusoidal current-phase relationship [197] and the universal ratio of the critical current and the normal state conductance [174]. Furthermore, soft-gap effects [198] have been shown to result in excess quasiparticle current for subgap bias voltages, limiting prospective applications such as topological circuits [9] and gate-controlled transmon qubits [199].

Here we investigate the high frequency radiation signatures of a voltage-biased semiconductor Josephson junction [106] by directly measuring the frequency-resolved spectral density for the first time. As a frequency-sensitive detector, we utilize a SIS junction, where the photon-assisted tunneling current [194] is determined by the spectral density of the coupled microwave radiation [92]. In addition to the detection of the monochromatic Josephson radiation, we demonstrate the presence of a broadband contribution, attributed to the shot noise of the nanowire junction [200].

7

7.2. DEVICE FABRICATION AND LAYOUT

Our setup follows the geometry of earlier experiments utilizing SIS junctions [194]. In contrast, our microwave radiation source is an InSb nanowire [128] Josephson junction (Fig. 7.1d) with a channel length of 100 nm. The junction leads (in brown in Fig. 7.1d) are created by removing the surface oxides by Ar ion milling and then *in-situ* sputtering of NbTiN superconducting alloy. Owing to the highly transparent contacts, this procedure enables induced superconductivity in the semiconductor channel [9, 199]. A predefined gate structure (purple regions in Fig. 7.1d) provides electrostatic control of the semiconductor channel and is covered by sputtering a 20 nm thick SiN_x dielectric layer.

The $I(V)$ characteristics of the two junctions are measured in a standard four point probe geometry via highly resistive Pt feedlines effectively decoupling the on-chip elements (Fig. 7.1) thermally anchored at 20 mK from the measurement setup. In order to gain access to a wider V_{NW} range, we use $R_1 = 1 \text{ k}\Omega$ in the nanowire biasing lines and $R_2 = 12 \text{ k}\Omega$ in the voltage measurement leads (see Fig. 7.1b).

The detector SIS split junction is shown in Fig. 7.1f and is fabricated using standard shadow evaporation techniques [201]. The typical normal state resistance was measured

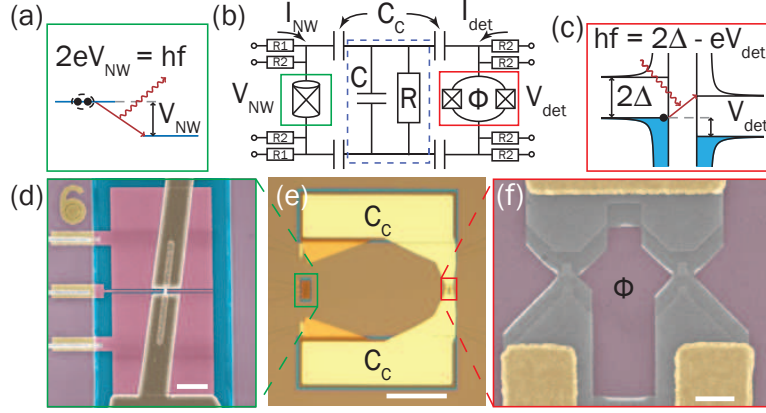


Figure 7.1: (a) Photon emission due to the inelastic Cooper-pair tunneling between condensate levels shifted by the bias voltage, V_{NW} . (b) The microwave equivalent circuit of the measurement setup, where R and C in the blue dashed box represent the microwave losses and stray capacitance, yielding a $2\pi f_0 = (RC)^{-1}$ upper cutoff frequency. The $C_c \gg C$ coupling capacitors have a negligible effect above a frequency of $2\pi f_c = (RC_c)^{-1}$ with $f_c \ll f_0$, but allow for the application of independent DC bias voltages V_{NW} and V_{det} . The $I_{NW}(V_{NW})$ and $I_{det}(V_{det})$ characteristics are measured through the Pt feedline resistors, depicted by R_1 and R_2 . (c) Photon-assisted quasiparticle tunneling for a detector voltage bias V_{det} and an incoming photon energy of hf . (d) False colored scanning electron micrograph of the nanowire Josephson junction contacted with NbTiN after being placed on three electrostatic gates. (e) Bright field optical image of the coupling circuitry before the NbTiN deposition step with the nanowire junction (green box) and the detector junction (red box). (f) False colored micrograph of the detector split junction with an applied magnetic flux Φ . The scale bars depict $1 \mu\text{m}$ (d), $20 \mu\text{m}$ (e) and $0.5 \mu\text{m}$ (f), respectively.

to be $20 \text{ k}\Omega$ for a nominal junction area of $100 \times 100 \text{ nm}^2$. The bottom and top Al layer thicknesses are 9 and 11 nm, respectively. The split junction geometry enables the flux control of the total Josephson coupling of the detector. To measure the quasiparticle tunneling response, we set $\Phi = \Phi_0/2$, with $\Phi_0 = h/2e$ the flux quantum, to minimize the Josephson coupling. Finally, we utilize two parallel plate capacitors of $C_c \approx 400 \text{ fF}$ with sputtered SiN_x dielectric which couple the nanowire junction to the detector in the frequencies of interest (Fig. 7.1e), yet enable independent voltage biasing and current measurements in the DC domain.

7.3. THEORY

The mesoscopic noise source under consideration is characterized by its current noise density, $S_I(f)$ [200], which results in the voltage noise density $S_V(f) = S_I(f)|Z(f)|^2$, where $Z(f)$ is the complex frequency-dependent impedance of the coupling circuit. In Fig. 7.1b, we depict a parallel RC network resulting in $Z(f) = R(1 - jf/f_0)/(1 + f^2/f_0^2)$ with $2\pi f_0 = (RC)^{-1}$ in the limit of negligible detector admittance, $r_{det}^{-1} = dI_{det}/dV_{det} \ll R^{-1}$.

We deduce the voltage noise density $S_V(f)$ starting from the equation for the photon-assisted current in the SIS detector [93, 194]:

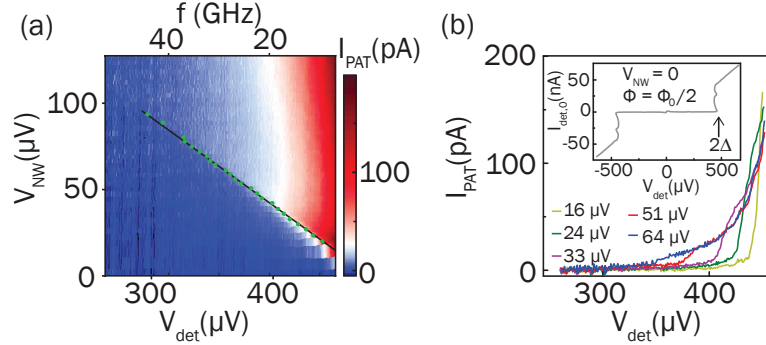


Figure 7.2: (a) Measured photon-assisted quasiparticle current I_{PAT} as a function of the detector bias voltage V_{det} and nanowire bias voltage V_{NW} . The green dots denote the extracted frequency on the upper axis for a given V_{NW} . The solid black line is the best linear fit with $f/V_{\text{NW}} = 475 \text{ MHz}/\mu\text{V}$. (b) Horizontal line traces at different V_{NW} values. The inset shows the full $I_{\text{det},0}(V_{\text{det}})$ characteristics of the detector when the Josephson radiation is absent. Note that the applied flux $\Phi = \Phi_0/2$ through the split junction results in a suppressed supercurrent branch. The arrow depicts $2\Delta/e = 480 \mu\text{V}$, the onset of the quasiparticle current.

$$I_{\text{PAT}}(V_{\text{det}}) = \int_0^\infty S_V(f) \left(\frac{e}{hf} \right)^2 I_{QP,0} \left(V_{\text{det}} + \frac{hf}{e} \right) df, \quad (7.2)$$

which describes the DC current contribution at an applied voltage $V_{\text{det}} < 2\Delta$. Crucially, this equation holds if the quasiparticle current in the absence of radiation has a well-defined onset, $I_{QP,0}(V_{\text{det}} < 2\Delta) = 0$, typically referred to as the quantum limit of the detector [93] and in the limit of weak coupling, where multiphoton processes do not contribute [92]. Note that Eq. 7.2 can be handled as a convolution of $S_V(f)/(hf)^2$ and $I_{QP,0}(V_{\text{det}})$.

In the presence of a monochromatic radiation, where $S_V(f) \sim \delta(f - \mathcal{F})$, Eq. 7.2 describes the shift of the initial $I_{QP,0}(V_{\text{det}})$ quasiparticle current by $\delta V_{\text{det}} = h\mathcal{F}/e$. This is the case of the Josephson radiation [194] with $S_I(f) = \frac{I_c^2}{4} \delta(f - \mathcal{F})$, where $h\mathcal{F} = 2eV_{\text{NW}}$ with V_{NW} the applied voltage bias on the emitter junction with a critical current I_c . On the other hand, quasiparticle shot noise is characterized by a frequency-independent contribution of $S_I = 2eIF$ with I being the applied current and F the Fano factor which is characteristic to the mesoscopic details of the junction [200].

The impedance $Z(f)$ of the environment results in a finite power dissipation $I_c^2 \text{Re}(Z(f))/2$ which gives rise to a DC current due to inelastic Cooper-pair tunneling (ICPT) processes in the NW Josephson junction (see Fig. 7.1a) [193]. This effect has been first addressed to calculate the shape of the supercurrent branch in overdamped SIS junctions and purely resistive environments [60]. Later, the theory was adapted for high channel transmissions [202]. It also has been shown that for an arbitrary $Z(f) \ll h/4e^2 \approx 6.5 \text{ k}\Omega$, the ICPT contribution can be evaluated as [193]

$$I_{\text{ICPT}} = \frac{I_c^2 \text{Re}(Z(f))}{2V_{\text{NW}}}, \quad (7.3)$$

with the critical current I_c and an applied voltage V_{NW} . Here, the junction effectively

probes the impedance $Z(f)$ at a frequency $f = 2eV_{\text{NW}}/h$.

Importantly, the two independently measured current values $I_{\text{PAT}}(V_{\text{det}})$ and $I_{\text{ICPT}}(V_{\text{NW}})$ depend on the same microwave environment, characterized by $Z(f)$. Thus, by evaluating both, we find $Z(f)$ and the Josephson coupling of the nanowire junction at the same time.

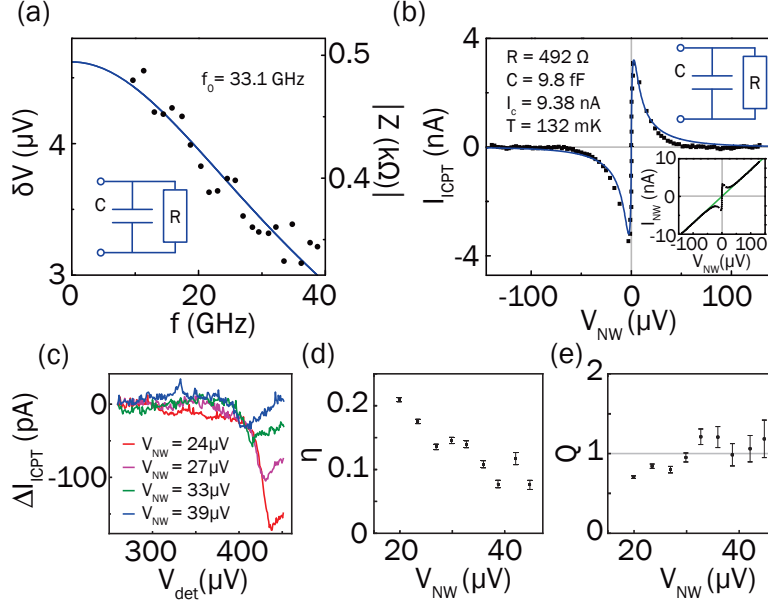


Figure 7.3: (a) The measured $\delta V(f) = I_c |Z(f)|$ voltage fluctuation on the detector junction. The solid line depicts the fitted cutoff with $2\pi f_0 = (RC)^{-1} = 33.1$ GHz. Right vertical axis shows the impedance $|Z(f)|$, see text. (b) Experimental $I_{\text{ICPT}}(V_{\text{NW}})$ trace of the nanowire junction exhibiting a current peak due to the supercurrent branch. The linear contribution with a resistance $R_{\text{NW}} = 14.03$ k Ω (green solid line, see inset for raw $I_{\text{NW}}(V_{\text{NW}})$ trace) is subtracted. The blue solid line depicts the fitted curve with $I_c = 9.38$ nA critical current and a noise temperature $T = 132$ mK. (c) Variation of the nanowire junction current ΔI_{ICPT} as a function of the detector voltage V_{det} . The extracted circuit efficiency η (d) and the detector quantum efficiency Q (e) as a function of V_{NW} , see text.

7.4. DISCUSSION

We demonstrate the detection of the Josephson radiation in Fig. 7.2. In panel (a) we plot the PAT current contribution as a function of the DC bias voltages V_{det} and V_{NW} . In Fig. 7.2b, we show line traces $I_{\text{PAT}}(V_{\text{det}})$ exhibiting well-defined onset values corresponding to a monochromatic Josephson radiation tuned by V_{NW} . Thus, we can deconvolute Eq. 7.2 to find the radiation frequency shown as green dots in Fig. 7.2a. We note however, that the measured $I_{\text{det},0}$ plotted in the inset of Fig. 7.2b is distorted due to self-heating effects in the SIS detector. Thus, we used a monotonous $I_{QF0}(V_{\text{det}})$ centered around the same quasiparticle onset. For the details of the deconvolution algorithm, and raw data files, see [203].

By evaluating the relation between V_{NW} and the radiation frequency (black line in

Fig. 7.2a), we find a ratio of $475 \pm 4.2 \frac{\text{MHz}}{\mu\text{V}}$ which is in reasonable agreement with $\frac{2e}{h} \sim 484 \frac{\text{MHz}}{\mu\text{V}}$ expected for the case of Cooper-pair tunneling [204]. The intersect for $f = 0$ is set by the quasiparticle current onset to be $2\Delta/e = 480 \mu\text{V}$ (see inset of Fig. 7.2b).

It is important to notice that the PAT current decreases with increasing frequency (Fig. 7.2b). By correcting for the $\sim f^{-2}$ dependence in Eq. 7.2, we find that the fluctuation amplitude $\delta V = I_c |Z(f)| \sim \sqrt{S_V}$ exhibits a characteristic cutoff frequency (Fig. 7.3a), even though the current oscillation amplitude of the Josephson junction is constant, see Eq. 7.1. Thus, we can attribute this cutoff to the coupling circuit impedance, $Z(f)$. We find a good agreement between the experimental data and the impedance of a single-pole RC network (solid blue line in Fig. 7.3a) yielding to a cutoff frequency $f_0 = (2\pi RC)^{-1} = 33.1 \text{ GHz}$.

Next, we turn to the measured $I(V)$ trace of the nanowire Josephson junction. The inset of Fig. 7.3b shows the raw curve, which exhibits a supercurrent peak around zero V_{NW} and a linear branch. The latter fits to a linear slope of $R_{\text{NW}} = 14.03 \text{ k}\Omega$ (solid green line). We then extract the $I_{\text{ICPT}}(V_{\text{NW}})$ component by removing this slope (black dots in Fig. 7.3b). In order to find the critical current and the noise temperature of the junction, we use the finite temperature solution of Ivanchenko and Zil'bermann [60] with substituting $|Z(f)|$ as the impedance of the environment [203]. With this addition, we find an excellent agreement with the experimental data (blue solid line in Fig. 7.3b), with $I_c = 9.38 \text{ nA}$ critical current. Notably, with the now determined value of I_c , we can extract $R = 492 \Omega$ and $C = 9.8 \text{ fF}$ fully characterizing the microwave environment of the junctions. In addition, we find $I_c R_{\text{NW}} = 132 \mu\text{V}$, which is close to the induced gap values measured in similar devices [9]. We also extract an effective noise temperature $T = 132 \text{ mK}$, which is higher than the substrate temperature of 20 mK , similarly to earlier experiments [202].

Thus far, we evaluated $I_{\text{ICPT}}(V_{\text{NW}})$ at $V_{\text{det}} \approx 50 \mu\text{V} \ll 2\Delta/e = 480 \mu\text{V}$, where $I_{\text{PAT}} \approx 0$, thus the detector load is negligible. However, depending on V_{NW} , we find a negative $\Delta I_{\text{ICPT}}(V_{\text{det}})$, i.e. a reduction of the emitter current, when the detector threshold is on resonance with the emitted frequency (Fig. 7.3c). We can understand this effect by the reduction of $Z(f)$ in Eq. 7.3 in the presence of a finite r_{det} in parallel with R . In first order, we find $\Delta I_{\text{ICPT}}/I_{\text{ICPT}} = -\text{Re}(Z(f))/r_{\text{det}} \approx -R/r_{\text{det}}$. By using the measured DC current values, we evaluate the efficiency of the coupling circuit to be the ratio of the absorbed and emitted power $\eta = P_{\text{det}}/P_{\text{emi}} = 2I_{\text{PAT}}/I_{\text{ICPT}}$ (Fig. 7.3d). We find typical values spanning $0.1 - 0.2$, an order of magnitude improvement over earlier reported values [91, 194]. The decrease of η with increasing f is consistent with the low-pass nature of the coupling circuit. We also calculate the detector quantum efficiency $Q = P_{\text{det}}/\Delta P_{\text{emi}} = 2I_{\text{PAT}}/\Delta I_{\text{ICPT}}$ (Fig. 7.3e) and find values scattering around unity. This value directly measures the ratio of electron and photon rate passing the detector junction, thus confirms that it is in the quantum limit [93].

We now turn to the shot noise contribution to I_{PAT} . We evaluate the measured data by including both $S_I \sim \delta(f - \mathcal{F})$ of the Josephson radiation, and $S_I = 2eIF$ of the shot noise with F being the Fano factor [200] in order to calculate I_{PAT} from Eq. 7.2. With setting $F = 0$, i.e. in the absence of shot noise, we find that the blue curves in Fig. 7.4 can fit the steps in I_{PAT} , however fail to describe the smooth background of the dataset. A much better agreement is reached by using a single global fit parameter $F = 0.88 \pm 0.11$ (red

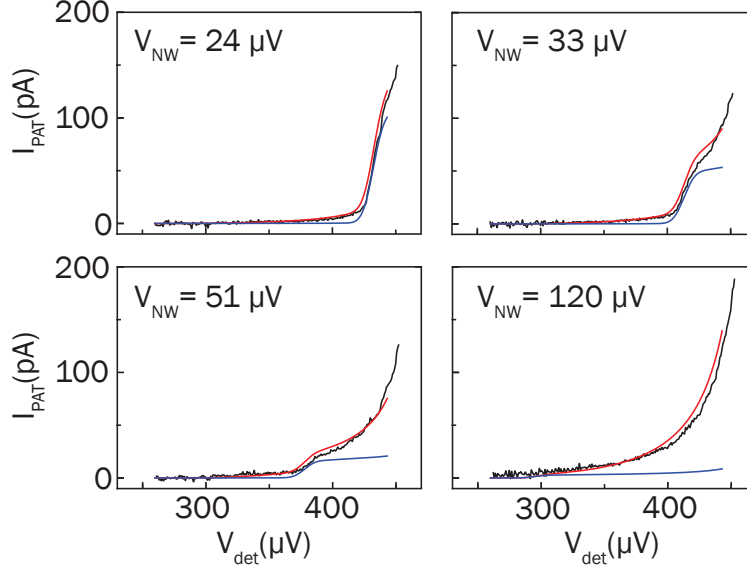


Figure 7.4: Detector $I_{\text{PAT}}(V_{\text{det}})$ line traces at various V_{NW} bias voltage values. The experimental data is shown by black lines. The blue lines depict the contribution of the Josephson radiation using the circuit parameters defined earlier. The red lines include the shot noise contribution with the sole global fit parameter $F = 0.88 \pm 0.11$, see text.

curves in Fig. 7.4. We note that the channel length of 100 nm is similar to the mean free path found earlier in the same nanowires [205]. Thus the extracted Fano factor, yielding to sub-Poissonian shot noise, is consistent with the presence of several transport modes of low transmission τ , where $F = 1 - \tau$ assuming identical quasiballistic channels. In contrast, $F = 1/3$ characteristic of diffusive normal transport [206] does not fit our data.

Furthermore, the extracted Fano factor does not agree with the shot noise signature of multiple Andreev reflections, where $F > 1$ values are anticipated due to the transport of multiple charge quanta both in the ballistic [207] and in the diffusive [208] limit. Our experiment thus provides insight to the nature of the charge transport at finite voltage bias in the nanowire Josephson junction and concludes that the finite subgap current can be attributed to single electron states inside the induced superconducting gap.

7.5. CONCLUSIONS

In conclusion, we built and characterized an on-chip microwave coupling circuit to measure the microwave radiation spectrum of an InSb nanowire junction with NbTiN bulk superconducting leads. Our results clearly demonstrate the possibility of measuring the frequency of the Josephson radiation in a wide frequency range, opening new avenues in investigating the 4π -periodic Josephson effect [7] in the context of topological superconductivity [8]. Based on the Fano factor, the shot noise contribution to the measured signal demonstrates the presence of subgap quasiparticle states and excludes multiple Andreev reflection as the source of subgap current of the nanowire Josephson junction.

8

FRACTIONAL JOSEPHSON RADIATION AT FINITE MAGNETIC FIELD

D. J. van Woerkom

The presence of Majorana zero modes (MZM) in Josephson junctions changes the properties of the junction radically. Due to the presence of MZM, Majorana bound states (MBS) are formed, which have a doubled phase periodicity (4π) compared to trivial Andreev bound states (ABS), which are 2π -periodic. Measuring a 4π signal in the MZM limit (semiconducting nanowire with strong spin-orbit coupling, in the proximity of a superconductor at finite magnetic field), is a strong signature of the presence of MZM. In this chapter, we measure radiation emitted from an InAs nanowire with an epitaxially grown aluminum shell with an on-chip detection circuit. The detected radiation shows a signature of 4π periodicity, namely emission at half of the Josephson frequency. We investigate this radiation as a function of external applied magnetic field and local electrostatic gates. The half-Josephson frequency is observed in a magnetic field range of ~ 100 – 300 mT, independent of the gate voltages, indicating that the measured signature is robust. This signature in our nanowire Josephson junction hints at the presence of MZM.

This work is being performed together with D. Laroche, D. Bouman, A. Proutski, R. J. J. van Gulik, M. P. Nowak, D. I. Pikulin, P. Krogstrup, J. Nygård, C. M. Marcus, L. P. Kouwenhoven, A. Geresdi

In this chapter, we report the status of a project that was not finished at the time of writing. As of now¹, we are still measuring a third device which shows similar effects to the first and second devices. Only data from the first device is used in this chapter. We are trying to make improvements in the analysis, meaning that this is also a work in progress. The improved analysis which we (are trying to) develop is not expected to change the observations shown in this chapter, and would only be a better way of presenting the data. A possible improved depiction of the data is shown in Figure F.5.

We start by explaining our motivation and giving an brief introduction in Section 8.1. Although the circuit we use in this chapter is very similar to the one used in the previous chapter, we discuss it briefly in Section 8.2, and the improvements made to it in Section 8.3. We start the experiment by showing (in Section 8.4) that at zero magnetic field we measure the Josephson radiation we expect for a trivial Josephson junction. By applying a sufficiently large magnetic field along the nanowire, we observe instead radiation at half the Josephson frequency, as reported in Section 8.5. We use electrostatic gates underneath the nanowire (weak link) and underneath the superconducting banks to further investigate this effect in Section 8.6. In Section 8.7, we comment on, and discuss the evolution of, the detected radiation as a function of phase velocity. Finally, we present preliminary conclusions and discussion in Section 8.8.

8.1. INTRODUCTION

As was explained in Chapters 2 and 3, MZM come with three distinct signatures: a zero bias conductance peak; non-abelian exchange statistics; and a 4π -periodic current (energy) phase relation in a Josephson junction. This last signature is a strong indication of the presence MZM when other effects, like Landau-Zener (LZ) tunneling, can be excluded. Demonstrating non-abelian exchange statistics is challenging because it requires precise control of multiple (more than 4) MZM[17, 35, 209].

Measuring the 4π -periodic current (energy) phase relation relies on the overlap of two MZM to form an MBS. Detection is expected to be challenging because the 4π signature is only visible at specific experimental timescales, as discussed in Section 3.4.4. Ref. [77] uses a similar system, which is expected to have MZM and should show the 4π signature. However, the signature is not reported because the measurement timescale is on the order of minutes, which is probably too slow to measure the 4π -periodic current phase relation.

In this chapter, we use a similar experimental setup to the one in Chapter 7, on which we have made improvements to make the experiment more compatible with magnetic field. These improvements are discussed more extensively in the next two sections.

8.2. MEASUREMENT TECHNIQUE

We use an on-chip detection technique, with an SIS Josephson junction as the detector. The junction has a normal-state resistance of $34\text{k}\Omega$. Under irradiation from a microwave radiation source, the current-voltage characterization of the SIS detector is distorted by an extra current for $V_{\text{det}} < 2\Delta$. This extra current is called the photon-assisted-tunneling (PAT) current, as derived in Section 3.6.

¹End of October 2016

The nanowire Josephson junction is used as a single-frequency microwave source via the AC Josephson effect. The AC Josephson effect gives current oscillations when the Josephson junction is voltage biased. The relation between the nanowire voltage and the detected frequency (f) is a constant $2e/h$ and determines the AC quantum voltage standard[210]. We do not measure this relation directly, because we do not convert the detected signal to frequency directly as we did in the previous chapter. Instead, we measure the nanowire and detector voltage bias and determine from the measured lock-in signal (see next section) the relation between the two voltages. This relation is a dimensionless slope, and is 2 (1) in the presence of 2π (4π) periodic Andreev (Majorana) bound states in a nanowire Josephson junction. Electrons (single charges) can tunnel in the presence of the MBS, instead of Cooper pairs (double charges) in the presence of ABS.

As noted, the voltage standard is the relation between the nanowire voltage and the emitted frequency. In the used detection scheme we are not able to measure this relation very precisely. This is because limitations of the circuit and noise in the measured current and voltage limit our accuracy.

8.3. TECHNICAL IMPROVEMENTS

Compared to the experiments described in the previous chapter, three major improvements have been made to improve magnetic field compatibility.

- First, the nanowires of these devices have been replaced by InAs nanowires with epitaxially-grown Al shells[20]. These nanowires have shown hard induced gap due to their clean interface with the superconductor[14, 21]. Also, in our measurements we see clear regions of low subgap current, two examples of which are shown in Figure 8.2c and d. The lack of subgap current in the nanowire, which generates white noise radiation, previously limited the experimental range to $V_{NW} \leq 40\mu\text{eV}$.

The nanowire is shown in Figure 8.1d, without the NbTiN contacts which are deposited in a later fabrication step. The nanowire is covered over its entire length with Al on two facets, as described in [20]. A wet-etch² is used to etch 200nm in the middle of the nanowire to form a Josephson junction weak link[14, 22, 64]. The weak link is aligned with the middle gate up to a precision of 20nm.

- The second improvement we have made is to change our measurement technique. In Chapter 7, the nanowire was voltage biased and the current was measured in the detector. The density of states (DOS) in the detector is distorted by Josephson radiation emission from the nanowire Josephson junction[92] and an extra current flow, I_{PAT} , is measured. An expression for I_{PAT} in the SIS detector is derived in Section 3.6. The nanowire and the PAT current is shown in Figure 8.3a-b for the device used in this chapter. To improve the sensitivity, we added a small AC voltage (between 15–30Hz), as in ref. [91]. The extra AC voltage on the nanowire Josephson junction modulates the Josephson frequency. This also modulates the onset of the PAT current, which is detected by lock-in in the SIS detector. The raw data is directly compared in Figure 8.3a-c, which shows the DC voltage and the lock-in

²Transene D etch at 50°C for 12 seconds

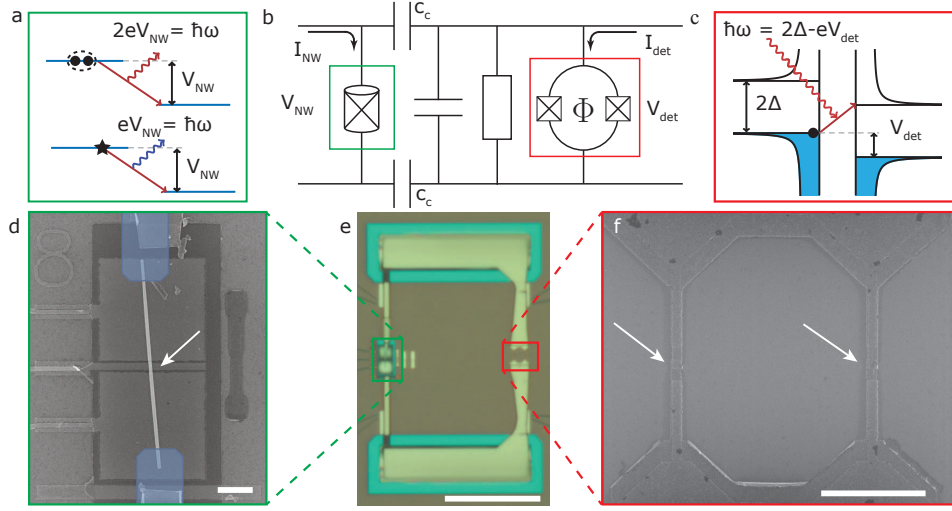


Figure 8.1: **a** Schematic view of inelastic Cooper-pair (electron) tunneling, generating photons with an energy of $2eV_{\text{NW}} = \hbar\omega$ ($eV_{\text{NW}} = \hbar\omega$). **b** Circuit equivalent to the device used for the experiment. On the left, the nanowire junction (green box) is connected to a voltage source to apply a voltage bias. The voltage drop over the nanowire is V_{NW} . The nanowire junction is coupled with capacitors $c_c \sim 400\text{fF}$ to an SIS detector junction (red box). The SIS detector can be (DC) voltage-biased separately and the resulting current can be measured. **c** Schematic view of the PAT detection mechanism in the SIS detector. Photons can be absorbed by a quasiparticle, resulting in a current flowing within the subgap of the SIS detector. **d** SEM image of a nanowire, deposited deterministically on top of the gates, which are covered with 30nm sputtered SiN_x . The white arrow points to the weak link, which can be tuned by the gate denoted by V_{mid} . The other gates are underneath the part of the nanowire still covered with aluminium. These gates are called the upper and lower side gates. In a later fabrication step, in the blue region, an argon etch and NbTiN deposition is performed. The scale bar denotes $1\mu\text{m}$. **e** Optical image of the complete device with the nanowire Josephson junction (green box) and SIS detector (red box) highlighted. The 10–100 μm -long Pt resistors are only partly visible. The scale bar denotes $20\mu\text{m}$. **f** SEM image of the SIS detector, which is a split junction making it possible to flux-tune the Josephson coupling. The junctions are indicated by the white arrows and are positioned in the middle of thin strips to avoid vortex creation near the junction at low magnetic fields. The scale bar denotes $1\mu\text{m}$.

response. The lock-in signal is maximal at the onset of the PAT current, which is a measure of the dominant emitter frequency, as explained in Section 3.6. To extract the slope of the detected signal, we found the maximum of the detected lock-in signal for each measured nanowire voltage. First, we interpolated the (typically 90–100) data points to create (100) equidistant data points, shown as the black line in the inset to Figure 8.3f. Then we smoothed the data with a Gaussian filter with a window of three data points. The effect of the smoothing can be seen in the red line (inset to Figure 8.3f). We then found the maximum of the lock-in signal and the full width at half maximum (FWHM) for all the line traces with fixed nanowire voltage. For all data shown in this chapter, we overlaid the raw data with the extracted maximum and FWHM to check if the peakfinder algorithm had been successful; an example is shown in Figure 8.3e. We fitted a line to the extracted peak positions

(using the FWHM as error, instrumental fit) and extracted a slope of 1.91 ± 0.03^3 .

- The last noticeable improvement was in the design of the SIS detector, which is a split junction (SQUID). In Figure 7.1f, an SEM image of the previous design is shown. This design allows vortex creation (very) close to the Josephson junction, locally reducing the superconducting gap Δ to zero energy. This reduction of the gap changes the local DOS and smooths the gap onset of the quasiparticle current, and is likely the reason for the low magnetic field compatibility. In the new design, shown in Figure 8.1f, the junction is connected to the coupling circuit by superconducting lines with a width of $\sim 100\text{nm}$. These thin lines make it energetically unfavorable to have vortex creation close to the Josephson junction, as described in Section 6.9.5 and in ref. [172]. Edge currents (Meissner currents) still decrease the DOS locally and soften the quasiparticle onset but this effect is less visible in the quasiparticle current, as shown in Figure 8.2b. Due to the thin strips, the heating of the quasiparticle onset (Figure 8.2a) is more pronounced, possibly due to the lack of vortices to evacuate the hot quasiparticles.

8.4. RADIATION AT ZERO MAGNETIC FIELD

We first characterize the device by investigating the radiation emitted at zero magnetic field. We obtain a slope of 2.0 ± 0.2^4 with this detection method for at least 8 different devices (6 nanowire junctions, including the sample from the previous section, and 2 SIS junctions) as the radiation source, at zero magnetic field. More importantly, we have never seen any sign of (half or double Josephson frequency) radiation, other than Josephson radiation from the inelastic Cooper-pair tunneling current (ICPT) in the emitter junction.

For the scan explored in Figure 8.3, we applied a gate voltage of 0.87V to the middle gate. We observed an asymmetric IV trace in the nanowire, shown in the inset to Figure 8.4a. The positive bias has a normal state resistance $R_{N,+} = 38\text{k}\Omega$, and the negative bias $R_{N,-} = 27\text{k}\Omega$. We do not quantitatively understand the exact underlying mechanism behind the asymmetry, but the mesoscopic nature of the sample can give rise to an asymmetric gate-induced barrier. The barrier asymmetry induces a transmission asymmetry between transport from left to right and vice versa. For typical measurements we applied a negative voltage, and as such we used $R_{N,-}$ to calculate the total Landauer transmission. For the used gate configuration, the Landauer transmission is $\sum_{i=1}^{N_{\text{CH}}} T_i = 0.48$. Unfortunately, the $R_{N,-}$ was insufficient to determine the number of channels in our nanowire. In addition, we currently try to use multiple Andreev reflection to determine the number of channels and their transmission. We also do shot noise detection to determine the Fano factor, as we did in the previous chapter. The Fano factor in combination with the normal state resistance can indicate if we are in the single- or many-channel-dominated regime.

³The slope is 1.97 ± 0.02 when the FWHM is not taken into account. The uncertainties are from the fit. Current and voltage uncertainties are not considered.

⁴Our data analysis seems to underestimate the slope by roughly 5%, as can also be seen in the orange data points in Figure 8.4d.

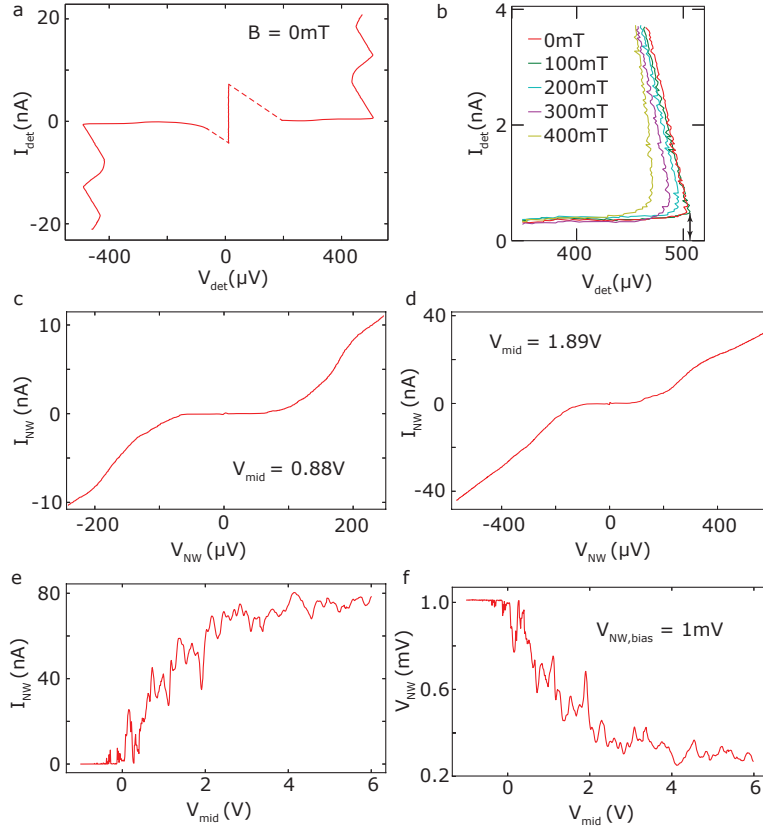


Figure 8.2: **a** Zero magnetic field IV trace of the SIS split Josephson junction. The quasiparticle onset shows backbending, which we consider to be an indication of excessive quasiparticle heating. The gap edge of this junction is used for PAT detection. The dashed regions show bias instabilities. **b** Zoomed-in view of the gap edge of the SIS split junction used for detection of high-frequency radiation for different applied magnetic fields. Low measurement gain was used, which is the reason for the large noise. **c, d** IV traces of the InAs nanowire Josephson junction with Al shell at two different mid gate voltages. A small supercurrent ($I_{SW} \sim 100 - 500 \text{ pA}$) can be seen in both scans at zero voltage. **e** Pinch-off curve, as a function of the mid gate, when the nanowire Josephson junction is voltage-biased with 1mV. The voltage was measured over the junction at the same time, and the result is shown in **f**. The fluctuations in current (and voltage) are reproducible and are attributed to mesoscopic conductance fluctuations. Due to the complex design and the importance of the gate capacitance to the nanowire, it is not possible to reliably extract the nanowire mobility. Note: a side gate voltage of 2.5V was applied to both side gates in **c-f**.

8

LZ tunneling can change the emission frequency of nanowire Josephson junctions by half, as discussed in Section 3.3.4. This was not observed for any gate configuration in any of the devices that were measured at zero magnetic field. This is supported by the low LZ probability, which is on the order of $p = e^{-\frac{(1-T)\Delta}{eV}} \sim 0.2$ if we assume one channel, a typical induced gap of $120 \mu\text{eV}$ [64] and a large voltage bias of $40 \mu\text{eV}$.

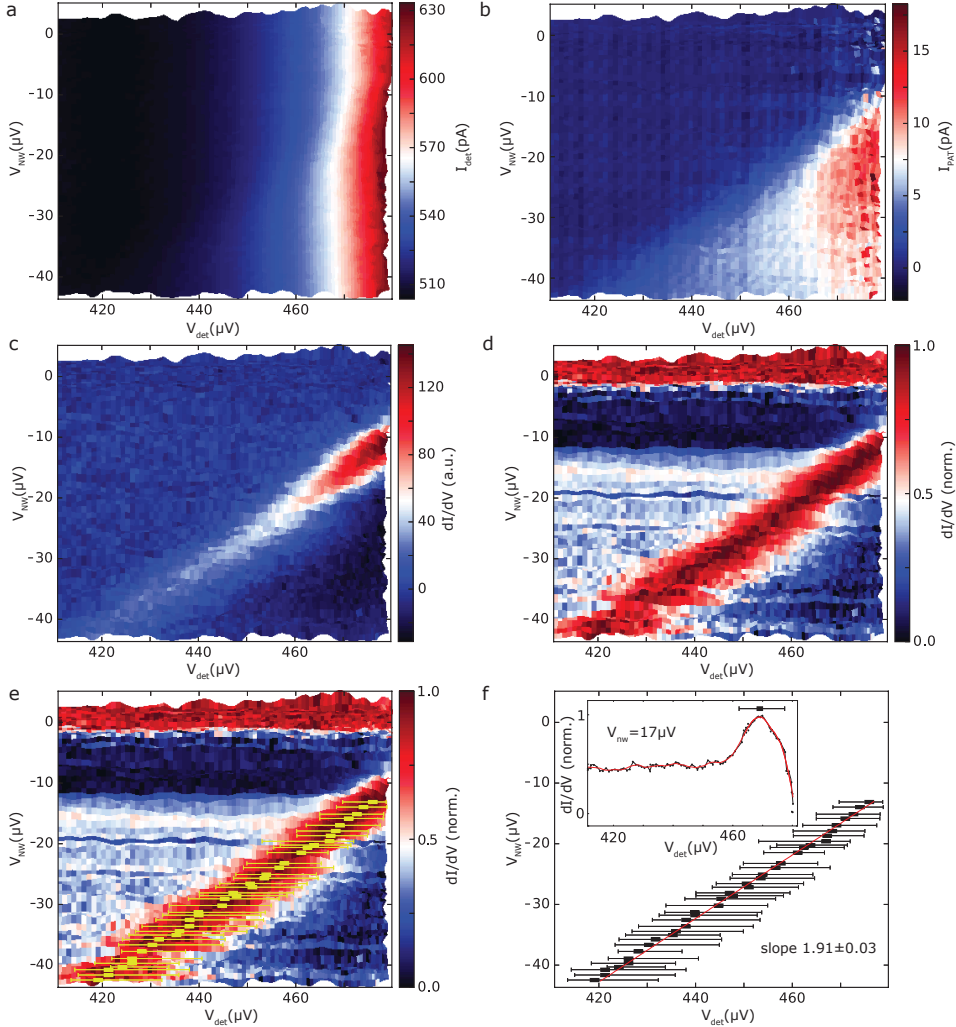


Figure 8.3: Different representations of the signal detected in the SIS split junction detector. **a** Direct subgap current near the gap edge of the SIS detector with irradiation from the nanowire Josephson junction. **b** The PAT current obtained by subtracting the IV trace at $V_{NW} = 0V$. The PAT current onset occurs at lower detector voltages, V_{det} , for more negative nanowire voltages, V_{NW} . The background interference is a result of the lock-in modulation. **c** The detected lock-in signal in the SIS detector, when a voltage oscillation (lock-in excitation) is added to the nanowire voltage, V_{NW} . **d** Same data as **c** but with the data normalized in the x -direction for each line trace. **e** The normalized lock-in signal, overlaid with data points extracted from the peak fitting algorithm. This was done for all the data to check the consistency of the peak fitting algorithm. **f** The extracted lock-in signal maximums for each line trace, fitted with a linear fit to extract the relation between nanowire and detector voltage. The FWHM are also taken into account in the fit (instrumental error fitting). Inset: A line trace of **e** with $V_{NW} = 17\mu V$, showing the mild data processing, the extracted maximum peak position and the FWHM obtained from the peak fitting algorithm.

8.5. RADIATION AT FINITE MAGNETIC FIELD

Due to the improved design of the SIS detector, we can now measure the nanowire radiation up to 325mT; Figure 8.4b shows an example taken at 200mT. We can fit a line up to $V_{\text{NW}} \sim 22\mu\text{V}$ and determine the ratio between the nanowire and detector voltages. The range of fitting is determined by checking the consistency of the extracted data points and the raw data, as shown in Figure E.1b in the Appendix. No clear peak is found by the algorithm after $V_{\text{NW}} \sim 22\mu\text{V}$, so data points beyond this voltage are not used for fitting.

The nanowire to detector voltage ratio is 1.14 ± 0.08 . As with the zero field data, we do not measure a value that is exactly an integer. Across the field range 170–325mT we observe a single slope fit close to 1, as shown in Figure 8.4d. Between 110–170mT, we observe a regime with two different slopes as a function of the voltage drop over the nanowire. The extracted data for 150mT is shown in Figure 8.4c, and the extracted values are overlaid with the raw data in Figure E.1a. A fit over all the found peak positions shows a fitted line with a slope of 1.52 ± 0.05 (red fit in Figure 8.4c). However, such a fit results in many data points below the fit for the region $V_{\text{NW}} > -25\mu\text{eV}$. We believe that the data is better described by two separate linear fits. The second line starts at a point, which we refer as the ‘kink’, which shows up around $V_{\text{NW}} \sim 20\mu\text{V}$ in the 150mT case⁵. The change in extracted slope is induced by increasing the nanowire voltage, which increases the phase velocity.

We can also analyze the length of the ~ 1 slope. The end of this slope is determined by the start of the ~ 2 slope (the blue data points in Figure 8.4e, or the example data set in Figure 8.4c) or the point where the signal is lost (the red data points in Figure 8.4e, or the example data set in Figure 8.4b). The blue data points represent the position of the ‘kink’, which seems to vary linearly with the magnetic field in the range 100–200mT. The fit has a slope of $122 \pm 17\mu\text{eV/T}$ and crosses the y -axis at $3.2 \pm 2.8\mu\text{eV}$. We cannot measure in the grey region in Figure 8.4e due to limitations in the detection range of the SIS detection junction.

Finally, we can analyse the 2Δ of the detector for different slopes by extrapolating the fits to zero nanowire voltage. The PAT current onset in the detector is at $eV_{\text{det}} = 2\Delta - \hbar\omega$, where $\hbar\omega = aeV_{\text{NW}}$, with a being the charge of the radiation source tunneling event and ω the frequency of the emitted signal, as explained in Section 3.6. Ideally, $a = 2$ for conventional Josephson radiation and $a = 1$ for fractional Josephson radiation. The values of 2Δ , extracted from the fits for the two different slopes, are not the same, as can be seen in Figure 8.4f. This is because, experimentally, a smooth transition between the slopes is observed, clearly visible in the raw data (Figure E.1a). We can compare the extracted value for 2Δ with the measured ‘ 2Δ ’ in direct transport, although extracting the exact value of 2Δ in direct transport is difficult⁶ due to heating of the quasiparticle branch. Even though we cannot accurately extract ‘ 2Δ ’, we have still plotted it as we believe it shows a good approximation of the trend in value with magnetic field. We find that there is small reduction in 2Δ with magnetic field, see Figure 8.2b and 8.4f.

⁵We also tried different fits, see Figure E.3, but currently we believe that two lines are the best description of the data.

⁶The largest detector voltage which we can reach in Figure 8.2b, indicated by the double-headed arrow for 0mT, is used as the ‘ 2Δ ’ in direct transport.

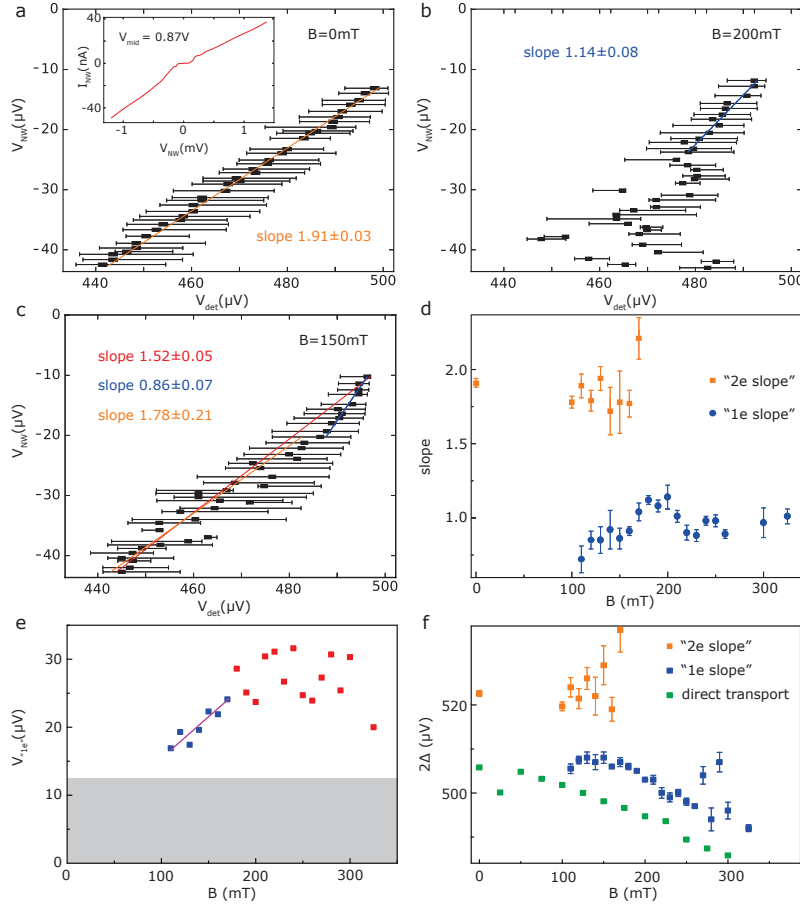


Figure 8.4: Analysis of the radiation emitted from the nanowire Josephson junction with the magnetic field applied along the nanowire ($< 5^\circ$) and with $V_{\text{mid}} = 0.87\text{V}$ and $V_{\text{sidegates}} = 1.75\text{V}$. A similar data set is shown in Figure E2 for a different gate configuration. **a** Same plot as 8.3f. Inset: the IV trace of the nanowire Josephson junction, used to determine the normal state resistance, $R_{N,\pm}$. **b** Extracted peak positions of the detected lock-in signal when a magnetic field of 200mT is applied along the nanowire. At $V_{\text{NW}} \sim 22\mu\text{V}$, the algorithm cannot find the peak reliably. In Figure E1b, the extracted peak positions are overlaid with the normalized raw data. The data up to $V_{\text{NW}} \sim 22\mu\text{V}$ shows a slope of 1.14 ± 0.08 between nanowire and detector voltage. **c** Extracted peak position of the lock-in signal in the detector at a magnetic field of 150mT. When all the data points are used for a linear fit (red), a slope of 1.52 ± 0.05 is obtained. Many data points, especially for low nanowire voltages, are below the fitted line. We believe the data is better described by two separate slopes, as shown by the blue and orange lines. In Figure E3, we show another possible fit which we believe is less appropriate. **d** The extracted slopes, before and after the ‘kink’. In the range $\sim 100\text{--}300\text{mT}$, a ~ 1 slope is fitted. **e** The end of the ~ 1 slope. For the blue data points, the ~ 1 slope ended due to the start of a second slope (effectively the position of the ‘kink’), while for the red data points it ended due to the lack of a visible signal in the data. **f** The extracted 2Δ for the different slopes, assuming that the slopes are linear up to zero nanowire voltage. The green points show the gap extracted from direct measurements. Due to quasiparticle heating, the exact value of 2Δ could not be extracted accurately from the IV trace, but this data shows the trend with magnetic field.

8.6. DETECTED RADIATION AS A FUNCTION OF GATE VOLTAGE

We also investigate the radiation detected in the SIS detector as a function of the gates ($V_{\text{mid}}, V_{\text{sidegates}}$) underneath the nanowire. There are three gates underneath the nanowire which can be changed independently, see Figure 8.1d. The middle gate (V_{mid}) is 200nm wide and is aligned (up to 30nm precision) with the nanowire weak link, namely the region where the aluminium (Al) has been removed from the nanowire. The other two gates ($V_{\text{sidegates}}$) are underneath the nanowire, which is covered by Al on 2 facets. The potentials of these gates are changed in unison.

The mid(dle) gate is expected to predominantly change the Josephson coupling between the two superconducting banks by changing the number of channels and their transmission. The side gates are designed to tune the chemical potential of the nanowire where it is covered by Al.

The chemical potential needs to be properly tuned to create MZM, see Section 3.4.2. These gates are important for checking the robustness of the detected signal, which is expected to be large in the case of a topological junction and weak for other effects[68, 82, 86].

First, we investigate the effect of the mid gate voltage at a magnetic field of 250mT. A mid gate voltage of 0.5–1.5V results in a conductance in the range 0.5–1.5 G_0 . Over the entire gate range a slope of ~ 1 is observed, as can be seen in Figure 8.5a. This is true even in the case of multiple channels (when the overall conductance is above $G_0 = \frac{2e^2}{h}$). Figure F4 in Appendix F shows the raw data and the peak positions of the detected frequency as a function of voltage bias for $V_{\text{mid}} = 1.375\text{V}$ and $R_{N,-} = 8.9\text{k}\Omega$.

As mentioned before, the mid gate predominantly changes the Josephson coupling by changing the transmission and the number of channels. The exact number of channels and transmission is unknown but if we assume a ballistic channel[64], the transmission, for the data shown in Figure 8.5b, is $T \sim 0.5 - 1.0$. The expected variation in LZ probability is expected to be large across this transmission range due to its exponential dependence, as shown in Figure 3.13g.

We can conclude that we do not observe any strong dependence on the gate voltage configuration. Even when the maximal transmission is only ~ 0.5 , we still observe a slope of ~ 1 . In addition, we do not observe an onset ~ 1 slope as a function of the nanowire voltage in our SIS detector range. We further discuss the behaviour of the observed 1 and 2 slope in the next section.

The two side gates, situated underneath the Al-covered parts of the nanowire, were changed together and the extracted slopes are shown in Figure 8.6. For applied voltages in the range $\sim 1.2 - 2.4\text{V}$, only a slope of ~ 1 is observed. In the case of a topological junction in the presence of MZM, the chemical potential is in the helical gap, as was mentioned in Section 3.4.2. Applying a gate voltage changes the chemical potential of the nanowire and it is possible to go outside the helical gap, resulting in the loss of the MZM. The appearance and disappearance of MZM with gate voltage tuning forms a so-called topological phase diagram and recently experimental evidence of this was claimed[15] for InSb nanowires in proximity to NbTiN. The absence of this effect in our experiment might be explained by heavy screening of the gate electrical field by the Al on the nanowire[139]. Another possible explanation is the strong coupling between the superconductor and the semiconducting nanowire, discussed in ref. [211]. In this ref-

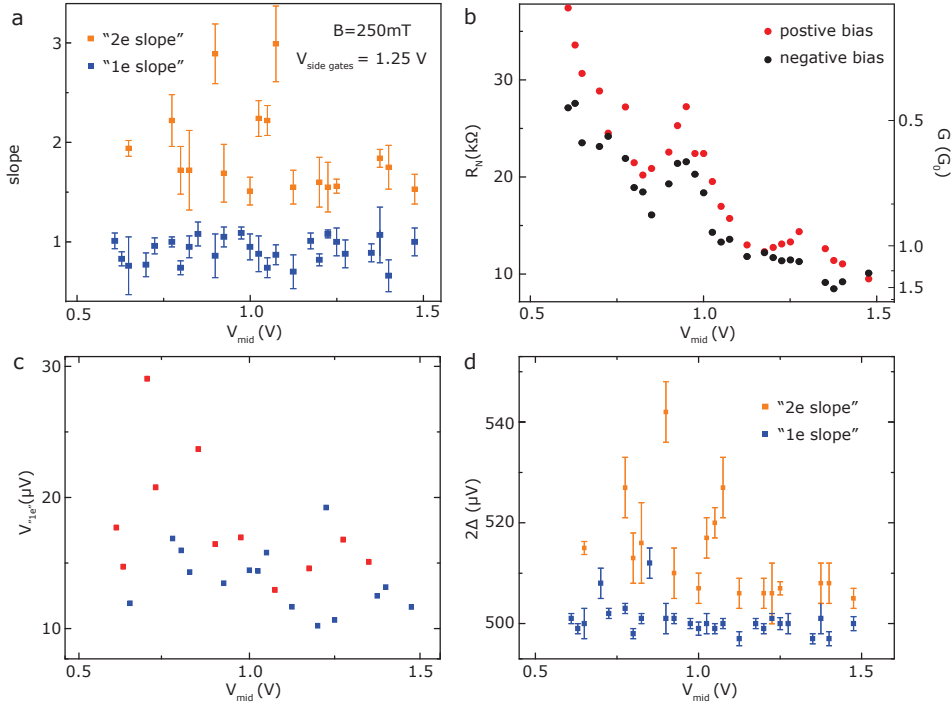


Figure 8.5: Investigation of the detected signal as a function of mid gate, with an applied magnetic field of 250mT along the nanowire and $V_{\text{sidegates}} = 1.25\text{V}$ in all cases. **a** The slopes extracted from fits using the peak positions extracted from the lock-in signal in the SIS detector. **b** The normal state resistances for positive (negative) bias in red (black). The nanowire is biased on the negative side for all data sets used in this figure. **c** The length of the '1e' line in the voltage measurements for the nanowire Josephson junction. This length is determined by the point where the ~ 2 slope begins for the blue data points. For the red data points, the length is determined by the last point where we can reliably fit the data. **d** The extracted slope is extrapolated to $V_{\text{NW}} = 0\text{V}$ to determine 2Δ . The 2Δ of the ~ 2 slope is systematically higher, as can be seen from the orange data points. The blue data points (associated with the ~ 1 slope) show a more consistent value for 2Δ .

erence, the authors expect the chemical potential to have a slowly-varying effect on the topological properties of MBS due to this strong coupling.

8.7. THE 1 AND 2 SLOPES

Observing 1 and 2 slopes in the SIS detector due to nanowire Josephson junction emission is not unexpected [82, 86]. However, the exact properties of the detected signal as a function of nanowire voltage, as measured in this experiment, were not predicted.

Before we discuss the data further, we must first distinguish between 1 and 2 slopes and f and $f/2$ radiation⁷. We refer to a 1 or 2 slope because we plot the signals detected in the SIS detector as V_{NW} against V_{det} . The dimensionless relation between these two voltages is $aV_{\text{NW}} = 2\Delta - eV_{\text{det}}$, as was discussed in Section 3.6, where $a = 1$ or $a = 2$ with

⁷ Josephson radiation is associated with 2π -periodic trivial Andreev bound states and fractional Josephson radiation is associated with 4π -periodic non-trivial Majorana bound states.

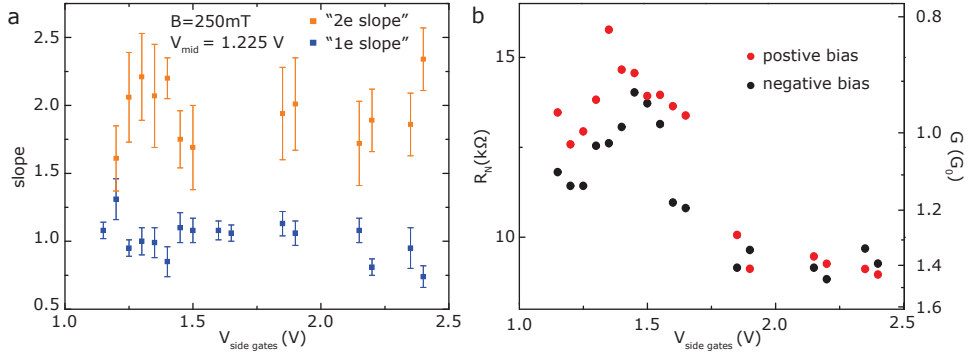


Figure 8.6: Investigation of the detected signal as a function of both side gate voltages, swept together, with an applied magnetic field of 250mT along the nanowire and $V_{\text{mid}} = 1.225\text{V}$ in all cases. **a** The extracted slopes, showing a slope of ~ 1 for a large range of side-gate voltages in all sets of measured data. **b** The normal state resistances for the positive and negative bias regimes.

or without the presence of MZM. The slope between these two voltages can change, as experimentally observed, by increasing V_{NW} (the phase velocity). The detected signal can start, for example, with a 1 (2) slope and then evolve at higher phase velocity to a 2 (1) slope, as is depicted with solid lines in Figure 8.7. Since the superconducting gap in the detector is fixed, the slopes can be extrapolated to zero phase velocity, which should have the same value of 2Δ . When this is the case, the 2 and 1 slopes correspond to single (f) and half ($f/2$) frequency, respectively.

The experimentally-observed slopes are sketched in Figure 8.7b. First, we observe a ~ 1 slope and then, without discontinuity, a ~ 2 slope. This means that the detected frequency is now increasing more quickly with applied nanowire voltage. In this case the 2Δ no longer stays the same when we extrapolate to zero phase velocity, as shown by the extracted data in Figures 8.4f and 8.5d. Having multiple superconducting gaps in the *detector* for a fixed magnetic field is possible[212, 213], but this is not expected to play a role in our experiment because we see the 2Δ variation as a function of nanowire voltage. It is possible that there may be a smooth transition region between f and $f/2$ emission instead of the abrupt change shown by the solid lines in Figure 8.7b. If indeed there is a region where the $f/2$ radiation is turning into f radiation, the detected frequency would increase more quickly with applied nanowire voltage, as we have possibly observed. Small deviations from $f/2$ and f radiation have been simulated several times[68, 82, 86, 214]⁸ and even measured[73, 91].

This abrupt slope change, as sketched in Figure 8.7 using the solid lines, is what is expected when the frequency is abruptly doubled. The simulated noise spectrum of a topological junction, as calculated in ref. [82], does not necessarily exhibit this, however. In this reference the frequency (f) slowly ‘crawls’ towards the half frequency ($f/2$). When the peak in the noise spectrum is in between f and $f/2$, the relative magnitude is low and the FWHM increases (see Figure 3 in ref. [82]). This could explain the relatively quick disappearance of the signal in Figure E.1 when we deviated from the ~ 1 slope.

⁸Dimitry Pikulin, our theory collaborator, also simulated this, trying to understand our system.

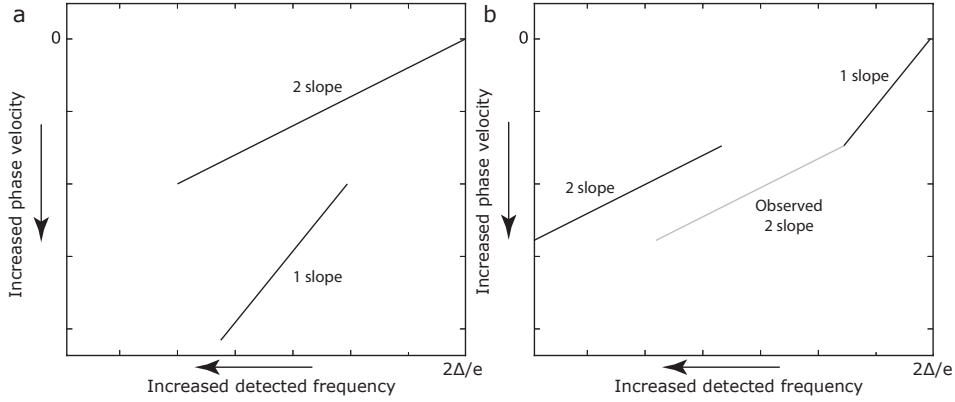


Figure 8.7: Schematic drawing of possible radiation slopes in the SIS detector. **a** At low phase velocity, there is a 2 slope, due to ‘normal’ 2π -periodic ABS. At higher phase velocity, due to LZ tunneling, half the Josephson frequency is measured, which should give a 1 slope. Due to the continuous increase of LZ probability with phase velocity, the 2 to 1 slope transition is probably not as abrupt as is depicted in this figure. **b** Schematic drawing where at low phase velocity a 1 slope is measured, for example because of the presence of MZM, while at higher phase velocity a 2 slope is restored. The abrupt jump (solid black lines) also shows a doubling in detected frequency. In the experiment, we measure a 1 slope at low phase velocity and then at the end point of the 1 slope we measure *without discontinuity* a 2 slope (grey dashed line). This means that we have not measured a doubling of the frequency but only a more rapid frequency increase as a function of nanowire voltage.

The effect responsible for the change of slope could be LZ tunneling, either to other ABS or the quasiparticle continuum. This latter case is extensively discussed in ref. [68], but there they find that the FWHM of the half frequency ($f/2$) increases at higher phase velocities (see Figure S1 in ref. [68]). The exact position stays very close to the half frequency ($f/2$) and maybe even reduces in frequency (Figure S1 in ref. [68], rightmost panel), which is also opposite to what we observe experimentally.

8

8.8. CONCLUSION AND DISCUSSION

The data discussed in this chapter is very preliminary⁹. We are now measuring a third sample. The second sample showed similar results to the one presented in this thesis, but the third sample shows more robustness in magnetic field: we measure a slope of ~ 1 up to ~ 700 mT.

In summary, we have 8 devices with a similar setup (including the device in Chapter 7) which *always* show a 2.0 ± 0.2 radiation slope at zero magnetic field. All three of the devices that can measure above 100mT without strong degradation of detection quality show a slope close to 1 in this region. This means that applied magnetic field is a necessary ingredient for the observation of a ~ 1 slope. In addition, we also observe that the ~ 1 slope is robust above a typical magnetic field of 100–125mT.

We also observe that the ~ 1 slope is very robust against changes in gate voltage, as

⁹This chapter is clearly not finished, either on the measurement side or the analysis and conclusion side. Many good and valid questions can be asked about this chapter, but we would like to point out that the rest of this thesis is also interesting to discuss.

discussed in Section 8.6. For a moderate applied magnetic field of at least 100mT, there is no gate range where the ~ 1 slope is absent for a large voltage range. Using nanowires from the same growth batch, ref. [14] reports that there is no need for (gate voltage) fine tuning to detect MZM. This could possibly be explained by the theory in ref. [211].

9

MICROWAVE SPECTROSCOPY OF SPINFUL ANDREEV BOUND STATES IN BALLISTIC SEMICONDUCTOR JOSEPHSON JUNCTIONS

**D. J. van Woerkom, A. Proutski, B. van Heck, D. Bouman,
J. I. Väyrynen, L. I. Glazman, P. Krogstrup,
J. Nygård, L. P. Kouwenhoven, A. Geresdi**

This is just an example of the quantum-mechanical penetration of a barrier. Josephson analyzed this situation and discovered that a number of strange phenomena should occur.

Richard P. Feynmann

We investigate Andreev bound states in InAs/Al core-shell nanowire junctions. We designed and characterized an on-chip microwave circuit coupling the nanowire junction to an Al/AlO_x/Al tunnel junction. The tunnel junction emitted photons at frequencies given by the AC Josephson relation $2eV_{\text{bias}} = hf$ to excited the Andreev bound states. Our circuit design allows for voltage, current and phase biasing the nanowire enabling the direct mapping of Andreev bound states. We investigate these Andreev bound states as a function of gate voltage and magnetic field with the ultimate goal of finding Majorana bound states.

This chapter has been published as arXiv:1609.00333.

9.1. INTRODUCTION

The superconducting proximity effect in semiconductor nanowires [106] has recently enabled the study of novel superconducting architectures, such as gate-tunable superconducting qubits [199, 215] and multiterminal Josephson junctions [137, 216]. As opposed to their metallic counterparts, the electron density in semiconductor nanosystems is tunable by external electrostatic gates providing a highly scalable and *in-situ* variation of the device properties [106, 199, 215]. In addition, semiconductors with large g -factor and spin-orbit coupling have been shown to give rise to exotic phenomena in superconductivity, such as φ_0 Josephson junctions [77] and the emergence of Majorana bound states [9, 151]. Here, we report microwave spectroscopy measurements [217] that directly reveal the presence of Andreev bound states (ABS) in ballistic semiconductor channels. We show that the measured ABS spectra are the result of transport channels with gate-tunable, high transmission probabilities up to 0.9, which is required for gate-tunable Andreev qubits [55, 70] and beneficial for braiding schemes of MZM [35]. For the first time, we detect excitations of a spin-split pair of ABS [218] and observe symmetry-broken ABS [75], a direct consequence of the spin-orbit coupling in the semiconductor.

The linear conductance $G = \frac{2e^2}{h} \sum T_i$ of a nanostructure between two bulk leads [219] depends on the individual channel transmission probabilities, T_i . Embedding the same structure between two superconducting banks with a superconducting gap of Δ gives rise to Andreev bound states (ABS) [220]. If the junction length is much smaller than the superconducting coherence length, ξ , i.e. in the short junction limit, then the ABS levels depend on the phase difference ϕ between the leads according to [98]:

$$E_{\text{ABS},i}(\phi) = \pm \Delta \sqrt{1 - T_i \sin^2 \frac{\phi}{2}}. \quad (9.1)$$

These subgap states with $|E_{\text{ABS}}| \leq \Delta$ are localized in the vicinity of the nanostructure and extend into the banks over a length scale determined by ξ ¹. Note that Eq. 9.1 is only valid in the absence of magnetic field, when each energy level is doubly degenerate.

Direct microwave spectroscopy has recently demonstrated the occupation of the ABS by exciting a Cooper pair in atomic junctions [217]. Unlike quasiparticle tunneling spectroscopy, which has also been used to detect ABS [221, 222], resonant excitation by microwaves is a charge parity-conserving process [223]. This property enables coherent control of ABS which is required for novel qubit architectures [55] and makes microwave spectroscopy a promising tool to detect Majorana bound states [224] in proximitized semiconductor systems [7, 8].

9.2. DEVICE SETUPS

We investigate ABS excitations in Josephson junctions that consist of indium arsenide (InAs) nanowires covered by epitaxial aluminium (Al) shells [21]. The junction, where the superconducting shell is removed, is 100 nm (device 1, see the red box in Fig. 9.1a) and 40 nm long (device 2), respectively. The nanowire is then embedded in a hybrid superconducting quantum interference device (SQUID) whose second arm is a conventional Al/AlO_x/Al tunnel junction (in yellow box), enabling the control of the phase drop

¹The length scale of the exponential cutoff of the wavefunction is $\xi / \sqrt{1 - E_{\text{ABS}}(\phi)^2 / \Delta^2}$

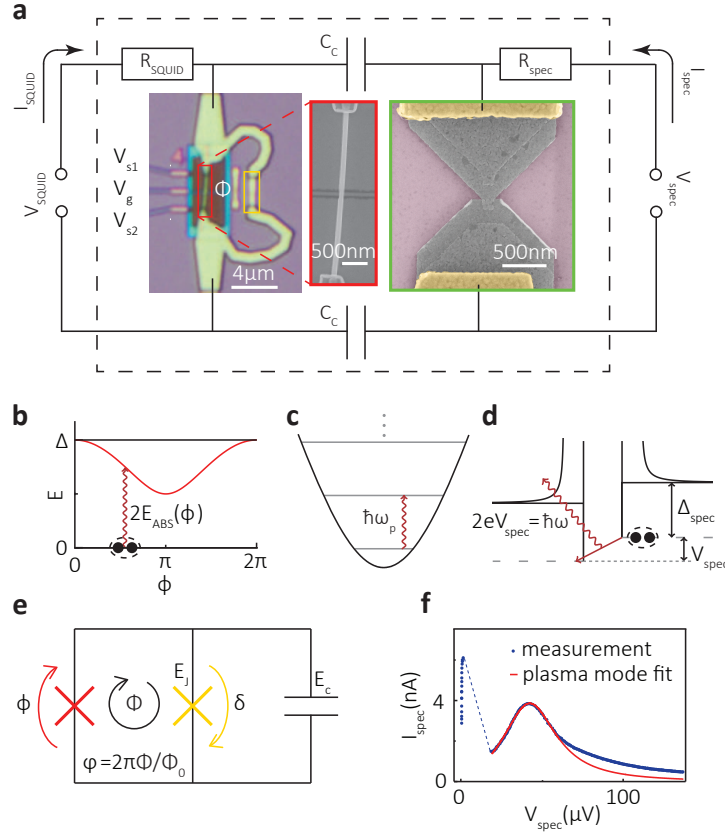


Figure 9.1: Device schematics and working principle. (a) Equivalent circuit diagram: Bright field optical image of the hybrid SQUID with one InAs semiconductor nanowire weak link (scanning electron micrograph, in the red box) and an Al/AlO_x/Al tunnel junction (enclosed by the yellow box). The SQUID is capacitively coupled to the spectrometer Al/AlO_x/Al Josephson junction (scanning electron micrograph, in green box) via C_c . The transmission of the semiconductor channel is tuned by the gate voltage, V_g . Additional gates near the electrodes are kept at a constant voltage $V_{s1,2}$. Circuit elements within the dashed box are located on-chip, thermally anchored to 12 mK. Panels (b) and (c) show the excitations of the hybrid SQUID: the Andreev bound state at $\hbar\omega = 2E_{\text{ABS}}(\phi)$ (b) and the plasma oscillations at $\hbar\omega = \hbar\omega_p$ (c) are excited by a photon energy $\hbar\omega = 2eV_{\text{spec}}$ set by the DC voltage bias of the spectrometer (d) with a superconducting gap Δ_{spec} . (e) Schematic circuit diagram of the hybrid SQUID. The total phase $\varphi = \phi + \delta$ is determined by the applied flux Φ . (f) The measured $I(V)$ trace of the spectrometer junction with the nanowire in full depletion, i.e. in the absence of ABS excitations. The red solid line shows the fit to the circuit model of a single resonance centered at $\hbar\omega_p$, see text. Images and data were all taken on device 1.

ϕ by means of the applied magnetic flux Φ through the SQUID loop. In the limit of a negligible loop inductance and an asymmetric SQUID, where the Josephson coupling of the nanowire is much smaller than that of the tunnel junction, the applied phase φ mostly drops over the nanowire link: $\phi \approx \varphi = 2\pi\Phi/\Phi_0$, where $\Phi_0 = h/2e$ is the superconducting flux quantum. We measure the microwave response [217, 223] of the nanowire junction utilizing the circuit depicted in Fig. 9.1a, where a second Al/AlO_x/Al tunnel junction (in

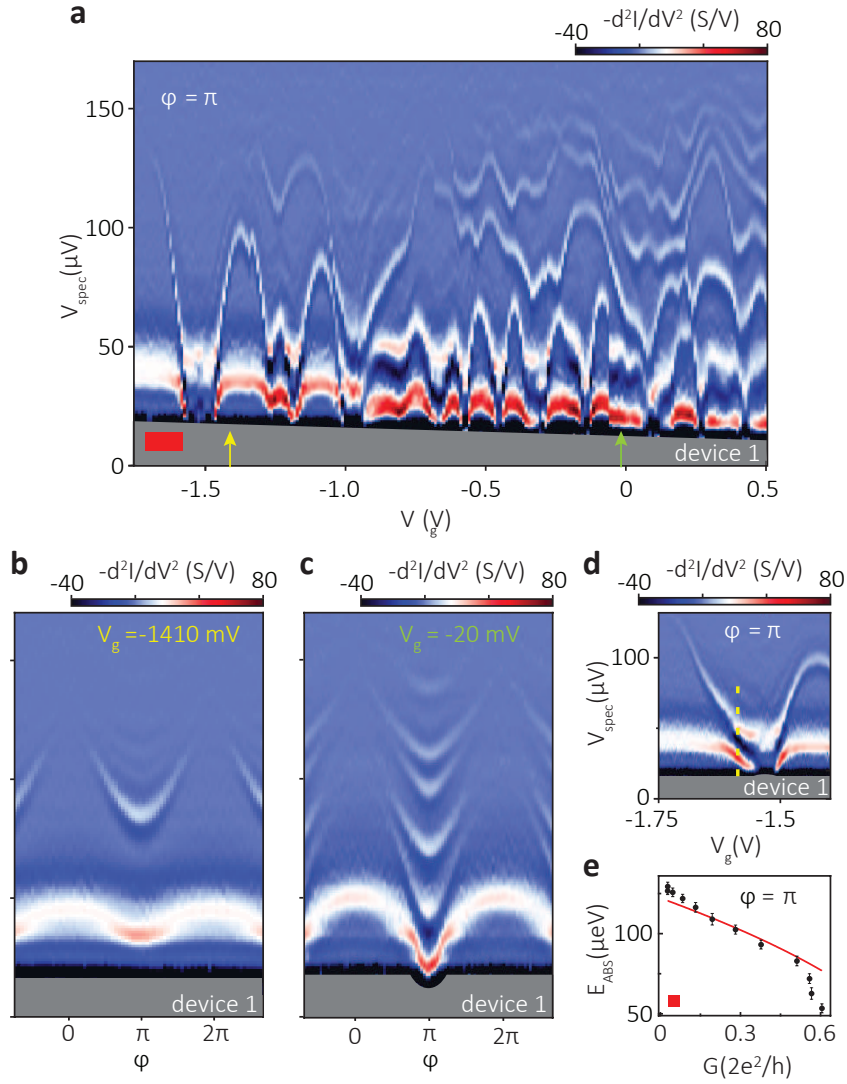


Figure 9.2: **Gate dependence of Andreev bound states.** (a) $-d^2I/dV^2$ of the spectrometer junction as a function of V_g at $\phi = \pi$, where $E_{\text{ABS},i} = \Delta\sqrt{1-T_i}$ in the short junction limit. Panels (b) and (c): $-d^2I/dV^2$ of the spectrometer junction as a function of $\phi = 2\pi\Phi/\Phi_0$ for one channel (b) and several channels (c). The qualitative agreement of the line shapes with Eq. 9.1 confirms the short junction behaviour. Arrows in panel (a) indicate V_g for these measurements. Weakly visible vertically shifted replicas of the ABS lines indicate higher order transitions, see text. (d) Strong hybridization between the ABS excitation and the plasma mode with a level repulsion of $\varepsilon = 22 \mu\text{eV}$ at the yellow dash line. (e) $E_{\text{ABS}}(\phi = \pi)$ as a function of the DC linear conductance G of the nanowire weak link in the gate span denoted by the red bar in panel (a). The solid red line shows the prediction of the single channel model with $\Delta = 122 \mu\text{eV} \pm 3 \mu\text{eV}$, see text. All data was taken on device 1. Grey regions denote lack of data due to bias instability of the circuit.

green box) is capacitively coupled to the hybrid SQUID and acts as a spectrometer. Further details on the fabrication process are given in section 9.9.1.

9.3. PLASMA MODE CHARACTERIZATION

In this circuit, inelastic Cooper-pair tunneling (ICPT, Fig. 9.1d) of the spectrometer junction is enabled by the dissipative environment and results in a DC current, I_{spec} [193]:

$$I_{\text{spec}} = \frac{I_{\text{c,spec}}^2 \text{Re}[Z(\omega)]}{2V_{\text{spec}}}. \quad (9.2)$$

Here $I_{\text{c,spec}}$ is the critical current of the spectrometer junction, V_{spec} is the applied voltage bias, and $Z(\omega)$ is the circuit impedance at frequency $\omega = 2eV_{\text{spec}}/\hbar$. Since $Z(\omega)$ peaks at the resonant frequencies of the hybrid SQUID [193, 217], so does the DC current I_{spec} , allowing us to measure the ABS excitation energies of the nanowire junction (Fig. 9.1b), as well as the plasma frequency of the SQUID (Fig. 9.1c).

First we characterize the contribution of the plasma mode with the nanowire junction gated to full depletion, i.e. $G = 0$. We show the $I(V)$ curve of the spectrometer junction of device 1 in Fig. 9.1f, where we find a single peak centered at $\hbar\omega_p/2 = eV_{\text{spec}} = 46 \mu\text{eV}$ and a quality factor $Q \approx 1$. In the limit of $E_C \ll E_J$, $\hbar\omega_p = \sqrt{2E_C E_J}$, where E_C is the charging energy of the circuit and E_J is the Josephson coupling of the tunnel junction (Fig. 9.1e). Estimating $E_J = 165 \mu\text{eV}$ from the normal state resistance [174], this measurement allows us to determine $E_C = 25.4 \mu\text{eV}$. The choice of a low quality factor in combination with a characteristic impedance $Z_0 = 551 \Omega \ll R_q = h/4e^2$ ensures the suppression of higher order transitions and parasitic resonances.

9.4. ABS GATE VOLTAGE DEPENDENCE

Next, we investigate the spectrometer response as a function of the gate voltage V_g applied to the nanowire. Note that the spectrometer response to the ABS transitions is superimposed on the plasma resonance peak. In order to achieve a better visibility of the ABS lines, we display $-d^2 I_{\text{spec}}/dV_{\text{spec}}^2(V_{\text{spec}})$ rather than $I_{\text{spec}}(V_{\text{spec}})$ (see section 9.9.4 for comparison). In the presence of ABS, the spectrum exhibits peaks at frequencies where $\hbar\omega = 2E_{\text{ABS},i}$ [223]. In Fig. 9.2a, we monitor the appearance of these peaks for an applied phase $\varphi = \pi$, where the ABS energy of Eq. 9.1 is $E_{\text{ABS},i}(\pi) = \Delta\sqrt{1 - T_i}$. Notably, for V_g values close to full depletion (see red bar in Fig. 9.2a), we see a gradual decrease of $E_{\text{ABS}}(\pi)$ with increasing V_g (black dots in Fig. 9.2e). In this regime, we find a good correspondence with Eq. 9.1, assuming single channel transport, $G = \frac{2e^2}{h} T$ (red solid line in Fig. 9.2e, see the section 9.9.5 for the details of the measurement of G). However, the observed $\Delta = 122 \mu\text{eV}$ is smaller than the $\Delta_{\text{Al}} \approx 200 \mu\text{eV}$ of the thin film Al contacts, in agreement with the presence of induced superconductivity in the nanowire [21]. Increasing V_g further, we observe a sequential appearance of peaks, which we attribute to the opening of multiple transport channels in the weak link and the consequent formation of multiple ABS [98] as the Fermi level, E_F increases. We also find a strong variation of E_{ABS} with V_g similarly to earlier experiments [106, 199, 215]. We attribute this observation to mesoscopic fluctuations in the presence of weak disorder [98], such that the mean free path of the charge carriers is comparable to the channel length.

9.5. ABS FLUX DEPENDENCE

Now we turn to the flux dependence of the observed spectrum, shown in Fig. 9.2b and 9.2c for two distinct gate configurations. We find a qualitative agreement with Eq. 9.1 with one transport channel in Fig. 9.2b and several channels in Fig. 9.2c confirming that our device is in the short junction limit. In addition, we observe the plasma mode at $eV_{\text{spec}} < 50 \mu\text{eV}$. We also find that the plasma mode $\hbar\omega_p$ oscillates with φ when the nanowire is gated to host open transport channels. This is expected due to the Josephson coupling of the nanowire becoming comparable to E_J , which also causes a finite phase drop, δ , over the tunnel junction. We also note the presence of additional, weakly visible lines in the spectrum which could be attributed to higher order processes [217]. However, we did not identify the nature of these excitations, and we focus on the main transitions throughout the current work.

In addition, we observe the occurrence of avoided crossings between the Andreev and plasma modes, as shown in Fig. 9.2d at $\varphi = \pi$. These avoided crossings require $\hbar\omega_p \approx 2\Delta\sqrt{1-T}$, which translates to a high transmission probability $T \approx 0.8 - 0.9$, and demonstrates the hybridization between the ABS excitation and the plasma mode. The coupling between these two degrees of freedom has previously been derived [223, 225], leading to a perturbative estimate for the energy splitting $\varepsilon \approx \Delta T (E_C/2E_J)^{1/4} \approx 40 - 70 \mu\text{eV}$, similar to the observed value of $22 \mu\text{eV}$. The discrepancy is fully resolved in the numerical analysis of the circuit model developed below.

9.6. HYBRID SQUID MODEL

We provide a unified description of the energy spectrum of the circuit as a whole, and consider the following Hamiltonian for the hybrid SQUID (Fig. 9.1e) [225]:

$$\hat{H} = E_C \hat{N}^2 + E_J (1 - \cos \hat{\delta}) + \hat{H}_{\text{ABS}}(\varphi - \hat{\delta}). \quad (9.3)$$

Here $\hat{\delta}$ is the operator of the phase difference across the tunnel junction, conjugate to the charge operator \hat{N} , $[\hat{\delta}, \hat{N}] = i$. The first two terms in Eq. 9.3 represent the charging energy of the circuit and the Josephson energy of the tunnel junction (Fig. 9.1e). The last term describes the quantum dynamics of a single-channel short weak link [70, 71], which depends on Δ and T . For the analytic form of \hat{H}_{ABS} , see section 9.10.2. To fully account for the coupling between the ABS excitation and the quantum dynamics of the phase across the SQUID, we numerically solve the eigenvalue problem $\hat{H}\Psi = E\Psi$ and determine the transition frequencies $\hbar\omega = E - E_{\text{GS}}$ with E_{GS} being the ground state energy.

This procedure allows us to fit the experimental data, and we find a good quantitative agreement as shown in Fig. 9.3a for a dataset taken at $V_g = -1410 \text{ mV}$ with the fit parameters $\Delta = 122 \mu\text{eV}$ and $T = 0.57$. The previously identified circuit parameters E_J and E_C are kept fixed during the fit. We note that the observed ABS transition (orange solid line) only slightly deviates from Eq. 9.1 (black dashed line). The modulation of the plasma frequency (green solid line) is then defined by the model Hamiltonian with no additional fit parameters. We further confirm the nature of the plasma and ABS excitations by evaluating the probability density $|\Psi(\delta, \sigma)|^2$ of the eigenfunctions of Eq. 9.3 at $\varphi = \pi$ (Fig. 9.3b). In the ground state of \hat{H} (GS) and in the state corresponding to the plasma excitation (green line in Fig. 9.3a), the probability density is much higher in the

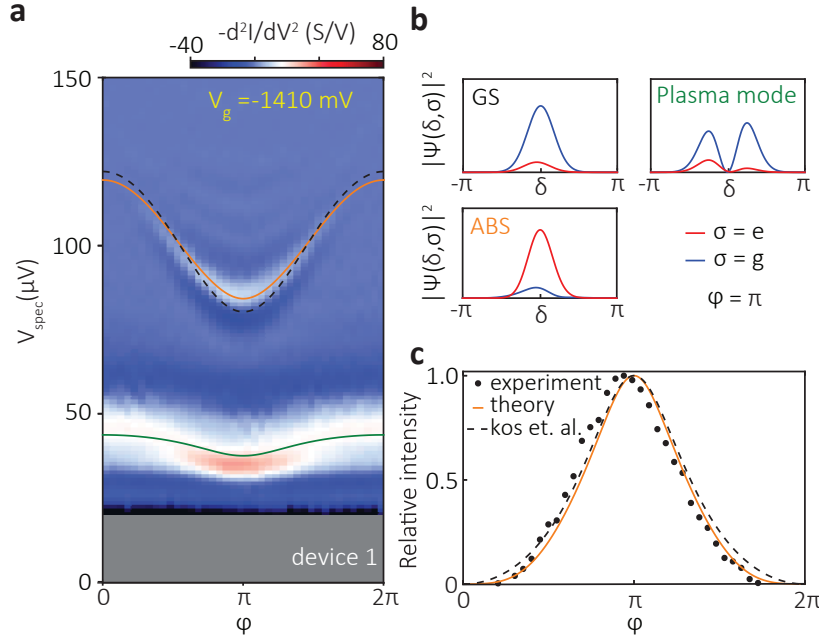


Figure 9.3: **Theoretical description of the transitions.** (a) Solid lines denote the transitions identified by the model described in the text, with Δ and T being free parameters. The experimental dataset is the same as the one shown in Fig. 9.2b. The dashed line shows Eq. 9.1 for the fitted $\Delta = 122 \mu\text{eV}$ and $T = 0.57$. (b) The probability density $|\Psi(\delta, \sigma)|^2$ in the ground state of the hybrid SQUID (GS), and in the two excited states depicted in panel (a), respectively. The weight in the ABS ground state ($\sigma = g$) and in the ABS excited state ($\sigma = e$) distinguishes between the plasma mode and the ABS. (c) The measured relative intensity of the ABS transition (black dots) compared to the theoretical expectation based on Eq. 9.3 (orange solid line) and from [223] (dashed black line) with no additional fitting parameters.

ground state of the weak link ($\sigma = g$, blue line) than in the excited state ($\sigma = e$, red line). In contrast, the next observed transition (orange line in Fig. 9.3a) gives rise to a higher contribution from $\sigma = e$ confirming our interpretation of the experimental data in terms of ABS excitations. Furthermore, the model can also describe measurement data with T close to 1, where it accurately accounts for the avoided crossings between the ABS and plasma spectral lines (see the section 9.9.6 for $T = 0.9$).

In Fig. 9.3c we show the visibility of the ABS transition as a function of the applied phase φ , which is proportional to the absorption rate of the weak link, predicted to be $\propto T^2(1-T)\sin^4(\varphi/2) \times \Delta^2/E_{\text{ABS}}^2(\varphi)$ [223]. We note that in the experimental data the maximum of the intensity is slightly shifted from its expected position at $\varphi = \pi$. This minor deviation may stem from the uncertainty of the flux calibration. Nevertheless, using $T = 0.57$, obtained from the fit in Fig. 9.3a, we find a good agreement with no adjustable parameters (black dashed line). A similarly good correspondence is also found with the full numerical model (orange line) based on Eq. 9.3.

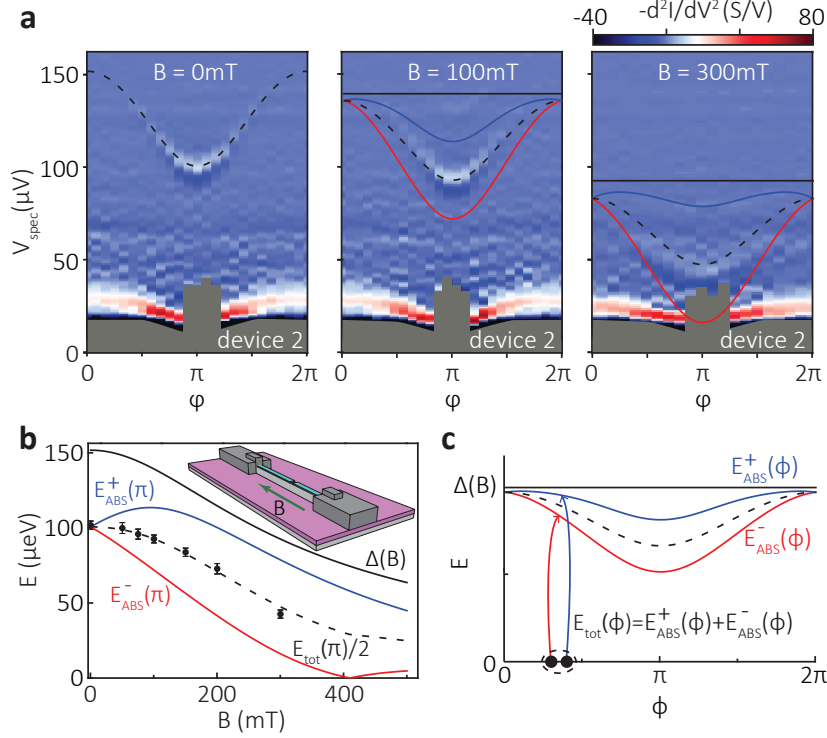


Figure 9.4: **Spectroscopy of spin-split Andreev bound states in a Rashba nanowire.** Panel (a) shows the flux dependence of the Andreev bound states at $B = 0$, 100 and 300 mT, respectively, applied parallel to the nanowire. The zero-field fit yields so $T = 0.56$ and $\Delta = 152 \mu\text{eV}$. Dash lines depict the fit of $E_{\text{tot}}(\phi) = E_{\text{ABS}}^+(\phi) + E_{\text{ABS}}^-(\phi)$ to the model described in the text. (b) Black dots show the measured $E_{\text{tot}}(\pi)$ as a function of B . The dashed line depicts the fit to the theory with $g = 14.7 \pm 0.6$ and $\sqrt{E_{\text{SO}} E_F} / \Delta = 0.32 \pm 0.02$, see text. The Zeeman-split ABS levels $E_{\text{ABS}}^{\pm}(\pi)$ and the proximity-induced gap $\Delta(B)$ obtained from the model are shown as visual guides. (c) $E_{\text{ABS}}^{\pm}(\phi)$ computed at $B = 100$ mT are shown as blue and red solid lines, together with the calculated transition energy $E_{\text{tot}}(\phi)$ (black dashed line). The experimental data was taken on device 2 at $V_g = 140$ mV. Grey regions denote lack of data due to bias instability of the circuit.

9.7. IN-PLANE MAGNETIC FIELD DEPENDENCE

We now discuss the evolution of the ABS as a function of an in-plane magnetic field B aligned parallel to the nanowire axis, which is perpendicular to the internal Rashba spin-orbit field (see the inset in Fig. 9.4b for measurement geometry). The applied field lifts the Kramers degeneracy of the energy spectrum, splitting each Andreev doublet into a pair $E_{\text{ABS}}^{\pm}(\phi)$. For small B , the splitting $E_{\text{ABS}}^+(\phi) - E_{\text{ABS}}^-(\phi)$ is linear in B , due to the Zeeman effect. However, the spin-split single particle levels are not accessible by microwave spectroscopy, which can only induce transitions to a final state with two excited quasiparticles. Thus we can only measure $E_{\text{tot}}(\phi) = E_{\text{ABS}}^+(\phi) + E_{\text{ABS}}^-(\phi)$ and expect no split of the measured spectral lines. The experimental data (Fig. 9.4a) shows that E_{tot} decreases with B , while the lineshape remains qualitatively intact.

In order to explain the field dependence of E_{tot} , we study the behaviour of ABS in a simple model consisting of a short Josephson junction in a one-dimensional quantum wire with proximity-induced superconductivity, Rashba spin-orbit and an applied Zeeman field parallel to the wire [7, 8, 226]. Within this model, we are able to find E_{ABS}^+ and E_{ABS}^- , and reproduce the observed quadratic decrease of the measured $E_{\text{tot}}(\pi)$ (black dots in Fig. 9.4b). Initially, as B is increased, the proximity-induced gap $\Delta(B)$ is suppressed (black solid line), while the energy $E_{\text{ABS}}^+(\pi)$ (blue solid line) increases due to the Zeeman split of the ABS. However, a crossing of the discrete ABS level with the continuum is avoided due to the presence of spin-orbit coupling, which prevents level crossings in the energy spectrum by breaking spin-rotation symmetry. The repulsion between the ABS level and the continuum causes a downward bending of $E_{\text{ABS}}^+(\pi)$, in turn causing a decrease in $E_{\text{tot}}(\pi)$ (black dashed line).

We perform the calculations in the limit where the Fermi level E_F in the wire is well above the Zeeman energy $E_Z = \frac{1}{2}g\mu_B B$ and the spin-orbit energy $E_{\text{SO}} = m\alpha^2/2\hbar^2$ with m the effective mass and α the Rashba spin-orbit coupling constant. In this case and in the short junction limit, the ratio $E_{\text{tot}}(\pi)/\Delta$ is a function of just two dimensionless parameters: E_Z/Δ and $\sqrt{E_{\text{SO}}E_F}/\Delta$. First we extract $\Delta = 152 \mu\text{eV}$ and $T = 0.56$ at $B = 0$ (leftmost panel in Fig. 9.4a). Then, we perform a global fit on $E_{\text{tot}}(\phi)$ at all B values and obtain a quantitative agreement with the theory for $g = 14.7 \pm 0.6$, which is in line with expected g -factor values in InAs nanowires [14, 22, 227] and $\sqrt{E_{\text{SO}}E_F}/\Delta = 0.32 \pm 0.02$. This model is consistent assuming $E_F > E_Z \approx 100 \mu\text{eV}$ at 300 mT. Thus we attain an upper bound $E_{\text{SO}} \lesssim 24 \mu\text{eV}$, equivalent to a Rashba parameter $\alpha \lesssim 0.12 \text{ eV\AA}$ in correspondence with earlier measurements on the same nanowires [14]. However, assuming the opposite limit, $E_F \approx 0$, the theory is not in agreement with the experimental data (see figure 9.16 for the comparison).

The theoretical energy spectrum shown in Fig. 9.4b predicts a ground state fermion-parity switch of the junction at a field $B_{\text{sw}} \approx 400$ mT, at which the lowest ABS level $E_{\text{tot}}^-(\pi) = 0$ (red line in Fig. 9.4b). This parity switch inhibits the resonant excitation of the Zeeman-split ABS levels [74] thus preventing microwave spectroscopy measurements for $B > B_{\text{sw}}$. This prediction is in agreement with the vanishing visibility of the ABS line at $B \approx B_{\text{sw}}$ in the experiment.

In addition to the interplay of spin-orbit and Zeeman couplings, the orbital effect of the magnetic field [228] is a second possible cause for the decrease of the ABS transition energy. Orbital depairing influences the proximity-induced pairing and results in a quadratic decrease of the induced superconducting gap: $\Delta(B) = \Delta(1 - B^2/B_*^2)$, where $B_* \sim \Phi_0/A$ and A is the cross-section of the nanowire. A simple model which includes both orbital and Zeeman effect, but no spin-orbit coupling, yields $B_* \approx 400$ mT when fitted to the experimental data (fig. 9.16c). In this case, the fit is insensitive to the value of the g -factor. However, the model also predicts the occurrence, at $\phi = \pi$, of a fermion-parity switch at a field $B_{\text{sw}} < B_*$ whose value depends on the g -factor. Because agreement with the experimental data imposes the condition that $B_{\text{sw}} > 300$ mT, in section 9.10.5 we show that this scenario requires $g \lesssim 5$, which is lower than g -factor values measured earlier in InAs nanowire channels [14, 22, 227]. Hence, we can conclude that the orbital effect can only play a subleading role in the observed suppression of the ABS transition energy. Note that in all cases we neglect the effect of B on the Al thin film,

justified by its in-plane critical magnetic field exceeding 2 T [229].

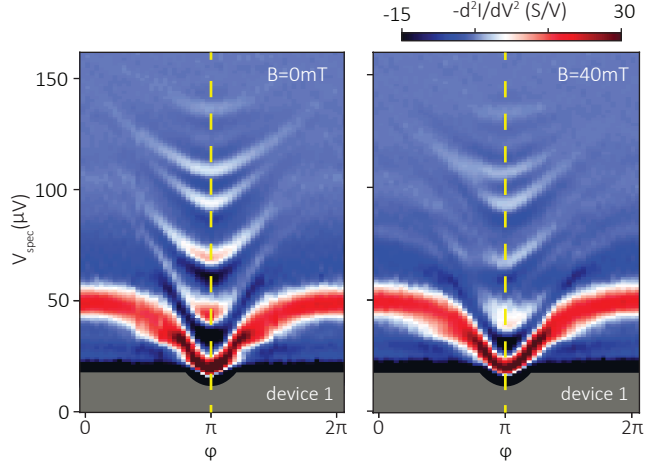


Figure 9.5: **Symmetry-broken ABS in magnetic field.** The symmetry axis at $\varphi = \pi$ at zero magnetic field is denoted by dashed yellow line. Note that at $B = 40$ mT the observed spectrum does not obey the mirror symmetry with respect to the same line. The data was taken on device 1 at $V_g = -20$ mV. Grey regions denote lack of data due to bias instability of the circuit.

We present the ABS spectrum in the presence of several transport channels in Fig. 9.5. While at zero magnetic field (left panel) the data is symmetric around $\varphi = \pi$, in a finite magnetic field (right panel) the data exhibits an asymmetric flux dependence (see the yellow dashed line as a guide to the eye). This should be contrasted with Fig. 9.4a where the data for a single-channel wire are presented at different values of the magnetic field: each of the traces is symmetric around $\varphi = \pi$. This behavior agrees with theoretical calculations in the short-junction limit, which show that this asymmetry can arise in a Josephson junction with broken time-reversal and spin-rotation symmetries as well as more than one transport channel [230]. While the data is asymmetric with respect to $\varphi = \pi$, there is no visible shift of the local energy minima away from this point. This observation is consistent with the absence of an anomalous Josephson current [77, 231, 232] for our specific field configuration (magnetic field parallel to the wire), in agreement with theoretical expectations [233–235].

9.8. CONCLUSION

In conclusion, we have presented microwave spectroscopy of Andreev bound states in semiconductor channels where the conductive modes are tuned by electrostatic gates and demonstrated the effect of Zeeman splitting and spin-orbit coupling. The microwave spectroscopy measurements shown here could provide a new tool for quantitative studies of Majorana bound states, complementing quasiparticle tunneling experiments. Furthermore, we have provided direct evidence for the symmetry breaking of Andreev bound states in a multichannel ballistic system. This result paves the way to novel Josephson circuits, where the critical current depends on the current direction, leading to super-

current rectification effects [236, 237] tuned by electrostatic gates.

In conclusion, we have presented microwave spectroscopy of Andreev bound states in semiconductor channels where the conductive modes are tuned by electrostatic gates and we have demonstrated the effect of Zeeman splitting and spin-orbit coupling. The microwave spectroscopy measurements shown here could provide a new tool for quantitative studies of Majorana bound states, complementing quasiparticle tunneling experiments [9, 227]. Furthermore, we have provided direct evidence for the time-reversal symmetry breaking of the Andreev bound state spectrum in a multichannel ballistic system. This result paves the way to novel Josephson circuits, where the critical current depends on the current direction, leading to supercurrent rectification effects [236, 237] tuned by electrostatic gates.

9.9. SUPPLEMENTARY INFORMATION

9.9.1. DEVICE FABRICATION

The devices are fabricated on commercially available undoped Si wafers with a 285 nm thick thermally grown SiO_x layer using positive tone electron beam lithography. First, the electrostatic gates and the lower plane of the coupling capacitors are defined and Ti/Au (5 nm/15 nm) is deposited in a high-vacuum electron-beam evaporation chamber. Next, the decoupling resistors are created using Cr/Pt (5 nm/25 nm) with a track width of 100 nm, resulting in a characteristic resistance of $100 \Omega/\mu\text{m}$. Then, a 30 nm thick SiN_x layer is sputtered and patterned to form the insulation for the coupling capacitors and the gates. We infer $C_c \approx 400 \text{ fF}$ based on the surface area of $6.5 \times 30 \mu\text{m}^2$ and a typical dielectric constant $\epsilon_r = 7$.

In the following step, the tunnel junctions are created using the Dolan bridge technique by depositing 9 and 11 nm thick layers of Al with an intermediate oxidization step *in-situ* at 1.4 mbar for 8 minutes. Then, the top plane of the coupling capacitors is defined and evaporated (Ti/Au, 20 nm/100 nm) after an *in-situ* Ar milling step to enable metallic contact to the Al layers. Next, the InAs nanowire is deterministically deposited with a micro-manipulator on the gate pattern [102].

The channel of device 1 is defined by wet chemical etch of the aluminium shell using Transene D at 54°C for 12 seconds. The channel of device 2 is determined by *in-situ* patterning, where an adjacent nanowire casted a shadow during the epitaxial deposition of aluminium [238]. The superconducting layer thickness was approximately 10 nm for both devices deposited on two facets.

Finally, the nanowire is contacted to the rest of the circuit by performing Ar plasma milling and subsequent NbTiN sputter deposition to form the loop of the hybrid SQUID. We show the design parameters of the devices in Table 9.1.

9.9.2. MEASUREMENT SETUP

The measurements were performed in a Leiden Cryogenics CF-1200 dry dilution refrigerator with a base temperature of 12 mK equipped with Cu/Ni shielded twisted pair cables thermally anchored at all stages of the refrigerator to facilitate thermalization. Noise filtering is performed by a set of π -LC filters ($\sim 100 \text{ MHz}$) at room temperature and copper-powder filters ($\sim 1 \text{ GHz}$) in combination with two-pole RC filters ($\sim 100 \text{ kHz}$) at

	Device 1	Device 2
Channel length (nm)	100	40
Tunnel junction area (nm ²)	400 × 120	200 × 120
Flux periodicity (μT)	38	120
Spectrometer junction area (nm ²)	120 × 120	120 × 120

Table 9.1: Geometry of the devices featured in the current study.

base temperature for each measurement line. The schematics of the setup is shown in Fig. 9.6.

9.9.3. DEVICE CIRCUIT PARAMETERS

We characterise the circuit based on the plasma resonance observed with the semiconductor nanowire gated to zero conductance, i.e. full depletion. In this regime, we infer the environmental impedance $\text{Re}[Z(\omega)]$ based on Eq. 9.2 and assume the following form, which is valid for a parallel LCR circuit:

$$\text{Re}[Z(x)] = \frac{Z_0 Q}{1 + \frac{Q^2}{x^2}(1 - x^2)^2}, \quad (9.4)$$

with $x = \omega/\omega_0$ the dimensionless frequency. The resonance of the circuit is centered at $\omega_0 = (LC)^{-1/2}$ with a quality factor of $Q = R\sqrt{\frac{C}{L}}$ and a characteristic impedance of $Z_0 = \sqrt{L/C}$. Consistently with this single mode circuit, we find one peak in the $I(V)$ trace of the spectrometer that we fit to Eq. 9.4 (Fig. 9.7). We find a good quantitative agreement near the resonance peak, however the theoretical curve consistently deviates at higher voltages, i.e. higher frequencies. We attribute this discrepancy to additional losses or other resonant modes of the circuit not accounted for by Eq. 9.4.

In addition, we use the superconducting gap and the linear resistance of the junctions to determine the Josephson energy E_J and the Josephson inductance L_J . With these, we infer the circuit parameters listed in Table 9.2.

9

9.9.4. SPECTRUM ANALYSIS

Peaks in the $I(V)$ trace of the spectrometer correspond to peaks in $\text{Re}[Z(\omega)]$, i.e. allowed transitions of the environment coupled to the spectrometer. In order to remove the smooth background of the plasma mode (see Fig. 9.7), we evaluate $-d^2 I/dV^2(V)$, the second derivative of the $I(V)$ to find peaks in $\text{Re}[Z(\omega)]$ after applying a Gaussian low pass filter with standard deviation of $1.5 \mu\text{V}$. We benchmark this method in Fig. 9.9, and find that the peaks where $-d^2 I/dV^2(V) > 0$ correspond to the peaks in $I(V)$ and hence $-d^2 I/dV^2(V)$ is a good measure of the transitions detected by the spectrometer junction.

Alternatively, the background can be removed by linewise subtracting the detector response at $\varphi = 0$ [217], where the ABS does not contribute to the spectrometer response [223]. We show the result of this analysis in Fig. 9.10. Notably, the phase dependence of the plasma mode gives rise to additional features near $\varphi = \pi$. Furthermore, datasets

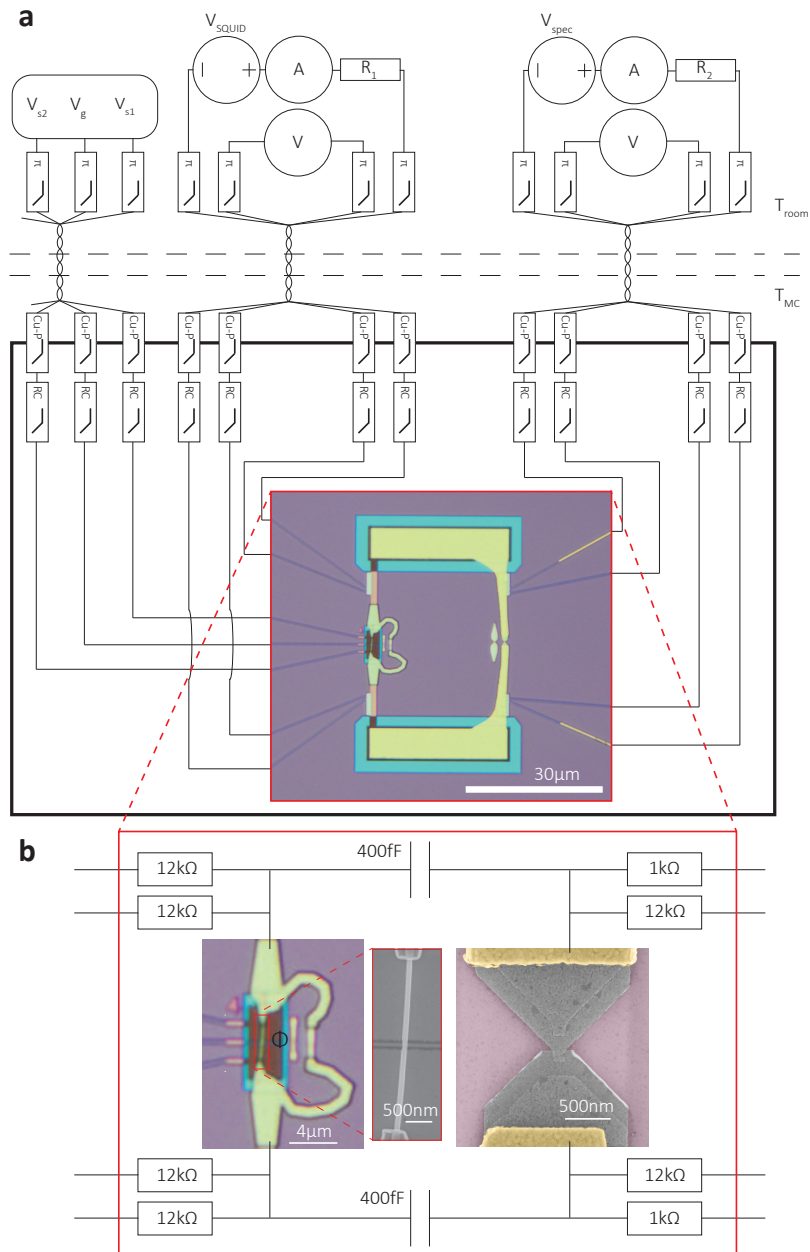


Figure 9.6: **Detailed schematics of the measurement setup.** The inset of panel (a) shows a bright field optical image of device 1. The solid black box denotes the radiation shielded environment thermally anchored to 12mK. (b) On-chip lumped circuit elements attached to the hybrid SQUID (on the left) and the spectrometer Josephson junction (on the right).

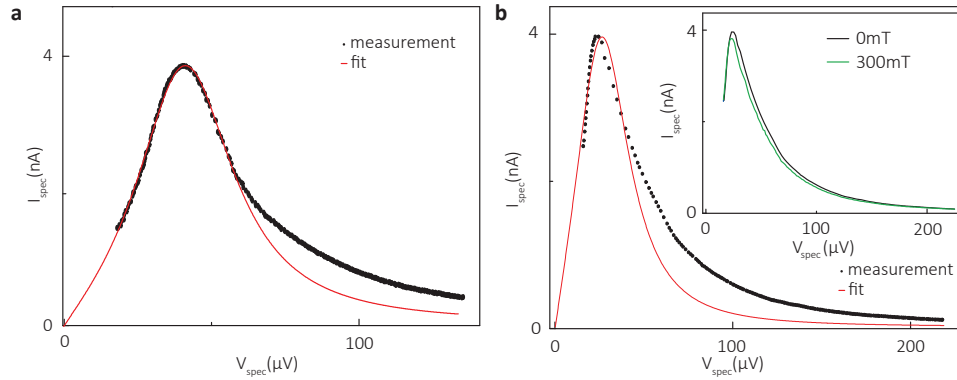


Figure 9.7: **Plasma resonance of the circuit.** The measured (black dots) and fitted (solid red line) $I(V)$ trace of the spectrometer junction for device 1 (a) and for device 2 (b) respectively, with the nanowire in full depletion. The fits are based on Eq. 9.4, see text. Note that we omitted the supercurrent branch for clarity. In panel (b), the inset shows the spectrometer response to an in-plane magnetic field of 300 mT.

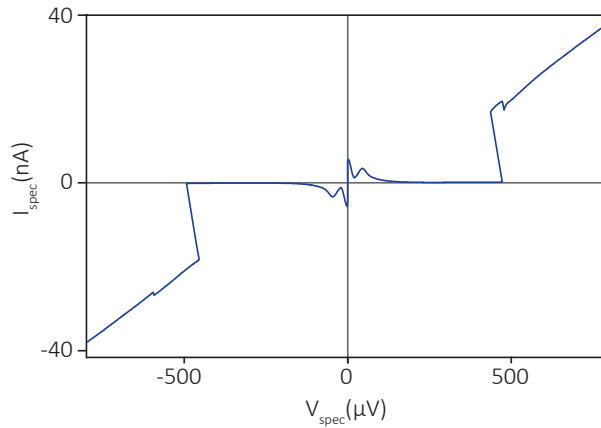


Figure 9.8: **Large scale $I(V)$ trace of the spectrometer junction.** The subgap features are shown in detail in Fig. 9.7a. The back-bending near $eV_{\text{spec}} \approx 2\Delta_{\text{spec}} = 482 \mu\text{eV}$ is attributed to a local overheating of the junction due to a large quasiparticle current density above the gap edge. The data was taken on device 1.

exhibiting the hybridization between the ABS and plasma mode cannot be evaluated by this method. However, the line subtraction and the second derivative are in agreement if there is sufficient spacing between the plasma mode and the ABS line (see Fig. 9.2b and Fig. 9.10 for comparison).

9.9.5. $I(V)$ TRACE OF THE HYBRID SQUID

We measure the $I(V)$ trace of the hybrid SQUID as a function of the gate voltage V_g at $V_{\text{spec}} = 0$ (Fig. 9.11) and find that the subgap conductance increases with increasing gate

	Device 1	Device 2
Tunnel junction resistance R_J (k Ω)	4.80	10.7
Tunnel junction gap Δ_J (μ eV)	245	250
Tunnel junction critical current $I_{c,J} = \frac{\pi\Delta_J}{2eR_J}$ (nA)	80.2	36.7
$E_J = \frac{\hbar I_{c,J}}{2e}$ (μ eV)	165	75.5
Tunnel junction inductance $L_J = \frac{\Phi_0}{2\pi I_{c,J}}$ (nH)	4.10	8.94
Spectrometer resistance R_{spec} (k Ω)	17.1	18.4
Spectrometer gap Δ_{spec} (μ eV)	241	249
Spectrometer critical current $I_{c,\text{spec}} = \frac{\pi\Delta_{\text{spec}}}{2eR_{\text{spec}}}$ (nA)	22.2	21.3
Shunt resistance R (Ω)	634	743
Shunt capacitance C (fF)	12.6	11.1
Charging energy $E_c = \frac{2e^2}{C}$ (μ eV)	25.44	29.1
Plasma frequency $f_p = \frac{1}{2\pi\sqrt{L_J C}}$ (GHz)	22.9	16.0
Characteristic impedance $Z_0 = \sqrt{\frac{L_J}{C}}$ (Ω)	551	897
Quality factor $Q = R\sqrt{\frac{C}{L_J}}$	1.15	0.83

Table 9.2: Circuit parameters of the devices featured in the current study.

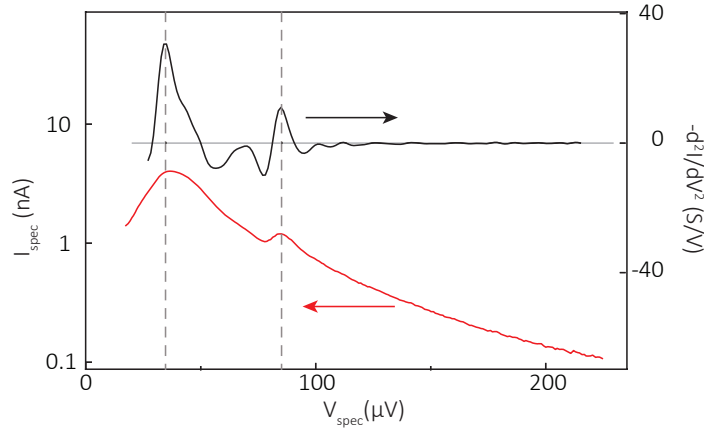


Figure 9.9: **Spectrum analysis by second derivative.** The $I(V)$ (red line, left axis) and the corresponding $-d^2I/dV^2(V)$ trace (black line, right axis) of the spectrometer showing the same peaks denoted by dashed lines. Note that only peaks above $-d^2I/dV^2(V) = 0$ (grey horizontal line) correspond to actual transitions. This dataset was taken on device 1, at $V_g = -1410$ mV, phase biased to $\varphi = \pi$.

voltage, in qualitative agreement with the contribution of multiple Andreev reflection (MAR). The zero voltage data corresponds to the supercurrent branch and the dashed lines denote the bias range where there is no data due to the bias instability of the driving

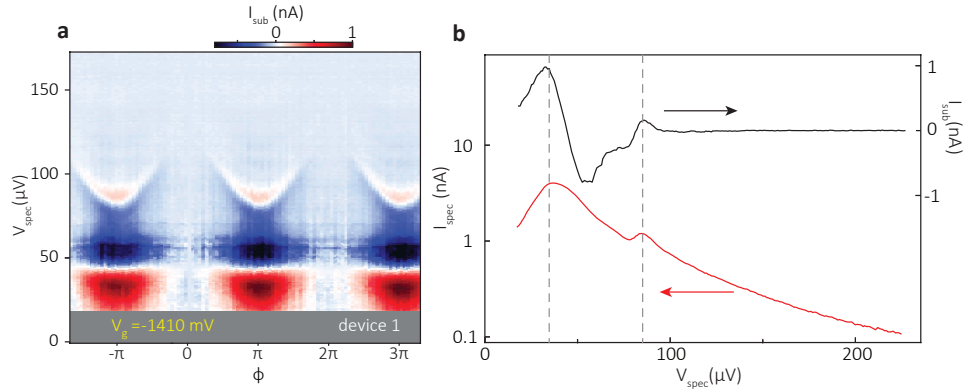


Figure 9.10: **Spectrum analysis by background subtraction.** (a) $I_{\text{sub}}(\phi) = I_{\text{spec}}(\phi) - I_{\text{spec}}(\phi = 0)$ spectrometer current after subtracting the line trace at $\phi = 0$. (b) Single linetrace of the raw data $I_{\text{spec}}(\phi = \pi)$ (red line, left axis) and $I_{\text{sub}}(\phi = \pi)$ (black line, right axis). This dataset was taken on device 1, at $V_g = -1410$ mV.

circuit. In addition, we find a back-bending at the gap edge $eV_{\text{SQUID}} = 2\Delta_J$, attributed to self-heating effects in the tunnel junction.

We evaluate G in Fig. 9.2e in the bias voltage range $-V_{\text{SQUID}} = 350 \dots 430 \mu\text{V} > 2\Delta$. We note that due to the soft superconducting gap in the nanowire junction, we did not identify MAR features after subtracting the current background of the tunnel junction.

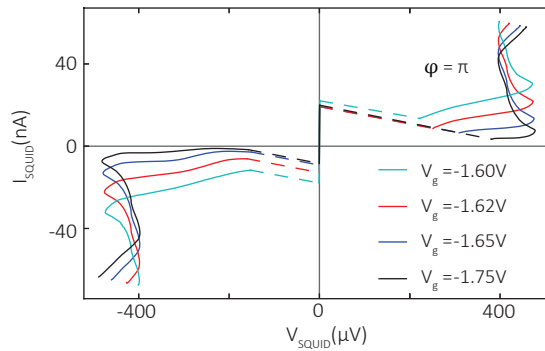


Figure 9.11: **The $I(V)$ trace of the hybrid SQUID.** At $V_g = -1.75$ V, the nanowire is in full depletion, thus the corresponding $I(V)$ trace represents the Al/AlO_x/Al tunnel junction in the hybrid SQUID. The bias voltage V_{SQUID} was swept from the left to the right. The data was taken on device 1.

9.9.6. FIT OF ABS WITH HIGH TRANSMISSION

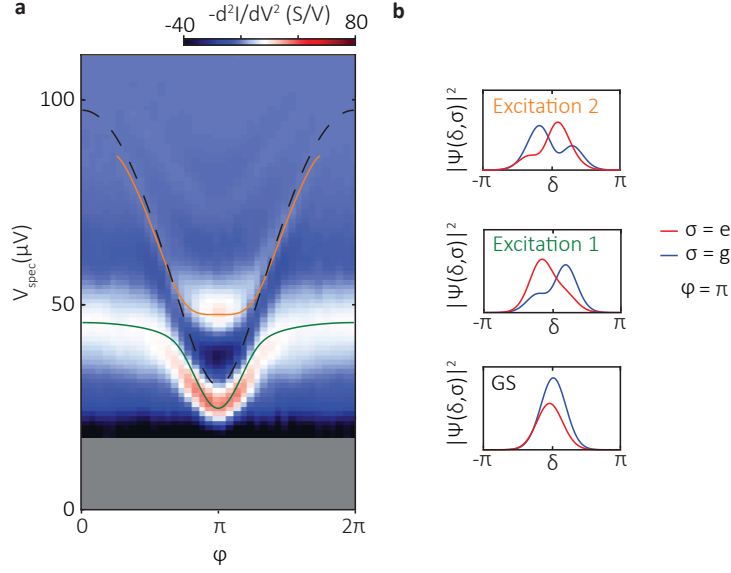


Figure 9.12: **Experimental data and fit to the theory for ABS with high transmission.** In this figure we show the numerical fit to the model of Eq. 9.3, similarly to Fig. 9.3a, but for a different dataset taken at $V_g = -1.525\text{V}$ on device 1. The figure shows that the model of Eq. 9.3 can accurately predict the avoided crossing originating in the coupling between the ABS and the plasma mode. Best-fit parameters are $\Delta = 97.5 \pm 1.7\ \mu\text{eV}$ and $T = 0.90 \pm 0.01$. Dashed line denotes the undressed Andreev level defined by Eq. 9.1. We note that the extracted value for Δ is lower than in Fig. 9.3a. This may stem from the fit underestimating the gap, since most of the datapoints are around $\varphi = \pi$, or due to a genuine dependence of Δ on V_g because of the change in the wavefunction overlap as a result of the electrostatic gating [239]. In panel (b), we show the probability density for the ground state (GS) and the two observed excited states denoted by the green and orange lines, respectively in panel (a) at $\varphi = \pi$.

9.9.7. SYMMETRY-BROKEN ABS IN BIPOLAR MAGNETIC FIELD

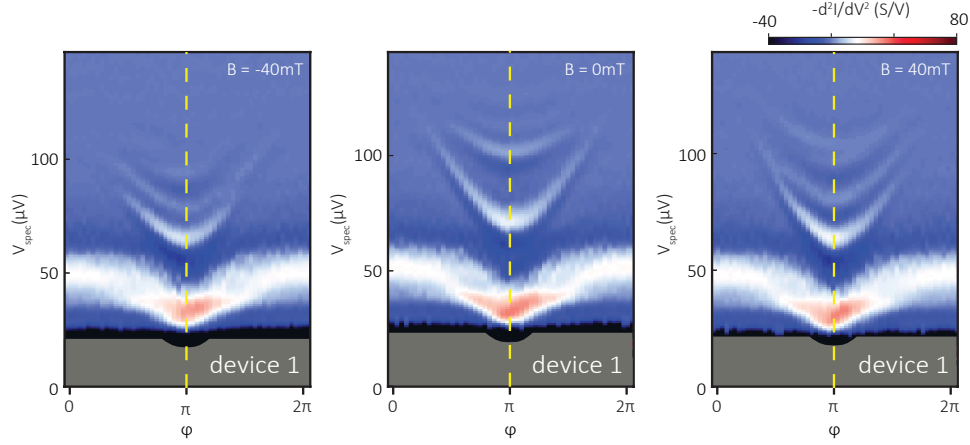


Figure 9.13: **Symmetry-broken ABS in a bipolar magnetic field.** The full spectrum is symmetric around $\varphi = \pi$ at zero magnetic field (center panel) with the mirror axis denoted by the yellow dashed line. Note the asymmetry of the two lowermost ABS transitions at $B = \pm 40$ mT. The antisymmetric contribution is most visible at $V_{\text{spec}} \approx 100 \mu\text{V}$, which develops an opposite shift for positive and negative magnetic fields, respectively. The data was taken on device 1 at $V_g = -770$ mV. Grey regions denote lack of data due to bias instability of the circuit.

9.10. THEORY

9.10.1. ESTIMATE OF THE ABS-PLASMA RESONANCE AVOIDED CROSSING

Before describing the quantum model of the circuit in detail, we discuss the estimate for the energy splitting at the avoided crossing between the ABS transition and the plasma frequency shown in Fig. 9.2d.

For simplicity, we model the plasma oscillations as a bosonic mode with a flux-independent frequency given by $\hbar\omega_p = \sqrt{2E_J E_C}$, and the weak link as a two-level system, with energies $\pm E_{\text{ABS}}(\varphi)$ defined by Eq. 9.1. This system with the two independent degrees of freedom is described by the Hamiltonian $\hat{H}_0 = \hbar\omega_p(\hat{a}^\dagger \hat{a} + \frac{1}{2}) + E_{\text{ABS}} \hat{\sigma}_3$. Next, we add the coupling term corresponding to the excitation of the weak link due to the voltage oscillations induced by the junction in the form

$$H_g(\varphi) = g(\varphi) \sqrt{z}(\hat{a}^\dagger + \hat{a}) \hat{\sigma}_1. \quad (9.5)$$

where $z = \sqrt{E_C/2E_J}$. This term describes a linear coupling between the two-level system and the phase difference across the junction. $g(\varphi)$ is then given by the current matrix element between the ground and excited states of the weak link, which was derived in Ref. [223]:

$$g(\varphi) = \Delta T \sqrt{1-T} \sin^2(\varphi/2) \frac{\Delta}{E_{\text{ABS}}(\varphi)}. \quad (9.6)$$

The square of this current matrix element gives the microwave absorption rate of the weak link, plotted in Fig. 9.3c (black dashed line). From the coupling Hamiltonian, we

immediately obtain that at $\varphi = \pi$, the splitting is

$$\varepsilon = \Delta T \sqrt{z}. \quad (9.7)$$

We note that Eq. 9.7 is the lowest-order estimate of the avoided crossing in the small parameter \sqrt{z} . The relatively high value $\sqrt{z} \approx 0.52$ of device 1 may explain the discrepancy between this simple estimate and the observed value which will be captured by the full model, see below. Finally, we note that the expression 9.6 was also derived in Ref. [225] starting from the full model (see next section). In particular, the quantity $\Omega_x(\varphi)$ in Ref. [225] is equal to $\sqrt{z}g(\varphi)$.

9.10.2. HAMILTONIAN DESCRIPTION OF THE HYBRID SQUID

We now describe the theoretical model of the hybrid SQUID that was used to fit the experimental data. Our model is based on Refs. [70] and [71]. The Hamiltonian of the model is Eq. 9.3, repeated here for convenience:

$$\hat{H} = E_C \hat{N}^2 + E_J(1 - \cos \hat{\delta}) + \hat{H}_{\text{ABS}}(\varphi - \hat{\delta}), \quad (9.8)$$

with $[\hat{\delta}, \hat{N}] = i$. The Hamiltonian of the weak link is [70]

$$\hat{H}_{\text{ABS}}(\varphi) = \Delta \hat{U}(\varphi) \left[\cos(\varphi/2) \hat{\sigma}_3 + \sqrt{1-T} \sin(\varphi/2) \hat{\sigma}_2 \right] \hat{U}^\dagger(\varphi) \quad (9.9)$$

with $\hat{U}(\varphi) = \exp(-i\sqrt{1-T}\hat{\sigma}_1\varphi/4)$. Here $\hat{\sigma}_2$ and $\hat{\sigma}_3$ are two Pauli matrices which act on a space formed by the ground state of the weak link and an excited state with a pair of quasiparticles in the weak link. By expanding the product above, the Hamiltonian can be put in the form $\hat{H}_{\text{ABS}}(\varphi) = V_2(\varphi)\hat{\sigma}_2 + V_3(\varphi)\hat{\sigma}_3$. The two functions V_2 and V_3 are:

$$V_2(\varphi) = \Delta \sqrt{1-T} \sin(\varphi/2) \cos(\sqrt{1-T}\varphi/2) - \Delta \cos(\varphi/2) \sin(\sqrt{1-T}\varphi/2), \quad (9.10)$$

$$V_3(\varphi) = \Delta \sqrt{1-T} \sin(\varphi/2) \sin(\sqrt{1-T}\varphi/2) + \Delta \cos(\varphi/2) \cos(\sqrt{1-T}\varphi/2), \quad (9.11)$$

We introduce the ground ($|g\rangle$) and excited states ($|e\rangle$) of the weak link in the presence of an equilibrium phase difference,

$$\hat{H}_{\text{ABS}}(\varphi) |g\rangle = -E_{\text{ABS}}(\varphi) |g\rangle, \quad (9.12a)$$

$$\hat{H}_{\text{ABS}}(\varphi) |e\rangle = +E_{\text{ABS}}(\varphi) |e\rangle, \quad (9.12b)$$

where $E_{\text{ABS}}(\varphi)$ is given in Eq. 9.1. In the basis $|\pm\rangle$ of eigenstates of $\hat{\sigma}_3$, $\hat{\sigma}_3|\pm\rangle = \pm|\pm\rangle$, they are given by

$$|g\rangle = c_{g+}(\varphi) |+\rangle + c_{g-}(\varphi) |-\rangle, \quad (9.13a)$$

$$|e\rangle = c_{e+}(\varphi) |+\rangle + c_{e-}(\varphi) |-\rangle, \quad (9.13b)$$

with coefficients

$$c_{g+}(\varphi) = i \frac{E_A(\varphi) - V_3(\varphi)}{\sqrt{2E_A(\varphi)[E_A(\varphi) - V_3(\varphi)]}}, \quad c_{g-}(\varphi) = \frac{V_2(\varphi)}{\sqrt{2E_A(\varphi)[E_A(\varphi) - V_3(\varphi)]}}, \quad (9.14a)$$

$$c_{e+}(\varphi) = -i \frac{E_A(\varphi) + V_3(\varphi)}{\sqrt{2E_A(\varphi)[E_A(\varphi) - V_3(\varphi)]}}, \quad c_{e-}(\varphi) = \frac{V_2(\varphi)}{\sqrt{2E_A(\varphi)[E_A(\varphi) + V_3(\varphi)]}}. \quad (9.14b)$$

The coefficients are normalized:

$$|c_{g+}(\phi)|^2 + |c_{g-}(\phi)|^2 = |c_{e+}(\phi)|^2 + |c_{e-}(\phi)|^2 = 1. \quad (9.15)$$

To find the resonant frequencies of the hybrid SQUID, we solve the eigenvalue problem $\hat{H}|\Psi\rangle = E|\Psi\rangle$ numerically. We adopt the basis $|\delta, \pm\rangle \equiv |\delta\rangle \otimes |\pm\rangle$ for the joint eigenstates of the $\hat{\delta}$ and $\hat{\sigma}_3$ operators: $\hat{\delta}\hat{\sigma}_3|\delta, \pm\rangle = (\hat{\delta}|\delta\rangle) \otimes (\hat{\sigma}_3|\pm\rangle) = \pm\delta|\delta, \pm\rangle$. For the numerical solution, we use a truncated Hilbert space where the phase interval $[-\pi, \pi)$ is restricted to M discrete points, with lattice spacing $2\pi/M$. A complete basis of the truncated Hilbert space is given by the $2M$ vectors $|\delta_k\rangle \otimes |\pm\rangle$ with $\delta_k = 2\pi k/M$ ($k = 0, \pm 1, \pm 2, \dots, \pm(M-1)/2$), and $|\pm\rangle$ the eigenvector of $\hat{\sigma}_3$. The Hamiltonian is thus represented as a $2M \times 2M$ matrix in this basis and diagonalized numerically. We choose the parameter M large enough to guarantee convergence of the eigenvalues.

Once the spectrum is known, we use the transition frequencies from the ground state, $\omega_n = E_n - E_{GS}$, to do a least-square fit to the experimental data. The details of the numerical procedure are listed in the Jupyter notebooks available at [240].

Once an eigenstate $|\Psi\rangle$ is determined numerically, we represent its two-component wave function in the basis of the weak link eigenstates $\{|g\rangle, |e\rangle\}$ from Eq. 9.13, evaluated at $\phi = \varphi$:

$$|\Psi\rangle = \sum_{\delta} \sum_{\sigma=g,e} \Psi(\delta, \sigma) |\delta, \sigma\rangle, \quad \Psi(\delta, \sigma) = \langle \delta, \sigma | \Psi \rangle, \quad (9.16)$$

where

$$|\delta, \sigma\rangle = |\delta\rangle \otimes (c_{\sigma+}(\varphi)|+\rangle + c_{\sigma-}(\varphi)|-\rangle). \quad (9.17)$$

The probability densities $|\Psi(\delta, \sigma)|^2$ plotted in Fig. 9.3b and Fig. 9.12b allow us to evaluate at a glance whether the eigenstate $|\Psi\rangle$ has a large overlap with the excited state $\sigma = |e\rangle$ of the (decoupled) weak link.

Finally, in Fig. 9.3c we show the numerical prediction for the visibility of the ABS transition as a function of the phase bias, ϕ . The visibility is determined by the absolute square of current operator matrix element $\langle GS | \hat{J}(\varphi) | \Psi \rangle$ between the ground state $|GS\rangle$ and the excited state $|\Psi\rangle$ of \hat{H} corresponding to the ABS transition. The current operator is [71]

$$\hat{J}(\varphi) = E_J \sin(\hat{\delta}) + \frac{\partial H_{ABS}(\varphi - \hat{\delta})}{\partial \hat{\delta}}. \quad (9.18)$$

9

9.10.3. EQUILIBRIUM PHASE DROP

We have assumed that the equilibrium phase drop across the weak link, ϕ , is close to the total applied phase, $\phi \approx \varphi$. Here, we verify this assumption by calculating the equilibrium phase drop of the hybrid SQUID model we presented in the previous section.

Since $\phi = \varphi - \delta$, (see Eq. 9.8), it is sufficient to show that the equilibrium phase drop $\delta \equiv \langle GS | \hat{\delta} | GS \rangle$ across the tunnel junction is small. δ is given by the position where the ground state Josephson energy of Eq. 9.8 is minimal for $E_C = 0$. From this condition, after taking a derivative of the Josephson energy, we obtain the following transcendental equation for δ :

$$E_J \sin(\delta) + \frac{\Delta T}{4} \frac{\sin(\delta - \varphi)}{\sqrt{1 - T \sin^2[(\varphi - \delta)/2]}} = 0. \quad (9.19)$$

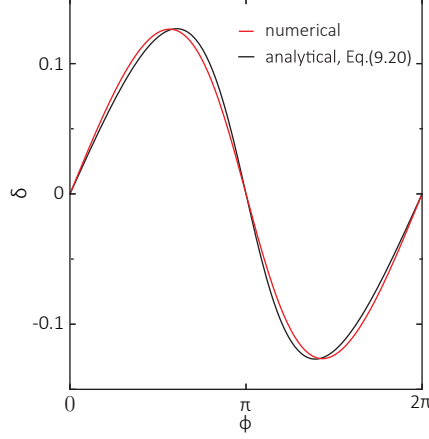


Figure 9.14: **Equilibrium phase drop δ across the tunnel junction.** The black line is given by Eq. 9.20, the red line by the numerical solution of Eq. 9.19. In both cases, we use the same circuit parameters as in Fig. 9.3a: $\Delta = 122 \mu\text{eV}$, $T = 0.57$, $E_J = 165 \mu\text{eV}$.

We note that the above expression defines a zero net current through the hybrid SQUID with the two arms hosting the same supercurrent. For $E_J \gg \Delta T/4$, a good approximate solution is given by

$$\delta \approx \frac{\Delta T}{4E_J} \frac{\sin(\varphi)}{\sqrt{1 - T \sin^2(\varphi/2)}}. \quad (9.20)$$

up to quadratic corrections in $(\Delta T/E_J)$. In Fig. 9.14 we show that for the parameters used in Fig. 9.3a, this approximate solution is very close to the exact, numerical one. Both exhibit a sinusoidal behavior with a maximum $\delta \approx 0.12$ at $\varphi \approx \pi/2$. This confirms that the phase drop across the weak link, $\phi = \varphi - \delta$, remains very close to the applied phase φ everywhere. In particular, ϕ is exactly equal to φ at $\varphi = n\pi$, where n is integer.

9.10.4. ANDREEV BOUND STATES IN A PROXIMITIZED RASHBA NANOWIRE IN A PARALLEL MAGNETIC FIELD

In this Section, we introduce the model used to describe the behavior of ABS as a function of the magnetic field B . We start from the standard Bogoliubov-de Gennes (BdG) Hamiltonian of a Rashba quantum wire with proximitized s -wave superconductivity and an external Zeeman field [7, 8]:

$$H_{\text{BdG}} = -\left(\frac{\partial_x^2}{2m} - E_F\right)\tau_z - i\alpha\partial_x s_z\tau_z + E_Z s_x + \Delta e^{i\phi\theta(x)\tau_z}\tau_x + V\delta(x)\tau_z. \quad (9.21)$$

Here, the two sets of Pauli matrices $\tau_{x,y,z}$ and $s_{x,y,z}$ act in the Nambu and spin spaces, respectively; $m = 0.023m_e$ is the effective mass in InAs [241], α is the Rashba spin-orbit coupling strength which defines $E_{\text{SO}} = m\alpha^2/2$. $E_Z = \frac{1}{2}g\mu_B B$ is the Zeeman energy, Δ is the proximity induced gap and θ is the Heaviside step function. The Fermi level E_F

is measured from the middle of the Zeeman gap in the normal state band dispersion, see Fig. 9.16. Note that starting with Eq. 9.21 we set $\hbar = 1$. The superconducting phase difference between the left lead ($x < 0$) and the right lead ($x > 0$) is denoted by ϕ . The last term of Eq. 9.21 models a short-range scatterer at $x = 0$, accounting for the finite channel transmission.

We seek bound state solutions of the the BdG equations,

$$H_{\text{BdG}} \Psi(x) = E \Psi(x), \quad (9.22)$$

at energies $|E| < \Delta$. We will consider in particular two opposite regimes: (a) $E_F \gg E_{\text{SO}}, E_Z, \Delta$ and (b) $E_F = 0$, see the two insets in the corresponding panels of Fig. 9.16. In order to find bound state solutions we proceed as follows:

1. We linearize the BdG equations for the homogeneous system ($V = 0, \phi = 0$) around $E = E_F$. In this way, we obtain two effective low-energy Hamiltonians, $H_{\text{eff}}^{(a)}$ and $H_{\text{eff}}^{(b)}$, which are linear in the spatial derivative. They can be written as:

$$H_{\text{eff}}^{(a)} = -i\nu \partial_x \tau_z \sigma_z - \nu q_0 \tau_z \rho_z + \frac{\Delta \alpha k_F}{\nu q_0} \tau_x \sigma_z + \frac{\Delta E_Z}{\nu q_0} \tau_y \rho_y, \quad (9.23a)$$

$$H_{\text{eff}}^{(b)} = -i\alpha \partial_x \tau_z \sigma_z + \Delta \tau_x + \frac{1}{2} E_Z \sigma_z (1 - \rho_z). \quad (9.23b)$$

We now have three sets of Pauli matrices: $\tau_{x,y,z}$ (Nambu space), $\rho_{x,y,z}$ (distinguishing the inner/outer propagating modes, and replacing the spin matrices $s_{x,y,z}$ of Eq. 9.21), and $\sigma_{x,y,z}$ (distinguishing left- and right-moving modes, and not to be confused with the σ matrices used in the previous Section). For regime (a), we have also introduced the Fermi momentum $k_F = \sqrt{2mE_F}$, the Fermi velocity $\nu = k_F/m$ and the energy difference $\nu q_0 = \sqrt{\alpha^2 k_F^2 + E_Z^2}$ between the two helical bands at the Fermi momentum. Note that, in the regime (b) where $E_F = 0$, the linearization requires $E_{\text{SO}} \gg \Delta, E_Z$, so it corresponds to the limit of strong spin-orbit coupling.

9

2. Using Eq. 9.21, we compute the transfer matrix \mathcal{T} of the junction in the normal state ($\Delta = 0$), at energy $E = E_F$. The transfer matrix gives a linear relation between the plane-wave coefficients of the general solution on the left and right hand sides of the weak link. In computing \mathcal{T} , we neglect all terms $\propto E_F^{-1}$ in regime (a). In regime (b), the transfer matrix is computed for $E_Z = 0$, since the effect of magnetic field on scattering can be neglected to due the small dwelling time in the short junction. At $E_Z = 0$, the transfer matrix depends on the single real parameter T , the transmission probability of the junction. The latter is given by $T = 4k_F^2/(4k_F^2 + V^2)$ in regime (a), and $T = 1/(1 + V^2/\alpha^2)$ in regime (b).
3. Using the transfer matrix \mathcal{T} as the boundary condition at $x = 0$ for the linearized BdG equations, we obtain the following bound state equation for E :

$$\det \left[1 - G(E) \tau_z \sigma_z \left(e^{-i\phi \tau_z / 2} \mathcal{T} - 1 \right) \right] = 0, \quad (9.24)$$

where $G(E)$ is the integrated Green's function,

$$G(E) = v \int \frac{dq}{2\pi i} e^{-iq \cdot 0} [H_{\text{eff}}(q) - E]^{-1}, \quad (9.25)$$

and $H_{\text{eff}}(q)$ is the Fourier transform of either of the linearized Hamiltonians of Eq. 9.23. [In regime (b), v must be replaced by α in the expression for $G(E)$]. In deriving the bound state equation, we have neglected the energy dependence of the transfer matrix, which is appropriate in the short junction limit. In regime (b), this also requires that the length of the junction is shorter than α/E_Z , so that we can neglect resonant effects associated with normal-state quasi-bound states in the Zeeman gap, which would lead to a strong energy dependence of the transmission [242]. Eq. 9.24 is analogous to the bound state equation for the ABS derived in Ref. [98], except that it is formulated in terms of the transfer matrix of the weak link, rather than its scattering matrix. Unlike its counterpart, Eq. 9.24 incorporates the effect of the magnetic field in the superconducting leads. It is thus appropriate to study the effect of a magnetic field on the ABS in the limit of uniform penetration of the field in the superconductor.

4. After performing the integral for $G(E)$, the roots of Eq. 9.24 can be determined numerically. For the two regimes, this leads to the typical behavior of the ABS shown in Fig. 9.16 against the experimental data. We find a better agreement with the experimental data for regime (a).

From $G(E)$, we can also compute the proximity-induced gap of the continuous spectrum $\Delta(B)$: $\Delta(B)$ is the minimum value of E such that the poles of $G(E)$ touch the real axis in the complex plane [of course, $\Delta(B)$ can also be found by minimizing the dispersion relation obtained by diagonalizing Eq. 9.23 in momentum space]. In regime (a), the relevant spectral gap is always at the finite momentum, so the behavior of $\Delta(B)$ depends on the strength of the spin-orbit coupling, as shown in Fig. 9.15. Two features are evident from the figure.

First, with increasing spin-orbit coupling, the linear behavior $\Delta(0) - \Delta(B) \propto B$ changes to a quadratic suppression $\Delta(0) - \Delta(B) \propto B^2$ for small B . This is due to the vanishing first-order matrix elements of the Zeeman interaction, due to the removal of the spin degeneracy of finite-momentum states by the spin-orbit interaction. Secondly, the proximity-induced gap $\Delta(B)$ never closes – as long as the superconductivity in the aluminium shell is present – because spin-orbit interaction competes with the Zeeman effect and prevents the complete spin polarization of the electrons. These two facts explain the behavior of $\Delta(B)$ shown in Fig. 9.4b. In regime (b) with $E_F = 0$, which is extensively discussed in the literature of Majorana bound states, $\Delta(0) - \Delta(B) \propto B$ due to the Zeeman-induced suppression of the gap for states at zero momentum (where spin-orbit is not effective).

An in-depth theoretical study of Eq. 9.24, including a detailed analysis of its roots at finite magnetic fields and the code used in the numerical solution, is in preparation. It will also be interesting to extend the current model beyond the linearization to allow the calculation of the spectrum at arbitrary values of E_F .

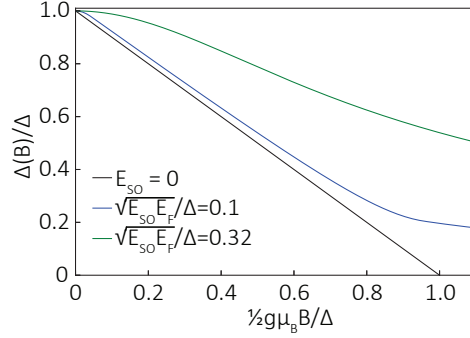


Figure 9.15: **The effect of the spin-orbit interaction and Zeeman field on the induced superconducting gap.** The lack of spin-orbit interaction leads to a linear decrease of $\Delta(B)$ (black line), which becomes parabolic in the limit of $\sqrt{E_{SO}E_F} \ll E_Z = \frac{1}{2}g\mu_B B$ (blue and green lines). The green line corresponds to the best fit to the experimental data.

9.10.5. ORBITAL FIELD

Because a quadratic suppression of $\Delta(B)$ and the ABS energies may also be due to the orbital effect of the magnetic field, without invoking spin-orbit interaction, it is important to compare the data with this scenario. In a simple model which includes orbital and Zeeman effect, the field-dependence of the Andreev bound states may be written down as follows:

$$E_{\text{ABS},\pm}^{(\text{orb})}(\phi, B) = \Delta(1 - B^2/B_*^2) \sqrt{1 - T \sin^2(\phi/2)} \pm (1/2)g\mu_B B. \quad (9.26)$$

Here, $B_* \sim \Phi_0/A$ is the magnetic field scale which governs the suppression of the proximity-induced gap due to the orbital field, A is the cross-section of the nanowire and $\Phi_0 = h/2e$. In writing Eq. 9.26, we have neglected the effect of the orbital field on the scattering at the junction. This should be a good approximation as long as the junction is modeled by a $\delta(x)$ potential with no dependence on the radial coordinate of the nanowire. Thus, essentially, the phase dependent part of the Andreev bound state energies can be obtained by replacing Δ with $\Delta(1 - B^2/B_*^2)$ in Eq. 9.1. In the absence of spin-orbit coupling, the Zeeman term enters additively in Eq. 9.26.

Using Eq. 9.26, we can perform a fit to the experimental data to determine the optimal value $B_* = 400 \pm 2$ mT. Note that the fit is insensitive to the value of g , since g drops out from the sum $E_{\text{ABS},+}^{(\text{orb})} + E_{\text{ABS},-}^{(\text{orb})}$. However, Eq. 9.26 predicts the occurrence of a fermion parity-switch at a field $B_{\text{sw}} < B_*$ given by the condition $E_{\text{ABS},-}^{(\text{orb})}(\phi, B_{\text{sw}}) = 0$. From this condition, and assuming the knowledge of both B_{sw} and B_* , the g -factor can then be deduced by inverting Eq. 9.26 at $\phi = \pi$,

$$g = \frac{\Delta\sqrt{1-T}}{\mu_B B_{\text{sw}}} (1 - B_{\text{sw}}^2/B_*^2) \quad (9.27)$$

The occurrence of this fermion-parity switch must be accompanied by a drastic disappearance of the ABS transition [74]. In the experiment, such disappearance can be excluded up to at least 300 mT. Therefore, by requiring that $B_{\text{sw}} > 300$ mT, we obtain an

upper bound of g ,

$$|g| < 5.08 \quad (9.28)$$

The above estimate motivates the approximation, where we attribute the quadratic suppression to the joint effect of spin-orbit and Zeeman couplings; the orbital effects may play only a sub-leading role.

9.10.6. FITS TO THE DATA

We have just presented three different scenarios that can be used to interpret the magnetic field dependence of the ABS transition energies. We have fitted all three models to the entire data set available, consisting of a flux bias sweep of the ABS spectra at six different magnetic fields ($B = 50, 75, 100, 150, 200$ and 300 mT). For each flux bias at which it was visible, we have extracted the position of the ABS transition. For each value of B we attributed to all the data points an error bar corresponding to the half-width at half-maximum of the ABS peak at $\varphi = \pi$, neglecting for simplicity the flux variation of the width. The total dataset consisted of more than 300 datapoints. We then performed a least-square fit to the ABS transition energies predicted by the three different models. The results are illustrated in Fig. 9.16.

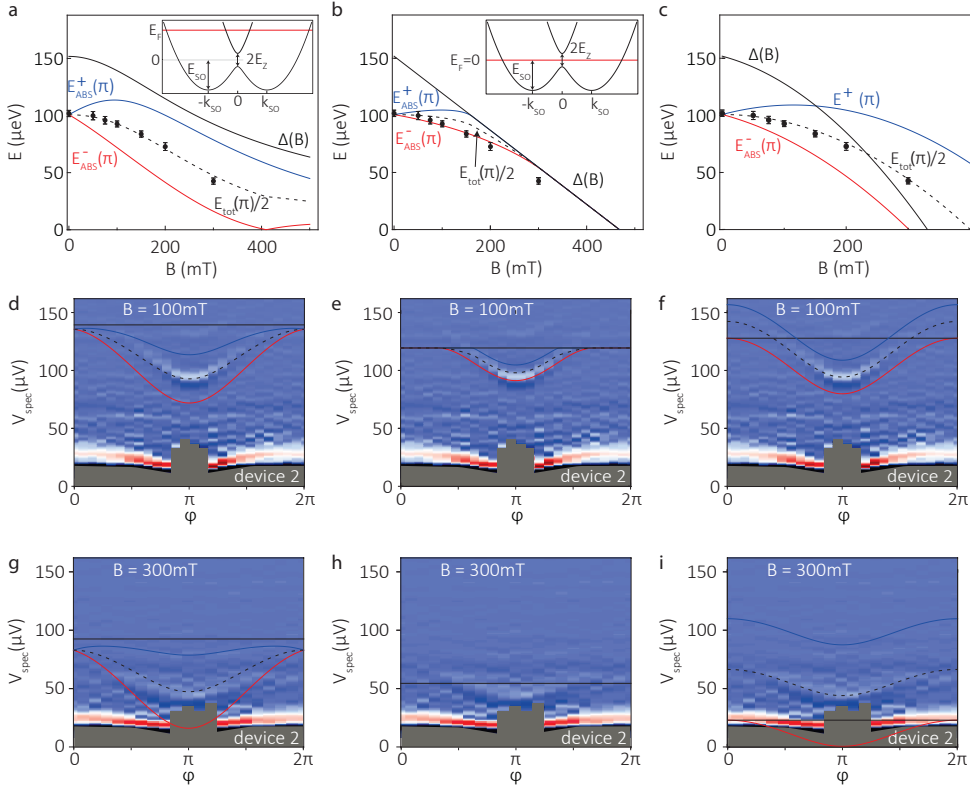


Figure 9.16: **The magnetic field dependence of ABS in high and low Fermi level regimes and for orbital magnetic field.** The top row shows the evolution of the spin split Andreev bound states $E_{\text{ABS}}^{\pm}(\pi)$ (blue and red lines, respectively), the superconducting gap $\Delta(B)$ (black solid line) and $E_{\text{tot}}(\pi) = E_{\text{ABS}}^{+}(\pi) + E_{\text{ABS}}^{-}(\pi)$ (dashed line) with the experimental data (black dots) for the large Fermi level limit (a), for zero Fermi level (b) and for orbital magnetic field (c). The corresponding ABS dispersion overlain on the measured spectrum as a function of φ at $B = 100$ mT (middle row, panels d, e and f) and at $B = 300$ mT (bottom row, panels g, h and i), respectively. Each row features the same experimental dataset. The global fit parameters for the left column are $g = 14.7 \pm 0.6$ and $\sqrt{E_{\text{SO}}}EF/\Delta = 0.32 \pm 0.02$. The middle column is evaluated with a single fit parameter $g = 11.2 \pm 0.1$. Note the lack of dispersion in panel (h), due to the merging of the Andreev bound states with the continuum, which causes all the lines to fall on top of each other. In the right column we use the best-fit value $B_* = 400 \pm 2$ mT and $g = 5$, the latter imposed by the lower bound on the parity switching field $B_{\text{sw}} > 300$ mT, where $E_{\text{ABS}}^{-}(\pi) = 0$.

10

OUTLOOK

David J. van Woerkom

Nature shows us only the tail of the lion.

Albert Einstein

Majorana zero energy modes (MZM) are interesting because of their expected non-abelian properties, which could be used for topological quantum computing. MZM are promising because they are more robust against local perturbations in the environment. However, before one can think of braiding experiments, which should reveal their non-abelian exchange statistics, more of their properties need to be characterized and discovered.

In this chapter, we discuss how our experiments could be improved in order to pave the way towards braiding. We also discuss questions that need to be answered before we can properly design devices capable of braiding MZM. We need to answer these questions experimentally, and find the coupling strengths in topological (multi-leg) Josephson junctions and the timescales required to perform the braiding.

10.1. INTRODUCTION

The objective of the institute/research group where the reported PhD research was performed is to build a quantum computer capable of outperforming a classical computer. The material system in this thesis focuses on the emergence of MZM, which can be used as topological quantum bits (qubits)[16, 17, 35]. Topological quantum computing is expected to be more robust against small fluctuations in the environment. At the moment, topological qubits are still being developed. For this reason, we focus in this outlook on the experiments necessary to further identify MZM and demonstrate their properties. This should lead to better control of the MZM, which should in turn lead finally to braiding and a topological qubit.

10.2. PERSPECTIVES ON MATERIAL IMPROVEMENT

The most important part of the devices used for MZM research is the combination of a semiconductor nanowire and a superconductor. It is this material combination that can lead to an inverse superconducting gap, called the topological gap, as was introduced in Section 3.4.2. It is important that this gap is uniformly induced in the nanowire, as then it leads to: (1) a hard gap in the nanowire[198] which suppresses the density of states (DOS) for the quasiparticles within; and (2) no creation of extra MZM.

The hard gap in the nanowire is important, as when there are no available states within the induced gap, quasiparticles must occupy states above the gap, which are exponentially suppressed with temperature. We find that the superconductor used in Chapter 6 has subgap states which reduce the effective gap to $15\text{-}25\mu\text{eV}$. This reduction in the effective gap was recently studied theoretically, and a model with disorder in the form of nonmagnetic scatterers and pairing-potential impurities was used to explain the subgap states and the reduced superconducting gap [87, 186]. The superconductor (NbTiN) used in Chapter 6 exhibits these subgap states and is therefore not favorable for MZM research. We suggest using Al, which has the lowest Dynes parameter ever reported[165]. The Dynes parameter is a measure of all the possible mechanisms that can make the measured DOS deviate from the expected textbook DOS, eq. 3.8. Even in combination with a nanowire, Al has shown parity effects[14, 22, 23].

In a recent study, it was also shown that a disorder superconductor can lead to pair-breaking in the induced superconductivity in the nanowire[243]. The pair-breaking leads to gap reduction, or even closure of the induced gap[79]. This pair-breaking is expected where there is moderate or strong coupling between the nanowire and a superconductor with disorder[243].

Figure 10.1 shows images of these nanowires in combination with the Al. The interface between the nanowire and the superconductor has been claimed¹ to be epitaxial [20], but it is at least clean enough to induce a hard superconducting gap in the nanowire[21]. These nanowires are a great improvement on the material system used in early MZM experiments[9, 108], but we still wish to suggest the following three improvements.

10

¹Based on questions raised by our material experts, the image shown in Figure 10.1b and published in ref. [20] is not enough to claim epitaxiality.

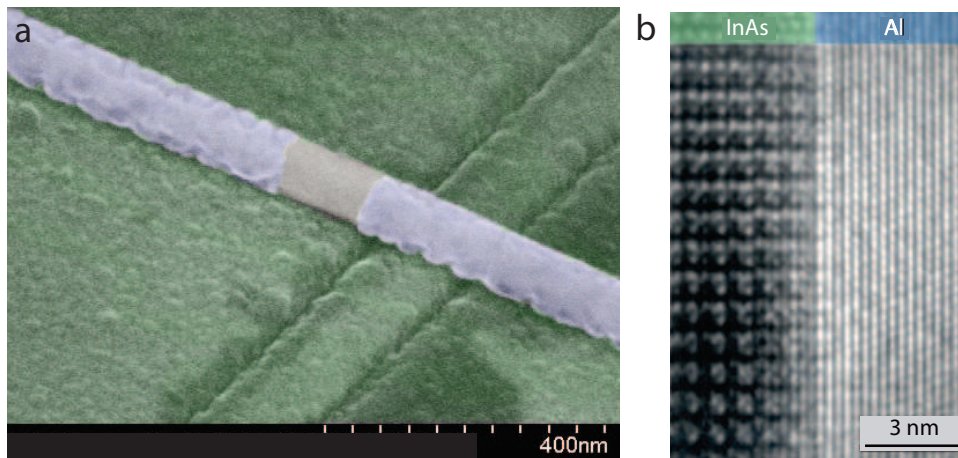


Figure 10.1: **a** False-colour SEM image of a nanowire Josephson junction (misaligned with the bottom gate). The purple indicates the Al on the nanowire (which is shown in brown). The Al thickness is not homogeneous over the nanowire facets. **b** Transmission electron microscope image, from ref. [20], showing a sharp and clean interface between the InAs and the Al.

1. **Use a nanowire semiconductor with a higher g -factor.** The nanowires in ref. [20] are InAs, which have a g -factor of 10–15 (see Chapter 9). Assuming a typical induced superconducting gap of $\sim 200\mu\text{eV}$, the lowest magnetic field where the topological transition can be expected is 0.5–0.7T. At this magnetic field, the host superconductor is strongly influenced. The quasiparticle DOS of the Al is spin-split[212]. Also, due to the spin splitting, the Cooper pairs are forced into finite momentum pairings, leading to modification of the DOS and reduction of the gap[244]. A magnetic field also leads to Meissner screening currents and vortex creation, which leads to local reduction of the superconducting gap.

The effects described above are proportional to the applied magnetic field. The creation of the topological gap requires a sufficiently large Zeeman energy, which is proportional to the magnetic field via the g -factor. For this reason InSb, which has a g -factor of 50–70[245], is more favorable because the required magnetic field for the topological transition is lower.

In general, InSb nanowires are not (or hardly) conductive at zero gate voltage, because the Fermi level is within the bandgap[12, 205]. When a superconductor is deposited, as for example was done in ref. [20], the semiconductor close to the interface cannot be gated due to screening of the superconductor. This lack of gating and the Fermi level in the bandgap creates an uncontrolled barrier between the metal/superconductor and the core of the nanowire. The induced superconducting gap in InAs, reported in refs. [21, 51], is probably so hard because InAs is known to have a surface accumulation layer [246, 247]. To overcome this problem, one can dope the surface of InSb *in situ*² or grow the InSb with doping to put the

²In a solution of sulphur, as in ref. [12], in (for example) a glove box attached to the nanowire growth machine before the deposition of a superconducting shell

Fermi level in the bandgap. In ref. [248], $\text{InAs}_x\text{Sb}_{1-x}$ is suggested to optimize spin-orbit strength, but perhaps Fermi level surface pinning can also be achieved due to the combination with As.

2. **Improve thickness homogeneity to have a constant superconducting gap in the (host) superconductor.** Variation of Al thickness leads to variations in the superconducting gap[249]. Because of this variation, local minima in the quasiparticle DOS can arise[184], which can trap quasiparticles. To reduce this effect, we need to eliminate the variations in superconductor thickness we currently have, see Figure 10.1a. In addition, this will also induce a uniform superconducting gap in the nanowire.
3. **Introduce a controlled barrier at the semiconductor/superconductor interface.** If the superconductor has disorder, this can also lead to pair-breaking in the induced superconductivity in the nanowire[243]. This ‘leaking’ of disorder into the nanowire depends on the coupling between the nanowire and the superconductor. Currently, this coupling is very strong for the Al and InAs material system, as can be seen from the TEM images shown in Figure 10.1b. Other signatures of strong coupling are visible in direct transport data, the hard induced gap and fact that the value of the induced gap is approximately the same as the superconducting gap of the host superconductor[21].

If it is possible to create a controlled barrier, for example by the atomic layer deposition of Al_2O_3 at the superconductor/semiconductor interface, then the disorder leakage can be reduced [243]. The induced gap in the nanowire can also be engineered to be smaller[250]. A (controlled) smaller induced gap leads to a lower magnetic field requirement for the topological phase transition.

If the three suggested improvements can be implemented, the topological transition is expected to occur at $\sim 40\text{mT}$ (with g -factor ~ 50 and $\Delta_{\text{NW}} \sim 60\mu\text{eV}$). This lower magnetic field value reduces the requirements on the MZM braiding and detection circuit.

Experimentalists often refer to the critical magnetic field of a superconductor, but superconductors lose their nice properties at a (much) lower magnetic field[12, 22, 64, 90].

10.2.1. GATES AND DIELECTRIC

Previous attempts to use local fine gates to show the non-local behaviour of MZM, sharing the same topological gap, were not successful[33]. The authors argued that local imperfections in the gates resulted in air voids between nanowire and dielectric, leading to non-uniform electrostatic gating. This non-uniform gating makes it challenging to tune the chemical potential in the helical gap, as required for MZM (see Section 3.4.2).

In the scanning electron microscope (SEM) image in Figure 10.2, we highlight a topological region (red line) in a nanowire with an MZM (green star). The first question that arises is, can the discontinuity in the gates at (1) keep the chemical potential within the helical gap and maintain a single topological region? And secondly, can the topological region be extended by the three fine gates at (2)? At the moment, experimental control of the MZM in tunnel spectroscopy is limited[15, 33]. To reduce the air voids and improve

the gating, one could do a 15nm-deep (HF-)etch in the SiO substrate before the 5/10nm Ti/Au gates are deposited. This technique is quick and easy to implement, and should increase electrostatic gate control.

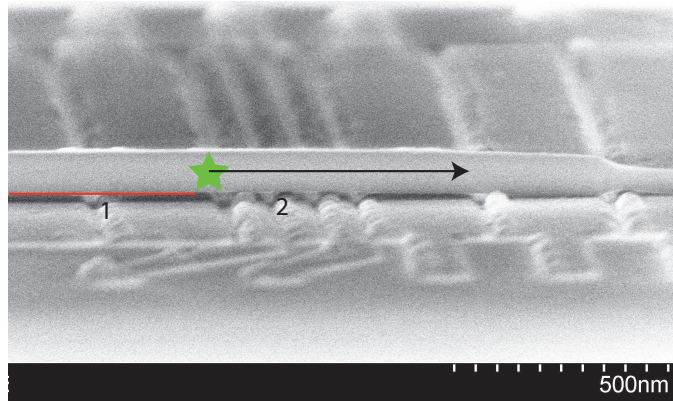


Figure 10.2: SEM image of a nanowire on local fine gates. Air voids are present between the nanowire and the dielectric, which leads to non-uniform gating[139]. This SEM image is an extreme case since the gold lift-off for the gates left small bumps, lifting the nanowire from the flat parts of the gates. The red line depicts the topological region, with the MZM at the end (green star). The question is: can the topological region be extended over the regions with air voids?

10.3. PERSPECTIVES ON POISONING DYNAMICS

In the experiment reported in Chapter 6, we used switching current measurements to determine the parity of a superconducting island. For islands formed by two SIS junctions in series, it has been shown that this measurement technique is a reliable way to determine the parity[155]. The island can also be formed by two nanowire Josephson junctions in series. These kinds of structures are often used in MZM braiding schemes[17, 35, 209, 251]. Figure 10.3a depicts an InAs nanowire with an Al shell, where two regions have been etched to form an island. We can also make an island by, for example, depositing NbTiN on an InSb nanowire, as shown in Figure 10.3b.

A challenge with this experiment is to determine the location of the poisoning. The supercurrent flows through the entire device and the poisoning can happen either in the Andreev bound states in the junction[54] or the island. By measuring the gate response it is possible to identify if the switching current fluctuation is periodic (island poisoning) or arbitrary (ABS poisoning).

A more promising direction for parity detection is the use of local measurement tools, such as for example (RF-)SET or (superconducting) resonators[209, 251].

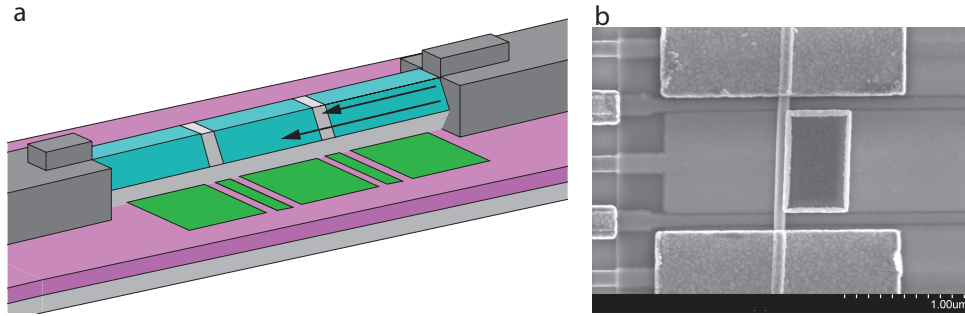


Figure 10.3: **a** Image of an InAs nanowire (grey) with a thin Al shell (cyan), which can form a superconducting island when two regions of Al are etched. The arrows indicate possible poisoning events by the lead, either to ABS in the junction or the island directly. Local gates (in green) are used to tune the coupling of the individual nanowire junctions and the island gate charge. **b** SEM image of a NbTiN superconducting island formed in an InSb nanowire with Au leads. The leads can be made from a superconductor to do switching current measurements.

10.4. PERSPECTIVES ON MAJORANA AND JOSEPHSON RADIATION DETECTION

The emission spectrum of a voltage-biased Josephson junction contains valuable information about the junction's properties. First, the Majorana bound states (MBS) can be identified. Secondly, the properties of the MBS depend on all the mutual interactions of the MZM in the topological junction, as explained in Section 3.4.3. Control of individual MZM and their effect on the MBS is key to achieving MZM braiding.

This has to be investigated experimentally in a time domain on the order of 10^{-5} – 10^{-9} s, the expected timescale for braiding[35]. The lowest frequency that we could resolve in the experiments reported in Chapters 7 and 8 was 5–7GHz, corresponding to a timescale of 10^{-10} s. To increase the timescale, we suggest using commercial microwave electronics to bring the emitted radiation to room temperature and measure the noise spectrum directly via a spectrum analyzer, as was done in ref. [73].

For PAT detection with an SIS junction, we only suggest technical improvements to the detection method, since that is currently the limiting factor of the experiment. The detection range should be increased by improving the lower frequency detection limit. Currently, it is limited by quasiparticle heating at $V_{\text{det}} = 2\Delta$, as shown in Figure 8.2a. This heating could be reduced by superconductor-insulator-normal-insulator-superconductor (SINIS) coolers[252], or controlled vortex creation in the vicinity of the junction[172].

The full width at half maximum (FWHM) of the detected frequency is large, especially when a magnetic field is applied. To improve this, a steeper quasiparticle onset is needed (at finite magnetic field). In Chapter 8, we used a lock-in technique to measure the radiation, which resulted in line widths of ~ 5 GHz. This could be improved by decreasing the magnetic field required for the topological transition, or improving the design of the detector. Ginzburg–Landau simulations could also be used to minimize vortex creation and Meissner currents close to the SIS detector.

10.5. PERSPECTIVES ON ANDREEV BOUND STATE SPECTROSCOPY

Most braiding schemes rely on Josephson coupling in semiconductor nanowire Josephson junctions[17, 35, 251]. The underlying mechanisms of Josephson coupling are Andreev bound states (ABS)[64]. These ABS can be very exotic due to the presence of the spin-orbit effect and the need for a magnetic field in these systems. In Chapter 9, we reported direct spectroscopy of ABS in nanowire Josephson junctions, including the Zeeman and spin-orbit effects in the analysis. To assure reliable and reproducible Josephson coupling for MZM braiding, further investigation of ABS with spin-orbit effect and finite magnetic field is needed.

10.5.1. MEASURE OF LONG-JUNCTION ANDREEV BOUND STATES

Andreev bound states were only investigated in short ballistic Josephson junctions, where the coherence length, ξ_{COH} , is (much) larger than the junction length, d . In the long-junction limit, $\xi_{\text{COH}} \ll d$, the ABS contribute to the supercurrent in both directions, leading to a net supercurrent proportional to the Thouless energy. The clear differences between short- and long-junction ABS are shown in Figure 3.7. In addition to the Andreev spectroscopy experiments reported in Chapter 9, we also measured nanowire Josephson junctions with etched Al windows of 200 and 400nm. The ABS in these junctions showed behaviour in accordance with eqs. 3.20 with $\Delta \sim 100\mu\text{eV}$. The estimated³ coherence length was $\xi_{\text{COH}} = \hbar v_{\text{F}}/\Delta \sim 400\text{nm}-1\mu\text{m}$, which places these longer junctions in the short/intermediate regime, $\xi_{\text{COH}} \gtrsim d$.

The typical length of an InAs nanowire with Al shell is 5-10 μm . This makes it possible to be in the long junction limit ($\xi_{\text{COH}} < d$) but not clearly so ($\xi_{\text{COH}} \ll d$). As this transition region is where many of the experiments [77, 106, 199, 215] were performed, it is very interesting to investigate this regime. ABS spectroscopy is the perfect experimental tool to investigate the underlying mechanism of the supercurrent by direct spectroscopy, in the short- and long-junction limits and the transition regime.

10.5.2. IMPROVE THE COUPLING CIRCUIT

The coupling circuit could be improved by adding inductive lines, for decoupling from the outside world on AC, in combination with smaller resistors to increase the quality factor (the quality factor reported in Chapter 9 being ~ 1) and decrease the ABS line width. If a higher quality factor could be achieved, one would also expect multi-photon processes at lower powers. In the experiment reported in ref. [217], a quality factor of ~ 13 was obtained, making it possible to excite the resonator *and* the ABS. Such an improvement could make the following experiments possible.

1. **Measurement and analysis of more complex multi-channel ABS spectra with Zeeman and spin-orbit effects.** Figure 9.5b shows an asymmetric multi-channel ABS spectrum. Due to the larger line width, it is not possible to resolve the individual spectral lines belonging to the ABS. With a higher quality factor, the lines are expected to be narrower and this complex spectrum could be analyzed in more detail. The extracted spectrum could then be compared, for example, to the models

³The host superconductor has $\Delta \sim 200\mu\text{eV}$. To estimate the Fermi velocity, v_{F} , we assume a Fermi energy, E_{F} , of 1-10meV and an effective electron m^* of $0.023m_{\text{e}}$, where m_{e} is the bare electron mass.

of ref. [75, 233]. With the addition of magnetic rotation, it would also be possible to measure the recently-discovered φ_0 junction[77] via direct spectroscopy.

2. **Measurements of ABS at ‘zero energy’, revealing the Majorana bound state, the Weyl singularity and perfect transmission ABS.** Because of bias instabilities in the spectrometer due to the supercurrent, it is not possible to do spectroscopy below $V_{\text{spec}} \sim 15\mu\text{V}$. This corresponds to 7–8GHz, which is accessible by commercial microwave excitation[55, 199], which can easily reach 20GHz. The proposed spectroscopy using the on-chip spectrometer would have a range of up to 230GHz, which could reveal the entire ABS spectrum.

The range below 7–8GHz is needed to investigate ‘zero energy’ states, such as Majorana bound states[224], the Weyl singularity[216], fermion switches in multi-terminal junctions[253] or superconducting devices with almost perfect transmission [12, 51]. This low range is accessible by a higher quality factor ($\sim 10 - 15$) circuit, which can raise the ABS spectrum and the plasma mode frequency due to higher-order processes[217, 225].

For the Weyl singularity[216] or fermion switches in multi-terminal junctions[253], nanowires with multiple legs are needed. These X- and T-shaped nanowires have been grown and are experimentally accessible[129, 137].

10.6. TOWARDS BRAIDING OF MAJORANA ZERO MODES

To successfully braid and demonstrate the non-abelian properties of MZM, we require precise control of at least four MZM and their mutual coupling[16, 17, 35, 209, 251, 254]. Braiding relies on turning the MZM coupling ‘on’ and ‘off’ by gate or flux control, and requires that the MZM at both ends of the nanowire share the same topological gap. These requirements have not been experimentally demonstrated.

The following questions need to be answered before one could think of undertaking a braiding experiment. We offer brief comments or suggestions for each of the questions.

1. What is the size of the MZM?

This is the coherence length associated with the topological gap. Albrecht *et al.*[14] claim to have extracted the coherence length from the MZM overlap energy splitting of five different samples, with different lengths and thus MZM overlaps. The coherence length depends on the Fermi velocity and the topological gap, which depends on the spin-orbit energy and the Zeeman energy, approximated by eq. 3.81. Based on the magnetic field onset and the behaviour of the MZM oscillations, we conclude that the details of the samples are different. The coherence length extracted from the five different oscillation amplitudes is nonetheless claimed to be one value, $\xi_{\text{COH}} \sim 260\text{nm}$.

The splitting of MZM due to finite wavefunction overlap can be observed[33] by direct-tunnel spectroscopy. This splitting can be investigated as a function of magnetic field and chemical potential to find the coherence length and thus the size of the MZM[81].

2. What is the strength of the MZM coupling?

MZM can be coupled by physical overlap to form an MBS, where eq. 3.87 describes the coupling. They can also be coupled by charging energy, as was used to couple and decouple them in ref. [17]. In this case the strength of the MZM coupling is the same as the energy which is needed to add an electron to the island. The coupling then depends on the ratio of the charging and Josephson energies, as explained in Section 3.5.

In more recent braiding schemes, the MZM are coupled via quantum dots[209, 251]. Understanding this coupling is key to any future plans for braiding.

MBS can be investigated in normal, multi-leg and quantum dot junctions with ABS spectroscopy. Unfortunately, the excitations to the continuum are not bright enough and the MBS cannot be mapped exactly. One could think of combining the microwave irradiation from the spectrometer junction with the switching current through the (multi-leg) topological junction to reveal the exact shape of the MBS. A similar experiment[255] was done with Al atomic junctions, and successfully extracted the superconducting gap, Δ .

3. What are the required time scales for braiding? A theoretician would answer⁴: 'Faster than the quasiparticle poisoning time but still slowly enough that the system stays in the ground state.' In ref. [256], a 32-page theoretical analysis of one specific case[35] is performed. This analysis gives an estimate of 100ns–100ps for certain steps of the braiding, but other steps can be done more slowly. Other braiding schemes rely on measurement-based or remote charge sensing, so the timescales for these schemes could be totally different.

The experiments reported in ref. [22, 90] are the first steps in finding experimentally achievable timescales. More experiments are needed to identify the required timescales for the different braiding schemes.

These questions are directly linked to braiding MZM and showing their non-abelian properties. Clear signatures of other properties are still lacking, showing that the MZM system is not completely understood. In this thesis, we have taken the first steps towards investigating the fractional Josephson effect in topological junctions. Recently, ref. [15] claimed to have found a topological phase diagram. Much research has also been done to find non-local effects (correlations) among MZM[33]. These are the experiments that are needed to understand the requirements for a braiding experiment.

⁴Really. Try this with a random theoretician.

A

APPENDIX

I start with introducing the commutation relations and definitions for MZM which are needed in the derivations used below.

$$\begin{aligned} \{c_n, c_m^\dagger\} &= \delta_{nm} \\ \{c_n, c_m\} = \{c_n^\dagger, c_m^\dagger\} &= 0 \end{aligned} \quad (\text{A.1})$$

$$\begin{aligned} \{\gamma_i, \gamma_j\} = \{\gamma_i^\dagger, \gamma_j^\dagger\} = \{\gamma_i^\dagger, \gamma_j\} &= 2\delta_{ij} \\ \gamma\gamma^\dagger = \gamma^\dagger\gamma &= 1 \end{aligned} \quad (\text{A.2})$$

$$\begin{aligned} \gamma_{2j-1} = \gamma_{2j-1}^\dagger &= (c_j^\dagger + c_j) \\ \gamma_{2j} = \gamma_{2j}^\dagger &= i(c_j^\dagger - c_j). \end{aligned} \quad (\text{A.3})$$

$$\begin{aligned} c_j &= \frac{1}{2}(\gamma_{2j-1} + i\gamma_{2j}) \\ c_j^\dagger &= \frac{1}{2}(\gamma_{2j-1} - i\gamma_{2j}). \end{aligned} \quad (\text{A.4})$$

They were also introduced in section 3.4.1 but repeated here for convenience.

A.1. DERIVATION OF THE BRAIDING OPERATOR.

We start with $U = e^{iH}$ which is unitary and can describe any operator if H is Hermitian, $H = H^\dagger$. H cannot be $\gamma_1\gamma_2$ since this is not Hermitian. $i\gamma_1\gamma_2$ is Hermitian and commutes

A

with the parity operator, $[i\gamma_1\gamma_2, P] = 0$, so it conserves parity. But having $i\gamma_1\gamma_2$ with a constant β is still fulfilling the requirements so we start with the expression $U = e^{\beta\gamma_1\gamma_2} = \cos(\beta) + \sin(\beta)\gamma_1\gamma_2$ [32]. We use this expression to find $\gamma_1 \rightarrow \gamma_2$, and we start with the following:

$$\begin{aligned}
U\gamma_1U^\dagger &= (\cos(\beta) + \sin(\beta)\gamma_1\gamma_2)\gamma_1(\cos(\beta) + \sin(\beta)\gamma_2\gamma_1) \\
&= \cos^2(\beta)\gamma_1 + 2\gamma_1\gamma_2\gamma_1\sin(\beta)\cos(\beta) + \gamma_1\gamma_2\gamma_1\gamma_2\gamma_1\sin^2(\beta) \\
&= (\cos^2(\beta) - \sin^2(\beta))\gamma_1 - 2\gamma_2\sin(\beta)\cos(\beta) \\
&= (\cos^2(\beta) - \sin^2(\beta))\gamma_1 - \gamma_2\sin(2\beta)
\end{aligned} \tag{A.5}$$

To obtain an operation that give $\gamma_1 \rightarrow \gamma_2$, the coefficient of γ_1 should be zero which can be obtained by setting $\beta = \pm\frac{\pi}{4}$. So this makes $U = \frac{1}{\sqrt{2}}(1 \pm \gamma_1\gamma_2)$, where + (-) corresponds to clockwise (anti-clockwise) interchange. So we derive the braiding operator for MZM and we observe that there is a different in clockwise and anti-clockwise interchanging.

A.2. CHECKING THE NON-ABELIANESS OF MZM

To prove the non-abelianess it is necessary to show that $U_{12}U_{23} \neq U_{23}U_{12}$ [31]. We derived U_{12} in the section above and $U_{23} = \frac{1}{\sqrt{2}}(1 \pm \gamma_2\gamma_3)$ can be obtained by replacing the indices.

$$\begin{aligned}
U_{12}U_{23} &= \frac{1}{2}(1 + \gamma_1\gamma_2)(1 + \gamma_2\gamma_3) \\
&= 1 + \gamma_1\gamma_2 + \gamma_2\gamma_3 + \gamma_1\gamma_2\gamma_2\gamma_3 \\
&= 1 + \gamma_1\gamma_2 + \gamma_2\gamma_3 + \gamma_1\gamma_3
\end{aligned} \tag{A.6}$$

and

$$\begin{aligned}
U_{23}U_{12} &= \frac{1}{2}(1 + \gamma_2\gamma_3)(1 + \gamma_1\gamma_2) \\
&= 1 + \gamma_2\gamma_3 + \gamma_1\gamma_2 + \gamma_2\gamma_3\gamma_1\gamma_2 \\
&= 1 + \gamma_1\gamma_2 + \gamma_2\gamma_3 - \gamma_1\gamma_3
\end{aligned} \tag{A.7}$$

so indeed $U_{12}U_{23} \neq U_{23}U_{12}$ hold and MZM are non-abelian particles. The order of changing them matter and thus non-trivial compared to 3D particles exchange depicted in figure 2.5.

A.3. USING THE BRAIDING OPERATOR U

To do braiding operators, the MZM operators need to be written as creation (c^\dagger) and anti-halation (c) since these are operating on the wavefunction $|n\rangle$ directly. These operations are as follows:

$$\begin{aligned}
c^\dagger|0\rangle &= |1\rangle & c^\dagger|1\rangle &= 0 \\
c|0\rangle &= 0 & c|1\rangle &= |0\rangle.
\end{aligned} \tag{A.8}$$

These relations together with eq. A.1 and A.3 are needed to calculate the result of the braiding. We start with:



$$\begin{aligned}
 U_{12}|0\rangle &= \frac{1}{\sqrt{2}}(1 + \gamma_1\gamma_2)|0\rangle \\
 &= \frac{1}{\sqrt{2}}\left(1 + i(c^\dagger + c)(c^\dagger - c)\right)|0\rangle \\
 &= \frac{1}{\sqrt{2}}\left(1 + i\left[c^\dagger c^\dagger + cc^\dagger - c^\dagger c + cc\right]\right)|0\rangle \\
 &= \frac{1}{\sqrt{2}}(1 + i)|0\rangle
 \end{aligned} \tag{A.9}$$

and also $U_{23}|00\rangle$ we want to investigate. Now $|\Psi\rangle = |n_1, n_2\rangle$ where c_1^\dagger, c_1 operates on n_1 and c_2^\dagger, c_2 operates on n_2 . Keeping track on the proper indices is important. Check the indices of eq. A.3 if you are confused.

$$\begin{aligned}
 U_{23}|00\rangle &= \frac{1}{\sqrt{2}}(1 + \gamma_2\gamma_3)|00\rangle \\
 &= \frac{1}{\sqrt{2}}\left(1 + i(c_1^\dagger + c_1)(c_2^\dagger - c_2)\right)|00\rangle \\
 &= \frac{1}{\sqrt{2}}\left(1 + i\left[c_1^\dagger c_2^\dagger + c_1 c_2^\dagger - c_1^\dagger c_2 - c_1 c_2\right]\right)|00\rangle \\
 &= \frac{1}{\sqrt{2}}\left(|00\rangle + i c_1^\dagger c_2^\dagger |00\rangle\right) \\
 &= \frac{1}{\sqrt{2}}(|00\rangle + i|11\rangle)
 \end{aligned} \tag{A.10}$$

B

APPENDIX

In the derivation of the $u_{\mathbf{k}}$ and $v_{\mathbf{k}}$ in section 3.2.1 we took the gap Δ real and positive. Actually the gap is better described by $\Delta e^{i\phi}$, with ϕ the phase of the Cooper-pair condensate. Making the Bogoliubov-de Gennes Hamiltonian:

$$H_{\text{BdG}} = \begin{pmatrix} \xi_{\mathbf{k}\uparrow} & \Delta e^{i\phi} \\ \Delta e^{-i\phi} & -\xi_{\mathbf{k}\downarrow} \end{pmatrix} \quad (\text{B.1})$$

The quasiparticles excitation are picking also a part up of this phase and needed to be redefined as:

$$\tilde{u}_{\text{e}} = e^{i\frac{\phi}{2}} u_{\text{e}} = e^{i\frac{\phi}{2}} u_{\mathbf{k}} \quad (\text{B.2})$$

$$\tilde{v}_{\text{e}} = e^{-i\frac{\phi}{2}} v_{\text{e}} = e^{-i\frac{\phi}{2}} v_{\mathbf{k}} \quad (\text{B.3})$$

$$\tilde{u}_{\text{h}} = e^{i\frac{\phi}{2}} u_{\text{h}} = -e^{i\frac{\phi}{2}} v_{\mathbf{k}} \quad (\text{B.4})$$

$$\tilde{v}_{\text{h}} = e^{-i\frac{\phi}{2}} v_{\text{h}} = e^{-i\frac{\phi}{2}} u_{\mathbf{k}}. \quad (\text{B.5})$$

This redefinition is necessary for describing the dynamics between superconductors. Actually the phase difference between the superconductor are describing more precise the dynamics as we will derive.

We want to investigate a SNS Josephson junction depicted in figure 3.6. To know which wavefunction are needed in all three regions we first described the processes which we can expected, bases on Andreev reflection. We start with an electron in the N-region moving to the right to the NS-interface where it got Andreev reflected, assuming first perfect transmission, $T = 1$. On this side an electron-like quasiparticle emerge. The Andreev reflection creates a hole on the normal part moving to the SN-interface and Andreev reflect there. Now a hole-like quasiparticle describes the wavefunction in this S-part. After the Andreev reflection an electron is created which can be consider as the original electron which started the explanation of this model. We set the SN-interface, with superconductor defined as S_1 , at $x = -\frac{d}{2}$ and superconducting phase $\phi_1 = -\frac{\delta}{2}$. The other

NS-interface, with superconductor defined as S_2 , is at $x = \frac{d}{2}$ and this superconductor has phase $\phi_2 = \frac{\delta}{2}$. This makes the phase difference δ between S_1 and S_2 . The wavefunction in each region is

B

$$\Psi_{S_1}(x) = a \begin{pmatrix} u_h e^{-i\frac{\delta}{4}} \\ v_h e^{i\frac{\delta}{4}} \end{pmatrix} e^{-ik_h x} \quad (\text{B.6})$$

$$\Psi_N(x) = b \begin{pmatrix} 1 \\ 0 \end{pmatrix} e^{ik_{N,e}x} + c \begin{pmatrix} 0 \\ 1 \end{pmatrix} e^{-ik_{N,h}x} \quad (\text{B.7})$$

$$\Psi_{S_2}(x) = d \begin{pmatrix} u_e e^{i\frac{\delta}{4}} \\ v_e e^{-i\frac{\delta}{4}} \end{pmatrix} e^{ik_e x}. \quad (\text{B.8})$$

Now we have to look at the continuity at the two interface and assume all the k 's are the same, this gives the following equations at $x = -\frac{d}{2}$:

$$a u_h e^{-i\frac{\delta}{4}} e^{ik\frac{d}{2}} = b e^{-ik\frac{d}{2}} \quad (\text{B.9})$$

$$a v_h e^{i\frac{\delta}{4}} e^{ik\frac{d}{2}} = c e^{ik\frac{d}{2}}. \quad (\text{B.10})$$

And for $x = \frac{d}{2}$:

$$b e^{ik\frac{d}{2}} = d u_e e^{i\frac{\delta}{4}} e^{ik\frac{d}{2}} \quad (\text{B.11})$$

$$c e^{-ik\frac{d}{2}} = d v_e e^{-i\frac{\delta}{4}} e^{ik\frac{d}{2}}. \quad (\text{B.12})$$

We can rewrite eqs. B.9 and B.10 as follows:

$$\frac{c}{b} = \frac{v_h}{u_h} e^{i\frac{\delta}{2}} e^{-ikd}. \quad (\text{B.13})$$

And we can do the same for the other interface:

$$\frac{c}{b} = \frac{v_e}{u_e} e^{-i\frac{\delta}{2}} e^{ikd}. \quad (\text{B.14})$$

Give us an equation without all the coefficients.

$$\frac{u_e v_h}{v_e u_h} = \frac{E + i\sqrt{\Delta^2 - E^2}}{E - i\sqrt{\Delta^2 - E^2}} = e^{2i(kd - \frac{\delta}{2})} \quad (\text{B.15})$$

We have used eqs. 3.3 and 3.4 and $E_{\pm} = \pm\sqrt{\xi_k^2 + \Delta^2}$. Because the wavefunction is constricted between two SN-interfaces it made sense that there is a constraint on the allowed values for E . Bound states have discrete energy states [48].

The solutions for the energies of the ABS are:

$$\pm E_{A,\pm,l} = \hbar \frac{v_F}{d} \left[\frac{\delta}{2} + \arcsin\left(\frac{E_A}{|\Delta|}\right) - \pi\left(\frac{1}{2} \pm l\right) \right]. \quad (\text{B.16})$$

Where we have use that the decaying part of the momentum k is given by $\frac{E}{\hbar v_F}$. This solution can be investigated in two limits. Which is defined by the length d of the junction with respect to the coherence length $\xi_{\text{COH}} = \frac{\hbar v_F}{\Delta}$. Which can be translated to an energy limit between Δ and $\frac{\hbar}{\tau} = \frac{\hbar v_F}{d}$ where τ is the time that an electron need to propagate from one to the other interface. The first limit is considered as the short junction limit, $d \ll \xi_{\text{COH}}$ or $\frac{\hbar\tau}{\Delta} \sim \frac{d}{\xi_{\text{COH}}} \ll 1$ the ABS energy is given by [40]:

$$E_A = \pm |\Delta| \cos \frac{\delta}{2}. \quad (\text{B.17})$$

Which are the Andreev bound states energies, E_A , for a short junction and perfect transmission. In the other limited $\frac{\hbar\tau}{\Delta} \sim \frac{d}{\xi_{\text{COH}}} \gg 1$ the ABS energies are given by:

$$\pm E_{A,\pm,l} \simeq \hbar \frac{v_F}{d} \left[\frac{\delta}{2} - \pi \left(\frac{1}{2} \pm l \right) \right] \quad (\text{B.18})$$

where $l = 0, 1, 2, \dots, N$. In this limit, $\hbar \frac{v_F}{d} \ll |\Delta|$, the coefficient of eq. B.16 is small, making also E_A small so we can neglected the arcsin-term. l can be increased till N is reached, which is the point that E_A reach $|\Delta|$ and the arcsin-term cannot be neglected anymore.

The last example that I would like to show briefly is the short junctions with finite transmission, $0 < T < 1$. We cannot take directly $d \rightarrow 0$, and let the transmission change by a δ -function potential. The reason is that at the NS-interface an electron can reflected partly as a hole (Andreev reflection) or as an electron (specular reflection). In the direction of the other SN-interface there is a wavefunction of an electron *and* a hole moving in both superconductors. Given the possibility of electron and hole like quasiparticles. In the case of $0 < T < 1$ we have to take in our model both electron and hole like quasiparticles wavefunction, which is making the derivation more complex. For this model we take $d \rightarrow 0$ and we obtain:

$$\Psi_{S_1}(x) = a_1 \begin{pmatrix} u_h e^{i\frac{\delta}{4}} \\ v_h e^{-i\frac{\delta}{4}} \end{pmatrix} e^{ik_h x} + a_2 \begin{pmatrix} u_e e^{i\frac{\delta}{4}} \\ v_e e^{-i\frac{\delta}{4}} \end{pmatrix} e^{-ik_e x} \quad (\text{B.19})$$

$$\Psi_{S_2}(x) = d_1 \begin{pmatrix} u_e e^{-i\frac{\delta}{4}} \\ v_e e^{i\frac{\delta}{4}} \end{pmatrix} e^{ik_e x} + d_2 \begin{pmatrix} u_h e^{-i\frac{\delta}{4}} \\ v_h e^{i\frac{\delta}{4}} \end{pmatrix} e^{-ik_h x}. \quad (\text{B.20})$$

Now we have to look at the continuity of the two wavefunction at $x = 0$. We assume $k_e \simeq k_h \simeq k_F = \frac{\sqrt{2m\mu}}{\hbar}$ which gives the following equations:

$$a_1 u_h e^{i\frac{\delta}{4}} + a_2 u_e e^{i\frac{\delta}{4}} = d_1 u_e e^{-i\frac{\delta}{4}} + d_2 u_h e^{-i\frac{\delta}{4}} \quad (\text{B.21})$$

$$a_1 v_h e^{-i\frac{\delta}{4}} + a_2 v_e e^{-i\frac{\delta}{4}} = d_1 v_e e^{i\frac{\delta}{4}} + d_2 v_h e^{i\frac{\delta}{4}}. \quad (\text{B.22})$$

The continuity of the derivative of the wavefunction, does not hold due to the presence of the δ -function potential at $x = 0$. In ref. [48] this example is also calculated but without superconducting phase and pure electron states. We obtain with the same approach as in Griffiths textbook:

$$a_1 u_h e^{i\frac{\delta}{4}} - a_2 u_e e^{i\frac{\delta}{4}} - \left(d_1 u_e e^{-i\frac{\delta}{4}} - d_2 u_h e^{-i\frac{\delta}{4}} \right) = -2i \sqrt{\frac{1-T}{T}} \left(a_1 u_h e^{i\frac{\delta}{4}} + a_2 u_e e^{i\frac{\delta}{4}} \right) \quad (\text{B.23})$$

$$a_1 v_h e^{-i\frac{\delta}{4}} - a_2 v_e e^{-i\frac{\delta}{4}} - \left(d_1 v_e e^{i\frac{\delta}{4}} - d_2 v_h e^{i\frac{\delta}{4}} \right) = -2i \sqrt{\frac{1-T}{T}} \left(a_1 v_h e^{i\frac{\delta}{4}} + a_2 v_e e^{i\frac{\delta}{4}} \right) \quad (\text{B.24})$$

With the combination of the last four equations it is possible¹ to calculate the allowed energy spectrum which is:

$$E_A = \pm |\Delta| \sqrt{1 - T \sin^2 \frac{\delta}{2}} \quad (\text{B.25})$$

We refer to ref. [257] for the derivation and the result of a long junction with $0 < T < 1$. In figure 3.7a in the main text we plot the results of this junction.

¹I was not able to do the derivation myself, but I trust ref. [40, 43, 257] and take their result

C

APPENDIX

The spin-orbit is a relativistic correction of an electron that is moving in an electric field. The electric field is generated the gradient of the potential, V . The change of potential could come from electrostatic gates or leads attached to the nanowire which is called Dresselhaus SOI. The internal SOI coming from the potential of the nuclei and is called Rasba SOI.

The electrical field for a moving charge is effectively a magnetic field. Electron change there spin-orientation to this magnetic field which is called B_{SO} . The contribution in the Hamiltonian for SOI in the most general form is [258]:

$$H_{SO} = \frac{\hbar}{4m^2 c^2} \sigma \cdot (p \times E). \quad (C.1)$$

Where m is the effective electron mass, $p = (p_x, p_y, p_z)^T$ the momentum, $E = (E_x, E_y, E_z)^T$ the electrical field which come from the gradient of the potential $E = -\nabla V$ and c is the speed of light.

Because we have a 1D nanowire the momentum is only in the x-direction which gives for the direction of the effective magnetic field $(p \times E) = (0, -p_x E_z, p_x E_y)^T$. Which make the SOI Hamiltonian for our nanowire:

$$H_{SO} = \frac{\hbar}{4m^2 c^2} (-p_x E_z \sigma_y + p_x E_y \sigma_z). \quad (C.2)$$

Analysing this last Hamiltonian we observe the spins are going to orientate between the y and z direction depending on the relative strength of the electric field z and y direction. It is important to notice that this effective magnetic field is always point perpendicular to the nanowire.

As mentioned before the electric field is depending on the details of gating, leads to the nanowire etc. To simplify the H_{SO} and the final Hamiltonian that is needed for MZS we only consider an electrical field in the z-direction.

$$H_{SO} = -\frac{E_z \hbar}{4m^2 c^2} p_x \sigma_y = -\frac{\alpha}{\hbar} p_x \sigma_y \quad (C.3)$$

Where we defined $\alpha = \frac{E_z \hbar^2}{4m^2 c^2}$ which is the spin-orbit strength. Note: E_z is the electrical field in the z-direction.

C

D

APPENDIX

We show phase dependence of ABS in a hybrid SQUID in figure 3.18. We varied the nanowire gaps and transmissions and keep the $I_{C,1}$ constant. This is an extension of section 3.3.5

D

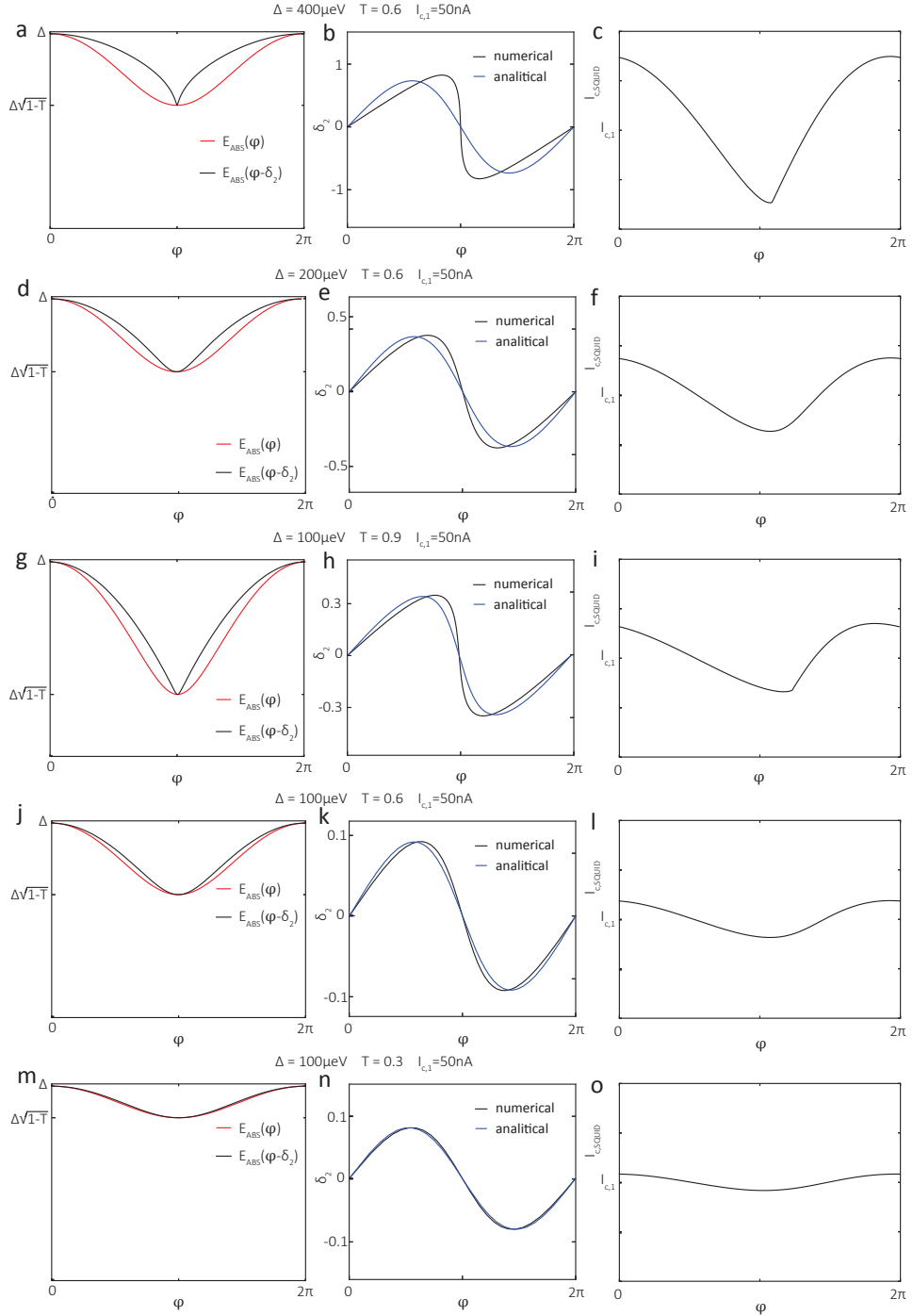


Figure D.1: **a-o** Examples of the ABS with and without linear phase drop due to applied flux. Numerically and analytical approximation of phase drop δ_2 over the strong junction as function of applied flux. And the maximum supercurrent of the nanowire SQUID. Δ varied between 400, 200, 100 μeV and transmission $T=0.9$, 0.6 and 0.3.

E

APPENDIX

In section 3.3.3 we discuss briefly the supercurrent and subgap behaviour of a SIS junction. The proper analysis of the SIS behaviour is covered by the $P(E)$ -theory which is well written in refs. [259, 260].

$P(E)$ is describing the probability of emitting the energy E in the environment which leads to an inelastic tunneling event. This could be an electron or a quasiparticle that tunnels or a Cooper-pair in a voltage bias junction. When a SIS junction is voltage biased the Cooper-pair condensates have an energy mismatch of $2eV_{\text{bias}}$. The probability to emit this energy to the $Z(\omega)$ -environment [259, 260]:

$$P(2eV_{\text{bias}}) = \frac{2}{eV_{\text{bias}}} \frac{\text{Re}[Z(\omega)]}{R_Q}. \quad (\text{E.1})$$

Experimentally it has shown to have good agreement for a voltage bias within the subgap of aluminium SIS junctions [193]. The SIS-junction and the environment is at sufficient low temperature that the tunnel processes are mainly described by emission. The probability of tunneling of Cooper-pairs leads to a rate which give a current. This a flow of Cooper-pairs at finite voltage bias which we call inelastic Cooper-pair current (ICPT). The current is given by:

$$I(V_{\text{bias}}) = 2e\Gamma(V_{\text{bias}}) = \frac{\pi e E_J^2}{\hbar} P(2eV_{\text{bias}}) = \frac{I_C^2}{2V_{\text{bias}}} \text{Re}[Z(\omega)]. \quad (\text{E.2})$$

The E_J is expected to be chosen that R_N is larger than R_Q . In this case the tunneling Hamiltonian can be expected to be a small perturbation of the quasiparticle states of the leads, which makes the derivation of ref. [260] valid.

We are now going to investigate multiple environmental impedances $Z_{\text{ENV}}(\omega)$. The junctions has its own resistance R and capacitance C from the RCSJ-model, see section 3.3.3. The subgap conductance is high and can be neglected. The total impedance is than given by:

$$Z(\omega) = \frac{1}{i\omega C + \frac{1}{Z_{ENV}(\omega)}}. \quad (E.3)$$

E.1. LCR-NETWORK ENVIRONMENT

In this thesis the environment can be characterized by an parallel inductance (L) and a resistor (R), see inset of figure E.1b. This make the total impedance:

$$Z(\omega) = \frac{1}{i\omega C + \frac{1}{R - \frac{i}{\omega L}}}. \quad (E.4)$$

We first investigate the ohmic environment by taking L out ($L \rightarrow \infty$). We set the capacitance $C = 10^{-14}$ F and vary the resistance. We have a RC network and we use eq. E.4 to calculate the real part of the impedance and eq. E.2 to calculate the ICPT. But this latter equation breaks down since we are not in the large voltage regime. The deviation is visible since we use for the calculation of the ICPT, $I_C = 65$ nA but the ICPT is much larger. For a pure ohmic regime the equations of Ivanchenko *et al* [60] are a better approximation and these are plotted in figure 3.11.

We consider further the complete LCR-parallel network shown in the inset of figure E.1b. We set $R = 500\Omega$, $C = 10$ fF and $L = 4$ nH, which are typical values of the used circuit as can be seen in Chapter 9. The LCR network has a resonance frequency that in Physics often a plasma frequency is called, it is given by, $f = \frac{1}{2\pi\sqrt{LC}}$. The width of plasma mode

divide by the frequency of the plasma mode is the quality factor, $Q = \frac{\Delta f}{f} = R\sqrt{\frac{C}{L}}$. This resonance peak is not always at the same frequency as the maximum in ICPT current. We can see this when we vary the parallel resistance in figure E.1c-d. The resonance of the impedance in the LCR-network is always at 25GHz but it goes to lower frequencies in the ICPT current when the parallel resistance is lowered. This can be attributed to the $1/V \sim 1/f$ dependence in eq. E.2.

When the inductance is changed, the position of the resonance peak is changed and the maximum in the real part of the impedance stays the same. In the ICPT current, again the $1/V \sim 1/f$ dependence as a strong influence and makes signal in the ICPT very different. In the limited of $L \rightarrow 0$ it is not possible to develop a voltage and no coupling is achieved. When L is large at low frequencies a voltage can already be developed and the ICPT is expected to be high as can be seen in figure E.1f.

The capacitance is at high frequencies a low impedance. This is the "leak" of your signal. You want to build up a voltage to achieve coupling but the capacitance is preventing this at high frequencies. In all the plots of the impedance in figure E.1 the decrease in $Re(Z)$ can be attributed to the "leaking" of the capacitance. This one we want to have as low as possible.

The above model is a classical model, we did not take multiphoton processes into account which is valid for $Z\left(\frac{1}{2\pi\sqrt{LC}}\right) \ll R_Q$.

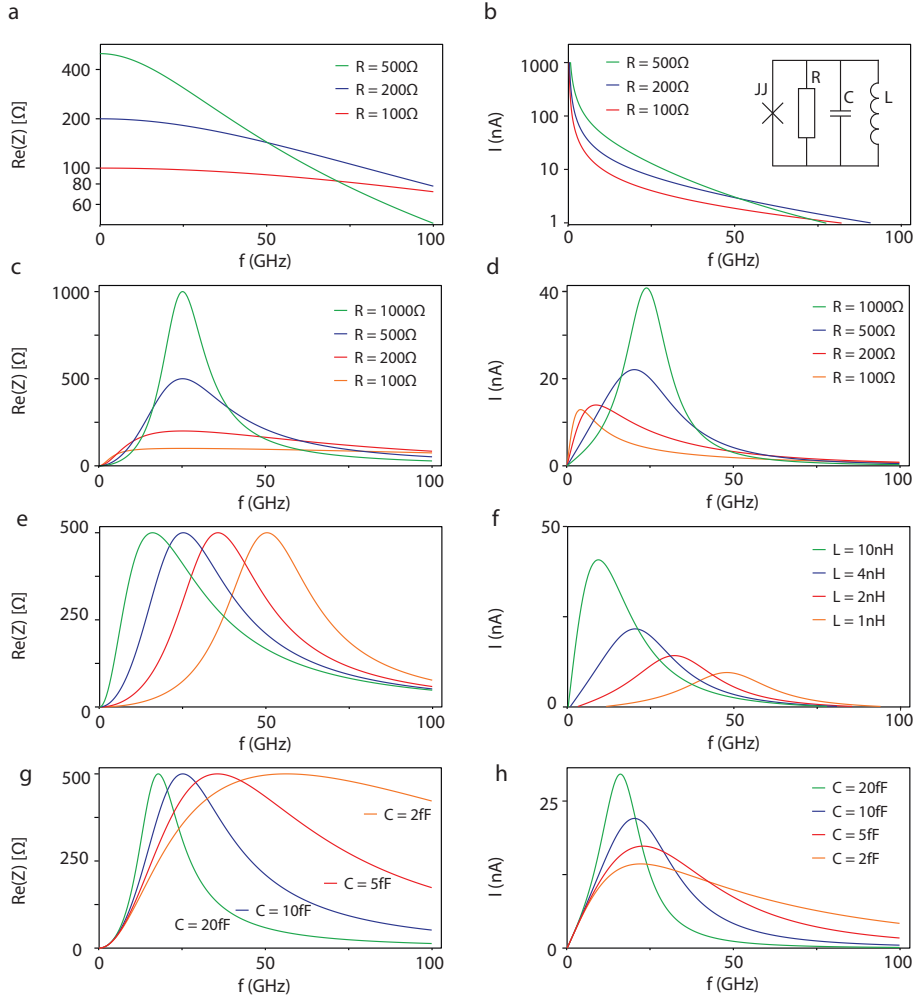


Figure E.1: Examples of $\text{Re}(Z)$ and ICPT current I as function of different values for L , C and R . Please note that the peaks of the resonances are not at the same frequencies in $\text{Re}(Z)$ and ICPT current I . **a,b** $L \rightarrow \infty$ and $C = 10^{-14} F$ and varying R . **c,d** $L = 4 \text{ nH}$ and $C = 10^{-14} F$ and varying R . **e,f** $R = 500 \Omega$ and $C = 10^{-14} F$ and varying L . **g,h** $L = 4 \text{ nH}$ and $R = 500 \Omega$ and varying C .

E.2. ABS IN THE ENVIRONMENT

An ABS level is a discrete level in the environment which can also dissipate current of a coupled SIS-junction. This technique of probing the ABS is performed in Chapter 9 and in ref. [217]. The absorption of microwave photons in the short SNS junction is studied in ref. [223]. The ABS is excited by breaking a Cooper-pair which will occupy the ABS. In ref. [223] also excitations to the continuum are considered but are expected to be much lower than excitation to two ABS. In our experiments these excitations are also not

measured. The breaking of the Cooper-pair a parity conserving excitation.

The strength of the absorption in the ABS is given by

$\propto T^2(1-T)\sin^4(\varphi/2) \times \Delta^2/E_{\text{ABS}}^2(\varphi)\delta(2eV_{\text{bias}} - 2E_{\text{ABS}})$. Here $\delta(x)$ is the Dirac-delta pulse (0 everywhere, except at $x = 0$ where the function is ∞). The current of the ICPT is not going to ∞ , the ABS is a fermionic mode and can only be excited once. The current is depending on the possibility to empty the state again by the continues drive (Rabi-drive) which is also discussed in ref. [223].

F

APPENDIX

This appendix shows extra figures with data as a support of Chapter 8. For more information about the figures see Chapter 8 or the caption of the figure of interest.

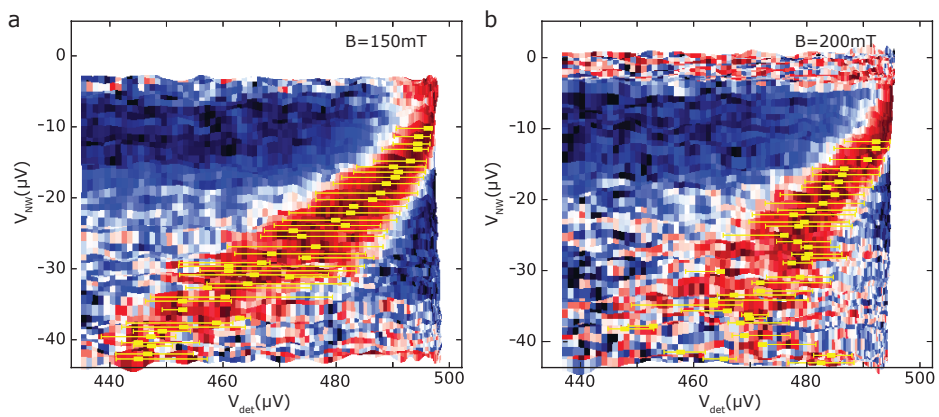


Figure E1: Extra data figures in addition to fig. 8.4. **a** The raw data (normalized in the x-direction) overlaid with the extracted maximum and the FWHM. The extracted datapoints are shown in fig. 8.4c. **b** Same as **a** but for fig. 8.4b.

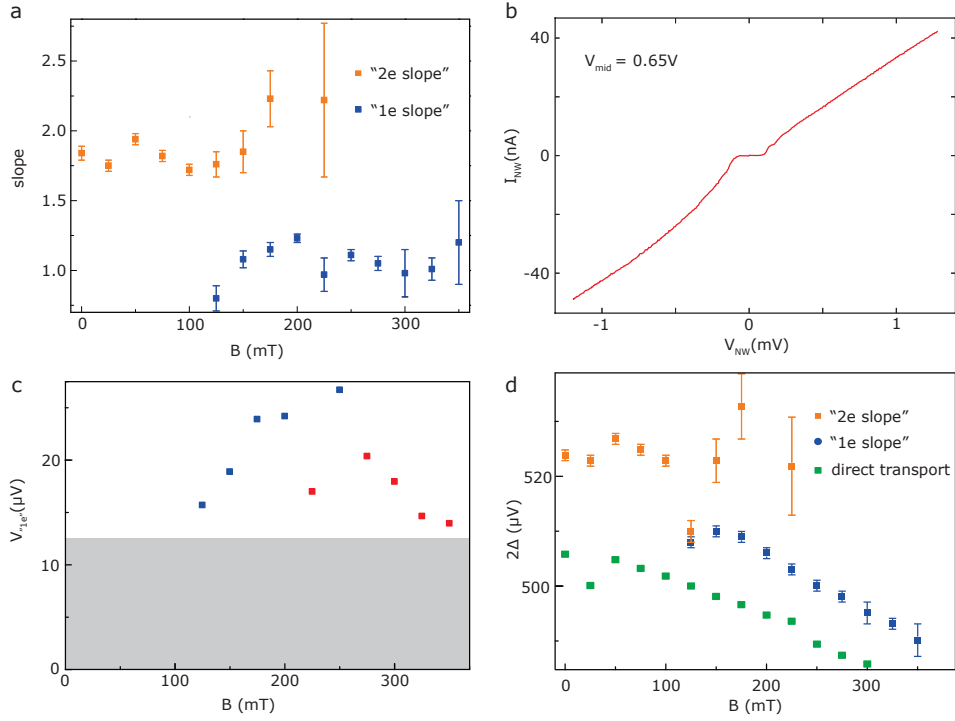


Figure E2: Similar data as shown in fig. 8.4 but with $V_{\text{sidegate}} = 1.25\text{V}$ and $V_{\text{mid}} = 0.65\text{V}$. **a** Extracted slopes at different applied magnetic fields along the nanowire. In a range of (125-225mT) magnetic field two different slopes of radiation in the detector is measured. **b** The measured current versus the measured voltage of the nanowire. The normal state resistance on the negative voltage bias is $R_{N,-} = 30.9\text{k}\Omega$. **c** The length of the ~ 1 slope. The end of the slope is determined by the start of the ~ 2 slope (blue datapoints) or by loss of the signal (red datapoints). **d** The extracted values for 2Δ are determined by extrapolating to slopes to $V_{\text{NW}} = 0\text{V}$.

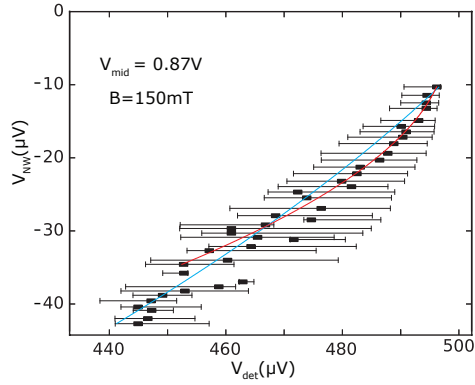


Figure E3: Different possible fits for the 150mT used in figure 8.4(c). The fit in cyan assumes a single slope (1.52 ± 0.05) but leaves many datapoints below the fit, especially around $V_{\text{NW}} \sim 20\mu\text{eV}$. The red line is a quadratic fit, which is only a good fit up to $V_{\text{NW}} \sim 30\mu\text{eV}$ but after this point all the datapoints are missed.

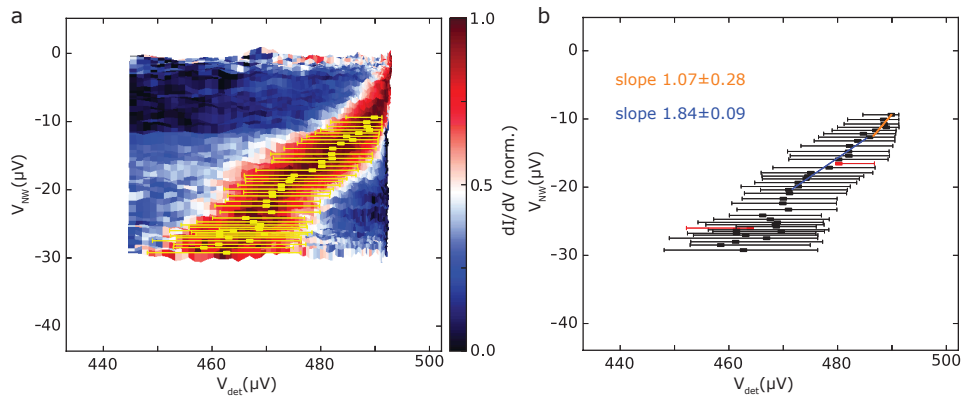


Figure E4: An example of the raw normalized data measured in the detector when the nanowire normal state resistance is $R_{N,-} = 8.9\text{k}\Omega$ which is below the resistance quantum, this indicated multiple channels. **a** Raw normalized data overlaid with the extracted maximum and the FWHM. The (raw) data is showing a single radiation peak with the accessible linewidth. **b** The extracted data points fitted with a two slopes up to $V_{\text{NW}} \sim 20\mu\text{eV}$. After $V_{\text{NW}} \sim 20\mu\text{eV}$ the slope seems to become steeper (more towards 1 again), without understanding the possible origin. The red data points are not taking into account since the peakfinder algorithm could not find a FWHM on one side.

F

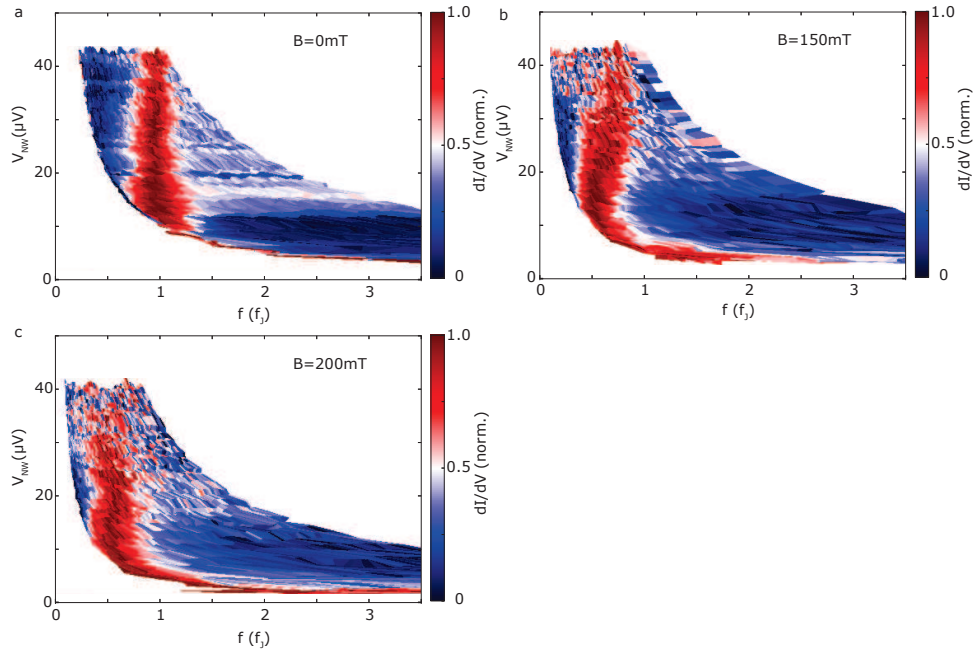


Figure E5: Same (raw) data as shown in figures F.1 and 8.3c as function of the calculated Josephson frequency for each voltage over the nanowire. The measured nanowire voltage, used on the y-axis, is multiplied by a factor -1 for convenience. **a** Detected lock-in signal in the SIS detector at a magnetic field of 0mT. A superconducting gap of $\Delta = 261\mu\text{eV}$ is used to calculate the frequency. **b** Detected lock-in signal in the SIS detector at a magnetic field of 150mT, $\Delta = 253\mu\text{eV}$. **c** Detected lock-in signal in the SIS detector at a magnetic field of 200mT, $\Delta = 251\mu\text{eV}$.

BIBLIOGRAPHY

- [1] Wilczek, F. Majorana returns. *Nature Physics* **5**, 614–618 (2009).
- [2] Heisig, J., Krämer, M., Pellen, M. & Wiebusch, C. Constraints on Majorana dark matter from the LHC and IceCube. *Physical Review D* **93**, 055029 (2016).
- [3] Majorana, E. A symmetric theory of electrons and positrons. Engl. transl. (Il Nuovo Cimento 14 (1937) 171-184). *Soryushiron Kenkyu* **63**, 149–162 (1981).
- [4] Kitaev, A. Y. Unpaired Majorana fermions in quantum wires. *Physics-Uspekhi* **44**, 131 (2001).
- [5] Stormer, H. L., Tsui, D. C. & Gossard, A. C. The fractional quantum Hall effect. *Reviews of Modern Physics* **71**, S298 (1999).
- [6] Heeres, R. W., Kouwenhoven, L. P. & Zwiller, V. Quantum interference in plasmonic circuits. *Nature nanotechnology* **8**, 719–722 (2013).
- [7] Lutchyn, R. M., Sau, J. D. & Das Sarma, S. Majorana fermions and a topological phase transition in semiconductor-superconductor heterostructures. *Phys. Rev. Lett.* **105**, 077001 (2010).
- [8] Oreg, Y., Refael, G. & von Oppen, F. Helical liquids and Majorana bound states in quantum wires. *Phys. Rev. Lett.* **105**, 177002 (2010).
- [9] Mourik, V. *et al.* Signatures of Majorana fermions in hybrid superconductor-semiconductor nanowire devices. *Science* **336**, 1003–1007 (2012).
- [10] Deng, M. T. *et al.* Anomalous zero-bias conductance peak in a Nb-InSb nanowire-Nb hybrid device. *Nano letters* **12**, 6414–6419 (2012).
- [11] Finck, A. D. K., Van Harlingen, D. J., Mohseni, P. K., Jung, K. & Li, X. Anomalous modulation of a zero-bias peak in a hybrid nanowire-superconductor device. *Phys. Rev. Lett.* **110**, 126406 (2013).
- [12] Zhang, H. *et al.* Ballistic Majorana nanowire devices. *arXiv:1603.04069* (2016).
- [13] Rokhinson, L. P., Liu, X. & Furdyna, J. K. The fractional AC Josephson effect in a semiconductor-superconductor nanowire as a signature of Majorana particles. *Nature Physics* **8**, 795–799 (2012).
- [14] Albrecht, S. M. *et al.* Exponential protection of zero modes in Majorana islands. *Nature* **531**, 206–209 (2016).

- [15] Chen, J. *et al.* Experimental phase diagram of a one-dimensional topological superconductor. *arXiv:1610.04555* (2016).
- [16] Alicea, J., Oreg, Y., Refael, G., von Oppen, F. & Fisher, M. P. A. Non-Abelian statistics and topological quantum information processing in 1D wire networks. *Nature Physics* **7**, 412–417 (2011).
- [17] Hyart, T. *et al.* Flux-controlled quantum computation with Majorana fermions. *Physical Review B* **88**, 035121 (2013).
- [18] Van der Sar, T. *et al.* Decoherence-protected quantum gates for a hybrid solid-state spin register. *Nature* **484**, 82–86 (2012).
- [19] Barends, R. *et al.* Superconducting quantum circuits at the surface code threshold for fault tolerance. *Nature* **508**, 500–503 (2014).
- [20] Krogstrup, P. *et al.* Epitaxy of semiconductor–superconductor nanowires. *Nature materials* **14**, 400–406 (2015).
- [21] Chang, W. *et al.* Hard gap in epitaxial semiconductor–superconductor nanowires. *Nature nanotechnology* **10**, 232–236 (2015).
- [22] Higginbotham, A. P. *et al.* Parity lifetime of bound states in a proximitized semiconductor nanowire. *Nature Physics* **11**, 1017–1021 (2015).
- [23] Sherman, D. *et al.* Normal, superconducting and topological regimes of hybrid double quantum dots. *Nature Nanotechnology* (2016).
- [24] Lafarge, P., Joyez, P., Esteve, D., Urbina, C. & Devoret, M. H. Two-electron quantization of the charge on a superconductor. *Nature* **365**, 422–424 (1993).
- [25] Joyez, P., Lafarge, P., Filipe, A., Esteve, D. & Devoret, M. H. Observation of parity-induced suppression of Josephson tunneling in the superconducting single electron transistor. *Phys. Rev. Lett.* **72**, 2458 (1994).
- [26] Magueijo, J. *A Brilliant Darkness: The Extraordinary Life and Mysterious Disappearance of Ettore Majorana, the Troubled Genius of the Nuclear Age* (Basic Books, 2009).
- [27] Dirac, P. A. M. The quantum theory of the electron. In *Proceedings of the Royal Society of London A: Mathematical, Physical and Engineering Sciences*, vol. 117, 610–624 (The Royal Society, 1928).
- [28] Dell Oro, S., Marrocci, S., Viel, M. & Vissani, F. Neutrinoless double beta decay: 2015 review. *Advances in High Energy Physics* **2016** (2016).
- [29] Gómez-Cadenas, J. J. & Martín-Albo, J. Phenomenology of neutrinoless double beta decay. *arXiv:1502.00581* (2015).
- [30] Nielsen, M. A. & Chuang, I. L. *Quantum computation and quantum information* (Cambridge university press, 2010).

- [31] Nayak, C., Simon, S. H., Stern, A., Freedman, M. & Das Sarma, S. Non-Abelian anyons and topological quantum computation. *Rev. Mod. Phys.* **80**, 1083–1159 (2008).
- [32] van Heck, B. & Akhmerov, A. R. *tiny.cc/topocm* (Online, 2015).
- [33] Mourik, V. & Zuo, K. *Signatures of Majorana Fermions in Hybrid Superconductor-Semiconductor Nanowire Devices*. Ph.D. thesis, TU Delft (2016).
- [34] van Heck, B., Akhmerov, A. R., Hassler, F., Burrello, M. & Beenakker, C. W. J. Coulomb-assisted braiding of Majorana fermions in a Josephson junction array. *New Journal of Physics* **14**, 035019 (2012).
- [35] Aasen, D. *et al.* Milestones toward Majorana-based quantum computing. *Phys. Rev. X* **6**, 031016 (2016).
- [36] Onac, G.-E. *High frequency noise detection in mesoscopic devices*. Ph.D. thesis, TU Delft (2005).
- [37] Onnes, H. K. The resistance of pure mercury at helium temperatures. *Commun. Phys. Lab. Univ. Leiden* **12**, 1 (1911).
- [38] Bardeen, J., Cooper, L. N. & Schrieffer, J. R. Theory of superconductivity. *Physical Review* **108**, 1175 (1957).
- [39] Tinkham, M. *Introduction to superconductivity* (Courier Corporation, 1996).
- [40] Kopnin, N. B. <http://tl.tkk.fi/opetus/supertheory/tfy-3.491/TheorySC06.pdf> (2006).
- [41] Chauvin, M. *The Josephson Effect in Atomic Contacts*. Ph.D. thesis, L'UNIVERSITE PARIS (2005).
- [42] Pillet, J.-D. *Tunneling spectroscopy of the Andreev bound states in a carbon nanotube*. Ph.D. thesis, L'UNIVERSITE PARIS VI (2011).
- [43] Bretheau, L. *Localized excitations in superconducting atomic contacts: Probing the Andreev doublet*. Ph.D. thesis, Ecole Polytechnique X (2013).
- [44] Fröhlich, H. Theory of the superconducting state. I. the ground state at the absolute zero of temperature. *Physical Review* **79**, 845 (1950).
- [45] Cooper, L. N. Bound electron pairs in a degenerate Fermi gas. *Physical Review* **104**, 1189 (1956).
- [46] Maxwell, E. Isotope effect in the superconductivity of mercury. *Physical Review* **78**, 477 (1950).
- [47] Reynolds, C. A., Serin, B., Wright, W. H. & Nesbitt, L. B. Superconductivity of isotopes of mercury. *Physical Review* **78**, 487 (1950).
- [48] Griffiths, D. J. *Introduction to quantum mechanics* (Pearson Education India, 2005).

- [49] Blonder, G. E., Tinkham, M. & Klapwijk, T. M. Transition from metallic to tunneling regimes in superconducting microconstrictions: Excess current, charge imbalance, and supercurrent conversion. *Physical Review B* **25**, 4515 (1982).
- [50] Beenakker, C. W. J. Quantum transport in semiconductor-superconductor microjunctions. *Physical Review B* **46**, 12841 (1992).
- [51] Kjaergaard, M. *et al.* Quantized conductance doubling and hard gap in a two-dimensional semiconductor-superconductor heterostructure. *Nature Communications* **7** (2016).
- [52] Josephson, B. D. Possible new effects in superconductive tunnelling. *Physics letters* **1**, 251–253 (1962).
- [53] Nazarov, Y. V. & Blanter, Y. M. *Quantum transport: Introduction to nanoscience* (Cambridge University Press, 2009).
- [54] Zgirski, M. *et al.* Evidence for long-lived quasiparticles trapped in superconducting point contacts. *Phys. Rev. Lett.* **106**, 257003 (2011).
- [55] Janvier, C. *et al.* Coherent manipulation of Andreev states in superconducting atomic contacts. *Science* **349**, 1199–1202 (2015).
- [56] Simmonds, R. W. *et al.* Decoherence in Josephson phase qubits from junction resonators. *Phys. Rev. Lett.* **93**, 077003 (2004).
- [57] Osbourne, K. & Martinis, J. M. Superconducting qubits and the physics of Josephson junctions. In *Les Houches conference proceedings* (2003).
- [58] Stewart, W. C. Current-voltage characteristics of Josephson junctions. *Applied Physics Letters* **12**, 277–280 (1968).
- [59] Tinkham, M. Josephson effect in low-capacitance tunnel junctions. In *Single Charge Tunneling*, 139–166 (Springer, 1992).
- [60] Ivanchenko, Y. M. & Zil’berman, L. A. The Josephson effect in small tunnel contacts. *Soviet Journal of Experimental and Theoretical Physics* **28**, 1272 (1969).
- [61] Calado, V. E. *et al.* Ballistic Josephson junctions in edge-contacted graphene. *Nature nanotechnology* (2015).
- [62] Heersche, H. B., Jarillo-Herrero, P., Oostinga, J. B., Vandersypen, L. M. K. & Morpurgo, A. F. Bipolar supercurrent in graphene. *Nature* **446**, 56–59 (2007).
- [63] Jarillo-Herrero, P., Van Dam, J. A. & Kouwenhoven, L. P. Quantum supercurrent transistors in carbon nanotubes. *Nature* **439**, 953–956 (2006).
- [64] van Woerkom, D. J. *et al.* Microwave spectroscopy of spinful Andreev bound states in ballistic semiconductor Josephson junctions. *arXiv:1609.00333* (2016).

- [65] Kammlhuber, J. *et al.* Conductance quantization at zero magnetic field in InSb nanowires. *Nano Letters* **16**, 3482–3486 (2016).
- [66] Chauvin, M. *et al.* Superconducting atomic contacts under microwave irradiation. *Phys. Rev. Lett.* **97**, 067006 (2006).
- [67] Averin, D. & Bardas, A. AC Josephson effect in a single quantum channel. *Phys. Rev. Lett.* **75**, 1831 (1995).
- [68] Houzet, M., Meyer, J. S., Badiane, D. M. & Glazman, L. I. Dynamics of Majorana states in a topological Josephson junction. *Phys. Rev. Lett.* **111**, 046401 (2013).
- [69] Bergeret, F. S., Virtanen, P., Heikkilä, T. T. & Cuevas, J. C. Theory of microwave-assisted supercurrent in quantum point contacts. *Phys. Rev. Lett.* **105**, 117001 (2010).
- [70] Zazunov, A., Shumeiko, V. S., Bratus, E. N., Lantz, J. & Wendin, G. Andreev level qubit. *Phys. Rev. Lett.* **90**, 087003 (2003).
- [71] Zazunov, A., Shumeiko, V. S., Wendin, G. & Bratus, E. N. Dynamics and phonon-induced decoherence of Andreev level qubit. *Physical Review B* **71**, 214505 (2005).
- [72] Cuevas, J. C., Heurich, J., Martín-Rodero, A., Yeyati, A. L. & Schön, G. Subharmonic Shapiro steps and assisted tunneling in superconducting point contacts. *Phys. Rev. Lett.* **88**, 157001 (2002).
- [73] Deacon, R. S. *et al.* Josephson radiation from gapless Andreev bound states in HgTe-based topological junctions. *arXiv:1603.09611* (2016).
- [74] Michelsen, J., Shumeiko, V. S. & Wendin, G. Manipulation with Andreev states in spin active mesoscopic Josephson junctions. *Physical Review B* **77**, 184506 (2008).
- [75] Yokoyama, T., Eto, M. & Nazarov, Y. V. Anomalous Josephson effect induced by spin-orbit interaction and Zeeman effect in semiconductor nanowires. *Physical Review B* **89**, 195407 (2014).
- [76] van Woerkom, D. J. *Majorana fermions in well aligned InSb-nanowires with superconducting and normal contacts*. Master's thesis, TU Delft (2012).
- [77] Szombati, D. B. *et al.* Josephson φ_0 -junction in nanowire quantum dots. *Nature Physics* (2016).
- [78] Leijnse, M. & Flensberg, K. Introduction to topological superconductivity and Majorana fermions. *Semiconductor Science and Technology* **27**, 124003 (2012).
- [79] Pikulin, D. I., Dahlhaus, J. P., Wimmer, M., Schomerus, H. & Beenakker, C. W. J. A zero-voltage conductance peak from weak antilocalization in a Majorana nanowire. *New Journal of Physics* **14**, 125011 (2012).

- [80] Liu, J., Potter, A. C., Law, K. T. & Lee, P. A. Zero-bias peaks in the tunneling conductance of spin-orbit-coupled superconducting wires with and without Majorana end-states. *Phys. Rev. Lett.* **109**, 267002 (2012).
- [81] Das Sarma, S., Sau, J. D. & Stanescu, T. D. Splitting of the zero-bias conductance peak as smoking gun evidence for the existence of the Majorana mode in a superconductor-semiconductor nanowire. *Physical Review B* **86**, 220506 (2012).
- [82] Pikulin, D. I. & Nazarov, Y. V. Phenomenology and dynamics of a Majorana Josephson junction. *Physical Review B* **86**, 140504 (2012).
- [83] Fu, L. & Kane, C. L. Josephson current and noise at a superconductor/quantum-spin-Hall-insulator/superconductor junction. *Physical Review B* **79**, 161408 (2009).
- [84] Badiane, D. M., Glazman, L. I., Houzet, M. & Meyer, J. S. AC Josephson effect in topological Josephson junctions. *Comptes Rendus Physique* **14**, 840–856 (2013).
- [85] Kwon, H.-J., Sengupta, K. & Yakovenko, V. M. Fractional AC Josephson effect in p- and d-wave superconductors. *The European Physical Journal B-Condensed Matter and Complex Systems* **37**, 349–361 (2004).
- [86] San-Jose, P., Prada, E. & Aguado, R. AC Josephson effect in finite-length nanowire junctions with Majorana modes. *Phys. Rev. Lett.* **108**, 257001 (2012).
- [87] Beshpalov, A., Houzet, M., Meyer, J. S. & Nazarov, Y. V. Theoretical model to explain excess of quasiparticles in superconductors. *Phys. Rev. Lett.* **117**, 117002 (2016).
- [88] Joyez, P. *The single Cooper pair transistor: A macroscopic quantum device*. Ph.D. thesis, Univ. Paris 6 (1995).
- [89] Koch, J. *et al.* Charge-insensitive qubit design derived from the Cooper pair box. *Physical Review A* **76**, 042319 (2007).
- [90] van Woerkom, D. J., Geresdi, A. & Kouwenhoven, L. P. One minute parity lifetime of a NbTiN Cooper-pair transistor. *Nature Physics* **11**, 547–550 (2015).
- [91] Billangeon, P.-M., Pierre, E., Bouchiat, H. & Deblock, R. AC Josephson effect and resonant Cooper pair tunneling emission of a single Cooper pair transistor. *Phys. Rev. Lett.* **98**, 216802 (2007).
- [92] Tien, P. K. & Gordon, J. P. Multiphoton process observed in the interaction of microwave fields with the tunneling between superconductor films. *Physical Review* **129**, 647 (1963).
- [93] Tucker, J. R. & Feldman, M. J. Quantum detection at millimeter wavelengths. *Reviews of Modern Physics* **57**, 1055 (1985).
- [94] van Gulik, R. J. J. Data analysis of measurement on nanodevices (2015). Bachelor Thesis.

- [95] Aguado, R. & Kouwenhoven, L. P. Double quantum dots as detectors of high-frequency quantum noise in mesoscopic conductors. *Phys. Rev. Lett.* **84**, 1986 (2000).
- [96] Schouten, R. N. <http://qtworke.tudelft.nl/schouten/> (Online, 2016).
- [97] Mueller, F. *et al.* Printed circuit board metal powder filters for low electron temperatures. *Review of Scientific Instruments* **84**, – (2013).
- [98] Beenakker, C. W. J. Universal limit of critical-current fluctuations in mesoscopic Josephson junctions. *Phys. Rev. Lett.* **67**, 3836–3839 (1991).
- [99] Pekola, J. P. Trends in thermometry. *Journal of low temperature physics* **135**, 723–744 (2004).
- [100] Proutski, A. *et al.* Electron-phonon coupling in a one-dimensional semiconducting nanowire. *In preparation* (2017).
- [101] Car, D. *Synthesis of InSb nanowire architectures: building blocks for Majorana devices*. Ph.D. thesis, Technische Universiteit Eindhoven (2016).
- [102] Flöhr, K. *et al.* Manipulating InAs nanowires with submicrometer precision. *Review of scientific instruments* **82**, 113705 (2011).
- [103] van der Molen, R. Creating the optimal NbTiN thin films (2014). Bachelor Thesis.
- [104] van Meurs, B. Optimizing sputtered NbTiN thin films & mobility of InSb nanowires (2015). Bachelor Thesis.
- [105] Hofstetter, L., Csonka, S., Nygård, J. & Schönberger, C. Cooper pair splitter realized in a two-quantum-dot Y-junction. *Nature* **461**, 960–963 (2009).
- [106] Doh, Y.-J. *et al.* Tunable supercurrent through semiconductor nanowires. *Science* **309**, 272–275 (2005).
- [107] Nadj-Perge, S., Frolov, S. M., Bakkers, E. P. A. M. & Kouwenhoven, L. P. Spin-orbit qubit in a semiconductor nanowire. *Nature* **468**, 1084–1087 (2010).
- [108] Churchill, H. O. H. *et al.* Superconductor-nanowire devices from tunneling to the multichannel regime: Zero-bias oscillations and magnetoconductance crossover. *Physical Review B* **87**, 241401 (2013).
- [109] Sau, J. D., Tewari, S. & Das Sarma, S. Experimental and materials considerations for the topological superconducting state in electron- and hole-doped semiconductors: Searching for non-Abelian Majorana modes in 1D nanowires and 2D heterostructures. *Physical Review B* **85**, 064512 (2012).
- [110] Potter, A. C. & Lee, P. A. Engineering a p+ip superconductor: Comparison of topological insulator and Rashba spin-orbit-coupled materials. *Physical Review B* **83**, 184520 (2011).

- [111] Ashcroft, N. W. & Mermin, N. D. *Solid state Physics* (Harcourt, 1976).
- [112] Blömers, C. *et al.* Hall effect measurements on InAs nanowires. *Applied physics letters* **101**, 152106 (2012).
- [113] Storm, K. *et al.* Spatially resolved Hall effect measurement in a single semiconductor nanowire. *Nature nanotechnology* **7**, 718–722 (2012).
- [114] Sze, S. M. & Ng, K. K. *Physics of semiconductor devices* (John Wiley & Sons, 2006).
- [115] Schroer, M. D. & Petta, J. R. Correlating the nanostructure and electronic properties of InAs nanowires. *Nano letters* **10**, 1618–1622 (2010).
- [116] Kretinin, A. V., Popovitz-Biro, R., Mahalu, D. & Shtrikman, H. Multimode Fabry-Perot conductance oscillations in suspended stacking-faults-free InAs nanowires. *Nano letters* **10**, 3439–3445 (2010).
- [117] Shtrikman, H., Popovitz-Biro, R., Kretinin, A. V. & Kacman, P. GaAs and InAs nanowires for ballistic transport. *IEEE Journal of Selected Topics in Quantum Electronics* **17**, 922–934 (2011).
- [118] Gupta, N. *et al.* Temperature-dependent electron mobility in InAs nanowires. *Nanotechnology* **24**, 225202 (2013).
- [119] Sourribes, M. J. L., Isakov, I., Panfilova, M., Liu, H. & Warburton, P. A. Mobility enhancement by Sb-mediated minimisation of stacking fault density in InAs nanowires grown on silicon. *Nano letters* **14**, 1643–1650 (2014).
- [120] Ford, A. C., Kumar, S. B., Kapadia, R., Guo, J. & Javey, A. Observation of degenerate one-dimensional sub-bands in cylindrical InAs nanowires. *Nano letters* **12**, 1340–1343 (2012).
- [121] Chuang, S. *et al.* Ballistic InAs nanowire transistors. *Nano letters* **13**, 555–558 (2013).
- [122] Bar-Sadan, M., Barthel, J., Shtrikman, H. & Houben, L. Direct imaging of single Au atoms within GaAs nanowires. *Nano letters* **12**, 2352–2356 (2012).
- [123] Wang, F. *et al.* Surface roughness induced electron mobility degradation in InAs nanowires. *Nanotechnology* **24**, 375202 (2013).
- [124] Jiang, X. *et al.* InAs/InP radial nanowire heterostructures as high electron mobility devices. *Nano letters* **7**, 3214–3218 (2007).
- [125] Van Tilburg, J. W. W. *et al.* Surface passivated InAs/InP core/shell nanowires. *Semiconductor science and technology* **25**, 024011 (2010).
- [126] Li, Y. *et al.* Dopant-free GaN/AlN/AlGaIn radial nanowire heterostructures as high electron mobility transistors. *Nano letters* **6**, 1468–1473 (2006).

- [127] Gobeli, G. W. & Allen, F. G. Photoelectric properties of cleaved GaAs, GaSb, InAs, and InSb surfaces; comparison with Si and Ge. *Physical Review* **137**, A245 (1965).
- [128] Plissard, S. R. *et al.* From InSb nanowires to nanocubes: Looking for the sweet spot. *Nano letters* **12**, 1794–1798 (2012).
- [129] Car, D., Wang, J., Verheijen, M. A., Bakkers, E. P. A. M. & Plissard, S. R. Rationally designed single-crystalline nanowire networks. *Advanced Materials* **26**, 4875–4879 (2014).
- [130] Penchev, M. V. *Indium Antimonide Nanowires: Synthesis, Characterization, and Applications*. Ph.D. thesis, Univ. of California Riverside (2012).
- [131] Dayeh, S. A., Soci, C., Paul, K., Edward, T. Y. & Wang, D. Transport properties of InAs nanowire field effect transistors: The effects of surface states. *Journal of Vacuum Science & Technology B* **25**, 1432–1436 (2007).
- [132] Du, J., Liang, D., Tang, H. & Gao, X. P. A. InAs nanowire transistors as gas sensor and the response mechanism. *Nano letters* **9**, 4348–4351 (2009).
- [133] Offermans, P., Crego-Calama, M. & Brongersma, S. H. Gas detection with vertical InAs nanowire arrays. *Nano letters* **10**, 2412–2415 (2010).
- [134] van Weperen, I., Plissard, S. R., Bakkers, E. P. A. M., Frolov, S. M. & Kouwenhoven, L. P. Quantized conductance in an InSb nanowire. *Nano letters* **13**, 387–391 (2013).
- [135] Schroder, D. K. *Semiconductor material and device characterization* (John Wiley & Sons, 2006).
- [136] Lu, W., Xie, P. & Lieber, C. M. Nanowire transistor performance limits and applications. *IEEE transactions on Electron Devices* **55**, 2859–2876 (2008).
- [137] Plissard, S. R. *et al.* Formation and electronic properties of InSb nanocrosses. *Nature nanotechnology* **8**, 859–864 (2013).
- [138] Wang, L., Wang, D. & Asbeck, P. M. A numerical Schrödinger–Poisson solver for radially symmetric nanowire core–shell structures. *Solid-State Electronics* **50**, 1732–1739 (2006).
- [139] Eeltink, D. *Electrostatic simulations of nanowire devices*. Master’s thesis, TU Delft (2013).
- [140] Nadj-Perge, S. *Single spins in semiconductor nanowires*. Ph.D. thesis, TU Delft (2010).
- [141] Kim, W. *et al.* Hysteresis caused by water molecules in carbon nanotube field-effect transistors. *Nano Letters* **3**, 193–198 (2003).
- [142] Wang, D. *et al.* Surface chemistry and electrical properties of germanium nanowires. *Journal of the American Chemical Society* **126**, 11602–11611 (2004).

- [143] Shur, M. S. Low ballistic mobility in submicron HEMTs. *IEEE Electron Device Letters* **23**, 511–513 (2002).
- [144] Chen, Z. & Appenzeller, J. Mobility extraction and quantum capacitance impact in high performance graphene field-effect transistor devices. In *Proc. IEEE Int. Electron Devices Meeting*, 1–4 (2008).
- [145] Hjort, M. *III–V Nanowire Surfaces*. Ph.D. thesis, Lund University (2014).
- [146] Hou, C. H. *et al.* Effects of surface treatments on interfacial self-cleaning in atomic layer deposition of Al₂O₃ on InSb. *Journal of The Electrochemical Society* **155**, 180–183 (2008).
- [147] Chu, S. *et al.* Electrically pumped waveguide lasing from ZnO nanowires. *Nature nanotechnology* **6**, 506–510 (2011).
- [148] Averin, D. & Nazarov, Y. V. Single-electron charging of a superconducting island. *Phys. Rev. Lett.* **69**, 1993–1996 (1992).
- [149] Clarke, J. & Wilhelm, F. K. Superconducting quantum bits. *Nature* **453**, 1031 (2008).
- [150] Risté, D. *et al.* Millisecond charge-parity fluctuations and induced decoherence in a superconducting transmon qubit. *Nat Commun* **4**, 1913 (2013).
- [151] Alicea, J. New directions in the pursuit of Majorana fermions in solid state systems. *Reports on Progress in Physics* **75**, 076501 (2012).
- [152] Read, N. Topological phases and quasiparticle braiding. *Phys. Today* **65**, 38 (2012).
- [153] Tuominen, M. T., Hergenrother, J. M., Tighe, T. S. & Tinkham, M. Experimental evidence for parity-based 2e periodicity in a superconducting single-electron tunneling transistor. *Phys. Rev. Lett.* **69**, 1997–2000 (1992).
- [154] Eiles, T., Martinis, J. M. & Devoret, M. H. Even-odd asymmetry of a superconductor revealed by the Coulomb blockade of Andreev reflection. *Phys. Rev. Lett.* **70**, 1862–1865 (1993).
- [155] Aumentado, J., Keller, M. W., Martinis, J. M. & Devoret, M. H. Nonequilibrium quasiparticles and 2e periodicity in single-Cooper-pair transistors. *Phys. Rev. Lett.* **92**, 066802 (2004).
- [156] Geerligs, L. J., Anderegg, V. F., Romijn, J. & Mooij, J. E. Single Cooper-pair tunneling in small-capacitance junctions. *Phys. Rev. Lett.* **65**, 377–380 (1990).
- [157] Shaw, M. D., Lutchyn, R. M., Delsing, P. & Echternach, P. M. Kinetics of nonequilibrium quasiparticle tunneling in superconducting charge qubits. *Phys. Rev. B* **78**, 024503 (2008).
- [158] Dolata, R., Scherer, H., Zorin, A. B. & Niemeyer, J. Single-charge devices with ultrasmall Nb/AlOx/Nb trilayer Josephson junctions. *Journal of Applied Physics* **97**, 054501 (2005).

- [159] Savin, A. M. *et al.* Parity effect in Al and Nb single electron transistors in a tunable environment. *Applied Physics Letters* **91**, – (2007).
- [160] Oliver, W. D. & Welander, P. B. Materials in superconducting quantum bits. *MRS Bulletin* **38**, 816–825 (2013).
- [161] Darlinski, A. & Halbritter, J. Angle-resolved XPS studies of oxides at NbN, NbC, and Nb surfaces. *Surface and Interface Analysis* **10**, 223–237 (1987).
- [162] Persky, M. J. Review of black surfaces for space-borne infrared systems. *Review of Scientific Instruments* **70**, 2193–2217 (1999).
- [163] Rainis, D. & Loss, D. Majorana qubit decoherence by quasiparticle poisoning. *Phys. Rev. B* **85**, 174533 (2012).
- [164] Lutchyn, R. M., Glazman, L. I. & Larkin, A. I. Kinetics of the superconducting charge qubit in the presence of a quasiparticle. *Phys. Rev. B* **74** (2006).
- [165] Saira, O.-P., Kemppinen, A., Maisi, V. F. & Pekola, J. P. Vanishing quasiparticle density in a hybrid Al/Cu/Al single-electron transistor. *Phys. Rev. B* **85**, 012504 (2012).
- [166] Dynes, R., Narayanamurti, V. & Garno, J. Direct measurement of quasiparticle-lifetime broadening in a strong-coupled superconductor. *Phys. Rev. Lett.* **41**, 1509–1512 (1978).
- [167] Rajauria, S. *et al.* Efficiency of quasiparticle evacuation in superconducting devices. *Phys. Rev. B* **85**, 020505 (2012).
- [168] Kauppila, V. J., Nguyen, H. Q. & Heikkilä, T. T. Nonequilibrium and proximity effects in superconductor-normal metal junctions. *Phys. Rev. B* **88** (2013).
- [169] Court, N. A., Ferguson, A. J., Lutchyn, R. & Clark, R. G. Quantitative study of quasiparticle traps using the single-Cooper-pair transistor. *Phys. Rev. B* **77**, 100501 (2008).
- [170] Moshchalkov, V. V. *et al.* Effect of sample topology on the critical fields of mesoscopic superconductors. *Nature* **373**, 319–322 (1995).
- [171] Peltonen, J. T., Muhonen, J. T., Meschke, M., Kopnin, N. B. & Pekola, J. P. Magnetic-field-induced stabilization of nonequilibrium superconductivity in a normal-metal/insulator/superconductor junction. *Phys. Rev. B* **84**, 220502 (2011).
- [172] Wang, C. *et al.* Measurement and control of quasiparticle dynamics in a superconducting qubit. *Nat Commun* **5**, 5836 (2014).
- [173] Toppari, J. J. *et al.* Cooper-pair resonances and subgap Coulomb blockade in a superconducting single-electron transistor. *Phys. Rev. B* **76**, 172505 (2007).
- [174] Ambegaokar, V. & Baratoff, A. Tunneling between superconductors. *Phys. Rev. Lett.* **10**, 486–489 (1963).

- [175] Matveev, K. A., Gisselält, M., Glazman, L. I., Jonson, M. & Shekhter, R. I. Parity-induced suppression of the Coulomb blockade of Josephson tunneling. *Phys. Rev. Lett.* **70**, 2940–2943 (1993).
- [176] Lutchyn, R. M. Effect of quantum fluctuations on even-odd energy difference in a Cooper-pair box. *Phys. Rev. B* **75**, 212501 (2007).
- [177] Massarotti, D. *et al.* Escape dynamics in moderately damped Josephson junctions. *Low Temperature Physics* **38**, 263–272 (2012).
- [178] Coon, D. D. & Fiske, M. D. Josephson AC and step structure in the supercurrent tunneling characteristic. *Physical Review* **138**, A744 (1965).
- [179] Matsunaga, T., Maezawa, H. & Noguchi, T. Characterization of NbTiN thin films prepared by reactive DC-magnetron sputtering. *Applied Superconductivity, IEEE Transactions on* **13**, 3284–3287 (2003).
- [180] Koch, C. C., Scarbrough, J. O. & Kroeger, D. M. Effects of interstitial oxygen on the superconductivity of niobium. *Physical Review B* **9**, 888 (1974).
- [181] Halbritter, J. On the oxidation and on the superconductivity of niobium. *Applied Physics A* **43**, 1–28 (1987).
- [182] Fulton, T. A. & Dunkleberger, L. N. Lifetime of the zero-voltage state in Josephson tunnel junctions. *Physical Review B* **9**, 4760 (1974).
- [183] Dubi, Y., Meir, Y. & Avishai, Y. Nature of the superconductor–insulator transition in disordered superconductors. *Nature* **449**, 876–880 (2007).
- [184] Sacépé, B. *et al.* Localization of preformed Cooper pairs in disordered superconductors. *Nature Physics* **7**, 239–244 (2011).
- [185] Coumou, P. C. J. J., Driessen, E. F. C., Bueno, J., Chapelier, C. & Klapwijk, T. M. Electrodynamic response and local tunneling spectroscopy of strongly disordered superconducting TiN films. *Physical Review B* **88**, 180505 (2013).
- [186] Bespalov, A., Houzet, M., Meyer, J. S. & Nazarov, Y. V. Density of states in gapped superconductors with pairing-potential impurities. *Physical Review B* **93**, 104521 (2016).
- [187] Kittel, C. *Introduction to solid state physics* (Wiley, 1996).
- [188] Geim, A. K. *et al.* Phase transitions in individual sub-micrometre superconductors. *Nature* **390**, 259–262 (1997).
- [189] Palacios, J. J. Vortex matter in superconducting mesoscopic disks: Structure, magnetization, and phase transitions. *Phys. Rev. B* **58**, 5948–5951 (1998).
- [190] Stan, G., Field, S. B. & Martinis, J. M. Critical field for complete vortex expulsion from narrow superconducting strips. *Phys. Rev. Lett.* **92**, 097003 (2004).

- [191] Aranson, I., Gitterman, M. & Shapiro, B. Y. Onset of vortices in thin superconducting strips and wires. *Phys. Rev. B* **51**, 3092–3096 (1995).
- [192] Giaever, I. Detection of the AC Josephson effect. *Phys. Rev. Lett.* **14**, 904–906 (1965).
- [193] Holst, T., Esteve, D., Urbina, C. & Devoret, M. H. Effect of a transmission line resonator on a small capacitance tunnel junction. *Phys. Rev. Lett.* **73**, 3455 (1994).
- [194] Deblock, R., Onac, E., Gurevich, L. & Kouwenhoven, L. P. Detection of quantum noise from an electrically driven two-level system. *Science* **301**, 203–206 (2003).
- [195] Hofheinz, M. *et al.* Bright side of the Coulomb blockade. *Phys. Rev. Lett.* **106**, 217005 (2011).
- [196] Xiang, J., Vidan, A., Tinkham, M., Westervelt, R. M. & Lieber, C. M. Ge/Si nanowire mesoscopic Josephson junctions. *Nature nanotechnology* **1**, 208–213 (2006).
- [197] Della Rocca, M. *et al.* Measurement of the current-phase relation of superconducting atomic contacts. *Physical review letters* **99**, 127005 (2007).
- [198] Takei, S., Fregoso, B. M., Hui, H.-Y., Lobos, A. M. & Das Sarma, S. Soft superconducting gap in semiconductor Majorana nanowires. *Phys. Rev. Lett.* **110**, 186803 (2013).
- [199] De Lange, G. *et al.* Realization of microwave quantum circuits using hybrid superconducting-semiconducting nanowire Josephson elements. *Phys. Rev. Lett.* **115**, 127002 (2015).
- [200] Blanter, Y. M. & Büttiker, M. Shot noise in mesoscopic conductors. *Physics reports* **336**, 1–166 (2000).
- [201] Dolan, G. J. Offset masks for lift-off photoprocessing. *Applied Physics Letters* **31**, 337–339 (1977).
- [202] Chauvin, M. *et al.* Crossover from Josephson to multiple Andreev reflection currents in atomic contacts. *Physical review letters* **99**, 067008 (2007).
- [203] Raw data and calculations available at <http://tinyurl.com/rawdata-pat>.
- [204] Parker, W. H., Taylor, B. N. & Langenberg, D. N. Measurement of $2e/h$ using the AC Josephson effect and its implications for quantum electrodynamics. *Phys. Rev. Lett.* **18**, 287 (1967).
- [205] Gül, Ö. *et al.* Towards high mobility InSb nanowire devices. *Nanotechnology* **26**, 215202 (2015).
- [206] Beenakker, C. W. J. & Büttiker, M. Suppression of shot noise in metallic diffusive conductors. *Physical Review B* **46**, 1889 (1992).
- [207] Cron, R., Goffman, M. F., Esteve, D. & Urbina, C. Multiple-charge-quanta shot noise in superconducting atomic contacts. *Physical review letters* **86**, 4104 (2001).

- [208] Hoss, T. *et al.* Multiple Andreev reflection and giant excess noise in diffusive superconductor/normal-metal/superconductor junctions. *Physical Review B* **62**, 4079 (2000).
- [209] Plugge, S., Rasmussen, A., Egger, R. & Flensberg, K. Majorana box qubits. *arXiv:1609.01697* (2016).
- [210] Houtzager, E., van den Brom, H. E. & van Woerkom, D. Automatic tuning of the pulse-driven AC Josephson voltage standard. *Proc. CPEM* 185–186 (2010).
- [211] Sticlet, D., Nijholt, B. & Akhmerov, A. Robustness of Majorana bound states in the short junction limit. *arXiv:1609.00637* (2016).
- [212] Meservey, R., Tedrow, P. M. & Fulde, P. Magnetic field splitting of the quasiparticle states in superconducting aluminum films. *Phys. Rev. Lett.* **25**, 1270 (1970).
- [213] Bruno, R. C. & Schwartz, B. B. Magnetic field splitting of the density of states of thin superconductors. *Phys. Rev. B* **8**, 3161–3178 (1973).
- [214] Sau, J. D. & Setiawan, F. Detecting topological superconductivity using the Shapiro steps. *arXiv:1609.00372* (2016).
- [215] Larsen, T. W. *et al.* Semiconductor-nanowire-based superconducting qubit. *Phys. Rev. Lett.* **115**, 127001 (2015).
- [216] Riwar, R.-P., Houzet, M., Meyer, J. S. & Nazarov, Y. V. Multi-terminal Josephson junctions as topological matter. *Nature communications* **7** (2016).
- [217] Bretheau, L., Girit, Ç., Pothier, H., Esteve, D. & Urbina, C. Exciting Andreev pairs in a superconducting atomic contact. *Nature* **499**, 312–315 (2013).
- [218] Chtchelkatchev, N. M. & Nazarov, Y. V. Andreev quantum dots for spin manipulation. *Phys. Rev. Lett.* **90**, 226806 (2003).
- [219] Landauer, R. Can a length of perfect conductor have a resistance? *Physics Letters A* **85**, 91–93 (1981).
- [220] Kulik, I. O. Macroscopic quantization and the proximity effect in SNS junctions. *Soviet Journal of Experimental and Theoretical Physics* **30**, 944–950 (1970).
- [221] Pillet, J.-D. *et al.* Andreev bound states in supercurrent-carrying carbon nanotubes revealed. *Nat. Phys.* **6**, 965–969 (2010).
- [222] Chang, W., Manucharyan, V. E., Jespersen, T. S., Nygård, J. & Marcus, C. M. Tunneling spectroscopy of quasiparticle bound states in a spinful Josephson junction. *Phys. Rev. Lett.* **110**, 217005 (2013).
- [223] Kos, F., Nigg, S. E. & Glazman, L. I. Frequency-dependent admittance of a short superconducting weak link. *Physical Review B* **87**, 174521 (2013).

- [224] Väyrynen, J. I., Rastelli, G., Belzig, W. & Glazman, L. I. Microwave signatures of Majorana states in a topological Josephson junction. *Phys. Rev. B* **92**, 134508 (2015).
- [225] Bretheau, L. *et al.* Theory of microwave spectroscopy of Andreev bound states with a Josephson junction. *Physical Review B* **90**, 134506 (2014).
- [226] Cheng, M. & Lutchyn, R. M. Josephson current through a superconductor/semiconductor-nanowire/ superconductor junction: Effects of strong spin-orbit coupling and Zeeman splitting. *Phys. Rev. B* **86**, 134522 (2012).
- [227] Das, A. *et al.* Zero-bias peaks and splitting in an Al-InAs nanowire topological superconductor as a signature of Majorana fermions. *Nature Physics* **8** (2012).
- [228] Nijholt, B. & Akhmerov, A. R. Orbital effect of magnetic field on the Majorana phase diagram. *Phys. Rev. B* **93**, 235434 (2016).
- [229] Meservey, R. & Tedrow, P. M. Properties of very thin aluminum films. *Journal of Applied Physics* **42**, 51–53 (1971).
- [230] Yokoyama, T., Eto, M. & Nazarov, Y. V. Josephson current through semiconductor nanowire with spin–orbit interaction in magnetic field. *Journal of the Physical Society of Japan* **82**, 054703 (2013).
- [231] Krive, I. V., Gorelik, L. Y., Shekhter, R. I. & Jonson, M. Chiral symmetry breaking and the Josephson current in a ballistic superconductor–quantum wire–superconductor junction. *Low temperature physics* **30**, 398–404 (2004).
- [232] Buzdin, A. Direct coupling between magnetism and superconducting current in the Josephson φ_0 junction. *Phys. Rev. Lett.* **101**, 107005 (2008).
- [233] Liu, J.-F. & Chan, K. S. Relation between symmetry breaking and the anomalous Josephson effect. *Phys. Rev. B* **82**, 125305 (2010).
- [234] Rasmussen, A. *et al.* Effects of spin-orbit coupling and spatial symmetries on the Josephson current in SNS junctions. *Physical Review B* **93**, 155406 (2016).
- [235] Konschelle, F., Tokatly, I. V. & Bergeret, F. S. Theory of the spin-galvanic effect and the anomalous phase shift φ_0 in superconductors and Josephson junctions with intrinsic spin-orbit coupling. *Physical Review B* **92**, 125443 (2015).
- [236] Villegas, J. E. *et al.* A superconducting reversible rectifier that controls the motion of magnetic flux quanta. *Science* **302**, 1188–1191 (2003).
- [237] Reynoso, A. A., Usaj, G., Balseiro, C. A., Feinberg, D. & Avignon, M. Anomalous Josephson current in junctions with spin polarizing quantum point contacts. *Phys. Rev. Lett.* **101**, 107001 (2008).
- [238] Krogstrup, P. *et al.* *In preparation* (2017).

- [239] Vuik, A., Eeltink, D., Akhmerov, A. R. & Wimmer, M. Effects of the electrostatic environment on the Majorana nanowire devices. *New Journal of Physics* **18**, 033013 (2016).
- [240] Raw data available at <http://tinyurl.com/rawdata-abs>.
- [241] Vurgaftman, I., Meyer, J. R. & Ram-Mohan, L. R. Band parameters for III-V compound semiconductors and their alloys. *Journal of Applied Physics* **89**, 5815–5875 (2001).
- [242] Nesterov, K. N., Houzet, M. & Meyer, J. S. Anomalous Josephson effect in semiconducting nanowires as a signature of the topologically nontrivial phase. *Phys. Rev. B* **93**, 174502 (2016).
- [243] Cole, W. S., Sau, J. D. & Das Sarma, S. Proximity effect and Majorana bound states in clean semiconductor nanowires coupled to disordered superconductors. *Phys. Rev. B* **94**, 140505 (2016).
- [244] Anthore, A., Pothier, H. & Esteve, D. Density of states in a superconductor carrying a supercurrent. *Phys. Rev. Lett.* **90**, 127001 (2003).
- [245] Nilsson, H. A. *et al.* Giant, level-dependent g factors in InSb nanowire quantum dots. *Nano letters* **9**, 3151–3156 (2009).
- [246] Olsson, L. *et al.* Charge accumulation at InAs surfaces. *Phys. Rev. Lett.* **76** (1996).
- [247] Bhargava, S., Blank, H.-R., Narayanamurti, V. & Kroemer, H. Fermi-level pinning position at the Au–InAs interface determined using ballistic electron emission microscopy. *Applied physics letters* **70**, 759–761 (1997).
- [248] Winkler, G. W., Soluyanov, A. A., Wu, Q., Troyer, M. & Krogstrup, P. Topological phases in $\text{InAs}_{1-x}\text{Sb}_x$: From novel topological semimetal to Majorana wire. *arXiv:1602.07001* (2016).
- [249] Court N A., A. J., Ferguson & Clark, R. G. Energy gap measurement of nanostructured aluminium thin films for single Cooper-pair devices. *Superconductor Science and Technology* **21**, 015013 (2007).
- [250] Schäpers, T. *Superconductor/semiconductor junctions*, vol. 174 (Springer Science & Business Media, 2001).
- [251] Karzig, T. *et al.* Scalable designs for quasiparticle-poisoning-protected topological quantum computation with Majorana zero modes. *arXiv:1610.05289* (2016).
- [252] Muhonen, J. T., Meschke, M. & Pekola, J. P. Micrometre-scale refrigerators. *Reports on Progress in Physics* **75**, 046501 (2012).
- [253] van Heck, B., Mi, S. & Akhmerov, A. R. Single fermion manipulation via superconducting phase differences in multiterminal Josephson junctions. *Phys. Rev. B* **90**, 155450 (2014).

-
- [254] Vijay, S. & Fu, L. Braiding without braiding: Teleportation-based quantum information processing with Majorana zero modes. *arXiv:1609.00950* (2016).
- [255] Bretheau, L., Girit, Ç., Urbina, C., Esteve, D. & Pothier, H. Supercurrent spectroscopy of Andreev states. *Physical Review X* **3**, 041034 (2013).
- [256] Hell, M., Danon, J., Flensberg, K. & Leijnse, M. Time scales for Majorana manipulation using Coulomb blockade in gate-controlled superconducting nanowires. *Physical Review B* **94** (2016).
- [257] Bagwell, P. F. Suppression of the Josephson current through a narrow, mesoscopic, semiconductor channel by a single impurity. *Physical Review B* **46**, 12573 (1992).
- [258] Desai, B. *Quantum mechanics with basic field theory* (Cambridge Uni. Press, 2010).
- [259] Falci, G., Bubanja, V. & Schön, G. Quasiparticle and Cooper pair tunneling in small capacitance Josephson junctions. *Zeitschrift für Physik B* **85** (1991).
- [260] Ingold, G.-L. & Nazarov, Y. V. Charge tunneling rates in ultrasmall junctions. In *Single charge tunneling*, 21–107 (Springer, 1992).

ACKNOWLEDGEMENTS

PhD research is not something that you do on your own. Many bright and smart people supported me and helped me to overcome my challenges. I am grateful to all of you: from cleaning staff to scientific staff and from my promotion commission to the Graduate School complaints commission, thank you.

It was you, Leo, who made my career dream of becoming a scientist come true. You gave me much freedom and great facilities, but I sometimes missed the moments when we were sitting next to each other checking the raw data, as we did during my master's. It was also great that you gave me the opportunity to work with Attila.

Attila, my Jedi master, we worked together on a few projects and I believe they were all quite successful. We are very opposite in many ways and that's why our two-man team was so complete. You taught me many new things, and it was great to be your padawan. I was not always easy to work with, so sorry for that.

From the old days, it was Vincent, Kun and Sergey who showed me the scientific world and explained me how it worked (or not). Thank you for changing my (scientific) diapers and making me ready to stand on my own two feet. I really enjoyed our time together at the start of the Majo-team. Önder, it's a shame the Majo-box was not a success and we decided to part ways; all the best at Harvard. Jakob, it's good that you also found out that there are more important things than your PhD; enjoy them. Johan, mister world traveller, thank you for your endless patience explaining the Janisses to me. Fei, it was nice to work next to you. I hope you become a partner one day and you get your Ferrari. Arjan, it's great to see you happy now. I hope that will continue for a long time. You also often helped me to get out of trouble with the bonder or whatever, thank you. Fanming, I hope you had as much as fun as I had, I find you adorable and good luck with your position in China. Daniel, no ballistic π junction (yet) but a ϕ_0 junction in Coulomb blockade, how cool! All the best with your wife, down under. Ilse, I hope you are now happy with the job and boyfriend you have found. Maja, all the best with William and I hope you find a nice position in Australia, or somewhere else with a lot of sunshine.

My bachelor's and master's students. René, you delivered very nice work and were very responsible and active in maintaining the collaboration with SQ. It is great that you have found a job with them, and good luck with your further career. Tamás, your passion and persistence in the cleanroom was amazing. I am glad that we will see each other more often in Zürich. Ruben, everything that you touch turns to gold, your coding skills are unique and your ability to understand physics is stunning. I hope we will work together once again side-by-side. Bram, thank you for tuning the NbTiN recipe up again. I wish you also the best with all your very important associated activities, and keep up the good work. Bas, good to see you back in the group as a master's student, it seems you liked it! Even if your BSc work did not become a paper, your motivation and working spirit were not the issue, they were great. Daniël, you chose me as your Jedi master and

we made great devices and did awesome experiments. I am happy to see you continuing 'my' projects fully independently as a PhD student.

Dominique, you are also continuing 'my' projects. Your experimental skills are of a very high standard and I am sure you will turn the projects into a success. It's great to have you.

The group also had many non-David-supervised students. First, Fokko, who also worked with Vincent during his master's. Good luck with running, finding a girl¹ and with your PhD. Thanks for all the conversations and not getting angry when I ate your food. Ludo, it's good that you followed your heart to Groningen where you had great success, both PhD and private wise. Debbie, I liked your discussions about life, and your report is still very useful. Good luck wherever you are on this planet speaking perfect English. Willemijn, glad that you continued as a PhD student, I know you are capable of it, good luck. Jasper, your contribution to the hard gap project was very important, it's just a pity the Majo-box of your master's project did not work. I hope during your PhD you make up for that and deliver great results; you are capable of it.

James and Alex, you are really cool and enjoy life. All the best and be a little bit nice to me this evening. I was always nice to you. Alex, I hope you have all the tough moments of your PhD behind you, and thank you for helping me out when I was not there. James, it is also nice to see you evolving, and I hope we will meet again to catch up.

Other younger-generation group members Jouri, Michiel, I am looking forward to your first-author work, I'm sure it will be great. Damaz, thank you for your help getting me to FOM Veldhoven. The dinner in Santa Barbara I also remember with a smile. John and Srijit, you both have amazing cleanroom and experimental skills. I know you will both be successful and our roads will cross again, hopefully including some beers!

Hans Mooij, I found our few conversations very inspiring. I hope you can continue research as long as you want. Leo DiCarlo, I hope you like me in the end, I like you at least in a good way. I am looking forward to drinking some beers and catching up in Zürich when you visit. Lieven, you taught me the basic stuff during the Mesoscopic course and now you are on my committee. I wish you all the best also with your family. Ronald, you were my 'Introduction to Quantum Mechanics' teacher and maybe I will ask you for your signature one day.

All the members of the committee, thank you for being a part of it. I am looking forward to your challenging questions.

Srijit, Toivo, Stefan, Ale and Chris, you made that special FOM Veldhoven unforgettable, it was great! Niels, Julia, Florian, Suzanne, Gabriel, Fokko, Francesco, Sonia, Adriaan and Jelmer, it was great to run behind or with you, it was fun. Julia, thank you for being my exhaust once in a while during our many conversations. Ale, your parties are great, I hope I will not miss too many. Good luck, first real quantum engineer. Nick, Jason, Marina and Olaf, your specialization was always very useful; keep up the good work.

Bram, Jelle, Remco, Mark and Siebe, I did not really break much more stuff than anybody else, I am just really honest. Still, I am grateful for all the times that you fixed stuff for me. Mark, our conversations were also often what I needed at that point, and good luck with the boefjes. Raymond, Raymond, Marijn, Nico and the zillions of internship

¹Rumours are that you've found one!

students, thank you for helping me with all kinds of electronic and fine mechanical problems.

The cleanroom staff were also very important for my research. I had great help from Marco, Marco, Frank, Arnold, Ewan, Roel, Hozanne, Charles, Anja and Eugene. Especially you, Marc, your help always came at the right moment. Thank you also for the very private conversations.

I also had great support from behind the scenes from Tineke, Anouschka and Kemo. And in the foreground, great support from my talking buddies, Heera and Simone. BTW you are also great mothers. Simone, you really took a load off my hands too, great support. I cannot wait till you become my PA after Leo's retirement. Also Chantal, Marja, Yuki, Jenny and Marion, thank you for all the assistance and help to get the group working better.

I also had great collaborators across the lab and across the globe. The nanowire-transmons with Gijs and Leo DiCarlo were really cool. Maja and James, it was not always easy but I hope the first results come out soon. Alex, maybe one day the nanowire thermometer and heat transfer junction gadgets will get published, keep going. Max, Kyle and Gijs, the nanowire Andreev qubit is the future (or not). It is a cool project and I am glad it seems to be working out. Good luck guys.

I had a great collaboration with the nanowire growers. The InSb nanowire from Diana, Sebastian and Erik even resulted in the mobility paper back in 2015. Thank you for these nice wires and get the beast in the cleanroom working, braiding is within reach. Anton and Sebastian, bad luck that the model did not describe our switching current data. Anton, special words for you, you're really a big guy, everything that you said I believed straight away. It's really cool to know you. Charlie, thank you for inviting me to Copenhagen, I enjoyed the visit and the lab is great. Also, together with Peter and Jasper you gave me access to the really awesome Copenhagen wires, which made my (PhD) life much easier. Michael, all your comments on my work and thesis were useful, and good luck with the family.

Jason Petta, Patrice Bertet, both your labs are so cool, thank you for inviting me over. It was a really tough decision to choose my postdoc. Future boss, I cannot wait to start and get my hands dirty in your cleanroom and lab. Andreas, after months behind the computer, I am very motivated to deliver some outstanding work. Let's rock some science!

I met many great people at conferences/workshops, a few that come to mind are Zazunov, Aguado, Martinis, De Franceschi and Marcus. You gave me the inspiration to get my ass back to the lab as soon as possible.

I am also fortunate to have met more than a dozen Nobel prize winners, of which the encounter with Philip W. Anderson was my most memorable one. Thank you to all of you for getting me out of my PhD frustration and motivating me to get going again.

Ook in mijn (semi-)privé heb ik veel aan mensen te danken. Coen Swarts, bedankt voor al die mooie lessen op de TH Rijswijk, heel inspirerend. Maudy, Sjoerd, Teun en de rest van het cluppie. Hoe vaak zaten we wel niet in de bieb te stoeien met het huiswerk tijdens onze master, we hebben het gehaald, yes! Chiel, mijn oude huisgenoot, we zijn goede vrienden en ik ben blij dat je mijn paranimf wil zijn, het gaat je goed met Zhara

en tot in Zürich. Gentlemens², dat er maar veel elitaire borrels mogen komen en dat we allemaal maar veel nakomelingen mogen krijgen om het dispuut in stand te houden, toffe tijd gasten!

Schoonfamilie, dank voor het accepteren dat ik Ilse 'heb', ik zal heel goed voor haar en ons gezin zorgen, dat beloof ik. We moeten elkaar echt niet uit het oog verliezen, ook niet als we in Zwitserland wonen, jullie mogen altijd langskomen. En Oma Herrie, speciale woorden voor u, ik hoop dat u nog lang in goede gezondheid bij ons mag zijn. Pieter-Jan en de kids, ik weet dat het allemaal goed gaat komen, met een ieder van jullie. Oma en Cor, ik hoop dat jullie ook nog lang in goede gezondheid bij ons zijn. Ik kan niet wachten tot jullie langskomen in Zwitserland, blijf van het leven genieten. Pap en mam, jammer dat jullie niet meer bij elkaar zijn. Gelukkig was dat tijdens mijn hele opvoeding wel zo en ik ben heel blij met hoe ik ben geworden en hoe ik in het leven sta. Ik wil jullie daarvoor uit de grond van mijn hart bedanken. Ik ben heel trots op jullie en ik hou heel veel van jullie, allebei³. Broers, Den en Vin, ik ben heel blij dat jullie mijn broers zijn en ik vind het geweldig dat jullie allebei een eigen weg bewandelen in de wereld. Waar, hoe of wanneer, wij zijn broers en kunnen altijd op elkaar rekenen. Vinnyboy, de cover van deze thesis is prachtig geworden, dank!

Ilse en Sam, jullie zijn het allerbelangrijkste voor mij op deze wereld, gister, vandaag en voor altijd. Ilse, ik snap dat je je vaak op een tweede plek voelde staan, maar dat was echt niet zo. Ik moest vaak aan je denken en ook aan deze dag, die wij *samen* bereikt hebben. Behalve dat je de liefde van mijn leven bent, ben je ook de vleugels van mijn vlucht. Wat ik vandaag in dit proefschrift heb afgeleverd kon ik alleen maar doen met jou aan mijn zijde. Ilse, ik hou van je.

Sam, jij ben de toekomst, mijn toekomst. Het mooiste wat er bestaat en papa zou alles inleveren voor jouw geluk, jouw geluk is ons geluk. Ik hoop dat wij nog vele mooie momenten mogen beleven en op een dag zal ik uitleggen wat dit boekje betekent. Je mag altijd onder onze vleugels schuilen en voor nu, ga zo door, je bent mijn trots.

²Thijs, Pluk, Bart, Herald en Maarten.

³Dat zeg ik te weinig, ik hoop dat jullie het gewoon voelen.



Figuur 1: Mijn PhD is over, ik heb mijn Marathon gerend. Ik ben er klaar mee, het ligt achter mij. Batterij opladen en op naar het volgende avontuur, bedankt voor alle hulp, het gaat jullie goed.

CURRICULUM VITÆ

David Johannes van Woerkom

4 July 1988 Born in Schiedam, The Netherlands.

EDUCATION

2000-2005	Secondary School Higher general continued education (HAVO) Schravenlant, Schiedam and 't Rijks, Bergen op Zoom
2005-2009	Bachelor of Engineering, Applied Physics The Hague University
2009-2012	Master of Science, Applied Physics Delft University of Technology
2012-2016	PhD research, Delft University of Technology Supervision by: L.P. Kouwenhoven Quantum Transport group, QuTech and Kavli Institute of Nanoscience
2017-	Postdoctoral research, ETH Zürich Supervision by: A. Wallraff Quantum Device lab

LIST OF PUBLICATIONS

1. *Magnetic field induced 4π periodic Josephson effect in InAs nanowires*
D. J. van Woerkom*, D. Laroche*, D. Bouman*, A. Proutski, R. J. J. van Gulik, M. P. Nowak, D. I. Pikulin, P. Krogstrup, J. Nygård, C. M. Marcus, L. P. Kouwenhoven, A. Geresdi
In preperation
2. *Electron-phonon coupling in a one-dimensional semiconducting nanowire*
A. Proutski, **D. J. van Woerkom**, R. J. J. van Gulik, D. Car, S. R. Plissard, E. P. A. M. Bakkers, L. P. Kouwenhoven, A. Geresdi
In preperation
3. *Circuit QED with Andreev bound states in a semiconducting nanowire Josephson junction*
M. Hays, G. de Lange, K. Serniak, **D. J. van Woerkom**, J. I. Väyrynen, B. van Heck, V. Sivak, U. Vool, P. Krogstrup, J. Nygård, L. Frunzio, A. Geresdi, L. I. Glazman, M. H. Devoret
In preperation
4. *A semiconductor nanowire Josephson junction microwave laser*
M. C. Cassidy, W. Uilhoorn, J. G. Kroll, D. de Jong, **D. J. van Woerkom**, J. Nygård, P. Krogstrup, L. P. Kouwenhoven
In preperation
5. *Supercurrent interference in few-mode nanowire Josephson junctions*
K. Zuo*, V. Mourik*, D. B. Szombati, B. Nijholt, **D. J. van Woerkom**, A. Geresdi, J. Chen, V. P. Ostroukh, A. R. Akhmerov, S. R. Plissard, D. Car, E. P. A. M. Bakkers, D. I. Pikulin, L. P. Kouwenhoven, S. M. Frolov
In preperation
6. *Josephson radiation and shot noise of a semiconductor nanowire junction*
D. J. van Woerkom, A. Proutski, R. J. J. van Gulik, T. Kriváchy, D. Car, S. R. Plissard, E. P. A. M. Bakkers, L. P. Kouwenhoven, A. Geresdi
arXiv:1702.02804
7. *Hard superconducting gap in InSb nanowires*
Ö. Gül, H. Zhang, F. K. de Vries, J. van Veen, K. Zuo, V. Mourik, S. Conesa-Boj, M. P. Nowak, **D. J. van Woerkom**, M. Quintero-Pérez, M. C. Cassidy, A. Geresdi, S. Kölling, D. Car, S. R. Plissard, E. P. A. M. Bakkers, L. P. Kouwenhoven
arXiv:1702.02578

8. *Microwave spectroscopy of spinful Andreev bound states in ballistic semiconductor Josephson junctions*
D. J. van Woerkom, A. Proutski, B. van Heck, D. Bouman, J. I. Väyrynen, L. I. Glazman, P. Krogstrup, J. Nygård, L. P. Kouwenhoven, A. Geresdi
arXiv:1609.00333
9. *Ballistic Majorana nanowire devices*
H. Zhang*, Ö. Gül*, S. Conesa-Boj, K. Zuo, V. Mourik, F. K. de Vries, J. van Veen, **D. J. van Woerkom**, M. P. Nowak, M. Wimmer, D. Car, S. R. Plissard, E. P. A. M. Bakkers, M. Quintero-Pérez, A. Geresdi, S. Kölling, S. Goswami, K. Watanabe, T. Taniguchi and L. P. Kouwenhoven
arXiv:1603.04069
10. *Realization of microwave quantum circuits using hybrid superconducting-semiconducting nanowire Josephson element*
G. de Lange, B. van Heck, A. Bruno, **D. J. van Woerkom**, A. Geresdi, S.R. Plissard, E.P.A.M. Bakkers, A.R. Akhmerov, L. DiCarlo
Physical Review Letters, **115**, 127002 (2015)
11. *Honderd biljoen deeltjes, niet één meer of minder!*
D. J. van Woerkom
Nederlands tijdschrift voor Natuurkunde, 03-2015
12. *One minute parity lifetime of a NbTiN Cooper-pair transistor*
D. J. van Woerkom*, A. Geresdi* and L.P. Kouwenhoven
Nature Physics, **11**, 547–550 (2015)
13. *Towards high mobility InSb nanowire devices*
Ö. Gül*, **D. J. van Woerkom***, I. van Weperen*, D. Car, S. R. Plissard, E. P. A. M. Bakkers and L. P. Kouwenhoven
Nanotechnology, **26**, 215202 (2015)
14. *Automatic tuning of the pulse-driven AC Josephson voltage standard*
E. Houtzager, H. E. Van den Brom, and **D. van Woerkom**
Proc. CPDM, 185-186 (2010)

*equal contribution